Alma Mater Studiorum · Università di Bologna

Dipartimento di Fisica e Astronomia "Augusto Righi"
Laurea Magistrale in Fisica del Sistema Terra

Multi-Scale Validation of a Coupled Physical Biogeochemical Model of the Northern Adriatic Sea

Supervisor:
Prof. Marco Zavatarelli

Co-supervisor:
Prof. Paolo Oddo

Submitted by:
Alessandro Gozzoli

Anno Accademico 2024/2025
Appello IV

I would like to express my deepest gratitude to Professor Marco Zavatarelli and Professor Paolo Oddo for their invaluable guidance, continuous support, and insightful supervision throughout the development of this thesis. Their expertise and constructive feedback have been essential to the successful completion of this work.

Abstract

This thesis presents a multi-scale validation of a coupled physical–biogeochemical model of the Northern Adriatic Sea. The modelling system couples the NEMO ocean general circulation model (OGCM, v3.6) with the Biogeochemical Flux Model (BFM), run on a domain covering the Northern Adriatic (43.50°N–46.00°N, 12.20°E–16.20°E) at 1 km horizontal resolution and 47 uniform vertical z-layers (2 m thickness), for a ten-year period (2000–2009) following a hindcast approach. The configuration includes an explicit benthic–pelagic coupling, realistic bathymetry (GEBCO), and river forcing with a focus on the Po River influence. The main model objectives are the correct reproduction of key physical processes (sea surface temperature, stratification, dense-water formation and cascading), the simulation of pelagic and benthic biogeochemical variables with emphasis on chlorophyll and dissolved oxygen, and the evaluation of the model skill across temporal and spatial scales using an extensive observational dataset (CMEMS satellite SST and Chl-a and CTD sampling obtained using DAPHNE/ ARPAE fixed stations, ADRIA cruises, and river discharge records).

A comprehensive validation framework is implemented. Basin-mean and spatial comparisons are supported by time-series diagnostics, seasonal decomposition, robust scatter regressions, efficiency metrics (R^2, Nash–Sutcliffe, Index of Agreement), spatial error components (mean bias, standard-deviation error, cross-correlation, unbiased RMSE), target plots, Taylor diagrams, and spectral analyses including Butterworth filtering and cross-wavelet coherence. A Region Of Freshwater Influence (ROFI) associated with the Po plume is identified using k-means clustering and traced via LOWESS-based trajectory estimation; bio-geophysical profiles within the ROFI are validated against in-situ vertical casts. Bottom-layer diagnostics focus on dense water volumes, bottom oxygen profiles and evolution, and the spatial extent of hypoxic masses.

Key results indicate that the coupled system reproduces the seasonal cycle and large-scale patterns of SST with generally high spatial coherence and positive efficiency metrics, while revealing localized biases (notably near the Po delta, Marano Lagoon and Kvarner Bay) and seasonal amplitude differences (largest mismatches in February–March and July–August). Spatial error maps and unbiased RMSE highlight areas of enhanced deviation likely linked to river plume dynamics and coastal processes.

Chlorophyll-a dynamics are captured in their broad temporal structure and spatial distribution: the model reproduces the winter peak and the seasonal cycle and shows good skill in temporal coherence with observations, although systematic offsets versus in-situ fluorimetric measurements (higher observed concentrations) and a slight phase lag (model peaks lagging observations by ~ 1 month) are documented. Trend analysis of modeled and observed chlorophyll identifies a statistically significant regime shift in the period around 2007; complementary analysis reveals a coincident breakpoint in Po discharge at 1 January 2007, implicating changes in river forcing as a major driver of the biogeochemical shift. Spatial diagnostics within the Po ROFI show that the model reproduces the plume footprint and its influence on surface chlorophyll distributions, but absolute magnitudes and fine-scale coastal contrasts remain challenging.

Dense-water formation and cascading are analyzed through objective volume metrics, lag-correlation analyses and transects: the simulation captures episodic production of North-Adriatic Dense Water (NAdDW) and its downslope propagation along the western margin, with notable interannual variability. Bottom oxygen diagnostics reveal recurrent hypoxic areas (maximum extent during July–September climatology), an intensification of hypoxic coverage beginning ca. 2004, but no persistent anoxic cells ($O_2 = 0$) in the simulated period. The modeled benthic oxygen fronts are spatially linked to the PO ROFI and to regions of elevated organic deposition in the western shelf.

Overall, the coupled model demonstrates robust skill in reproducing multi-scale physical and biogeochemical patterns of the Northern Adriatic, while identifying clear directions for improvement: refinement of river forcing and nutrient loads, enhanced representation of small-scale coastal processes and plume dynamics, possible inclusion of a more detailed diagenetic sediment module, and targeted parameter calibration to reduce chlorophyll magnitude bias and timing offsets. These improvements would strengthen applicability for management-oriented scenario testing (e.g., hypoxia risk, eutrophication trends) and for long-term climate sensitivity studies. The thesis delivers a transparent, reproducible validation protocol that can be extended to other shelf systems and to future coupled model developments.

Contents

Chapter 1
Introduction

1.1 The Adriatic Sea

The Adriatic Sea (*Figure 1.1*) is a semi-enclosed basin of the Mediterranean Sea, oriented along a northwest–southeast axis and bounded to the west by the Italian peninsula and to the east by the Balkan peninsula. Its latitudinal extent lies approximately between 45°N, near the Gulf of Trieste, and 40°N in the Strait of Otranto, the only direct connection with the Ionian Sea and, consequently, with the eastern Mediterranean basin (Artegiani et al., 1997a; Cushman-Roisin et al., 2001). In terms of size, the basin extends for $\sim$ 800 km in length, with a typical width between $\sim$ 150 and $\sim$ 200 km, narrowing toward the south; the Strait of Otranto, about 70–80 km wide, features a sill with depths close to 800 m, key factors for the dynamics of exchanges with the rest of the Mediterranean (Cushman-Roisin et al., 2001).

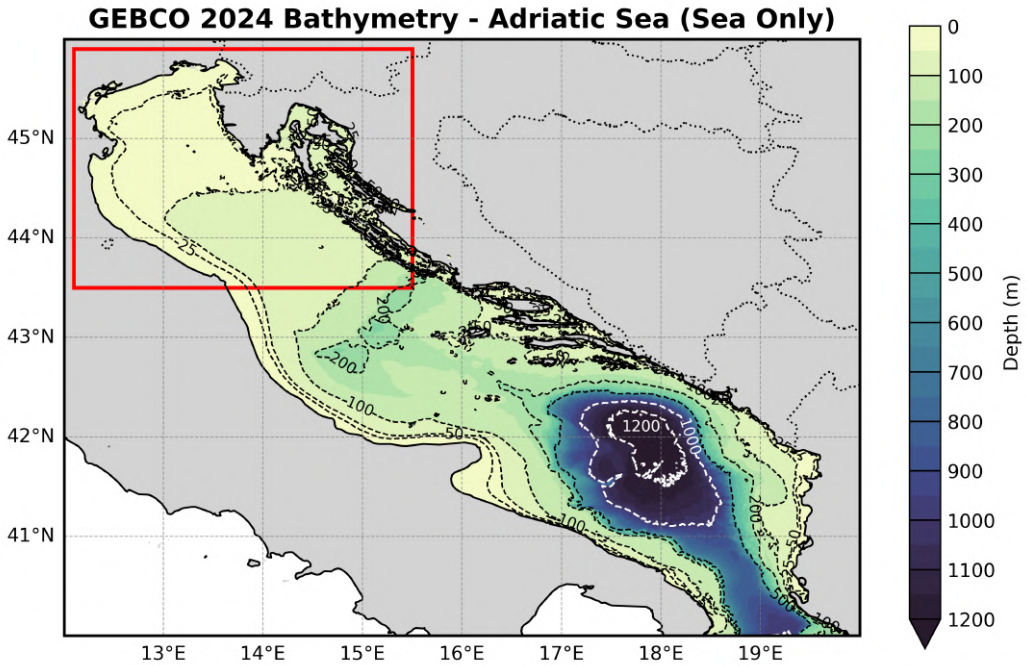

Figure 1.1: Representation of the entire Adriatic basin. The color scale indicates bathymetric depth (GEBCO Bathymetric Compilation Group, 2021; dataset updated to 2024), while the dashed lines show the main isolines at 25, 50, 100, 200, 500, 1000 and 1200 m depth. The 1000 and 1200 m isolines are drawn in white exclusively for graphical readability. The red area represents the northern adriatic basin and the main area of study.

The Northern Adriatic, whose area is highlighted within *Figure 1.1*, is characterized by a vast and shallow continental shelf typically less than 50 m deep. It receives substantial riverine inputs, most notably from the Po, which strongly influence salinity,

nutrient supply, and stratification patterns. This freshwater influence, together with intense air–sea interactions over the shallow shelf, makes the northern sector the main area of interaction between atmospheric forcing and surface thermohaline fields in the basin (Artegiani et al., 1997a; Cushman-Roisin et al., 2001). Seasonal stratification, frequent stratification breakdowns, and strong shelf–slope exchanges drive variability in primary productivity, coastal circulation and the dispersion of river-borne material.

The Adriatic seafloor morphology naturally divides the basin into three sub-basins. The Middle Adriatic, extending roughly between Ancona and the Bay of Kotor, has depths ranging from 100 m to 270 m and is characterized by depressions (Pomo/Pelagosa) and a sill that dynamically separates it from the southern domain, favoring seasonal baroclinic configurations and water mass transitions (Artegiani et al., 1997b). The Southern Adriatic hosts the South Adriatic Pit that exceeds 1200 m depth and plays a key role in ventilation and the formation of dense winter waters, contributing to basin-scale thermohaline circulation and exchanges through the Strait of Otranto (Artegiani et al., 1997b; Cushman-Roisin et al., 2001).

This combination of factors, including geographic position, basin dimensions, and morphology (characterized by an elongated axis, a relatively deep but narrow communication sill, an extensive northern shelf, and a deep southern pit), along with the limited connection with the rest of the Mediterranean through the Strait of Otranto, makes the Adriatic Sea a system particularly sensitive to river inputs, atmospheric forcing, and regional-scale climate change. Emphasizing the Northern Adriatic allows a focused study of shelf processes, freshwater influence, and air–sea interactions while preserving the larger-basin context needed to interpret shelf–basin exchanges and their implications for circulation, biogeochemistry, and marine ecology. These characteristics configure the basin as a natural laboratory for studying the dynamics of semi-enclosed systems, with significant implications for ocean circulation, biogeochemistry, and marine ecology

1.1.1 Circulation of the Northern Adriatic

The circulation of the Adriatic Sea (Figure 1.2) is characterized by a complex and seasonally variable system, influenced by atmospheric, hydrographic, and morphological factors. The configuration of the basin, elongated along a northwest–southeast axis and bounded by continental and mountain coasts, determines a generally cyclonic surface circulation at basin scale with localized shelf-confined dynamics in the Northern Adriatic (NAd) that are determinative for local transport, mixing and biogeochemistry (Artegiani et al., 1997a; Artegiani et al., 1997b). Over the shallow northern shelf (typically < 50 m), the circulation is strongly modulated by wind events, in particular *Bora* episodes, and by the large Po freshwater plume, which together generate a pattern of interacting gyres, coastal jets and along-shelf currents whose geometry reflects the coastline and the shelf bathymetry (Kuzmić et al., 2006).

Seasonal variability is a dominant trait of northern circulation. During winter the shelf tends toward a more barotropic state: strong winds and cooling deepen the mixed layer and frequently homogenize the water column across much of the shelf, producing a more coherent alongshore southward coastal flow along the Italian (western) margin and favoring shelf–slope exchanges (Artegiani et al., 1997a).

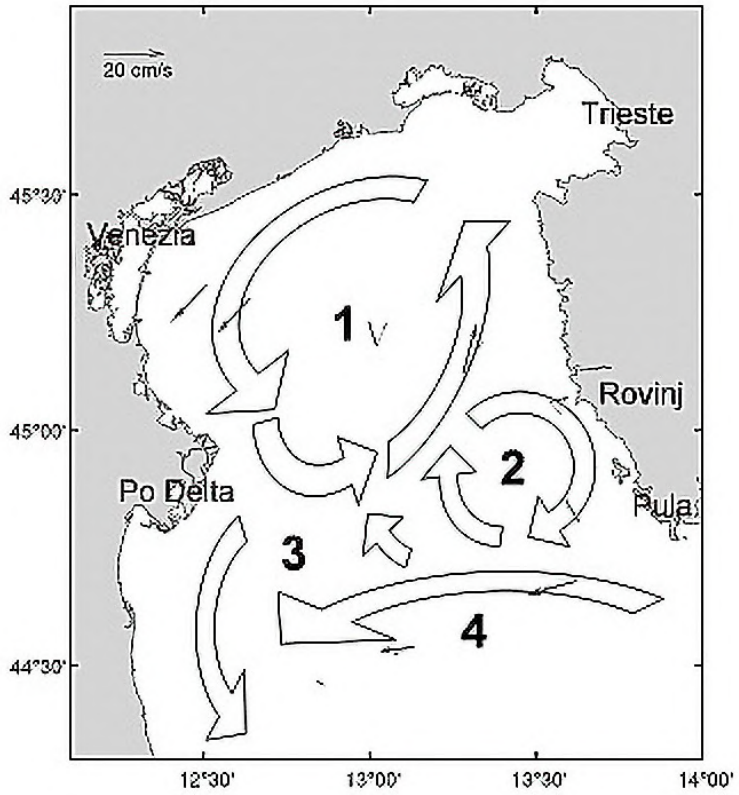

Figure 1.2: Schematic of the bora-response pattern in the Northern Adriatic, showing the Trieste and Senj cyclonic gyres, the Rovinj anticyclonic gyre, and the south-of-Po southward branch linking to the Western Adriatic Current (Kuzmić et al., 2006).

Under intense bora forcing this winter circulation assumes a more complex, multigyral structure: a prominent Trieste cyclonic gyre (**1**) forms in the far north with a strongly polarized northwestern arm constrained by the narrow coastal strip and a more offshore northeastern arm, producing almost depth-independent, rectilinear alongshore transports in the downwind direction; to the west, an anticyclonic cell near the Istrian coast (the Rovinj gyre (**2**)) develops closer to shore with generally lower peak speeds and more variable, clockwise rotation, participating in nearshore recirculation and the generation of filaments and eddies (Kuzmić et al., 2006). South of the Po Delta the flow more commonly organizes into a predominant southward branch that feeds the Western Adriatic Current (WAC) (**3**), while a dynamical transition zone of relatively sluggish circulation between this southward branch and flows emanating from northern arms controls exchange between the northern shelf and the middle Adriatic; the northern arm of the Senj cyclonic gyre (**4**), located farther south of the Po–Pula line, is less geometrically constrained and exhibits more meandering, lateral variability that can either feed the WAC or promote cross-shelf exchanges (Kuzmić et al., 2006).

In contrast, spring–summer is dominated by strong thermal and salinity stratification produced by surface heating and the Po freshwater plume, which isolates the surface layer and favors a shelf-scale cyclonic circulation cell in the northern sector together with coastal jets and frontal structures at the Po mouth and along the western coast (Artegiani et al., 1997b). Under stratified conditions the Trieste gyre and Rovinj anticyclonic cell remain key organizers of nearshore transport: the Trieste gyre tends

to concentrate and export buoyant plumes along preferential arms, while the Rovinj cell traps and recirculates nearshore waters along the Istrian margin; episodic eddies shed from these features and from the meandering Senj arm drive cross-shelf export and filamentary pathways that ventilate the shelf and deliver river-borne nutrients and sediments offshore. The south-of-Po southward branch functions as the principal conveyor toward the middle Adriatic, but its strength and spatial coherence are modulated by local wind curl and the relative positions of the neighbouring gyres (Kuzmić et al., 2006; Artegiani et al., 1997b).

Because the Northern Adriatic is much shallower than the middle and southern basins, classical thermocline-level circulation patterns identified at depths near ~ 75 m do not directly apply over large portions of the shelf; the seasonal thermocline is often close to the seabed or absent, and many subsurface recirculations and deeper currents characteristic of the Middle and Southern Adriatic are muted or confined to the shelf break and nearby depressions. Consequently, exchanges between the Northern Adriatic and the rest of the basin are governed primarily by shelf–slope processes at the break, by episodic wind-driven events that reorganize the multigyral pattern, and by the net along-shelf transports associated with the Trieste gyre, the Rovinj anticyclonic cell, the south-of-Po southward branch, and the meandering Senj arm, four interacting features whose relative intensity and positions determine pathways for along-shelf export, retention, and cross-shelf exchange (Kuzmić et al., 2006; Artegiani et al., 1997a; Artegiani et al., 1997b).

1.1.2 Rivers and Fresh Water Input

The river network discharging into the Adriatic, shown in *Figure 1.3*, plays a structural role in determining the physical, chemical, and biological states of the shelf. The Po River represents the main contributor to the Northern Adriatic and controls most of the external inputs that modulate stratification, coastal turbulence, and nutrient availability for primary productivity (Cozzi and Giani, 2011). Alongside the Po, western tributaries such as the Adige, Brenta, Piave, and Isonzo provide significant contributions in terms of freshwater and particulate matter; on the eastern side and in the more southern sectors, the Neretva and the Drin river basin play a more local role in the longitudinal distribution of nutrients (Grilli et al., 2020; Ricci et al., 2022).

The river discharge role is manifested through two main and closely linked mechanisms affecting the physical and biogeochemical functioning of the basin: first, the direct supply of freshwater mass, which modifies the surface density balance and thus coastal circulation (generation of *plumes* and ROFI - *Regions Of Freshwater Influence*); second, the transfer of biogeochemical loads (dissolved and particulate nutrients, organic matter, sediments), which act as drivers of productivity and water quality.

In the Northern Adriatic, the magnitude of the Po runoff and its seasonal variability, determines recurrent conditions across the year: high spring and autumn discharges are accompanied by increases in *nitrogen*, *phosphorus*, and *silica* loads, generating conditions favorable for the development of *phytoplankton* blooms and, in extreme cases combined with weak hydrodynamic conditions, to episodes of bottom *hypoxia* (Penna et al., 2004; Cozzi and Giani, 2011). During periods with above-climatology discharges, the Po *plume* front extends tens of kilometers along the coast and offshore, transporting not only freshwater but also a substantial nutrient load that can stimulate

surface productivity and alter the local biogeochemical balance (Penna et al., 2004; Cozzi and Giani, 2011).

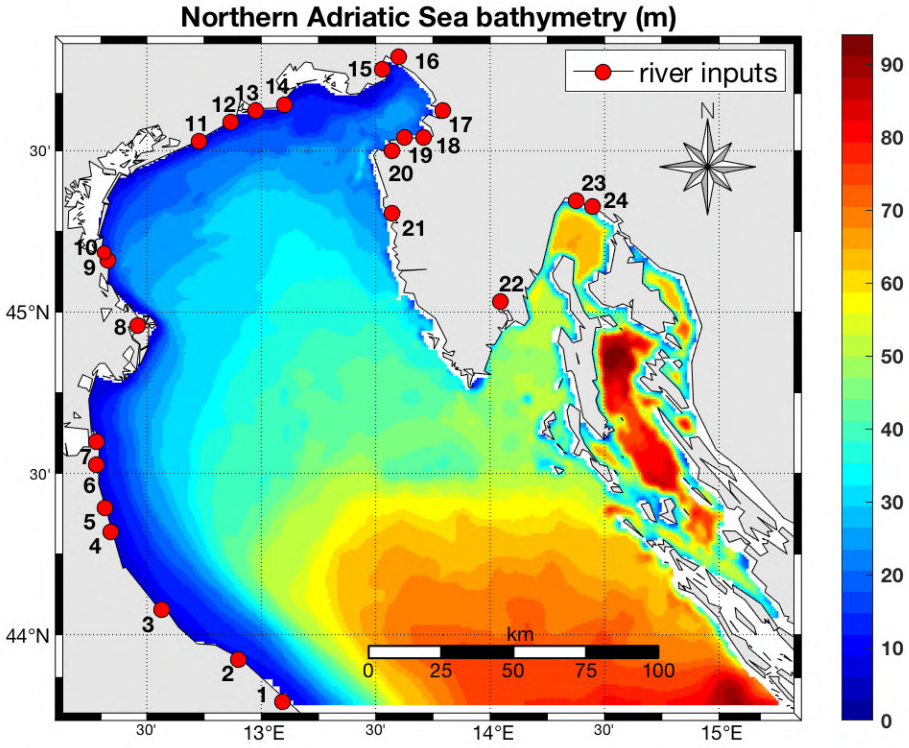

Figure 1.3: Map representing the coastal and bottom morphology of the Adriatic Sea. The red dots show the locations of the main rivers discharging into the domain: 1: Metauro, 2: Foglia, 3: Marecchia, 4: Savio, 5: Fiumi Uniti, 6: Lamone, 7: Reno, 8: Po, 9: Adige, 10: Bacchiglione, 11: Piave, 12: Livenza, 13: Canale Lovi, 14: Tagliamento, 15: Isonzo, 16: Timavo, 17: Rizana, 18: Drnica, 19: Dragonia, 20: Badasevica, 21: Mirna, 22: Rasa, 23: Rjecina, 24: Ivan. (Scroccaro et al., 2022)

Recent reconstructions of river discharge and nutrient loads confirm the dominant role of the Northern Adriatic in receiving freshwater and biogeochemical inputs, alongside a marked interannual and decadal variability of fluxes (Aragão et al., 2024; Cozzi and Giani, 2011). This variability is increasingly modulated by climatic and anthropogenic factors: rising air and sea temperatures, altered precipitation regimes, and enhanced frequency of extreme droughts have reduced summer discharges from major rivers, especially the Po, leading to lower freshwater and nutrient inputs into the northern basin (Zanchettin et al., 2008; Montanari et al., 2023). Long-term analyses document high interannual to multidecadal fluctuations in Po runoff, influenced by both climatic oscillations and land-use pressures (Zanchettin et al., 2008), while recent exceptional droughts (e.g., 2022) highlight the growing sensitivity of the system to hydrological extremes. Concurrently, improvements in wastewater treatment and phosphate-use reduction have contributed to declining phosphorus loads and a progressive reorganization of trophic conditions in the Northern Adriatic (Cozzi and Giani, 2011; Mozetič et al., 2010). The particulate fractions transported by the Po remain a major source of sediment and organic matter, affecting turbidity and benthic processes, whereas the dissolved components continue to regulate surface productivity and phytoplankton composition (Penna et al., 2004; de Wit and Bendoricchio, 2001).

1.1.3 Ecology and Biogeochemistry of the North Adriatic Basin

The biogeochemical framework of the North Adriatic arises from the interaction between terrestrial inputs (*nitrates* NO_3^-, *ammonium* NH_4^+, *silicates* $Si(OH)_4$), microbial and *physic* transformations (*primary uptake*, *nitrification*, *denitrification*, *remineralization*), and physical processes of dilution and transport. Historically, the northern part of the basin has been subject to strong *eutrophic* pressures linked to high riverine loads, but since the 1990s–2000s a trend toward decreasing mean $Chlorophyll-a$ concentration has been observed at many coastal stations. This can be interpreted as a progressive *re-oligotrophication* driven both by phosphate input control policies and by changes in hydrological discharge that affect its intensity and seasonality (Cozzi and Giani, 2011; Mozetič et al., 2010). These changes profoundly influence development of hypoxic zones in restricted coastal areas, especially when reduced deep ventilation limits the subsurface waters ventilation (Solidoro et al., 2009; Mozetič et al., 2010).

Within this biogeochemical framework, the structure and functioning of the pelagic trophic system can be interpreted through the notion of a *continuum* of trophic *paths*, ranging from the classical herbivorous chain (*herbivorous web*), dominated by large *phytoplankton* and transfer toward *macro-zooplankton* and fish, to the *microbial* web and the so-called *microbial loop*, where small *autotrophs*, *heterotrophic bacteria*, and *protozoa* govern the internal recycling of matter and nutrients (Legendre and Rassoulzadegan, 1995).

The concept of the *microbial loop*, introduced and developed in classical literature, highlights how a significant fraction of fixed *carbon C* is released as dissolved organic matter (**DOM**) or as rapidly degradable particulates. This matter provides substrate for *heterotrophic bacteria*, which, through their activity and through predation by *micro-grazers* (*heterotrophic flagellates*, *ciliates*), remineralize nutrients (in particular NH_4^+), which can then be reused by smaller *phototrophs*. In many circumstances, the combination of high bacterial productivity, significant **DON** production, and strong *microbial grazing* pressure establishes an efficient recycling circuit in the surface layer, with limited export of matter to deeper layers and with a greater dependence of primary production on regenerated nutrients rather than on allochthonous nitrate inputs (Azam et al., 1983).

Legendre and Rassoulzadegan (1995) provide a particularly useful conceptual synthesis for interpreting these dynamics: they propose that the position of a system along the *trophic continuum* can be diagnosed through a set of ratios among functional variables (such as **DOC/DON**, NH_4^+/NO_3^-, mean *phytoplankton* size, intensity of *micro-grazing*). The resulting interpretation is that conditions of strong thermal stratification, low vertical *mixing*, and predominance of internal **DOM** sources favor pathways dominated by the *microbial loop*, while conditions of strong mixing and abundant new nutrients favor *blooms* of *large diatoms* and the development of the *herbivorous chain*. This framework, graphically represented in *Figure 1.4*, helps to understand why, within the same basin, seasons and microenvironments with very different trophic pathways can coexist, and why changes in nutrient supply or form can shift the system along the *continuum* (Legendre and Rassoulzadegan, 1995).

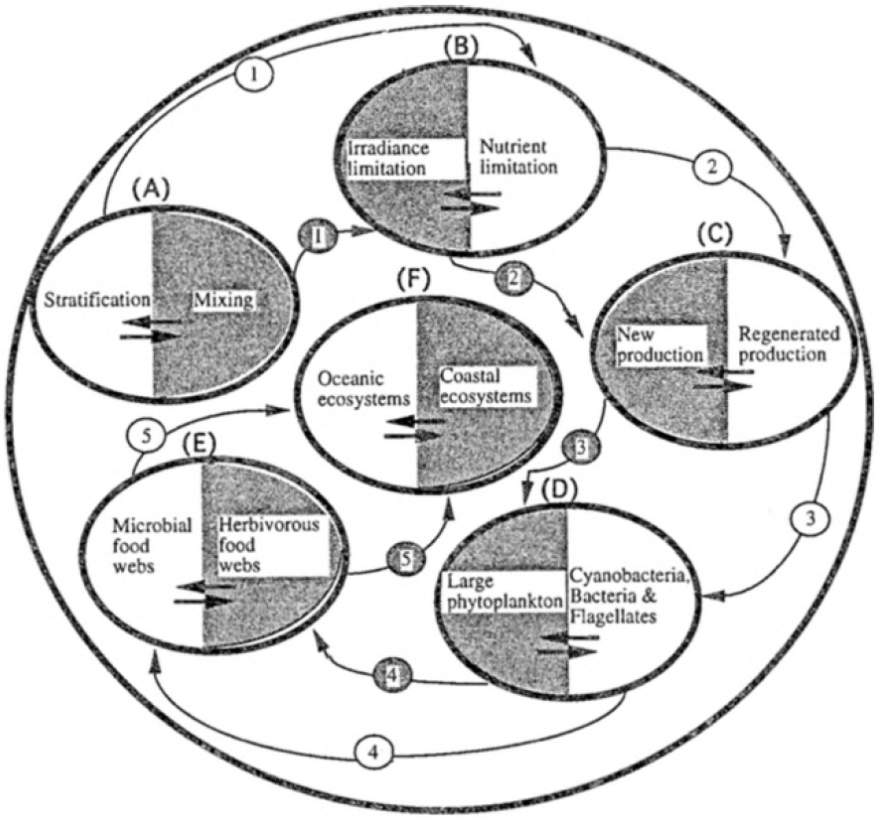

Figure 1.4: Scheme of the conditions influencing the development of coastal and oceanic pelagic ecosystems, from Legendre and Rassoulzadegan (1995). The phases considered include hydrodynamics, nutrient origin, phytoplankton production, associated organisms, food web, and ecosystem type. Two main pathways are distinguished: the herbivorous web (grey areas) and the microbial web (*microbial loop*, non-shaded areas).

Experimental studies and observations also emphasize two microscopic mechanisms of great functional relevance: on the one hand, the *exudation* and possible lysis of *phytoplankton*, releasing **DOM** with variable composition and $C : N$ ratio; on the other, the *predation* dynamics on bacteria by *micro-grazers*, which determine the rate and form of remineralization. When the **DON** pool is relatively rich and the **DOC/DON** ratio favors the production of qualitatively suitable substrate, bacteria can contribute to the net supply of *ammonium* through cycles of *predation* and *excretion*, which are then rapidly used by small *phytoplankton* fractions. Conversely, under conditions of N-poor substrate or high $C : N$ ratio, bacteria may become competitors with microalgae for inorganic nutrients, reducing new production and imposing a different *trophic architecture* (Azam et al., 1983; Legendre and Rassoulzadegan, 1995).

According to Miller (2004), temperature, metabolic rates, and associations between free-living bacteria and particle-attached bacteria modulate the rate of microbial processes and the likelihood that part of the microbial biomass is exported in particulate form. Miller emphasizes the need to consider the *time scale* of processes: while large *diatom blooms* can dominate seasonal variability, the background work of the *microbial loop* can act as a *"conveyor belt"* that maintains functional stability and recycling during *inter-bloom* periods (Miller, 2004).

In the specific context of the North Adriatic, the conjunction of climatic trends (warming, increased stratification) and changes in freshwater and nutrient availability (sum-

mer reduction of discharge and decline in absolute *phosphorus* contributions in some decades) creates a scenario favorable to a greater role of *microbial recycling* in the surface layer. This functional *shift* is consistent with observations of a mean decrease in $Chlorophyll-a$ and with the documented prevalence of smaller-sized *phytoplankton* communities in areas most influenced by the Po River (Mozetič et al., 2010; Cozzi and Giani, 2011; Giani et al., 2012). On the one hand, the strengthening of the *microbial loop* tends to retain matter and reduce **POC** export to the seabed; on the other, it may impair the efficiency of transfer toward higher trophic levels (potentially reducing the effectiveness of the herbivorous chain for fish production), while still leaving open the possibility of sporadic proliferation episodes (*mucilage*, algal blooms) when favorable hydrodynamic and nutrient conditions coexist (Deserti et al., 2005; Grilli et al., 2020).

1.2 Dense Water Masses

The genesis of dense water masses in the Adriatic is a process resulting from the atmosphere–ocean surface interactions: surface cooling, evaporation, and variability of river inputs combine to reduce the stability of the water column and trigger deep convection or *mixing* within the shelf environment (Artegiani et al., 1997b). Episodes of strong, cold, and dry winds, primarily the *Bora*, induce *sensible* and *latent* heat fluxes toward the atmosphere, which can enhance evaporation, thereby increasing surface density through both temperature loss and salinity increase (Jeffries and Lee, 2007).

The preconditioning phase during the warm and autumn seasons plays a decisive role in the formation of dense waters in the Northern Adriatic. A dry and warm summer, characterized by strong evaporation and reduced river discharges, increases surface salinity and weakens stratification, creating favorable initial conditions for wintertime convection (Supić and Vilibić, 2006; Vilibić et al., 2023). Under such conditions, subsequent atmospheric forcing, particularly episodes of cold, dry Bora winds, can effectively trigger dense water formation over the shallow northern shelf through intense surface cooling and vertical mixing. Conversely, years with high summer and autumn river inputs strengthen the freshwater lens and the pycnocline, thereby inhibiting or confining convective processes to smaller, localized areas. The interplay between these preconditioning factors and the intensity and persistence of winter wind events ultimately determines both the extent and efficiency of dense water formation in the Northern Adriatic, which represents one of the primary sources of dense water for the entire Adriatic basin.

1.2.1 Causes and Formation of the Dense Water Masses

In the Adriatic, the two main areas affected by this phenomenon are the northern shelf, where dense water masses can form through *shelf convection*, and the center of the southern gyre, where *open-ocean convection* may occur (Supić and Vilibić, 2006; Vilibić et al., 2023).

Shelf convection leads to the formation of the **North Adriatic Dense Water** (**NAdDW**) and is the dominant process on the northern shelf (Supić and Vilibić, 2006). This mechanism is triggered by strong and persistent Bora outbreaks, which

cause intense cooling of the shelf water column and vertical mixing extending for tens of meters, generating relatively homogeneous density water masses (Jeffries and Lee, 2007; Mihanović et al., 2013).

The typical sequence of **NAdDW** formation consists of a summer–autumn preconditioning phase, characterized by high baseline salinity and shallow *mixed layer* depth, followed by sufficiently intense winter Bora episodes capable of inducing the collapse of stratification and the full ventilation of the water column (Jeffries and Lee, 2007; Mihanović et al., 2013). Observational and modeling analyses indicate that the amount of **NAdDW** produced in a given winter depends nonlinearly on both the intensity and duration of Bora phases and on the initial hydrological state (e.g., river discharges and residual stratification). Thus, high temporal resolution datasets are required for accurate quantification (Supić and Vilibić, 2006; Mihanović et al., 2013).

In contrast, *open-ocean convection* in the southern sector is favored by cyclonic baroclinic configurations, which induce isopycnal uplift (*doming*) and increase surface salinity, thereby predisposing the water column to convection during episodes of strong atmospheric cooling (Artegiani et al., 1997b; Manca et al., 2002).

The fundamental difference between the two mechanisms lies in the spatial scale and preconditioning requirements: *shelf convection* is closely linked to shelf morphology and river inputs, while *open-ocean convection* primarily depends on basin-scale baroclinic structure and cyclonic circulation (Artegiani et al., 1997b). In addition, the topography of the northern shelf, characterized by escarpments and slopes toward the central and southern sectors, controls the pathways and transformation of the dense waters formed, influencing their capacity to ventilate the deep layers of the basin (Bergamasco et al., 1999; Manca et al., 2002).

1.2.2 Movement of the North Adriatic Dense Water Mass

Once formed over the northern shelf, the *North Adriatic Dense Water* (**NAdDW**) begins to flow downslope under the influence of gravity and the local bathymetry, following a well-defined pathway along the western Adriatic margin (Bergamasco et al., 1999). A representative scheme of the movement of dense masses along bathymetry is shown in *Figure 1.5*.

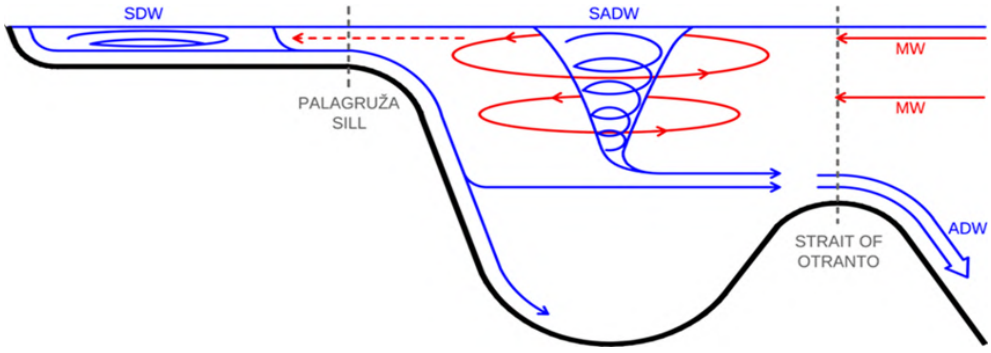

Figure 1.5: Not-to-scale schematic of a section of the Adriatic basin and its related circulation. (Vodopivec et al., 2022)

These dense waters, typically generated during strong winter Bora outbreaks, descend through a network of coastal depressions and channels, forming bottom-trapped den-

sity currents that gradually progress toward deeper parts of the basin. The topographic control exerted by the continental slope and submarine canyons modulates both the velocity and spatial extent of these flows, which often converge into the western Adriatic trough and continue southward as a dense bottom layer. Along their descent, **NAdDW** masses undergo progressive modification through entrainment and mixing with ambient waters, particularly in correspondence with sills, canyons, and irregular bottom features. This transformation results in a gradual decrease of density as the waters move southward. Eventually, part of the **NAdDW** flow reaches the central Adriatic depressions, where it contributes to the renewal of intermediate and deep layers, while a significant fraction continues its course toward the *Southern Adriatic Pit*, where it accumulates and mixes with locally formed *Adriatic Dense Water* (**ADW**) (Manca et al., 2002; Pranić et al., 2023). This cascading process represents a crucial link between the shelf processes of the northern basin and the deep ventilation of the southern sectors, maintaining the overall thermohaline structure and facilitating exchanges through the Strait of Otranto toward the Ionian Sea (Bergamasco et al., 1999; Pranić et al., 2023). *Figure 1.6* shows the pathway of the *dense water mass* relative to surface currents.

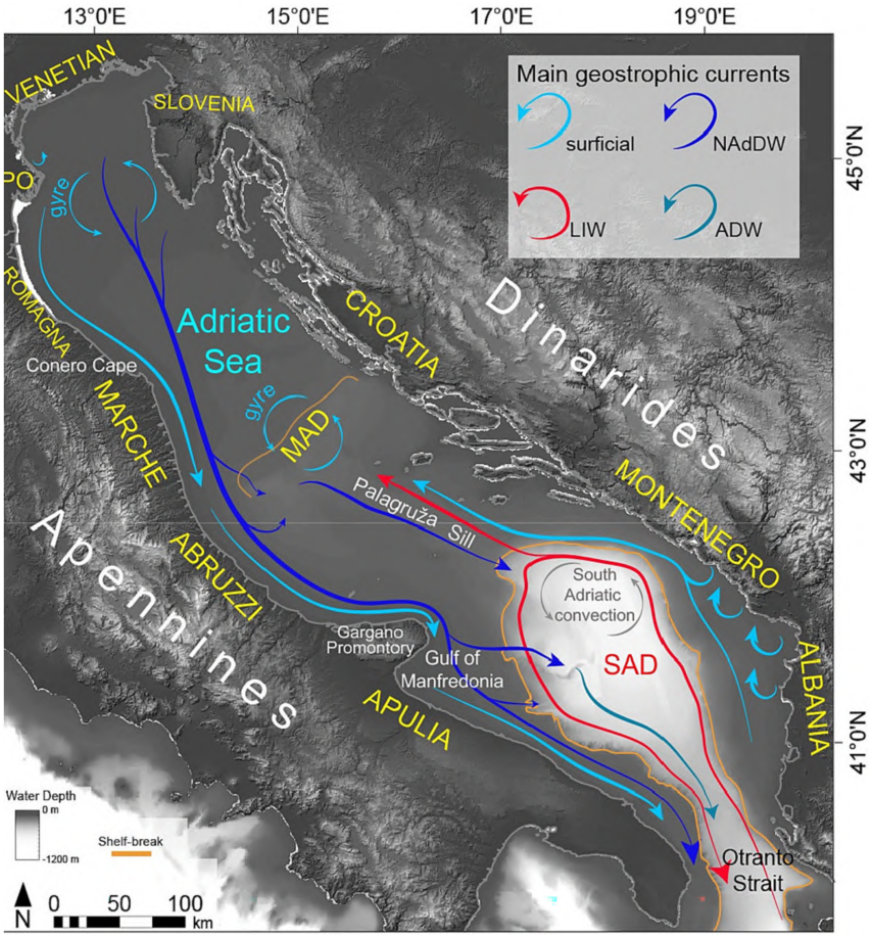

Figure 1.6: Diagram representing typical pathways of Adriatic circulation. Details are shown for surface circulation (light blue), Levantine Intermediate Waters (LIW) (red), Adriatic Deep Water (ADW) (indigo). The pathway of the North Adriatic Dense Water (NAdDW) is shown in blue, descending along the western margin toward the central and southern depressions. (Amorosi et al., 2022)

From a temporal perspective, NAdDW formation and cascading are episodic processes, tightly linked to the occurrence and intensity of winter cold-air outbreaks. The amount of dense water produced each year and its penetration depth depend on both the strength of the atmospheric forcing and the preconditioning of the northern shelf. High-resolution coupled atmosphere–ocean models are therefore essential to resolve the complex dynamics of Bora-driven cooling, small-scale mixing, and the cascading pathways of NAdDW, which play a fundamental role in ventilating the deep Adriatic and sustaining its long-term thermohaline balance (Bergamasco et al., 1999; Pranić et al., 2023).

1.3 Anoxic Events

The critical reduction of dissolved oxygen concentration in coastal seas, commonly defined as hypoxia (operational thresholds often set at $O_2 \leq 2$ ml/L or $\leq 62.5, \mathrm{mmol/m^3}$) and anoxia (concentrations approaching zero), represents one of the most evident consequences of physical and biogeochemical alterations affecting continental shelves ecology and populations (Diaz and Rosenberg, 2008). These conditions arise from changes in water column stratification, nutrient enrichment, and circulation dynamics, and in turn exert profound effects on benthic communities and ecosystem functioning, leading to altered species composition, mass mortality events, and shifts in trophic structure.

The oxygen budget of a coastal water column can be considered as the result of sources and sinks: among the main terms are the horizontal and vertical transport of oxygenated water, air–sea exchange, and biological consumption through respiration both in the water column and at the benthic layer; hypoxia emerges when the supply terms do not balance the local demand (Djakovac et al., 2015).

1.3.1 Anoxic Water Masses in the Northern Adriatic

In the Northern Adriatic, three recurring factors combine to produce conditions favourable to hypoxia: high primary production with consequent sedimentation of organic matter that fuels benthic demand (Degobbis et al., 2000), marked summer stratification that isolates the bottom from oxygen replenishment (Faganeli et al., 2009), and relatively long residence times in gulfs and enclosed basins that reduce hydrodynamic flushing (Justić, 1991).

Seasonal stratification, developing in late spring and summer, reduces vertical diffusivity K_v and prevents oxygenated mixing of deep waters; meanwhile, organic matter produced at the surface or aggregated in mucilage sinks and is mineralised at the sediment, generating strong benthic consumption that can exhaust the available oxygen in the bottom layer (Djakovac et al., 2015; Faganeli et al., 2009).

Summer warming further lowers oxygen solubility and increases microbial metabolic rates (increasing R_{wc} and R_{b}), while prolonged meteorological calm reduces surface mixing and bottom ventilation (Diaz and Rosenberg, 2008).

Specifically, continental inputs (with the Po River as the dominant contributor in terms of freshwater, sediments, and nutrients) represent the primary source of organic

matter and nutrients that fuel productivity and subsequent organic sedimentation in the Northern Adriatic (Cossarini et al., 2012; Giani et al., 2012).

Local morphology amplifies the issue: shallow areas, enclosed basins, or limiting sills (such as some northern gulfs) have a higher probability of experiencing hypoxic conditions, as the combined effect of high organic sedimentation and limited hydrodynamic exchange favours oxygen depletion (Justić, 1991; Stachowitsch, 1991).

Historical and long-term studies show that the frequency and extent of hypoxic events have varied over the twentieth century, with decades characterised by greater extensions of low-oxygen zones during phases of intense oligotrophication; however, non-linear relationships between anthropogenic loads, hydrological regimes, and meteorological conditions make the temporal dynamics complex (Degobbis et al., 2000; Djakovac et al., 2015).

1.4 Thesis Objective

The primary objective of this thesis is to deliver a comprehensive and multi-scale validation of a fully coupled high-resolution physical and biogeochemical modeling system applied to the Northern Adriatic Sea, and to do so in a manner that evaluates its capacity to reproduce the basin's key processes while diagnosing the mechanisms that shape both model skill and limitations. The work integrates satellite and in-situ observations, river discharge records and a suite of advanced diagnostics in order to assess how faithfully the model represents the thermal, dynamical and ecological state of a shallow and river-dominated shelf characterised by strong seasonality, episodic dense-water formation, intense air–sea exchanges and complex biogeochemical interactions. The validation strategy therefore combines traditional field and point metrics with spectral, spatial and temporal analyses so that performance is assessed not only in terms of statistical accuracy but also in terms of phase coherence, scale-dependent fidelity and the realism of the underlying processes.

A central component of the validation involves a rigorous evaluation of the model's physical core and its ability to reproduce sea surface temperature, stratification patterns, vertical mixing, and the formation and cascading of North Adriatic Dense Water. These diagnostics are evaluated at both basin-wide and pixel-by-pixel levels and are quantified through skill scores such as correlation coefficient, bias, root mean square error, Nash–Sutcliffe efficiency, and the Index of Agreement, together with graphical diagnostics such as Taylor diagrams, target plots, and spectral tools that reveal scale-dependent coherence and the distribution of energy across frequencies. The intention is to verify that mean seasonal structures, interannual variability, and episodic events that drive biogeochemical responses are captured with sufficient realism to support mechanistic interpretation while identifying the types of amplitude, phase, or spectral mismatches that can propagate through the ecosystem component of the model.

An equally important aspect of the thesis is the validation of biogeochemical state variables including surface chlorophyll, dissolved oxygen and nutrient fields, together with their spatial gradients associated with the Po River plume and other coastal sources. The evaluation examines the capacity of the model to reproduce seasonal cycles, contrasts between offshore and nearshore regions, sub-seasonal variability and interannual

trends, and to determine whether mismatches emerge from internal process representation such as coastal versus open-sea production regimes, benthic–pelagic coupling or microbial dynamics, or instead from the characteristics of external forcings. Eulerian and Lagrangian diagnostics are applied to assess plume extent, persistence and connectivity in the Region of Freshwater Influence in order to link variations in freshwater and riverine inputs to changes in nutrient availability, phytoplankton production and cross-shelf exchanges.

A further objective of this thesis is to quantify long-term trends and identify regime shifts by combining model outputs with satellite and in-situ time series. The analysis targets statistically significant breakpoints and trend inversions potentially linked to variations in river discharge, nutrient loads or regional circulation, and investigates how these changes permeate through functional planktonic groups, particulate pools and benthic oxygen dynamics. The methodological framework includes breakpoint and trend-break analyses that separate pre-regime and post-regime behaviour and evaluate spatially where modelled trends coincide with or diverge from observational patterns, with particular attention to plume-influenced coastal margins where river forcing can generate abrupt ecosystem responses.

Since reliable model evaluation requires reproducibility and operational usability, the thesis also advances a systematic and transferable validation protocol that integrates data harmonisation, automated diagnostic plotting and a hierarchy of performance metrics into a coherent and reproducible pipeline. This protocol is intended to support calibration, inter-model comparisons and operational monitoring by providing consistent basin-scale and pixel-scale diagnostics, by linking statistical summaries to spectral and spatial analyses and by making explicit the connection between variability in external forcing, particularly riverine inputs, and the model response. The framework is designed to be applicable beyond the Northern Adriatic case study and to be generalisable to other shelf and coastal environments where river-dominated dynamics and benthic–pelagic coupling are central to basin functioning.

The overarching purpose of the thesis is therefore not only to evaluate whether the coupled NEMO and BFM configuration can reproduce observed patterns of temperature, circulation, chlorophyll and oxygen but also to uncover the structural sensitivities and feedbacks that control model–observation discrepancies, such as the partitioning between coastal and offshore productivity, the representation of benthic oxygen demand and the degree of sensitivity to prescribed river forcing. By integrating diagnostics of physical dynamics, biogeochemical state variables and external forcing pathways, the work aims to identify targeted improvements that can reduce biases in phytoplankton biomass and particulate export, correct benthic oxygen imbalances and mitigate excessive sensitivity to changes in river regimes. In doing so, the thesis seeks to strengthen the suitability of the modelling system for mechanistic studies and for the evaluation of ecosystem responses to climate variability and anthropogenic forcing.

Chapter 2

The Numerical Model

The area of interest analysed in this study, shown in *Figure 2.1*, encompasses almost the entirety of the northern portion of the Adriatic basin, commonly referred to as the *Northern Adriatic* (NAD). This spatial domain extends between latitudes 43.50°N and 46.00°N and longitudes 12.20°E and 16.20°E, covering an overall surface area of approximately $\sim 30,000$ km^2.

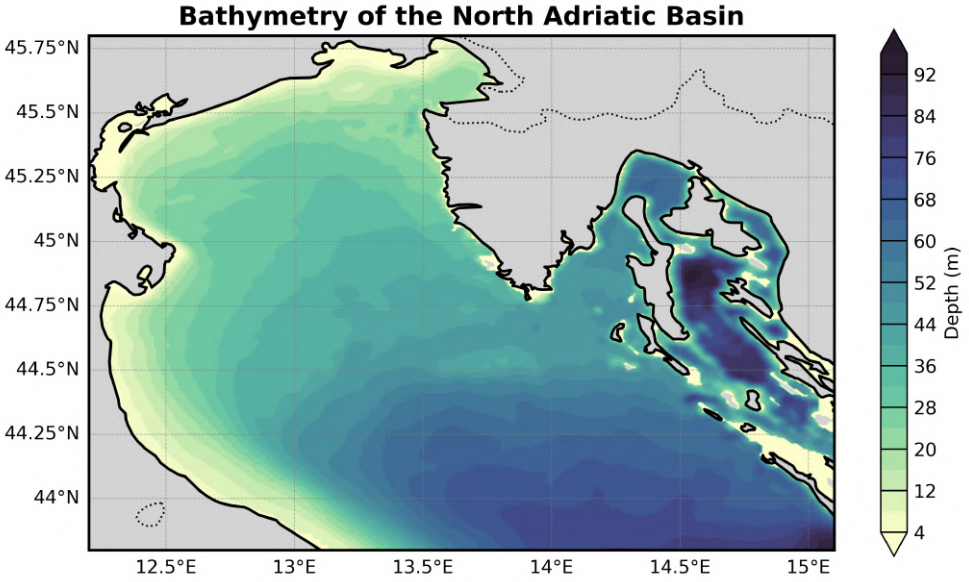

Figure 2.1: Portion of the basin covered by the numerical simulation. The colour scale represents depth in metres [m], with yellow indicating shallower areas and blue indicating deeper ones. Vertical resolution is 2.0 m.

The modelling configuration adopted provides a horizontal resolution of 1 km $\times$ 1 km, resulting in a computational grid composed of 278 $\times$ 315 cells, ensuring an adequate level of detail for the representation of coastal and sub-basin processes.

Vertically, the domain is discretised into 47 *z-layers* of uniform thickness 2 m, corresponding to a maximum resolvable depth of 94 m. This configuration allows for sufficiently accurate description of both surface phenomena, influenced by atmospheric and river forcing, and the dynamics of the deeper layers of the basin.

The simulation was run for a period of 10 years (2000–2009 inclusive) and included the explicit coupling of two numerical ocean models: **NEMO**, used for the simulation of the *General Circulation Model*, and a **Biogeochemical Fluxes Model** (**BFM**), for the biogeochemical components. The flow scheme representing the exchange of information between the two architectures is shown in *Figure 2.2*.

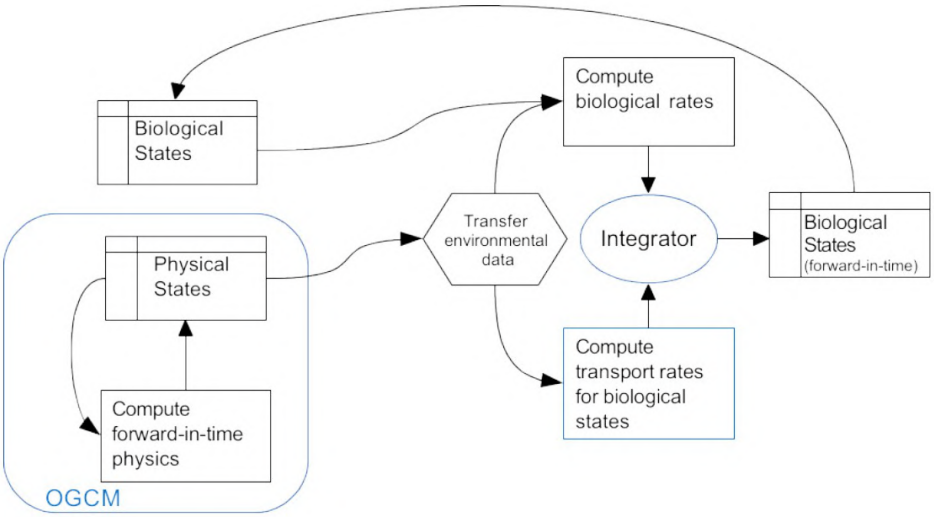

Figure 2.2: Scheme representing the flow and exchange of information between the **NEMO** architecture and the state variables simulated by the **BFM**. *Blue* cells represent processes and routines solved exclusively by the *OGCM*. (Lovato and Butenschön, 2023)

2.1 GCM Characteristics

The *General Circulation Model* (*GCM*) is implemented using **NEMO v3.6** (Madec and Team, 2016), a numerical model based on the solution of the *Primitive Navier–Stokes Equations*, defined by the system of equations of *motion*, *mass continuity*, and *tracer transport*, as well as a nonlinear equation of state (**EOS-80**) which allows linking tracers (such as *salinity* and *temperature*) to the fluid velocity. The system of equations is reported below in vector form:

$$\frac{\partial \mathbf{U}}{\partial t} + (\mathbf{U}\cdot\nabla)\mathbf{U} + f\,\mathbf{k}\times\mathbf{U} = -\frac{1}{\rho_0}\nabla p + \nabla\cdot\mathbf{D}^U + \mathbf{F}^U, \tag{2.1}$$

where

$$\mathbf{U} = (\mathbf{U}_h, w) \tag{2.2}$$

is the *velocity vector*, with $\mathbf{U}_h$ the horizontal component and w the vertical component;

$$f = 2\,\boldsymbol{\Omega}\cdot\mathbf{k} \tag{2.3}$$

is the *Coriolis parameter*, defined as the scalar product between the *Earth rotation vector* ($\boldsymbol{\Omega}$) and the *local vertical unit vector* ($\mathbf{k}$); ρ_0 is the reference density, and p the pressure; $\mathbf{D}^U$ and $\mathbf{F}^U$ represent, respectively, the turbulent viscosity terms and surface forcings.

For the tracers T (potential temperature) and S (salinity), the advection–diffusion equations are:

$$\frac{\partial T}{\partial t} + (\mathbf{U}\cdot\nabla)\,T = \nabla\cdot D^T + F^T, \quad \frac{\partial S}{\partial t} + (\mathbf{U}\cdot\nabla)\,S = \nabla\cdot D^S + F^S, \tag{2.4}$$

where D^T, D^S and F^T, F^S indicate, respectively, turbulent diffusivity and surface forcings for temperature and salinity.

These equations, together with the equation of state $\rho = \rho(T, S, p)$ (Madec and Team, 2016; NEMO Consortium, 2016), constitute the core of the Primitive Navier–Stokes Equations solved by NEMO v3.6.

The equation of state $EOS-80$ (UNESCO - International Council for the Exploration of the Sea, 1980) is expressed as:

$$\rho(S,T,p) = \rho_w(T,p) + A(T,p)\,S + B(T,p)\,S^{3/2} + C\,S^2 \tag{2.5}$$

with

$$\rho_w(T,p) = \rho_0 + a_1 T + a_2 T^2 + a_3 T^3 + a_4 T^4 + a_5 T^5 + \left(b_0 + b_1 T + b_2 T^2 + b_3 T^3\right) p + c_0\, p^2, \tag{2.6}$$

$$\begin{aligned} A(T,p) &= A_0 + A_1 T + A_2 T^2 + A_3 T^3 + \left(D_0 + D_1 T + D_2 T^2\right) p, \\ B(T,p) &= B_0 + B_1 T + B_2 T^2 + E_0\, p, \\ C &= C_0. \end{aligned} \tag{2.7}$$

The numerical coefficients (units: ρ in kg/m^3, T in °C, S in PSU, p in dbar) are defined by UNESCO (UNESCO - International Council for the Exploration of the Sea, 1980) and are reported in *Table 2.1*:

Coeff.	**Value**	**Coeff.**	**Value**
ρ_0	999.842594	a_1	$+6.793952 \times 10^{-2}$
a_2	-9.095290×10^{-3}	a_3	$+1.001685 \times 10^{-4}$
a_4	-1.120083×10^{-6}	a_5	$+6.536332 \times 10^{-9}$
b_0	$+8.244930 \times 10^{-1}$	b_1	-4.089900×10^{-3}
b_2	$+7.643800 \times 10^{-5}$	b_3	-8.246700×10^{-7}
c_0	$+5.387500 \times 10^{-9}$	A_0	$+0.824493$
A_1	-4.089900×10^{-3}	A_2	$+7.643800 \times 10^{-5}$
A_3	-8.246700×10^{-7}	D_0	$+5.387500 \times 10^{-9}$
D_1	-8.246700×10^{-7}	D_2	$+7.643800 \times 10^{-5}$
B_0	-5.724660×10^{-3}	B_1	$+1.022700 \times 10^{-4}$
B_2	-1.654600×10^{-6}	E_0	$+4.831400 \times 10^{-4}$
C_0	$+4.831400 \times 10^{-4}$		

Table 2.1: Values of coefficients used in the **EOS-80** equation of state (UNESCO - International Council for the Exploration of the Sea, 1980).

2.2 Approximations Used

The approximations used by the model are based on simplifications of the full equations of motion, in particular the Boussinesq hypothesis, the hydrostatic hypothesis, incompressibility, the formulation of the *turbulence closure hypothesis*, as well as the assumption of a spherical Earth and the *thin–shell approximation*. In compact form, the main ones are listed below:

Boussinesq Hypothesis
Small density variations are neglected everywhere except in the buoyancy term, where

$$\rho = \rho_0 + \rho', \qquad \rho' \ll \rho_0, \tag{2.8}$$

and only the product $\rho' g$ is retained in the momentum equation. This allows density fluctuations to generate buoyancy while treating the reference density ρ_0 as constant elsewhere.

Hydrostatic Hypothesis

$$\frac{\partial p}{\partial z} \;=\; -\,\rho\, g \tag{2.9}$$

where p is pressure, z the vertical coordinate positive upward, ρ the local density, and g the acceleration of gravity.

Incompressibility

$$\frac{\mathrm{D}\rho}{\mathrm{D}t} \;=\; 0 \quad \Longrightarrow \quad \nabla \cdot \mathbf{U} \;=\; 0\,, \tag{2.10}$$

with $\mathrm{D}/\mathrm{D}t$ the material derivative, consistent with the Boussinesq hypothesis.

Turbulence closure hypothesis
NEMO v3.6 adopts a generic length scale (GLS) eddy viscosity model, in which the turbulent diffusivity term $\mathbf{D}^U$ is parameterized as

$$\mathbf{D}^U \;=\; \nabla\cdot\big(K_M(z)\,\nabla\mathbf{U}\big), \tag{2.11}$$

where $K_M(z)$ is the vertical turbulent viscosity obtained from solving the turbulence transport balance equations (TKE and mixing length).

Spherical Earth
The model uses spherical coordinates (λ, φ, r) with constant Earth radius R_E, expressed in the system

$$\begin{aligned} x &= (R_E + z)\cos\varphi\ \cos\lambda, \\ y &= (R_E + z)\cos\varphi\ \sin\lambda, \\ z &= (R_E + z)\sin\varphi. \end{aligned} \tag{2.12}$$

Thin–shell approximation
It is assumed $\delta r = z \ll R_E$, neglecting first-order radial variations in the calculation of geometric terms, simplifying spherical metrics and keeping vertical dependence only in dynamic and thermodynamic terms.

2.3 Discretization Methods

For horizontal discretization, an Arakawa–C type grid is used, while the fundamental equations are integrated through a source splitting method, with a fixed time step of 120 s. In detail:

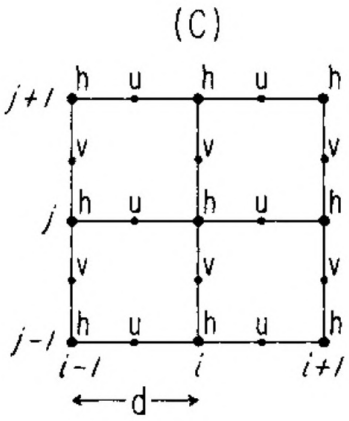

Figure 2.3: Layout of the Arakawa–C grid. (Arakawa and Lamb, 1977)

Arakawa–C Grid
The Arakawa–C grid is a staggered grid in which the horizontal velocity components u and v are defined at half-cell points along the sides of the squares, while scalar variables (pressure, temperature, salinity) are located at the cell centers. This arrangement minimizes the "checker-board mode" and improves the representation of discretized divergences and curls (Arakawa and Lamb, 1977). Figure 2.3 illustrates the arrangement of variables within each cell.

Source splitting (operator splitting)
The time integration method used in NEMO v3.6 is based on operator splitting (*source splitting* or *operator splitting*):

$$\frac{\partial \mathbf{Q}}{\partial t} = \mathcal{A}(\mathbf{Q}) + \mathcal{P}(\mathbf{Q}) + \mathcal{F}(\mathbf{Q}), \tag{2.13}$$

where $\mathbf{Q}$ is the vector of dynamic-thermodynamic variables, $\mathcal{A}$ denotes the advective contribution, $\mathcal{P}$ the contribution due to pressure and geopotential, and $\mathcal{F}$ the forcing terms (Coriolis, turbulent diffusion, etc.). Integration occurs in three sub-steps according to the Strang scheme (Strang, 1968) (Figure 2.4):

$$\mathcal{A}_{1/2} \;\rightarrow\; (\mathcal{P} + \mathcal{F}) \;\rightarrow\; \mathcal{A}_{1/2}$$

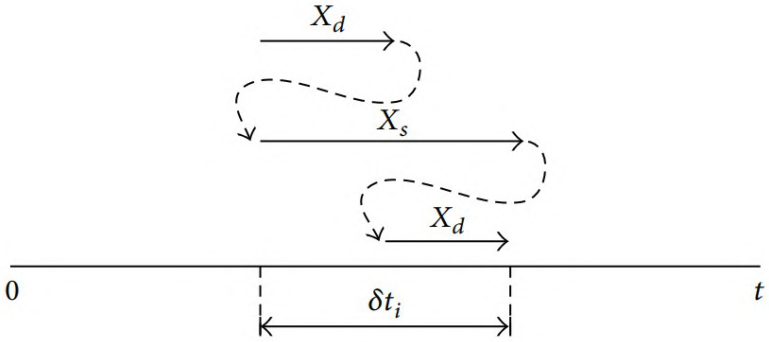

Figure 2.4: Typical scheme of *Strang splitting* taken from a publication by Zhou et al. (2014): half-step execution with the first operator (advection $\mathcal{A}$), full step with the second (pressure $\mathcal{P}$ and forcing $\mathcal{F}$), then half step again with the first.

This approach ensures second-order temporal accuracy, preserving the separation between transport physics and forcing physics.

2.4 Avvection and Diffusion Schemes

For the simulation of temperature, salinity, and biogeochemical tracers, a *mixed upstream/monotonic upwind scheme for conservation laws* (MUSCL) advection scheme

is used. In NEMO v3.6, this is implemented according to the formulation of van Leer (van Leer, 1979), whose graphical representation is shown in *Figure 2.5.*

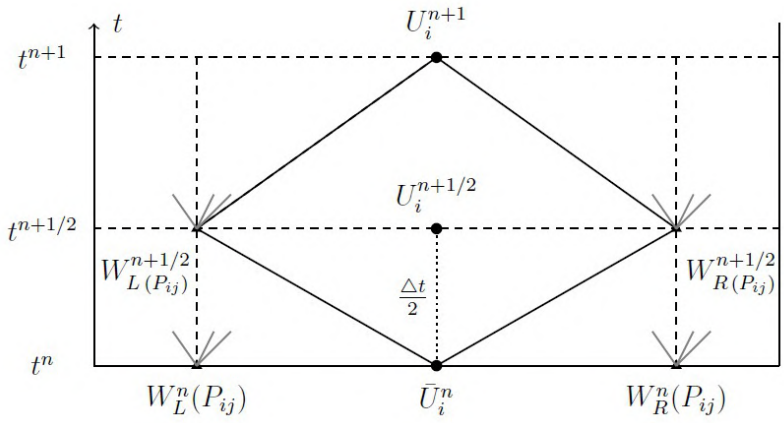

Figure 2.5: Linear reconstruction scheme MUSCL according to van Leer (1979). Filled dots show cell values q_{i-1}, q_i, q_{i+1}; dashed lines indicate reconstructions at cell edges $q_{i\pm1/2}$ calculated with the van Leer limiter $\phi(r)$. Adapted from a publication by Chiapolino et al. (2017).

MUSCL reconstructs state values at cell edges using *slope limiters* to ensure monotonicity and second-order spatial accuracy, solving local Riemann problems to compute numerical fluxes. In compact form:

$$\hat{q}_{i\pm1/2} = q_i \pm \frac{1}{2}\,\phi(r_i)\,(q_{i+1} - q_i), \tag{2.14}$$

where

$$r_i = \frac{q_i - q_{i-1}}{q_{i+1} - q_i}, \quad \phi(r) = \max\big(0, \min(2r,\,1), \min(r, 2)\big) \tag{2.15}$$

is the *van Leer* limiter (van Leer, 1979).

MUSCL is combined with an upstream approach at critical points (such as river mouths), achieving robustness and preservation of positivity of concentrations (Lévy et al., 2001).

For horizontal diffusion of momentum and tracers, NEMO adopts a biharmonic operator (∇^4), which translates into:

$$\mathbf{D}(\psi) = -\,K\,\nabla^4\psi \quad \Longrightarrow \quad \mathbf{D}(\psi)_i = -\,K\,\Delta^2(\Delta^2\psi)_i, \tag{2.16}$$

where ψ is the scalar quantity (e.g., concentration) and K is the fourth-order diffusivity coefficient. The use of the biharmonic operator improves spectral separation, selectively damping the smallest scales without affecting mesoscale dynamics (Hecht and Smith, 2008; Graham and et al., 2018).

Vertical turbulence is modeled through the *Generic Length Scale* (*GLS*) scheme, which solves two prognostic equations for *turbulent kinetic energy* (k) and a *mixing length scale* (ψ) (Umlauf and Burchard, 2003). The adopted closure is of the k–ϵ type, where the *dissipation* term ϵ is defined as a function of k and ψ:

$$\begin{aligned} \frac{\partial k}{\partial t} &= \frac{\partial}{\partial z}\left(K_k \frac{\partial k}{\partial z}\right) + P - \epsilon, \\ \frac{\partial \psi}{\partial t} &= \frac{\partial}{\partial z}\left(K_\psi \frac{\partial \psi}{\partial z}\right) + \psi\left(\beta_1 \frac{P}{k} - \beta_2 \frac{\epsilon}{k}\right), \end{aligned} \tag{2.17}$$

where P represents the *turbulent production* due to vertical velocity gradients, K_k and K_ψ are the *turbulent diffusivities*, and $\epsilon = k^{3/2}/\psi$ follows the standard *closure hypothesis* formulation (Umlauf and Burchard, 2003; Reffray et al., 2015).

The **Canuto Stability Functions (type A)** (Canuto et al., 2010) are also used, linking the *gradient Richardson number* Ri_g to the modulation of vertical turbulence, controlling transport of both *momentum* and *tracers*. In *Figure 2.6*, these functions are shown as functions of Ri_g and the density ratio R_r, highlighting how turbulence decreases under strong stratification.

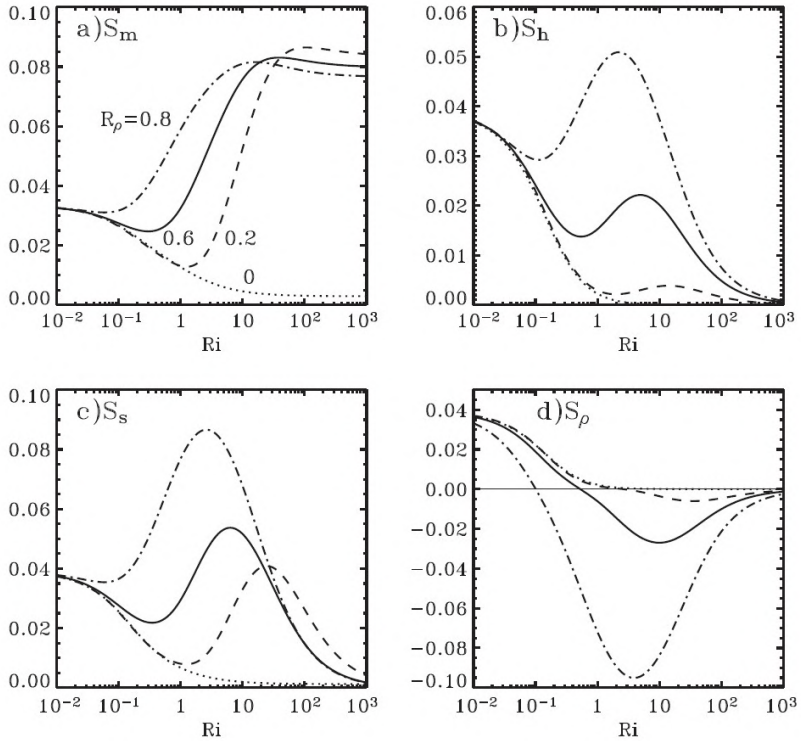

Figure 2.6: Graphs of the *Canuto Stability Functions (type A)* as functions of the gradient Richardson number Ri_g and the density ratio R_r. The curves show turbulent fluxes of **momentum** (a) and **scalar** fluxes: (b) heat, (c) salt and (d) density, for different values of R_r. Increasing stratification (high Ri_g) progressively suppresses turbulence. Adapted from Canuto (Canuto et al., 2010).

This approach ensures accuracy both in strongly mixed regimes (low Ri_g) and in stratified conditions (high Ri_g), as shown in several validation studies (Reffray et al., 2015).

2.5 BFM Characteristics

The *Bio-Geochemical* (**BFM**) model is a marine ecosystem model based on the use of functional groups and the representation of biomass. It solves the system of biogeo-

chemical variables in *Eulerian* coordinates through a suite of chemical and biological processes that reproduce the *pelagic* and *benthic* dynamics typical of a marine ecosystem, including the exchange of essential elements (e.g., C, N, P, Si) (Vichi et al., 2023).

The biogeochemical variables of the model are organized into *Chemical Functional Families* (*CFF*), which include three main categories: *inorganic*, *living*, and *non-living organic*. Within the *living* family, *Living Functional Groups* (*LFG*) are also defined, representing groups of organisms characterized by similar ecological functions. All the CFFs and the associated pelagic processes reproduced within the model are represented in *Figure 2.7*. (Vichi et al., 2023)

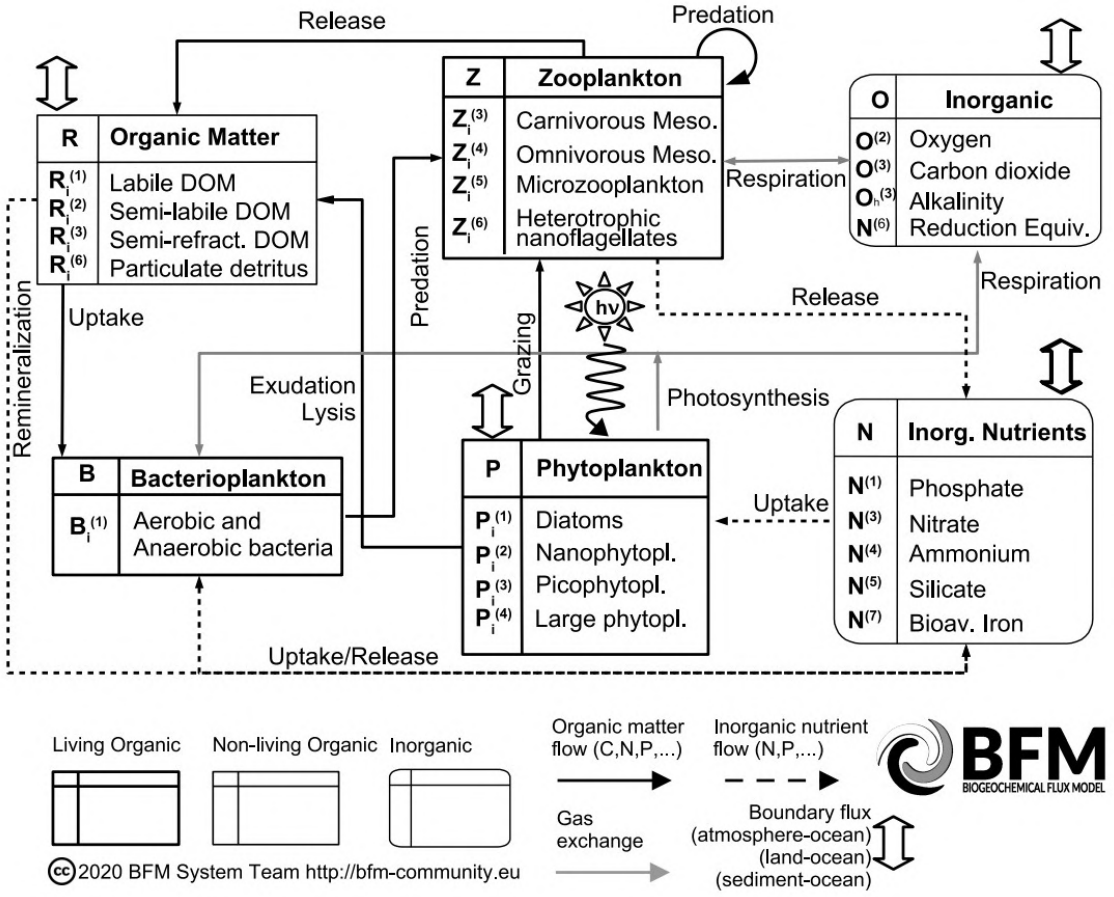

Figure 2.7: Diagram representing the state variables of the **BFM** architecture and their *pelagic* interactions. The reported processes and variables are considered *standalone*, so no coupling with the **NEMO** architecture or other numerical models is currently considered. (Vichi et al., 2023)

The full set of pelagic state variables reproduced within the simulation and used in this project is reported in *Table 2.2*. Although *Table 2.2* lists all of the principal model variables, the primary variables used to validate the model in this work are **Chla** (*total Chlorophyll* $-$ *a*) and **O2o** (*dissolved oxygen*). For this reason, the subsequent subsections provide detailed equations and explanations for the chlorophyll fields (including group-specific chl:C diagnostics following the *Geider* approach (Geider et al., 1996; Geider et al., 1997) implemented in BFM and for the oxygen budget; other variables are described at the level of their role in the *microbial loop*, *grazing pathways* and *stoichiometric coupling*.

Code	Description	Units
Chla	Total Chlorophyll-a	mg Chl/m^3
O2o	Dissolved Oxygen	mmol O_2/m^3
N1p	Inorganic Phosphate	mmol P/m^3
N3n	Inorganic Nitrate	mmol N/m^3
N4n	Inorganic Ammonium	mmol N/m^3
P1c	Carbon content in Diatoms	mg C/m^3
P2c	Carbon content in Nanoflagellates	mg C/m^3
P3c	Carbon in Picophytoplankton	mg C/m^3
P4c	Carbon in Large Phytoplankton	mg C/m^3
Z3c	Carbon in Carnivorous Mesozooplankton	mg C/m^3
Z4c	Carbon in Omnivorous Mesozooplankton	mg C/m^3
Z5c	Carbon in Microzooplankton	mg C/m^3
Z6c	Carbon in Heterotrophic Nanoflagellates	mg C/m^3
R6c	Refractory Particulate Organic Carbon	mg C/m^3

Table 2.2: Subset of pelagic state variables used in the model, including chlorophyll, oxygen, nutrients, phytoplankton, zooplankton, and organic matter.

2.5.1 Formalism and Generic Tendencies

BFM formulates each state variable in rates-of-change form. A generic state variable C is governed by

$$\frac{dC}{dt} = \sum_{\text{sources}} \mathcal{S} - \sum_{\text{sinks}} \mathcal{L}, \tag{2.18}$$

where the source and sink terms $(\mathcal{S}, \mathcal{L})$ are functions of environmental drivers and other state variables; specific parameterizations can be switched on/off via namelist options (Vichi et al., 2023). To ease reading of the equations that follow, the most relevant symbols and ecological parameters used throughout the chlorophyll and oxygen formulations are summarized within *Table 2.3*. These parameters are the principal tuning knobs that control *photoacclimation*, *grazing* and *microbial dynamics* in BFM; their values and group-dependent variants are available in the BFM namelists. (Vichi et al., 2023)

Symbol	Description	Units
θ^0_{chl}	Maximum chl:C ratio (group-specific)	dimensionless (0–1)
α^*, α^0_{chl}	Initial slope / effective quantum efficiency.	Eq. 2.19 consistent
E_{PAR}	Active radiation available to phytoplankton.	μmol photons m^{-2} s^{-1}
P_l	Group-specific light exposure / attenuation factor.	dimensionless
τ_{chl}	Chlorophyll acclimation timescale.	d (days)
r^0_p	Reference photosynthetic rate per unit carbon.	d^{-1}
Ω^c_o, Ω^n_o	Stoichiometric conversion coefficients.	mol O per mol C (or N)
β_B	Bacterial growth efficiency.	dimensionless (0–1)
μ_Z	Prey half-saturation constant.	mg C m^{-3}
$\delta_{Z,i}$	Prey suitability matrix entries.	dimensionless (0–1)

Table 2.3: Parameters used in the chlorophyll, oxygen and grazing/microbial formulations. Values and group-specific defaults are documented in the BFM namelists. (Vichi et al., 2023)

2.5.2 Chlorophyll and the Geider-based chl:C Diagnosis

Chlorophyll dynamics in BFM are split into *production/acclimation* and *loss* terms (*grazing*, *degradation*). The model diagnoses a target chlorophyll-to-carbon ratio ρ_{chl} for each phytoplankton functional group using a *Geider*-like formulation (Geider et al., 1996; Geider et al., 1997) adapted to the model. The diagnosed ratio is then approached through an *acclimation/relaxation* towards the target with a group-specific timescale τ_{chl} (see Table 2.3).

A compact expression for the diagnosed chl:C ratio used in BFM is:

$$\rho_{chl} \;=\; \theta^0_{chl}\,\frac{\left.\dfrac{dP_c}{dt}\right|_{\text{gpp}}}{\alpha^*\,E_{PAR}\,P_l}, \tag{2.19}$$

where $dP_c/dt|_{\text{gpp}}$ is gross primary production (C uptake), θ^0_{chl} is a group-specific maximum chl:C, α^* an effective initial slope (quantum-yield-like), E_{PAR} the available PAR and P_l a light availability factor (Vichi et al., 2023).

An alternative rearrangement used is

$$\rho_{chl} \;=\; \theta^0_{chl}\,\frac{f_E\,r^0_p\,P_c}{\alpha^0_{chl}\,E_{PAR}\,P_l}, \tag{2.20}$$

where r^0_p is a reference photosynthetic rate per unit carbon and f_E is a light-regulating function. Once the target ρ_{chl} is computed, the instantaneous chl concentration for each phytoplankton group is relaxed via an acclimation timescale τ_{chl}.

The total model Chla is the sum across groups (converted via group-specific chl:C). (Vichi et al., 2023)
The chlorophyll budget therefore includes production tied to carbon uptake and losses:

$$\frac{d(\text{Chl})}{dt} = \sum_{j\in\text{phy}} \left[\rho^{(j)}_{chl}\,\left.\frac{dP^{(j)}_c}{dt}\right|_{\text{gpp}} \;-\; \text{loss}^{(j)}_{\text{grazing}} \;-\; \text{degradation}^{(j)} \right], \tag{2.21}$$

with group-specific parameterizations for *degradation/lysis* and *grazing*-coupled *loss* fractions. (Vichi et al., 2023)

2.5.3 Dissolved Oxygen: Budget and Principal Terms

Dissolved oxygen is computed from the stoichiometric sum of biological production and consumption terms together with physical exchange. Referring to the inline parameter definitions in Table 2.3, the biological tendency can be expressed compactly as:

$$\begin{aligned}\left.\frac{dO}{dt}\right|_{\text{bio}} = \Omega^c_o \sum_{j\in\text{phy}} \left(\left.\frac{dP^{(j)}_c}{dt}\right|_{\text{gpp}} - \left.\frac{dP^{(j)}_c}{dt}\right|_{\text{rsp}} \right) - \Omega^c_o \left.\frac{dB_c}{dt}\right|_{\text{rsp}} \\ -\Omega^c_o \sum_{k\in\text{zoo}} \left.\frac{dZ^{(k)}_c}{dt}\right|_{\text{rsp}} - \Omega^n_o \left.\frac{dN^{(4)}}{dt}\right|_{\text{nit}} + \dots\end{aligned} \tag{2.22}$$

where Ω^c_o and Ω^n_o are stoichiometric conversion factors (C→O, N→O), the sums run over *phytoplankton* and *zooplankton* groups respectively, and nitrification consumes

oxygen. Additional terms include oxygen impacts associated with formation and re-oxidation of reduction equivalents under low-oxygen conditions. Air-sea gas exchange and physical transport are added as boundary/advective-diffusive terms in the full model implementation. (Vichi et al., 2023)

2.5.4 Representation of the Microbial Loop and Herbivory Web

The BFM is able to explicitly represents both the microbial loop (**DOM/POC** → bacteria → micrograzers) and direct herbivory (*phytoplankton* → *zooplankton*). Key components include:

- **Sources of DOM/POC:** phytoplankton exudation, cell lysis, sloppy feeding (egestion), and particulate breakdown, parameterized as fractions of production, grazing egestion, and lysis events.
- **Bacterial uptake and growth:** multiple bacterial parameterizations are available; uptake follows *Monod*-like kinetics with maximum uptake rates and growth efficiencies (β_B), and temperature-dependent respiration partitions substrate between growth and loss.
- **Micrograzer coupling:** heterotrophic nanoflagellates and microzooplankton graze bacteria and small detritus, providing a pathway back to higher trophic levels and closing the microbial loop.
- **Herbivory (zooplankton ingestion):** ingestion is computed from prey availability using prey suitability and capture-efficiency weighting:

$$F_Z = \sum_i \delta_{Z,i}\, e_{Z,i}\, X_i, \tag{2.23}$$

with capture efficiency often represented as

$$e_{Z,i} \;=\; \frac{X_i}{X_i + \mu_Z}, \tag{2.24}$$

where μ_Z is a half-saturation constant and $\delta_{Z,i}$ the prey suitability matrix entry.

Routing between microbial recycling and herbivory is emergent and depends on prey densities, capture efficiencies (μ_Z), and parameterized fractions of exudation/lysis; these controls are exposed through namelist options (e.g., BACT version, exudation fractions) so that users can reproduce alternate ecological scenarios. (Vichi et al., 2023)

2.6 Bathymetry Profile

The bathymetric profile of the domain was obtained through bilinear interpolation of data provided by GEBCO 2021. This database represents a continuous global model of the oceanic and terrestrial seafloor with a spatial resolution of approximately 15 arc-seconds (equivalent to 500 m at the average Adriatic latitude), produced within

the framework of the Nippon Foundation–GEBCO Seabed 2030 project (GEBCO Bathymetric Compilation Group, 2021).
The GEBCO 2021 model integrates direct measurements (multibeam echo-sounder, single-beam, seismic) with interpolated data based on gravitational or algorithmic methods (satellite gravity inversion, simulation models) in areas of limited coverage, using a fusion approach through the regional centers of the Seabed 2030 project and the Global Center of the British Oceanographic Data Centre (GEBCO Bathymetric Compilation Group, 2021).

Given the modest depth of the northern Adriatic basin, it is classified as a coastal marine ecoregion and submerged continental shelf of the Mediterranean (Spalding et al., 2007; Malanotte-Rizzoli, 2014). Geomorphologically, the Northern Adriatic represents a broad shelf of ancient fluvial origin, with depths generally less than 100 m and predominantly sandy or muddy bottoms (Malanotte-Rizzoli, 2014). For this reason, the model includes the implementation of an explicit benthic–pelagic coupling that captures the bidirectional flows of nutrients and organic matter between sediment and water column, allowing a more accurate simulation of oxygen dynamics, benthic remineralization, and pelagic primary productivity even under environmental change conditions (Griffiths et al., 2017). This enables the overlying water column to interact with all major biogeochemical processes and cycles.

2.7 Boundary Conditions

The **Lateral Boundary Conditions** are treated with a *no-slip* condition, imposing zero velocity at the closed domain boundaries.

The **Bottom Friction** is modeled through a *quadratic*, *non-linear* formulation:

$$\tau_b = C_d \, \rho_0 \, |\mathbf{U}_b| \, \mathbf{U}_b, \tag{2.25}$$

where τ_b is the *bottom stress*, $\mathbf{U}_b$ is the *velocity* near the bottom, and C_d is the associated *drag coefficient*, which depends on *roughness* and *local stratification* (Madec and Delecluse, 1998; Griffies and Hallberg, 2000).

The numerical model calculates surface fluxes of momentum, mass, and heat at the atmosphere–ocean interface through *bulk formulae* calibrated by Castellari et al. (1998).

The **Momentum Flux** is expressed as:

$$\boldsymbol{\tau} \; = \; \rho_{\text{air}} \, C_D \, |\mathbf{U}| \, \mathbf{U}, \tag{2.26}$$

where ρ_{air} is the air density, $\mathbf{U}$ the wind velocity at 10 m height, and C_D the drag coefficient, which is a function of $U = |\mathbf{U}|$.

The **Sensible Heat Flux** is expressed as:

$$H \; = \; \rho_{\text{air}} \, c_p \, C_H \, |\mathbf{U}| \, (T_{\text{air}} - T_{\text{s}}), \tag{2.27}$$

where c_p is the specific heat capacity of air at constant pressure, and C_H the sensible heat transfer coefficient.

The **Latent Heat Flux** is given by:

$$E \;=\; \rho_{\text{air}}\, L_v\, C_E\, |\mathbf{U}|\, (q_{\text{air}} - q_{\text{s}}), \tag{2.28}$$

where L_v is the latent heat of vaporization and C_E the latent heat transfer coefficient; q_{air} and q_{s} are the specific humidity of the air and the saturation humidity at the sea surface, respectively. The coefficients C_D, C_H, and C_E are chosen according to the calibrated set proposed by Castellari et al. (1998), based on closure of the Mediterranean heat budget and analysis of observations from 1980–1988.

Regarding river forcings, the *Boundary Conditions* include contributions of **Momentum Flux** and **Nutrients** from 24 rivers; river discharge values used in the model are based on observations (see Section 4.1). The climatological discharge of the Po River is approximately 1500 m^3/s, corresponding to about 30% of the total discharge into the northern Adriatic basin (NAD), identified as the main input to the NAD. The salinity of river inputs is fixed at 15 psu according to Zavatarelli and Pinardi (2003) and Oddo et al. (2005). Discharges from other rivers and their nutrient inputs (*nitrates*, *phosphates*, and *silicates*) are treated using yearly values from Ludwig et al. (2009), implemented in the model as monthly average concentration fields following the Po's monthly variability.

At the open southern boundary, the physical model components are introduced via *one-way off-line nesting*, extracting boundary fields from a larger-scale model and imposing them unidirectionally (without feedback) at every model time step. In this case, boundary conditions are taken from the Mediterranean Forecasting System (`CMEMS MEDSEA_ANALYSISFORECAST_PHY_006_013_EAS6`), which provides sea surface elevation, mean bathymetry, horizontal velocity profiles as a function of depth, and vertical profiles of temperature and salinity interpolated along the southern model boundary (Clementi et al., 2021).

For interpolation along the open boundary, the formalism of Oddo and Pinardi (2008) is adopted, combining *radiation* and *tidal-inflow* schemes. In particular, the *radiation* condition according to Orlanski (1976) ensures that barotropic and baroclinic waves propagate out of the domain without spurious reflections, imposing:

$$\frac{\partial \phi}{\partial t} + c\,\frac{\partial \phi}{\partial n} = 0 \tag{2.29}$$

where ϕ is the variable (e.g., sea level elevation or velocity component), c the estimated phase speed, and n the normal to the boundary.

The **Flather** scheme introduces, for the barotropic component, an adjustment term between the predicted and observed elevation:

$$u_b = u_i + \frac{g}{\sqrt{gh}}\,\Delta\eta \tag{2.30}$$

where u_b is the boundary velocity, u_i the model-computed internal velocity, $\Delta\eta$ the difference between the superior and local model elevation, g gravitational acceleration, and h the boundary bathymetry (Flather, 1976). The same approach, with identical boundary condition schemes, is applied to biogeochemical components and tracers, ensuring coherence between physical and biogeochemical forcings along the entire southern domain boundary.

2.7.1 Benthic Boundary Layer Boundary Conditions

Following the approach of Mussap and Zavatarelli (2017), the benthic boundary layer in the simulation is treated as an active interface that closes pelagic particulate and dissolved tracer budgets through a set of lower-boundary fluxes rather than as a passive, fixed condition. Particulate organic matter produced in the water column is allowed to settle to the seabed and is removed from the pelagic compartments as a deposition flux at the lowest model level; this deposited material is then subject to benthic remineralization, which returns dissolved inorganic nutrients (N, P, Si) to the bottom water and consumes oxygen according to parameterized benthic turnover rates. The net effect of these benthic fluxes, whose main chain of processing is

$$deposition \rightarrow remineralization \rightarrow nutrient\ return + O_2\ demand\ , \tag{2.31}$$

is applied at each time step as the bottom boundary condition for pelagic tracers, so that sediment processes directly feed back on near-bottom concentrations and on the overlying water column through vertical diffusive/advective exchanges. (Mussap and Zavatarelli, 2017)

Exchange across the sediment–water interface is represented by two mechanistic terms that were treated as tunable boundary parameters: a sedimentation/deposition term (the vertical flux of particulate matter settling onto the seabed) and an effective benthic–pelagic diffusive term (representing bioturbation and porewater–bottom-water exchange). Mussap and Zavatarelli (2017) determined the best-reference values for these parameters via sensitivity experiments, and the same conceptual structure, implementing the deposition flux from the pelagic POM pool and prescribing a benthic return proportional to the deposited organic load, was adopted for this work This parameterized two-way coupling reproduces the principal benthic controls on nutrient recycling and oxygen consumption reported for shallow northern-Adriatic shelves. (Mussap and Zavatarelli, 2017)

The benthic boundary conditions are applied at the lowest sigma layer of the model, and at each model time step the pelagic-to-benthic deposition flux and the benthic-to-pelagic remineralization/oxygen-demand fluxes are computed and imposed as boundary tendencies for the water-column tracers. The choice to use an intermediate-complexity "*benthic return*" formulation is adopted, rather than a full diagenetic sediment model, as it has been deemed sufficiently able to reproduce the main benthic–pelagic feedbacks in shallow-shelf systems while keeping the model tractable for management-oriented experiments, as seen by the finding of Mussap and Zavatarelli (2017).

2.7.2 Oxygen Dynamics at the Benthic Boundary Layer

As the main biogeochiemical variable use for the model's validation at the benthic layer is the dissolved oxygen concentration, the equations used within this boundary layer are reported

Oxygen dynamics in the benthic layer are represented explicitly and act as the principal link between pelagic remineralization and sedimentary redox processes. In the model the sediment porewater oxygen is assumed to equilibrate rapidly at the resolved time scales, and the benthic oxygen field is therefore computed from a

steady/diagnostic balance that accounts for vertical diffusion within the *oxic* sediment horizon and for the main biogeochemical sinks: aerobic oxidation of deposited organic matter, nitrification of ammonium, and re-oxidation of reduced species. In one spatially resolved form (porewater vertical coordinate z) the oxygen balance can be written as

$$\frac{\partial O}{\partial t} \;=\; D_O\,\frac{\partial^2 O}{\partial z^2} \;-\; M_{\mathrm{ox}}(O) \;-\; M_{\mathrm{nit}}(O) \;-\; M_{\mathrm{rox}}(O) \qquad (0 \le z \le D^{(1)}), \tag{2.32}$$

where D_O is the effective molecular/turbulent diffusivity in sediments, M_{ox} represents oxygen consumption by aerobic heterotrophic respiration of organic matter, M_{nit} the oxygen demand associated with nitrification, M_{rox} the oxygen consumed by re-oxidation of reduced compounds, and $D^{(1)}$ is the oxic penetration depth. This formulation is solved assuming local equilibrium to obtain porewater oxygen and the oxic-layer thickness as a function of the imposed benthic loads and oxygen demand. (Mussap and Zavatarelli, 2017)

Instead of prescribing a fixed *oxic* depth, the model prognostically evolves the oxygen penetration depth $D^{(1)}$ toward an equilibrium value $D^{(1)}_{\mathrm{eq}}$ using a relaxation-type equation of the form

$$\frac{\mathrm{d}D^{(j)}}{\mathrm{d}t} \;=\; \nu_D\,\frac{h_D^{(j)}}{h_D^{(j)} + D^{(j)}}\,\left(\frac{D^{(j)}_{\mathrm{eq}}}{D^{(j)}}\right)^{\sigma}\,\left(D^{(j)}_{\mathrm{eq}} - D^{(j)}\right), \qquad j = 1, 2, \tag{2.33}$$

where ν_D is a relaxation frequency, $h_D^{(j)}$ is a reference depth that controls the sensitivity of the relaxation at small $D^{(j)}$, and σ is an exponent that damps short-scale variability (Mussap and Zavatarelli, 2017). This formulation allows the *oxic* (and the *denitrification*) horizons to respond dynamically to changes in organic loading and benthic respiration, avoiding abrupt switches and producing physically smooth adjustments of penetration depths.

At the level of benthic state variables, oxygen consumption appearing in the water-column tendencies is computed as the integrated effect of aerobic decomposition, nitrification and re-oxidation terms arising from the benthic food web and microbial activity. In flux-form notation the net benthic oxygen sink that is coupled back to the bottom water includes:

- the oxygen demand due to respiration of benthic consumers and microbial decomposers;
- the oxygen consumed in nitrification of ammonium released by remineralization;
- oxygen used to re-oxidize reduced chemical species produced in anoxic microzones.

These contributions are assembled into a single benthic oxygen-demand flux and imposed as a bottom boundary tendency for the pelagic oxygen tracer at every time step; simultaneously, the remineralization terms provide bottom-water sources of dissolved inorganic nutrients (NH_4^+, PO_4^{3-}, $Si(OH)_4$) following a stoichiometric partitioning (Mussap and Zavatarelli, 2017).

Two practical modelling consequences of this benthic oxygen formulation are important for Northern Adriatic applications. First, the oxic-penetration depth and

oxygen-demand flux respond nonlinearly to changes in particulate organic matter deposition (e.g., pulses following Po high-discharge events), so episodic increases in deposition can rapidly reduce $D^{(1)}$ and raise benthic O_2 consumption, promoting hypoxic conditions in bottom waters. Second, the explicit representation of nitrification and re-oxidation links benthic oxygen drawdown to the nitrogen cycle: strong benthic remineralization increases ammonium efflux, which in turn elevates nitrification oxygen demand and further tightens the coupling between benthic oxygen consumption and pelagic nutrient regeneration. (Mussap and Zavatarelli, 2017)

2.8 Model Data Initialization

The numerical initialization of the numerical simulation is a crucial step that strongly influences the model's ability to reproduce the observed variability in the basin. Within the model, the initial fields and the data for the lateral boundary conditions of the biogeochemical tracers were derived from a climatology obtained through a long-term (30 years) *hindcast* activity, carried out with a *coupled* system composed of the *Princeton Ocean Model* (**POM**) and the *Biogeochemical Flux Model* (**BFM**) (Scroccaro et al., 2022). This basin climatology provides consistent fields of temperature, salinity, and biogeochemical tracers, which are subsequently used to impose the *boundary conditions* and the initial profiles of the basin under analysis.

The model climatology is therefore derived from a long-term *hindcast* exercise. This technique was employed to address the need to avoid possible unrealistic chemical-physical discontinuities at the *boundaries* and to ensure an *initial condition* that is dynamically and biogeochemically consistent with the basin's mean conditions (Zavatarelli and Pinardi, 2003).

For a precise definition, a *hindcast* is a numerical simulation limited to a historical period that has already been observed and has two main objectives:

- to autonomously reproduce the climatic and interannual variability of the study region, constructing climatological statistics (seasonal means, mean vertical profiles, temporal distributions of tracers);
- to provide forcing fields and *boundary conditions* consistent for subsequent operational and experimental applications.

The *hindcast* thus acts as a "historical spin-up" and as a climatological archive: repeated temporal integration reduces possible transient effects related to arbitrary *initial conditions* and provides a set of simulated states that reflect the observed natural variability (Scroccaro et al., 2022; Zavatarelli and Pinardi, 2003).

It is also important to discuss the intrinsic limitations of this strategy: the model climatology reflects the choices of parameterization, the quality of the atmospheric and river forcing used in the hindcast, and the assumptions implemented in the biogeochemical model; therefore, any systematic errors in representing river nutrient loads or in the benthic–pelagic exchange processes will propagate into the climatology and, consequently, into the initial and boundary conditions of the operational system (Scroccaro et al., 2022; Zavatarelli and Pinardi, 2003).

Chapter 3
Satellite Observations

Satellite validation data were acquired from the CMEMS open-access portal for the validation of the numerical simulation. Specifically, L3s *processing level* data were used: *merged multi-sensor* products combining observations from different satellites and sensors, processed and remapped onto a common grid.

Within CMEMS, L3s (*Level 3 super-collated*) represents an intermediate stage in the remote sensing chain: compared to L2 products, which are calibrated and georeferenced but still *swath*-based, L3s products integrate multiple observations to reduce noise, increase coverage, and improve temporal continuity (Clementi et al., 2021). L3s products aggregate and intercalibrate observations from thermal infrared radiometers such as AVHRR and ATSR from various ESA and NOAA/EUMETSAT missions (Pisano et al., 2024; CMEMS - SST Production Centre, 2024). Only nighttime observations are used to minimize diurnal warming, ensuring the surface layer background temperature is accurately represented (CMEMS - SST Production Centre, 2024).

L3s datasets are subject however to the presence of *data gaps*, which must be considered when comparing with model fields to avoid statistical biases. Nevertheless, they remain a valuable source for model validation, retaining radiometric and spatial quality close to original satellite observations while benefiting from partial multi-sensor fusion.

CMEMS also provides L4-level products obtained via *Optimal Interpolation* (OI), a statistical data assimilation method estimating a continuous field by combining a background field (e.g., from climatologies or models) with a vector of satellite observations (Bretherton et al., 1976; Reynolds et al., 2007).

Within CMEMS, OI is applied to interpolate L3s (*merged multi-sensor*) products onto a regular daily or weekly grid, compensating for *data gaps* due to phenomena such as cloud cover (Pisano et al., 2024). However, in the study area, the sparse observational density (*null collinearity*) is also highlighted in the CMEMS *Quality Information Document* (QUID) shown as *Figure 3.1*, which displays the spatial distribution of *match-up* points between MED-REP-L4, MED-REP-L3S products, and *drifter* data from 2005 to 2021 (Pisano et al., 2024).

Under these conditions, the analysis are forced toward the background signal, reducing if not nullifying the impact of observations. Preliminary tests (not reported in this work) highlighted significant discrepancies between L3s and L4 fields, indicating a loss of observational information in favor of the interpolated component. For these reasons, L3s products were chosen for validation, prioritizing their greater fidelity to raw observations, even at the cost of the presence of *data gaps*.

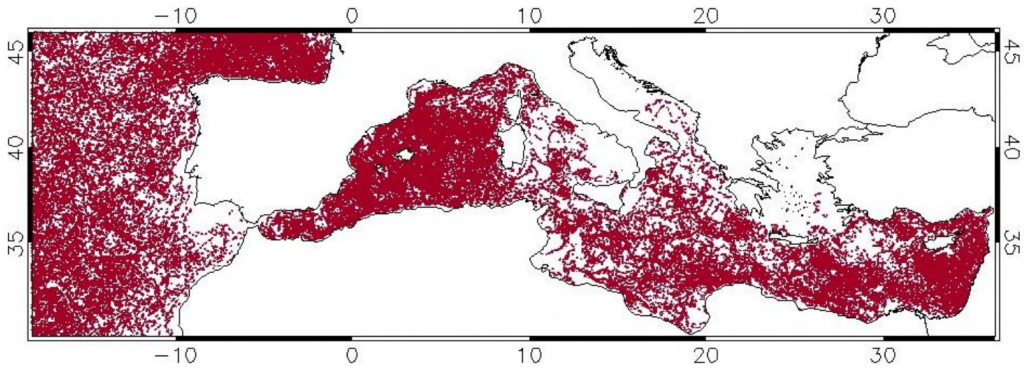

Figure 3.1: Image showing the spatial distribution of collinear points where **MED-REP-L4**, **MED-REP-L3S**, and **drifter data** are available within the analysis window 2005–2021. A significant lack of collinear points can be observed across nearly the entire Adriatic basin. (Pisano et al., 2024)

3.1 Adjusted Sea Surface Temperature

The temperature dataset used for validation represents the *sub-skin temperature* at approximately 20 cm depth and it is the product `SST_MED_PHY_L3S_MY_010_042` E.U. Copernicus Marine Service Information (CMEMS) (2024), a *Reprocessed* (REP) dataset for the Mediterranean basin (MED) obtained through multi-sensor fusion (processing level L3S). This product provides daily (nighttime) estimates of *Adjusted Sea Surface Temperature* (SST) in Kelvin, subsequently converted into degrees Celsius, and the performance of the satellite observations is reported in *Table 3.1.*

Start Date	End Date	Parameter	Value
2005-01-27	2021-12-31	BIAS	0.012 ± 0.001 K
2005-01-27	2021-12-31	RMSD	0.387 ± 0.001 K
2005-01-27	2021-12-31	Nr. of matchups	417780

Table 3.1: Summary statistics between the the `MED-REP-L3S` product and drifter data at matchup points. Each includes a 95% confidence interval. (Pisano et al., 2024)

The observed dataset is provided at a spatial resolution of $0.05° \times 0.05°$. Given the difference in resolution compared to the numerical simulation, which has a grid spacing of $1\,\text{km} \times 1\,\text{km}$, the dataset was reprojected using the *CDO* (*Climate Data Operator*) software with the *nearest neighbor* method. This interpolation method assigns to each target grid point the value of the nearest point in the original grid, without averaging or weighting. Formally, given a target point with spatial coordinates $\mathbf{x}$, the interpolated value $f(\mathbf{x})$ is defined as

$$f(\mathbf{x}) = f(\mathbf{x}_i) \quad \text{with} \quad \mathbf{x}_i = \arg\min_{\mathbf{x}_j} \|\mathbf{x} - \mathbf{x}_j\|, \tag{3.1}$$

where $\mathbf{x}_j$ are the known points of the source grid and $\|\cdot\|$ denotes the Euclidean norm in geographic space.

This operation allowed the generation of two grids with the same spatial resolution, thereby facilitating a direct comparison between observed and simulated data. It is

important to underline that this processing was carried out exclusively for comparative purposes to facilitate the comparison between the two grids and does not alter the physical properties of the original data.

3.2 Chlorophyll-a

The product used for the validation of the $Chlorophyll - a$ is `OCEANCOLOUR_MED_BGC_L3_MY_009_143` E.U. Copernicus Marine Service Information (CMEMS) (2023), also provided by CMEMS.

The dataset provides the concentration of phytoplankton chlorophyll (CHL), derived using regional empirical algorithms specific to the waters of the Mediterranean. For open ocean waters, the algorithms of Volpe et al. (2019) are applied, based on the spectral relationship between ocean reflectance ratios and chlorophyll concentration:

$$\mathrm{CHL} = 10^{\left(a_0 + a_1 R + a_2 R^2 + a_3 R^3 + a_4 R^4\right)}, \tag{3.2}$$

where $R = \log_{10}\left(\frac{R_{rs}(443)}{R_{rs}(555)}\right)$ is the logarithmic ratio between normalized remote-sensing reflectance at wavelengths of 443 nm and 555 nm, and a_i are empirical coefficients determined for the Mediterranean region.

For coastal waters, characterized by higher contents of dissolved organic matter and suspended inorganic particulate matter, the algorithm of Berthon and Zibordi (2004) is used, formulated for the bio-optical conditions typical of the northern Adriatic:

$$\mathrm{CHL} = \alpha \left[\frac{R_{rs}(490)}{R_{rs}(555)}\right]^{\beta}, \tag{3.3}$$

where α and β are coefficients calibrated for optically complex environments.

Chapter 4
In-situ Observations

In order to obtain direct observational feedback, in addition to the modelling component, a set of *in situ* data was utilized. These observations serve a dual purpose: on one hand, they provide essential information to characterize the boundary conditions of the system, such as river flow regimes, where discharge and concentration values represent crucial inputs for the simulation; on the other hand, they offer a solid basis for independent validation of the model results.

Specifically, data from coastal stations were used, obtained through surveys conducted with **CTD** probes (*Conductivity, Temperature, Depth*), instruments capable of simultaneously measuring conductivity (and thus salinity), temperature, and depth, thereby mapping the vertical hydrological structure of the water column.

4.1 Po's River Flow Regimes Data

For the characterization of freshwater inputs to the Northern Adriatic, daily discharge measurements of the Po River recorded by the regional hydrometric monitoring network managed by ARPAE were used. The hydrometric section selected for this study is located at Pontelagoscuro (Ferrara), the terminal section of the Po River basin used as a reference in basin budget analyses and hydrological validation activities (ARPAE Emilia-Romagna, 2024). The geographical location conventionally associated with the station is approximately 44°53′19″ N, 11°36′30″ E (coordinates expressed in degrees, minutes, and seconds) (Luo et al., 2024; Vörösmarty et al., 2003), and the section drains a basin area of about 7.0×10^4 km^2 (ARPAE Emilia-Romagna, 2024). *Figure 4.1* shows a map indicating the geographical location of the station.
The instantaneous discharge Q of the river is defined through the normal component of velocity across the section A:

$$Q(t) \;=\; \int_A \mathbf{u}(\mathbf{x}, t) \cdot \mathbf{n} \, \mathrm{d}A \tag{4.1}$$

where $\mathbf{u}$ is the velocity vector and $\mathbf{n}$ is the unit normal vector to the section; in operational practice, this continuous expression is discretized into vertical columns or cells of the section, yielding the standard discrete relation

$$Q(t) \;\approx\; \sum_{i=1}^{N} \bar{u}_i(t) \, A_i, \tag{4.2}$$

with $\bar{u}_i$ being the average velocity in cell i and A_i the area of the cell (a direct velocity–area measurement) (Mueller et al., 2013; Rantz et al., 1982).

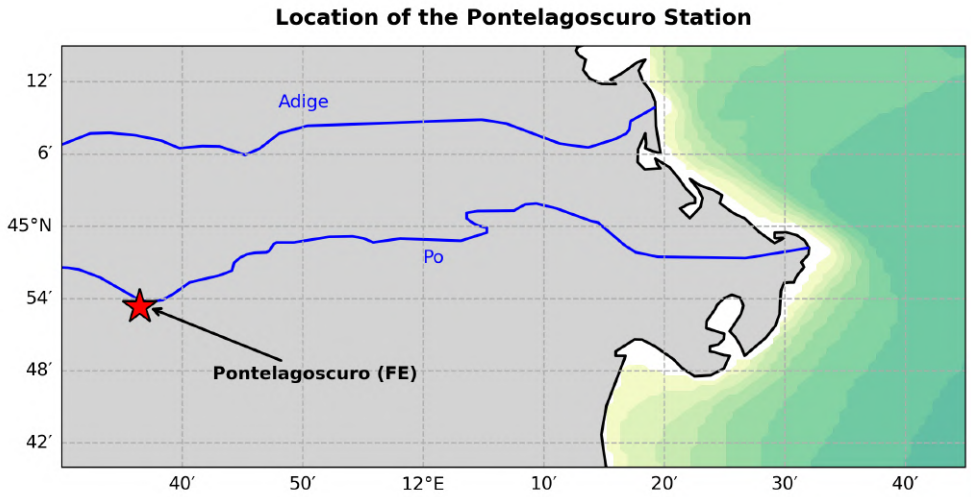

Figure 4.1: Portion of a map showing the Po and Adige river courses; the red marker indicates the geographical location of the ARPAE Pontelagoscuro (FE) monitoring station.

In operational hydrometric networks, continuous discharge measurement is often obtained indirectly by measuring the water level (*stage*) $h(t)$ and applying a calibration curve (*rating curve*) that relates the stage to discharge via an empirical relationship (*power-law*):

$$Q(h) \;=\; a\,[h - c]^b, \tag{4.3}$$

where a, b, and c are parameters calibrated through absolute discharge measurements and spot sampling (Rantz et al., 1982; Filippucci, 2022). Such absolute measurements are generally obtained via direct current velocity measurements (e.g., with mechanical current meters) or, more recently, through velocity profiles acquired with an *Acoustic Doppler Current Profiler* (**ADCP**) either deployed from a vessel or mounted (Mueller et al., 2013). ADCP campaigns provide $\bar{u}_i$ measurements throughout the water column and allow direct estimation of Q using the discrete formula above; the obtained values are then used to calibrate or update the rating curve.

From an instrumental point of view, the automatic measurement of the stage $h(t)$ at stations such as Pontelagoscuro can be performed using submerged pressure transducers, ultrasonic sensors, or radar sensors installed on the riverbank; the choice of instrument depends on operational constraints, maintenance requirements, and bed conditions (*sedimentation*, *biofouling*). The direct measurements used to calibrate the rating curve (**ADCP** or *current meters*) are subject to quantifiable errors and limitations under particular flow regimes (e.g., measurements in very shallow water or in mobile-bed conditions). For this reason, hydrometric practice involves repeated measurement campaigns and quality control procedures (Mueller et al., 2013; Rantz et al., 1982).

The recorded time series, used as a *boundary condition* for the model, consists of daily discharge observations available for the period 1980–2010, provided as daily averages by the monitoring network. This time window allows the construction of climatologies and anomaly analyses over multi-annual and seasonal intervals. The time series of daily discharge values of the Po River within the analysis window is shown in *Figure 4.2*.

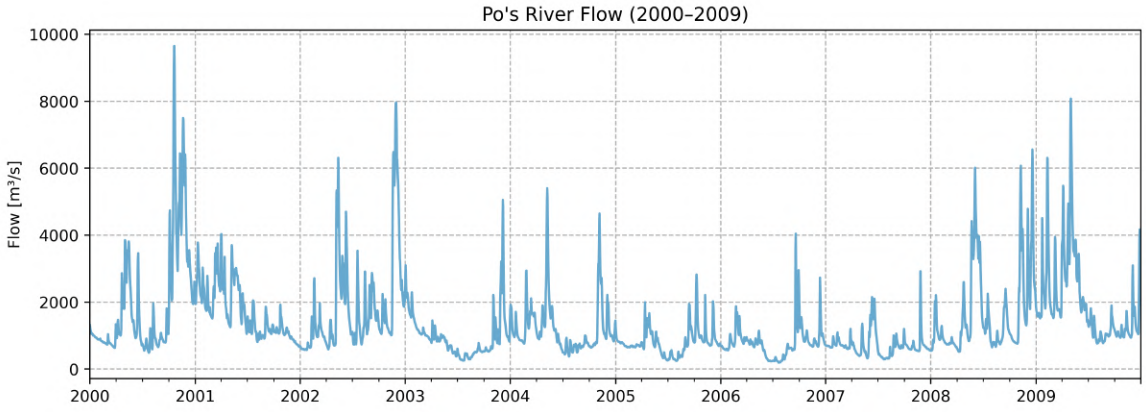

Figure 4.2: Graph showing the discharge flow from the Po River recorded at the Pontelagoscuro (FE) station within the analysis time window.

Figure 4.3 shows the corresponding climatologies.

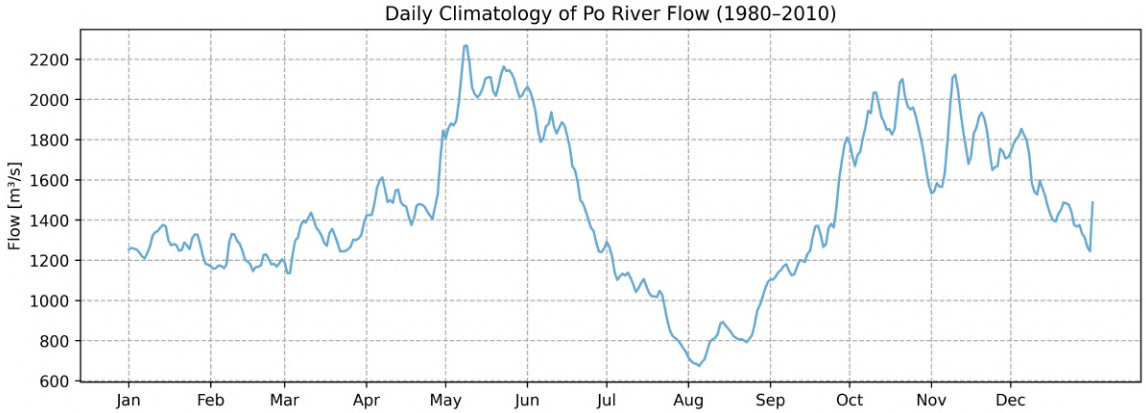

Figure 4.3: Graph representing the climatology of discharge flow from the Po River recorded at the Pontelagoscuro (FE) station over the entire data period provided by ARPAE (1980–2010).

Figure 4.4 shows the climatological distribution of discharge anomalies, defined relative to a climatological mean value of 1500 m^3/s.

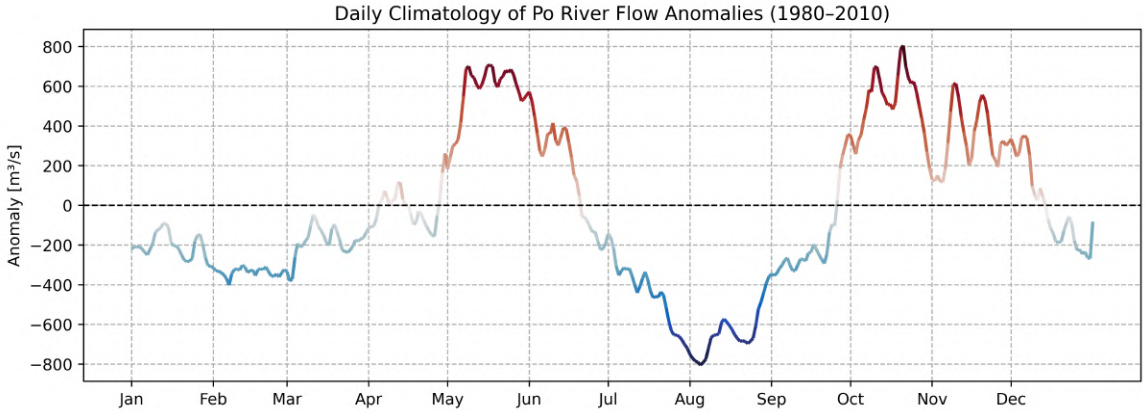

Figure 4.4: Graph showing the discharge flow from the Po River recorded at the Pontelagoscuro (FE) station relative to its climatological mean value of 1500 m^3/s. The time window considered represents the entirety of the data provided by ARPAE (1980–2010).

The analysis of the last graph in particular allows the identification of monthly and seasonal periods during which peaks or reductions in river discharge occur. Specifically, between May and the second half of June, and again between October and early December, high values around 2000 m^3/s are recorded. Conversely, between July and September a marked decrease is observed, with discharges less than half the climatological average: about 650 m^3/s compared to the 1500 m^3/s mean.

4.2 Daphne-ARPAE Fixed Stations

To provide an additional comparison with observational data useful for model validation, the Daphne-ARPAE station network was used, consisting of **CTD** probes positioned at various distances from the coast and at different depths..

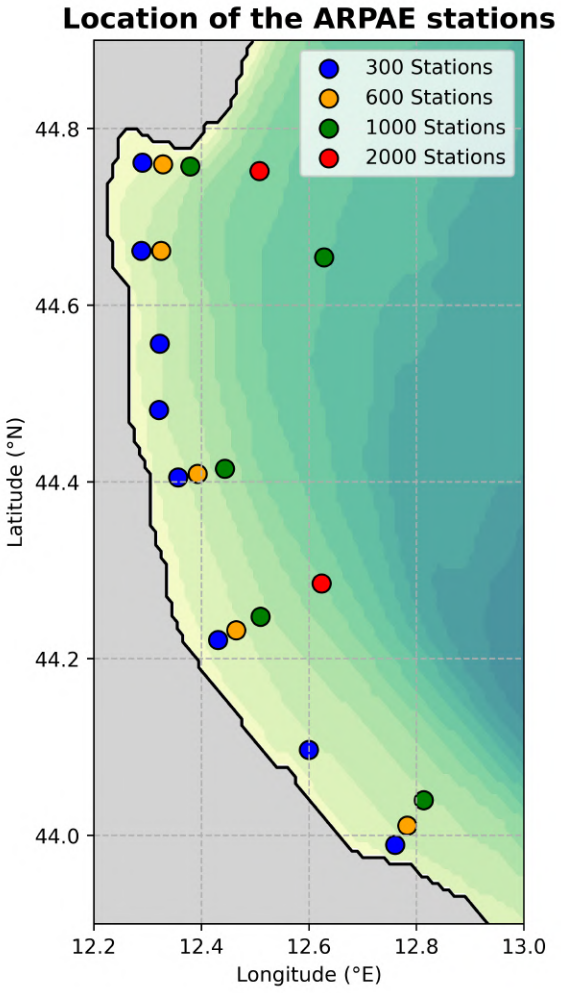

Figure 4.5: Geographic area of the ARPAE *in-situ* stations. The stations are grouped according to the color code corresponding to each group. The color scale used within the basin represents the maximum depth of the *z-layers*, according to a vertical discretization of $dz = 2\ m$.

The area of interest included the Po River mouth and the southern zone up to the boundary of the analyzed basin, so as to capture the most complex dynamics characterizing this region

The stations used were grouped according to their ID, following the classification provided in the ARPAE dataset. Specifically, four groups of stations were identified based on their distance from the coastline:

- **Group 300**: $\sim$ 3 km from the coast;
- **Group 600**: $\sim$ 6 km from the coast;
- **Group 1000**: $\sim$ 10 km from the coast;
- **Group 2000**: $\sim$ 20 km from the coast.

It should be noted that the station with ID 1019 is actually located at a considerably greater distance than the 10 km indicated by ARPAE; despite this discrepancy, it was retained in Group 1000 to maintain consistency with the official station classification. Further details on station characteristics are provided in *Table 4.1*.

ID	Location	Prof. max (m)	WGS84	
			Lat	Lon
Group 300				
302	Lido di Volano	6.7	44.4569	12.1741
304	Porto Garibaldi	9.1	44.3969	12.1729
306	Casalborsetti	10.2	44.3341	12.1933
308	Marina di Ravenna	8.1	44.2889	12.1926
309	Lido Adriano	9.4	44.2431	12.2139
314	Cesenatico	8.3	44.1326	12.2584
317	Rimini	9.9	44.0582	12.3599
319	Cattolica	11	43.5931	12.4559
Group 600				
602	Lido di Volano	7.8	44.4557	12.1969
604	Porto Garibaldi	12	44.3971	12.1950
609	Lido Adriano	11.4	44.2456	12.2356
614	Cesenatico	10.2	44.1394	12.2786
619	Cattolica	12.1	44.0003	12.4697
Group 1000				
1002	Lido di Volano	10.1	44.4544	12.2275
1004	Porto Garibaldi	14.8	44.3972	12.2257
1009	Lido Adriano	15.1	44.2460	12.2669
1014	Cesenatico	12.3	44.1484	12.3059
1019	Cattolica	13.6	44.0238	12.4879
Group 2000				
2004	Porto Garibaldi	26.5	44.3973	12.3013
2014	Cesenatico	22.0	44.1711	12.3739

Table 4.1: Metadata of ARPAE stations divided by group; reported are: station ID, location, maximum depth, and WGS84 coordinates (Lat/Lon). Coordinates are limited to the 4° decimal place.

The Daphne-ARPAE measurements use multiparameter CTD probes (Idronaut OCEAN SEVEN 316Plus by *Sea-Bird*) to collect the physical and biogeochemical observations employed in this study (ARPAE Emilia-Romagna, 2009; ISPRA - Istituto Superiore per la Protezione e la Ricerca Ambientale, 2012). These instruments measure key water column properties: temperature is recorded by a fast-response thermistor; salinity is derived from electrical conductivity combined with temperature and pressure, expressed according to the Practical Salinity Scale (PSS-78); dissolved oxygen is measured with a Clark-type polarographic electrode; and chlorophyll-a is estimated via optical fluorimetry, detecting fluorescence emitted by pigments after absorbing blue-green light, as a proxy for phytoplankton biomass. This integrated sensor setup allows ARPAE-Daphne stations to generate consistent time series of physical and biogeochemical parameters, providing essential reference data for interpreting coastal dynamics and validating numerical models.

4.2.1 Daphne-ENEA Dataset

A second subset of in situ observational data was employed to validate the simulation results within the Po River ROFI area. These measurements were obtained during a supposed monitoring campaign carried out by Daphne and whose data has been provided by ENEA (Italian National Agency for New Technologies, Energy and Sustainable Economic Development) throughout 2006 using the same **CTD** (*Conductivity, Temperature, Depth*) probes used within the ARPAE-Daphne dataset.

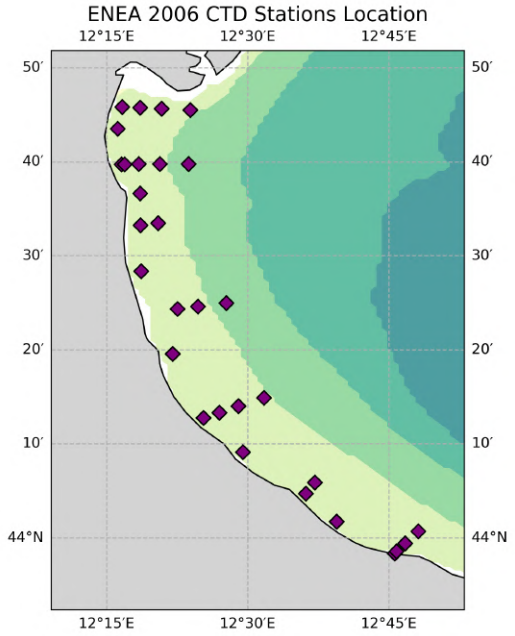

Figure 4.6: Map showing the geographical positions of the CTD stations within the Daphne-ENEA dataset. The color scale within the basin represents the bathymetry.

The corresponding geographical positions of the sampling stations are displayed in *Figure 4.6*.

The main differene within this dataset difference lies in the storage format of the oxygen data, which in this case is expressed in ppm (parts per million). Furthermore, in contrast to the approach applied to the ARPAE dataset, no subdivision into subsets was performed for this dataset. This decision is justified by the fact that the maximum depth recorded remains constant across the entire network of sampling stations, ensuring a uniform sampling depth throughout the dataset. As a result, the dataset can be treated as a single, coherent unit for the purposes of analysis, without the need to account for variability in depth-related parameters.

Additional information regarding the number of samples during the campaign, as well as the precise temporal window over which the sampling was conducted, is reported in *Table 4.2*

Season	Sampling Period	Number of Samplings
DJF (Winter)	December 4 – February 21	57
MAM (Spring)	March 1 – May 29	132
JJA (Summer)	June 5 – August 28	108
SON (Autumn)	September 1 – November 29	120

Table 4.2: Sampling campaigns conducted by ENEA aboard the research vessel *Daphne II*, divided by season, with sampling period and number of samplings.

4.3 ADRIA Cruises

Finally, the third *in situ* dataset used for validation, particularly for the analysis of *dense water mass* formation processes, originates from the **ADRIA** oceanographic

campaigns conducted in 2001, 2002, and 2003 as part of the activities of the NATO *Undersea Research Centre* (NURC, formerly SACLANTCEN). The campaigns, known as **ADRIA01**, **ADRIA02**, and **ADRIA03**, were primarily aimed at characterizing the hydrographic and dynamic conditions of the northern and central Adriatic Sea, with particular focus on the processes of formation, mixing, and ventilation of dense waters generated along the continental shelf edge. The locations of the samplings used in this project are shown in *Figure 4.7*.

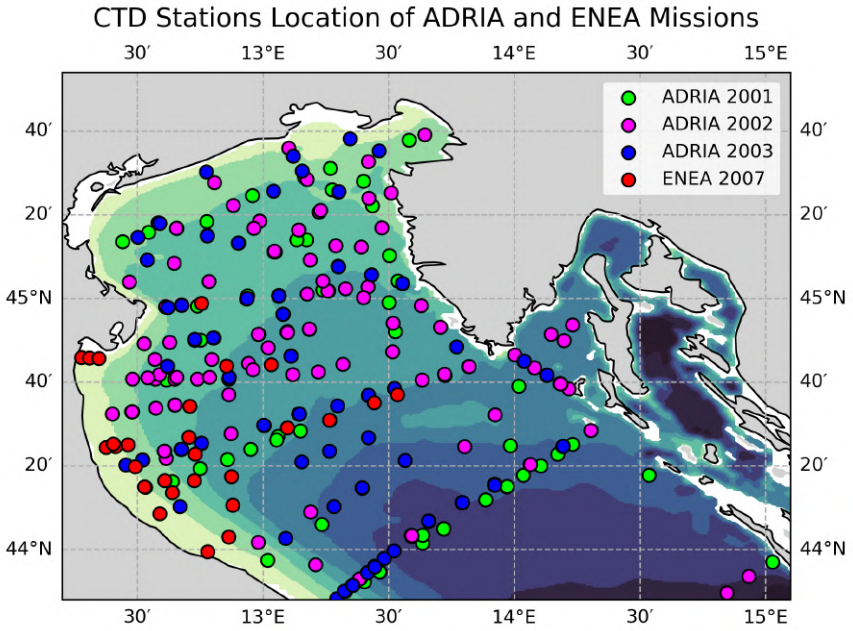

Figure 4.7: Map showing the geographical positions of the CTD stations relative to the ADRIA and ENEA samplings during the measurement campaign. Each marker is color-coded relative to its campaign: lime for ADRIA 2001; magenta for ADRIA 2002; blue for ADRIA 2003 and red for ENEA 2007. The color scale within the basin represents the bathymetry.

During the missions, carried out aboard the oceanographic vessel *R/V Alliance*, numerous vertical profiles were collected using **CTD** (*Conductivity, Temperature, Depth*) probes for measuring conductivity, temperature, and depth, from which salinity and potential density fields were derived. The surveys covered a wide portion of the basin, including the northern Adriatic shelf, the central area, and, in some cases, the southern pit. The campaigns were conducted in different seasons (winter 2001, autumn 2002, and spring 2003) to investigate the seasonal and interannual variability of dense water formation processes and the basin's response to atmospheric cooling events and Bora wind forcing.

In addition to the main physical parameters, the CTD probes were equipped with auxiliary sensors for measuring dissolved oxygen, turbidity, and fluorescence, allowing for a more comprehensive characterization of the hydrographic and biogeochemical state of the water column. The data collected, subsequently processed and made available by NURC, represent one of the most complete observational datasets for validating numerical models of circulation and *dense water mass* formation in the northern Adriatic (Wang et al., 2005; Boldrin et al., 2009).

In order to further expand the observational basis used for the validation of the model results, an additional dataset was integrated, originating from an oceanographic

campaign conducted by ENEA between February 19 and 24, 2007. The inclusion of this dataset addresses the need for broader spatial coverage within the northern basin, which is significantly greater than that of the 2006 campaign previously described in Section 4.2.1. This extended coverage improves the representativeness of the winter hydrological conditions, providing a more comprehensive overview of the processes of formation and distribution of dense water masses in the Northern Adriatic.

Additional informations regarding each campaign are reported in *Table 4.3*.

Campaign	**Sampling Period**	**Number of Samplings**
ADRIA 2001	January 28 – February 10, 2001	162
ADRIA 2002	September 16 - October 9, 2002	489
ADRIA 2003	April 27 - May 4	159
ENEA 2007	February 19 – February 24, 2007	27

Table 4.3: Sampling campaigns conducted by ENEA aboard the research vessel *Daphne II*, and ADRIA campaigns, with sampling period and number of samplings.

Chapter 5
Methods - Datasets Pre-Processing

Before proceeding with the analyses and the validation of simulation results, a pre-processing phase was carried out on both satellite and model datasets. The aim was to identify possible inconsistencies in the time series and to make them directly comparable.

5.1 Satellite Data Interpolation

The first step in pre-processing the satellite data involved a series of analyses aimed at verifying dataset completeness and identifying any missing data fields. These gaps may arise from missed satellite passes over the area of interest or from complete cloud coverage that prevented signal acquisition; a phenomenon typical when using L3 data.

The datasets used in the analyses were first subjected to a temporal consistency check to identify *gaps* in the time series that were not due to missing observations but rather to the actual absence of data within the dataset.

The gaps identified in the datasets are reported in *Table 5.1*.

Dataset	**Missing Days**	**Total Days**
`NADR-SST-SAT-CMEMS-2000-2009-l3-daily`	3653	0
`NADR-CHL-SAT-CMEMS-2000-2004-l3-daily`	1818	9
`NADR-CHL-SAT-CMEMS-2005-2009-l3-daily`	1826	0

Table 5.1: Statistics on temporal coverage and missing data for each daily CMEMS dataset for the northern Adriatic basin (2000–2009).

The missing days within the time series are mainly concentrated in the years 2000–2001 and are reported in detail in *Table 5.2*:

Missing Days		
2000-05-19	2000-11-17	2001-11-06
2000-05-25	2000-11-18	2001-11-18
2000-07-10	2000-12-09	2001-03-24

Table 5.2: List of days initially missing in the dataset `NADR-CHL-SAT-CMEMS-2000-2004-l3-daily`.

These days were initialized and filled with `NaN` values, thus restoring the time series to its correct length of 3653 days.

Subsequently, an analysis of *Missing fields* was conducted by identifying temporally valid days within the series but characterized by a spatial field without any observational data (complete lack of useful coverage).

This analysis was implemented by verifying, for each *time step*, the presence of at least one valid numerical value within the domain of interest. Formally, for each instant t_i, the indicator function was calculated:

$$\delta(t_i) = \begin{cases} 1 & \text{if } \exists\ x, y \quad \text{such that } D(x, y, t_i) \neq \text{NaN}, \\ 0 & \text{if } \forall\ x, y \qquad D(x, y, t_i) = \text{NaN}, \end{cases} \tag{5.1}$$

where $D(x, y, t_i)$ represents the dataset value at the spatial point (x, y) at time t_i. Days with $\delta(t_i) = 0$ were classified as *Missing fields*.

The total number of *Missing fields* identified for each dataset is reported in *Table 5.4*:

Variabile	**Nr. of Missing Daily Fields**
Sea Surface Temperature	301
Chlorophyll-a	487

Table 5.3: Statistics on missing daily fields for the satellite variables *Adjusted Sea Surface Temperature* and *Chlorophyll-a*.

This step allowed for the complete identification and correction of *gaps* present within the satellite dataset.

The final pre-processing step involved bilinear interpolation of both satellite datasets.

This method is based on two successive linear interpolations along the coordinate directions, allowing a continuous and smooth estimate between grid nodes (Farrell, 2008; Press et al., 2007).

Let

$$\begin{aligned} Q_{11} &= f(x_1, y_1), \\ Q_{21} &= f(x_2, y_1), \\ Q_{12} &= f(x_1, y_2), \\ Q_{22} &= f(x_2, y_2) \end{aligned} \tag{5.2}$$

be the known values at the corners of a quadrilateral defined by the points (x_1, y_1), (x_2, y_1), (x_1, y_2), (x_2, y_2), with $x_1 \leq x \leq x_2$, $y_1 \leq y \leq y_2$ as by the scheme shown in *Figure 5.1*.

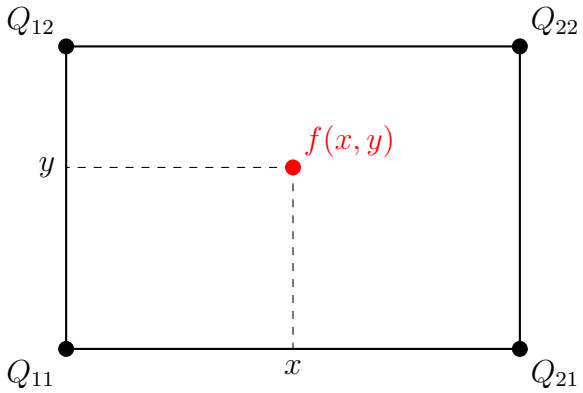

Figure 5.1: Simplified diagram of the quadrilateral used for bilinear interpolation. The markers Q_{kk} indicate the known points, while $f(x, y)$ represents the interpolated grid point.

Bilinear interpolation computes the value $f(x, y)$ inside this rectangle as:

$$f(x,y) = \frac{1}{(x_2 - x_1)(y_2 - y_1)} \big[Q_{11}(x_2 - x)(y_2 - y) + Q_{21}(x - x_1)(y_2 - y) + Q_{12}(x_2 - x)(y - y_1) + Q_{22}(x - x_1)(y - y_1) \big]. \tag{5.3}$$

This formula expresses the interpolated value as a weighted average of the values at the four vertices, with the weights determined by the relative distance of the point (x, y) from each vertex (Press et al., 2007).

For the application of this interpolation technique, values from a source grid (*numerical model*) are mapped onto a destination grid (*satellite*). For each point of the destination grid, the quadrilateral in the source grid containing it is identified, and bilinear interpolation is applied using the four nearest values.

In the presence of extreme values or outliers, it is common to define *outlier* thresholds to exclude such points from interpolation, setting them as missing data (`NaN`). The chosen *thresholds* are:

Variable	**Outliers**
Sea Surface Temperature	$8 \leq x \leq 35$
Chlorophyll-a	$0 \leq x \leq 15$

Table 5.4: *Thresholds* used for *Adjusted Sea Surface Temperature* and *Chlorophyll-a* data in order to identify possible *outliers* to be excluded during interpolation.

A minimum number of usable data points is also imposed to ensure the validity of the interpolation:

$$N_{\text{obs}} = \sum_{(x,y)} \mu(x, y), \quad \text{with } N_{\text{obs}} > N_{\text{min}}. \tag{5.4}$$

To improve spatial continuity and fill data gaps, an iterative method for extending valid values is applied. Given a data field $M(x, y)$ with missing values, an extended

matrix M^* is defined that assigns to each initially missing point the average value calculated from its valid neighbors:

$$M^*_{t+1}(x,y) = \begin{cases} M_t(x,y) & \text{if } M_t(x,y) \neq \text{NaN}, \\ \frac{1}{|\mathcal{N}(x,y)|} \sum_{(x',y') \in \mathcal{N}(x,y)} M_t(x',y') & \text{otherwise}, \end{cases} \tag{5.5}$$

where $\mathcal{N}(x,y)$ denotes the set of adjacent points (8-connectivity or grid points) to (x,y), and t represents the current iteration. The process continues for a fixed number of iterations or until changes become negligible (Farrell, 2008).

5.2 Model Data Masking

The pre-processing of the model data did not require the same checks performed on the satellite data, as the dataset was already complete. However, a series of preparatory steps were carried out to ensure a direct and consistent comparison with the satellite data.

In order to obtain two datasets suitable for direct comparison, it was necessary to account for the cloud coverage typical of L3 satellite data. The cloud coverage mask, computed from the satellite data, was used to identify invalid pixels due to atmospheric contamination or lack of observation exclusively within the northern Adriatic basin.

To maintain consistency between the two datasets, this mask was also applied to the model data according to the relation:

$$M_{\text{masked}}(x,y,t) = \begin{cases} M(x,y,t), & \text{if } C(x,y,t) = 0, \\ \text{NaN}, & \text{if } C(x,y,t) = 1, \end{cases} \tag{5.6}$$

where $M(x,y,t)$ represents the original model field and $C(x,y,t)$ is the binary cloud coverage mask (0 = valid, 1 = cloud covered).

In this way, the same gaps present in the satellite data are introduced also in the numerical simulation, ensuring a unique and physically consistent comparison, as shown in *Figure 5.2*.

In cases of total absence of satellite data, the corresponding day in the model dataset was marked as a *gap*, in order to maintain consistency between the two time series.

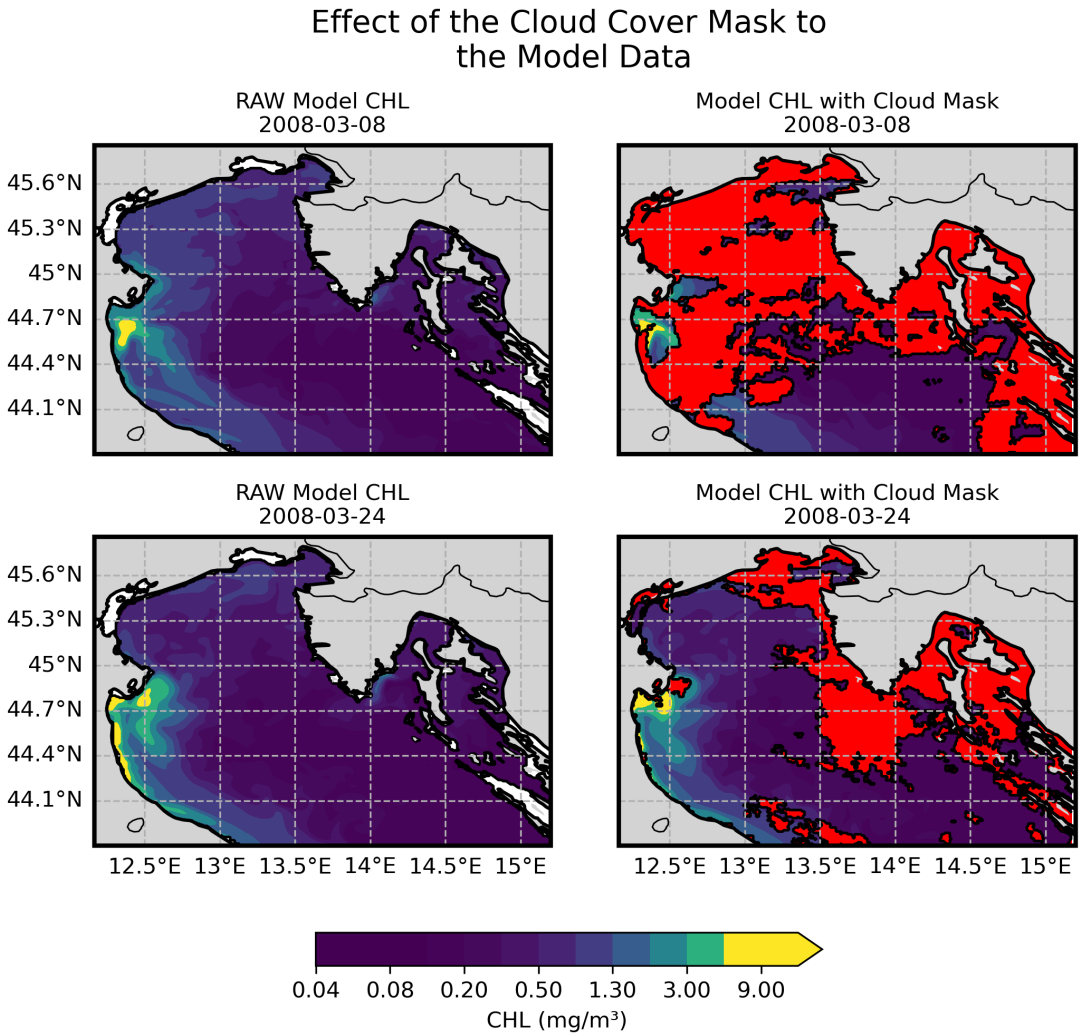

Figure 5.2: Result of applying the cloud cover mask to the model data. Starting from the complete data (left), gaps are formed (right).

With this last step, the preprocessing necessary for data validation was concluded, ensuring full consistency between satellite and model datasets. The following sections will present the methods and analytical techniques adopted in the project.

Chapter 6
Methods - Diagnostics Criteria

6.1 Timeseries and Outliers

Once the pre-processing of the satellite and model datasets was completed, the three-dimensional fields (*time*, *latitude*, *longitude*) were used to generate two basin-averaged timeseries, aimed at analyzing and validating their temporal evolution.

For each valid day $d \in [1, N_{\text{days}}]$, the model and satellite fields were extracted in a two-dimensional form (ϕ, λ), applying both the *land* and cloud coverage masks, in order to exclude all cells where at least one of the two datasets contains missing values.

Formally, let $M_d(\phi, \lambda)$ be the model field on day d and $S_d(\phi, \lambda)$ the satellite field. The validity mask is defined as:

$$\mathcal{V}_d(\phi, \lambda) = \begin{cases} 1, & \text{if } M_d(\phi, \lambda) \neq \text{NaN} \ \wedge \ S_d(\phi, \lambda) \neq \text{NaN} \\ 0, & \text{otherwise} \end{cases} \tag{6.1}$$

The validated fields are therefore:

$$M_d^*(\phi, \lambda) = M_d(\phi, \lambda) \cdot \mathcal{V}_d(\phi, \lambda) \tag{6.2}$$
$$S_d^*(\phi, \lambda) = S_d(\phi, \lambda) \cdot \mathcal{V}_d(\phi, \lambda) \tag{6.3}$$

The daily spatial average over the entire basin is obtained by computing the mean of only the valid values:

$$BA_{\text{mod}}(d) = \frac{1}{N_{\text{val}}(M_d^*)} \sum_{\phi,\lambda} M_d^*(\phi, \lambda) \tag{6.4}$$

$$BA_{\text{sat}}(d) = \frac{1}{N_{\text{val}}(S_d^*)} \sum_{\phi,\lambda} S_d^*(\phi, \lambda) \tag{6.5}$$

where $N_{\text{val}}(\cdot)$ indicates the number of valid elements on day d.

Finally, to avoid inconsistencies caused by null values (0) resulting from complete masking, the daily averages in such cases were set to `NaN` in both datasets:

$$\text{if} \quad BA_{\text{mod}}(d) = 0 \quad \Rightarrow \quad BA_{\text{mod}}(d) = BA_{\text{sat}}(d) = \text{NaN} \tag{6.6}$$

To assess the temporal performance of the model, the simulated *timeseries* was employed in two structurally complementary analyses: quantifying the systematic deviation relative to observed data via the *BIAS*, and characterizing the statistical distribution to identify potential anomalous values.

The *BIAS* is defined as the arithmetic mean of the differences between model simulations and satellite observations over the considered period:

$$\text{BIAS} = \frac{1}{N_{\text{val}}} \sum_{d=1}^{N_{\text{val}}} \left(BA_{\text{mod}}(d) - BA_{\text{sat}}(d) \right), \tag{6.7}$$

where N_{val} is the number of days for which valid data are available in both timeseries.

Simultaneously, to explore the presence of *outliers*, a *boxplot* representation was used, computed on a monthly basis for both the satellite and model datasets. In this representation, the median serves as the central indicator of the distribution, the lower (Q_1) and upper (Q_3) quartiles define the average range, and the distance between them defines the *InterQuartile Range* (IQR):

$$\text{IQR} = Q_3 - Q_1 \tag{6.8}$$

The whiskers extend to limit values calculated based on the range $Q_1 - 1.5\,\text{IQR}$ and $Q_3 + 1.5\,\text{IQR}$, while points outside this range are considered *outliers*.

The integration of the *BIAS* and the *boxplots* allows for a comprehensive assessment of the simulation quality: the former quantifies the average and systematic deviation, while the latter highlights variability, the presence of anomalies, and the seasonal distribution of the data.

6.2 Scatterplots

To evaluate and validate seasonal performance, the datasets were subdivided on a seasonal basis through the application of a temporal mask defined as:

$$\text{Season}(m) = \begin{cases} \text{Winter} & \text{if } m \in \{12, 1, 2\} \\ \text{Spring} & \text{if } m \in \{3, 4, 5\} \\ \text{Summer} & \text{if } m \in \{6, 7, 8\} \\ \text{Autumn} & \text{if } m \in \{9, 10, 11\} \end{cases} \tag{6.9}$$

where m represents the month number within the year. The application of the mask generated four seasonal sub-datasets, each of which was visually represented via scatterplots.

For each seasonal subset, model performance was examined by comparing values derived from satellite observations with the corresponding model simulations through several regression techniques. First, a robust Huber regression (Huber, 1981) was adopted, which combines the properties of least squares regression with greater resistance to the presence of outliers. This method minimizes a loss function $\rho(r)$ that behaves quadratically for small residuals and linearly for larger absolute values, according to:

$$\rho(r) = \begin{cases} \frac{1}{2} r^2 & \text{if } |r| \leq \delta, \\ \delta \left(|r| - \frac{\delta}{2} \right) & \text{if } |r| > \delta, \end{cases} \tag{6.10}$$

where r is the residual and δ is the threshold parameter controlling the transition between the two regimes.

Alongside this methodology, a local regression technique **LOWESS** (*Locally Weighted Scatterplot Smoothing*) (Cleveland, 1979) was also employed. This non-parametric approach is able to adapt to nonlinear structures present in the data, which were particularly evident in this study within the *chlorophyll-a* data. In this approach, the regression curve estimate $\hat{y}(x)$ is obtained through a weighted average of surrounding points, with weights w_i computed via a tricubic function:

$$w_i = \left(1 - \left|\frac{x_i - x}{h}\right|^3\right)^3, \quad \text{for } \left|\frac{x_i - x}{h}\right| < 1, \tag{6.11}$$

where h defines the smoothing window width, which was set to 0.3 in this study.

Both techniques were applied to the seasonal *scatterplots* and compared to the ordinary linear regression line (*perfect-fit*) to identify any systematic deviations and seasonal variations in model response. This combined analysis allowed the robustness to outliers inherent in Huber regression to be integrated with the flexibility of LOWESS regression to detect nonlinear patterns, thereby providing a more comprehensive picture of the model's seasonal performance.

6.3 Seasonal Decomposition

The seasonal decomposition is a widely used technique to analyze time series by breaking them down into three interpretable components: trend, seasonality, and residual (noise). The *additive model* assumes that the observed series y_t is the sum of these components:

$$y_t = T_t + S_t + R_t, \tag{6.12}$$

where T_t represents the long-term trend, S_t the seasonal component, and R_t the residual noise (Cleveland et al., 1990; Hyndman and Athanasopoulos, 2018).

The trend T_t describes the general direction of the series over time (e.g., gradual increase or decrease). In this project, a first-order regression line is used to represent it. The seasonality S_t captures repetitive variations with a fixed period (e.g., monthly or annual fluctuations) and in this project is estimated using a moving average with a 30-day window. Finally, the residual R_t includes variations not explained by the first two components, typically white noise or exceptional events. This technique is illustrated in *Figure 6.1* and was implemented trough three main steps:

Trend estimation T_t: the long-term trend is approximated through a linear polynomial regression on the time series data. Denoting by t the number of days elapsed since the start of the series and y_t the observed value:

$$T_t = \beta_0 + \beta_1 t, \tag{6.13}$$

where the coefficients β_0 and β_1 are estimated via *least squares*.

Seasonality estimation S_t: the trend obtained in the previous step is removed by computing a centered moving average of width d on the detrended values:

$$S_t = \frac{1}{d} \sum_{i=-k}^{k} \big(y_{t+i} - T_{t+i}\big), \tag{6.14}$$

with $k = \lfloor (d-1)/2 \rfloor$. This operation isolates the seasonal component by smoothing short-term residual variations.

Residual calculation R_t: finally, the irregular component is obtained by subtracting both the trend and the estimated seasonality from the observed series:

$$R_t = y_t - T_t - S_t. \tag{6.15}$$

This approach assumes a linear additive decomposition of the components and constant seasonality amplitude. A known limitation is the lack of estimates for the first and last k points, where the centered moving average is not defined, requiring the exclusion of these intervals from quantitative analysis.

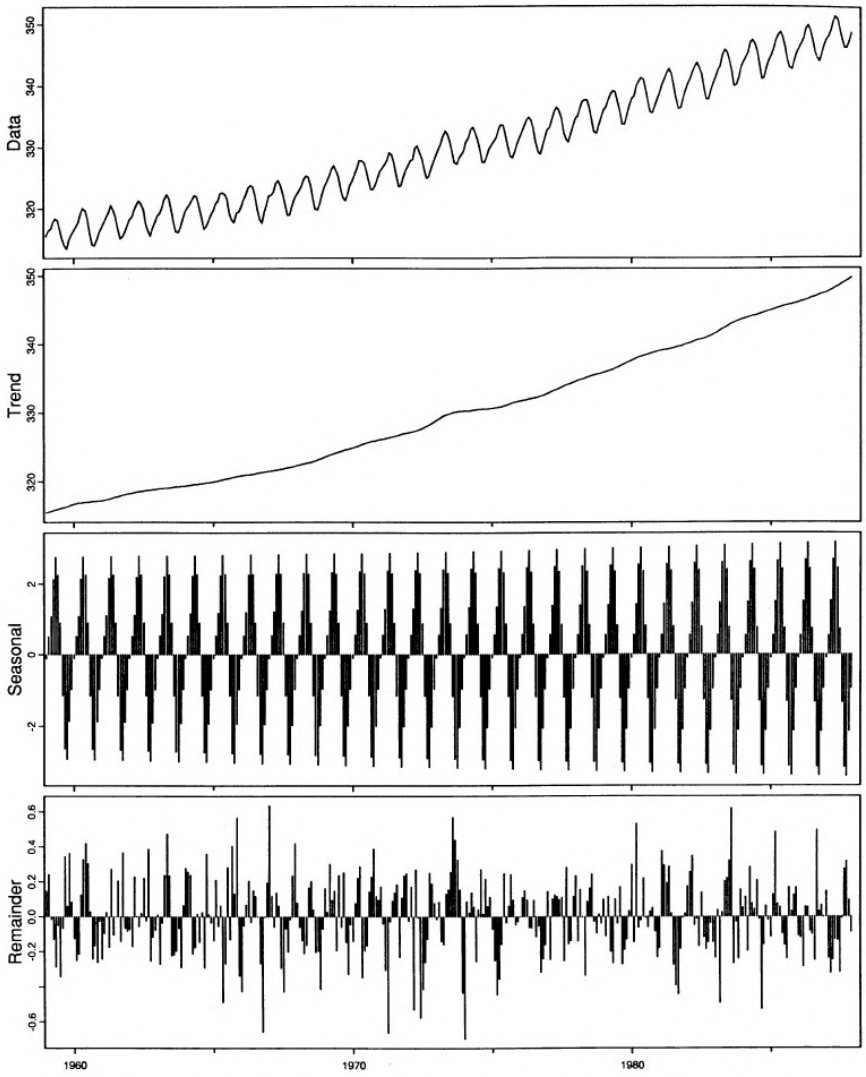

Figure 6.1: Example of additive seasonal decomposition of a CO_2 dataset using the STL procedure. Vertical axis units are in *ppm* (Cleveland et al., 1990). The first plot shows the raw data. The **trend** (second plot) shows the long-term trend, the **seasonality** (third plot) displays periodic cyclical variations, and the **residual** (fourth plot) shows the remaining noise component.

6.4 Efficiency Criteria

In order to quantitatively and temporally evaluate the model's performance, several efficiency indices have been developed based on the comparison between simulation results and satellite data. These indices allow for an objective and rigorous estimate of the model's performance.

Efficiency Criteria represent mathematical measures designed to quantify the ability of a simulation model to accurately reproduce available experimental observations (Beven, 2001). In many formulations, such indices are based on the cumulative sum of error terms, each defined as the normalized difference between the observed value, O_t, and the simulated value, S_t, at each time t:

$$e_t = \frac{O_t - S_t}{O_t}. \tag{6.16}$$

(Krause et al., 2005). Since this approach considers only a single dimension of temporal variability, previous studies and the proposed criteria will use a type of data called **Basin Averages (BA)**.

Because errors tend to increase when the variable takes on high values (e.g., *peak flows*) and decrease in the presence of low values and variability (e.g., *base flows*), specific calibrations have been introduced to reduce the sensitivity of such criteria to isolated peaks, ensuring greater emphasis on cyclical and systematic behaviors.

It is worth noting that the criteria proposed here originate in the hydrological field, where they were developed for the study of discharges and flows. In the present work, these criteria are applied to two variables with profoundly different behaviors: sea surface temperature (SST), characterized by a marked seasonal cycle, and chlorophyll-a, whose trend is intrinsically more erratic and subject to sporadic peaks, despite the cyclicality of *bloom* phenomena. This approach allows highlighting differences in results and behaviors of the two application fields.

The various efficiency criteria used are illustrated below.

6.4.1 Coefficient of determination R^2

The **coefficient of determination** R^2, defined as the square of the Bravais–Pearson correlation coefficient, quantifies the fraction of the variance in the observed data explained by the model. It is calculated as:

$$R^2 = \left(\frac{\sum_{i=1}^{n} \left(O_i - \bar{O}\right)\left(P_i - \bar{P}\right)}{\sqrt{\sum_{i=1}^{n} \left(O_i - \bar{O}\right)^2} \sqrt{\sum_{i=1}^{n} \left(P_i - \bar{P}\right)^2}} \right)^2 , \tag{6.17}$$

where O_i and P_i are the observed and predicted values, respectively, and $\bar{O}$ and $\bar{P}$ are their means (Krause et al., 2005).

The two fundamental components within equation (6.17) are:

Observed–predicted covariance

$$\sum_{i=1}^{n}\big(O_i - \bar{O}\big)\,\big(P_i - \bar{P}\big), \tag{6.18}$$

which measures the joint variability of the two datasets and indicates the extent to which the two signals co-vary (Krause et al., 2005).

Product of standard deviations

$$\sqrt{\sum_{i=1}^{n}\big(O_i - \bar{O}\big)^2} \;\times\; \sqrt{\sum_{i=1}^{n}\big(P_i - \bar{P}\big)^2}, \tag{6.19}$$

which represents the individual dispersion of the observed and simulated series, thus normalizing the covariance term (Krause et al., 2005).

Thanks to this formulation, R^2 synthesizes in a single index the ratio between shared variability and the total variability of the two series, assuming values between 0 (no agreement) and 1 (perfect agreement).

Additional information can be obtained by using the **weighted** version wr^2, which combines R^2 with the slope coefficient b of the regression line, thereby accounting for possible *biases*. It is defined as:

$$wr^2 \;=\; \begin{cases} |b| \;\cdot\; R^2, & b \le 1, \\ |b|^{-1} \;\cdot\; R^2, & b > 1, \end{cases} \tag{6.20}$$

where b represents the slope of the regression line. When $b < 1$, the multiplicative factor $|b|$ penalizes underestimations of the model, whereas when $b > 1$, the term $|b|^{-1}$ penalizes overestimations. Thanks to this formulation, wr^2 provides a more comprehensive assessment of model performance, combining a measure of linear correlation (via R^2) with an explicit indication of systematic bias (via b) (Krause et al., 2005).

6.4.2 Nash-Sutcliffe Efficiency

The **Nash–Sutcliffe Efficiency** (NSE or, smiply E), introduced by Nash and Sutcliffe (Nash and Sutcliffe, 1970), is a widely used metric to evaluate the performance of hydrological models by comparing simulations with observed data. It is defined as:

$$E = 1 - \frac{\sum_{i=1}^{n}(O_i - P_i)^2}{\sum_{i=1}^{n}(O_i - \overline{O})^2} \tag{6.21}$$

where O_i and P_i are the observed and predicted values at time i, respectively, and $\overline{O}$ is the mean of the observed values.

This index compares the mean squared error to the variance of the observed data, taking values between 1 (perfect performance) and $-\infty$. A value of 0 indicates that the model is no better than using the observed mean, while negative values denote performance worse than the mean (Krause et al., 2005).

However, the NSE has some limitations:

- it is sensitive to extreme values and tends to overestimate performance during peak flows and underestimate it during low flows (Legates and McCabe, 1999);
- it is not very sensitive to systematic over- or underestimation errors, especially during low flows;
- basins with reduced dynamics tend to show lower NSE values even with good simulations.

To mitigate these limitations, several variants have been introduced:

Log-NSE

The logarithmic form of the index is expressed as:

$$\ln E = 1 - \frac{\sum_{i=1}^{n} (\ln O_i - \ln P_i)^2}{\sum_{i=1}^{n} \left(\ln O_i - \ln \overline{O}\right)^2} \tag{6.22}$$

The logarithmic transformation reduces the influence of peak flows while emphasizing low-flow conditions (Krause et al., 2005). This allows greater sensitivity to systematic errors at low flows but may reduce the representation of high-flow events.

Generalized (or modified) version with exponent j

A further generalization is expressed as:

$$E_j = 1 - \frac{\sum_{i=1}^{n} |O_i - P_i|^j}{\sum_{i=1}^{n} \left|O_i - \overline{O}\right|^j} \tag{6.23}$$

Using lower exponent values, such as $j = 1$, reduces sensitivity to peaks, improving overall evaluation, while values $j > 2$ increase sensitivity to high flows (useful for flood forecasting, though not considered in this study). Values $j < 2$ generally reduce sensitivity to outliers but may worsen overall evaluation, leading to poorer results (Krause et al., 2005). The choice of the exponent j is therefore directly dependent on the type of model used; for the present purposes, the proposed exponent is $j = 1$.

Relative version

Finally, the relative version is defined as:

$$E_{\text{rel}} = 1 - \frac{\sum_{i=1}^{n} \left(\frac{O_i - P_i}{O_i}\right)^2}{\sum_{i=1}^{n} \left(\frac{O_i - \overline{O}}{\overline{O}}\right)^2} \tag{6.24}$$

This version quantifies differences as relative deviations, reducing the influence of absolute differences in peaks while making the index more sensitive to systematic bias in over- or underestimation, especially during low flows (Krause et al., 2005).

In all proposed forms of the index, values range between 1.00 and $-\infty$, with 0.00 representing the minimum acceptable model performance. Below this value, the model's performance is no better than the observed climatological mean.

6.4.3 Index of Aggreement

The **Index of Agreement** (d) was proposed by Willmott (Willmott, 1981) to overcome the insensitivity of indices such as the Nash–Sutcliffe efficiency (E) and the coefficient of determination (r^2) with respect to differences between the means and variances of observations and predictions (Legates and McCabe, 1999). The index quantifies the degree of agreement between simulated and observed values, accounting for both the magnitude of deviations and their temporal trends.

The mathematical definition of the index is given by:

$$d = 1 - \frac{\sum_{i=1}^{n}(O_i - P_i)^2}{\sum_{i=1}^{n}\left(|P_i - \overline{O}| + |O_i - \overline{O}|\right)^2} \tag{6.25}$$

where, again, O_i and P_i represent the observed and predicted values at time i, respectively, while $\overline{O}$ is the mean of the observed values. The numerator represents the mean squared error between observed and simulated values, whereas the denominator, called the *potential error*, represents the maximum possible deviation between each pair of values. This normalized comparison ensures that d takes values between 0 (no agreement) and 1 (perfect agreement) (Krause et al., 2005).

Generalized (or modified) version with exponent j

As with the NSE index, modified versions of d exist that use a generic exponent $j \in N$:

$$d_j = 1 - \frac{\sum_{i=1}^{n}|O_i - P_i|^j}{\sum_{i=1}^{n}\left(|P_i - \overline{O}| + |O_i - \overline{O}|\right)^j} \tag{6.26}$$

For this index as well, using $j = 1$ significantly reduces the overestimation of peak-flow events, improving the overall model evaluation. However, lower values of j generally produce lower values of d_j compared to the $j = 2$ version, leaving a wider range for model calibration but potentially giving a poorer impression of predictive skill (Krause et al., 2005). Conversely, increasing j enhances sensitivity to high-flow conditions, which can be useful in contexts such as flood forecasting. As with the NSE index, in the present study this version is applied with $j = 1$.

Relative version

A further variant is the relative version of the index, d_{rel}, in which the differences between observed and simulated values are normalized with respect to the observed values:

$$d_{\text{rel}} = 1 - \frac{\sum_{i=1}^{n}\left(\frac{O_i - P_i}{O_i}\right)^2}{\sum_{i=1}^{n}\left(\frac{|P_i - \overline{O}| + |O_i - \overline{O}|}{\overline{O}}\right)^2} \tag{6.27}$$

This normalization reduces the influence of absolute deviations during peak-flow events, thereby attenuating sensitivity to high-intensity outliers. However, it increases sensitivity to systematic under- or overestimation errors, especially during low-flow periods, thus highlighting potential persistent biases in the model (Krause et al., 2005).

6.5 Error Decomposition

A further analysis of model efficiency was carried out by examining in detail the different components of error, including *Mean Bias*, *Correlation Coefficient*, *Standard Deviation Error*, and *unbiased Root Mean Square Error* (uRMSE). This approach was adopted with the aim of more precisely identifying the basin areas most affected by simulation errors. For this purpose, the analysis was performed using point-based data and evaluating their temporal evolution, in order to capture both local dynamics and seasonal or episodic variations that influence the model's ability to faithfully reproduce observed phenomena.

The error components and the equations used to define them are presented below.

6.5.1 Mean Bias

The **Mean Bias** (MB) is a statistical measure used to quantify the systematic bias of a model, i.e., the tendency of a simulation to overestimate or underestimate observed values. It is particularly useful in the early stages of calibration of hydrological or environmental models (Oke et al., 2002). It is defined as the arithmetic mean of the differences between simulated and observed series:

$$\mathrm{MB} = \frac{1}{n}\sum_{t=1}^{n}(Q_{\mathrm{sim},t} - Q_{\mathrm{obs},t}) \tag{6.28}$$

where $Q_{\mathrm{sim},t}$ is the simulated value at time t, $Q_{\mathrm{obs},t}$ is the corresponding observed value, and n is the total number of observations. A positive MB value indicates that the model tends to overestimate the observed data, while a negative value indicates a systematic underestimation (Oddo et al., 2022). An MB close to zero suggests the absence of significant bias, whereas high positive or negative values highlight specific critical issues within the simulation.

However, this metric presents some important limitations. Firstly, the *mean bias* (MB) provides no information on the magnitude of residual variability nor on the temporal distribution of errors. For instance, a mean value close to zero may conceal compensating errors, where overestimations and underestimations balance each other out, without implying actual model accuracy (Murphy, 1992). Moreover, MB does not allow distinguishing whether the bias is constant over time or concentrated in specific periods, such as during extreme high-flow or low-flow events, thus limiting its diagnostic capability especially in detailed analyses.

To overcome these limitations, the analyses proposed here adopted the creation of *"climatological months (and years)"*, i.e., monthly reference maps, with the aim of studying the average monthly behavior of MB and other error components. This approach makes it possible to more effectively identify seasonal variations and to improve the understanding of the temporal dynamics of model errors.

6.5.2 Standard Deviation Error

The **Standard Deviation Error** (SDE) is a statistical measure that quantifies the difference in variability between a simulated series and the observed one. Formally,

the SDE is defined as the difference between the standard deviation of the simulations, σ_{sim}, and that of the observations, σ_{obs}:

$$\text{SDE} = \sigma_{\text{sim}} - \sigma_{\text{obs}} \tag{6.29}$$

This metric makes it possible to assess the ability of the model to correctly reproduce the amplitude of temporal or spatial fluctuations of the observed data. An SDE value close to zero indicates a good capacity of the model to replicate the natural variability of the variable under study, whereas a positive or negative value respectively indicates an overestimation or underestimation of variability.

6.5.3 Cross Correlation

The **Cross Correlation** (CC) is a statistical measure that quantifies the relationship between two time series, highlighting the similarity of their temporal trends. It is defined as:

$$CC = \frac{\sum_{i=1}^{N}(m_i - \bar{m})(o_i - \bar{o})}{\sqrt{\sum_{i=1}^{N}(m_i - \bar{m})^2 \sum_{i=1}^{N}(o_i - \bar{o})^2}} \tag{6.30}$$

where m_i and o_i represent the simulated and observed values at time i, respectively, while $\bar{m}$ and $\bar{o}$ are the temporal means of the series m and o (Oke et al., 2002).

This measure provides information on the strength and direction of the linear relationship between the two series. A CC value of 1 indicates a perfect positive correlation, -1 a perfect negative correlation, and 0 no linear correlation. It is particularly useful for assessing whether the simulations correctly reproduce the temporal trends of the observations, without necessarily preserving the same amplitude of fluctuations.

6.5.4 uRMSE

The **Unbiased Root Mean Squared Error** (uRMSE) is a statistical measure used to quantify the deviation between two data series, generally between modeled and observed values, while removing the effect of the mean bias. It is defined as:

$$\text{uRMSE} = \sqrt{\frac{1}{N}\sum_{i=1}^{N}\left[(m_i - \overline{m}) - (o_i - \overline{o})\right]^2} \tag{6.31}$$

where m_i and o_i represent the modeled and observed values, respectively, while $\overline{m}$ and $\overline{o}$ are their corresponding temporal or spatial means. This metric is particularly effective in assessing the variance of discrepancies by eliminating the systematic component (bias) between the two series (Oddo et al., 2022).

Compared to the traditional RMSE, which incorporates both the mean error and the variation of the data, the uRMSE provides a more specific indication of the residual dispersion or variability between models and observations, excluding the mean difference. This characteristic allows for a more precise evaluation of the model's ability to reproduce temporal or spatial dynamics without being affected by a constant offset (bias) (Legates and McCabe, 1999; Moriasi et al., 2007).

6.6 Taylor Diagrams

Taylor diagrams provide a graphical tool designed to concisely and quantitatively summarize the degree of agreement between a modeled field and an observed one, integrating in a single representation information on linear correlation, relative variability, and centered error. Originally introduced by Taylor (Taylor, 2001), they are based on three fundamental statistical metrics: the *Linear Correlation Coefficient (R)*, the *Normalized Standard Deviation* (σ^*), and the *Centered Root Mean Square Error* (RMSD$'$).

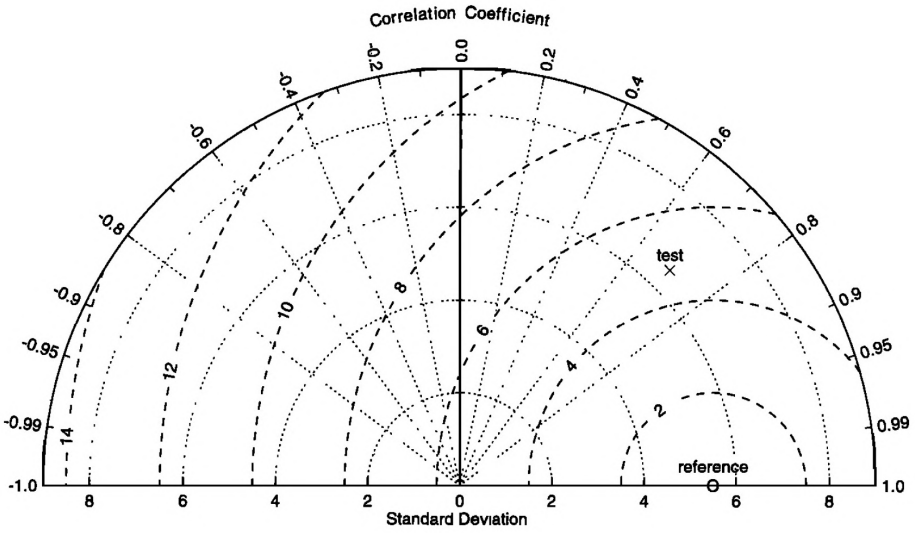

Figure 6.2: Original example of a Taylor diagram from Taylor (2001). The angular position of the points represents the correlation R, while the radial distance represents the normalized standard deviation σ^*. The distance from the reference point (in black) is proportional to the centered error RMSD$'$.

In the diagram, an example of which is reported in *Figure 6.2*, the angular axis is defined by the correlation coefficient:

$$R = \frac{\sum_{i=1}^{N}(m_i - \bar{m})(o_i - \bar{o})}{\sqrt{\sum_{i=1}^{N}(m_i - \bar{m})^2}\sqrt{\sum_{i=1}^{N}(o_i - \bar{o})^2}} \tag{6.32}$$

where m_i and o_i represent the modeled and observed values, respectively, while $\bar{m}$ and $\bar{o}$ are their means. The radial amplitude is instead proportional to the normalized standard deviation:

$$\sigma^* = \frac{\sigma_m}{\sigma_o}, \tag{6.33}$$

which makes it possible to evaluate whether the variability of the model faithfully reproduces that of the observations. The distance between each point representing the model and the reference point (*Reference* or *Ref*), located at ($\sigma^* = 1, R = 1$), is proportional to the value of the *Centered Root Mean Square Error*:

$$\mathrm{RMSD}' = \sqrt{\frac{1}{N}\sum_{i=1}^{N}\left[(m_i - \bar{m}) - (o_i - \bar{o})\right]^2}. \tag{6.34}$$

The adoption of this tool in operational oceanography and climate sciences has proven particularly useful for simultaneously analyzing discrepancies in phase and amplitude between models and observations. As highlighted by Jolliff et al. (2008), the polar representation makes it possible to visually compare multiple simulations against a single observational dataset, clearly showing how variations in correlation and standard deviation are reflected in the overall centered error, as illustrated in two example plots extracted from the aforementioned paper and reported here in *Figure 6.3*.

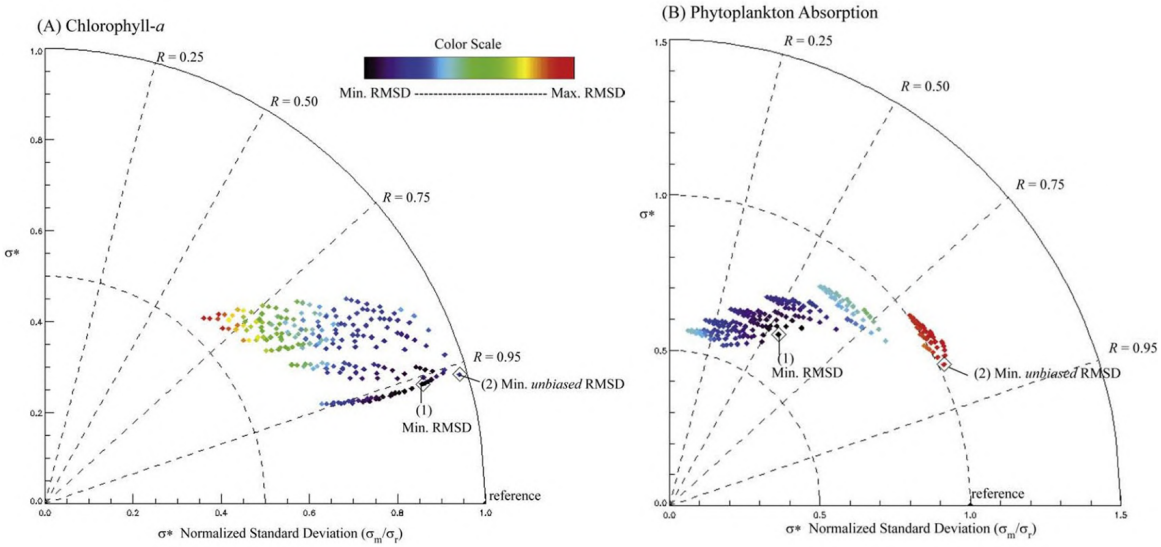

Figure 6.3: Application of Taylor diagrams, adapted from Jolliff et al. (2008). The points represent different model configurations compared with observed fields of surface chlorophyll and phytoplankton absorption coefficients. Proximity to the reference point indicates greater agreement between model and observations in terms of phase and amplitude. The proposed color scale shows the different RMSD values associated with the markers.

Despite its concise effectiveness, the Taylor diagram does not explicitly include the mean bias between model and observations. This implies that two simulations with similar correlation and variability characteristics may appear indistinguishable on the diagram, even if one presents a significant systematic error. As suggested by Jolliff et al. (2008), it is therefore necessary to complement its interpretation with additional bias analyses or with methodological extensions that allow for its explicit representation.

6.7 Target Plots

Target plots represent a Cartesian evolution of Taylor diagrams, designed to provide a more comprehensive picture of discrepancies between numerical models and reference data. Unlike polar diagrams, which synthesize phase and amplitude in a single representation, target diagrams explicitly separate the systematic *bias* from the residual error, allowing a clearer understanding of how each component contributes to the overall simulation error.

The fundamental element of these diagrams is the relation:

$$\mathrm{RMSD}^2 \;=\; B^2 \;+\; \mathrm{RMSD}'^2 \tag{6.35}$$

where:

- RMSD is the *Root Mean Square Error*, which quantifies the overall magnitude of deviations between the simulated series m_i and the reference series o_i (Jolliff et al., 2008). It is expressed as

$$RMSD = \sqrt{\frac{1}{N}\sum_{i=1}^{N}(m_i - o_i)^2}; \tag{6.36}$$

- B is the mean bias, i.e., the average difference between simulated and observed values (Jolliff et al., 2008), estimated as

$$B = \frac{1}{N}\sum_{i=1}^{N}(m_i - o_i); \tag{6.37}$$

- RMSD$'$ is the *Unbiased Root Mean Square Error*, calculated after removing the bias from the series, where $\bar{m}$ and $\bar{o}$ are their respective temporal means (Jolliff et al., 2008). It is estimated as

$$RMSD' = \sqrt{\frac{1}{N}\sum_{i=1}^{N}\left[(m_i - \bar{m}) - (o_i - \bar{o})\right]^2} \tag{6.38}$$

In the Cartesian plane of the target diagram, the horizontal axis X represents RMSD$'$, while the vertical axis Y represents B. Each point $s = (X, Y)$ corresponds to the comparison between a set of simulations and the reference field: the Euclidean distance of point s from the origin,

$$\sqrt{X^2 + Y^2}, \tag{6.39}$$

is exactly equal to the value of RMSD, thus providing an immediate and visually intuitive measure of the total error.

To ensure comparability across variables with different units or magnitudes, normalized variants of these metrics with respect to the standard deviation of the reference field σ_r are adopted:

$$\mathrm{RMSD}^* = \frac{\mathrm{RMSD}}{\sigma_r}, \quad B^* = \frac{B}{\sigma_r}, \quad \mathrm{RMSD}'^* = \frac{\mathrm{RMSD}'}{\sigma_r}. \tag{6.40}$$

In this normalized space, illustrated in *Figure 6.4* extracted directly from Jolliff et al. (2008), the line $\mathrm{RMSD}'^* = 1$ (marker M_0) identifies simulations whose total RMSD coincides with the intrinsic variability of the observations: such models do not provide improvements compared to the simple temporal mean hypothesis ($\mathrm{MEF} = 1 - (\mathrm{RMSD}^*)^2 \leq 0$) (Nash and Sutcliffe, 1970; Stow et al., 2009).

It is also possible to introduce markers based on correlation thresholds R. Recalling the relationship linking correlation, normalized standard deviation, and centered error:

$$\mathrm{RMSD}'^{*2} = 1 + \sigma^{*2} - 2\,\sigma^*\,R, \tag{6.41}$$

where $\sigma^* = \sigma_m/\sigma_r$, for each value $R_1 > 0$ the minimum RMSD$'^*$ achievable in the absence of bias is defined as:

$$\mathrm{MR}_1 = \sqrt{1 + R_1^2 - 2\,R_1^2}. \tag{6.42}$$

The line connecting the origin to the point $(\mathrm{MR}_1, 0)$ delimits the area of simulations with correlation at least equal to R_1, supporting an interpretation based on reliability thresholds (Jolliff et al., 2008).

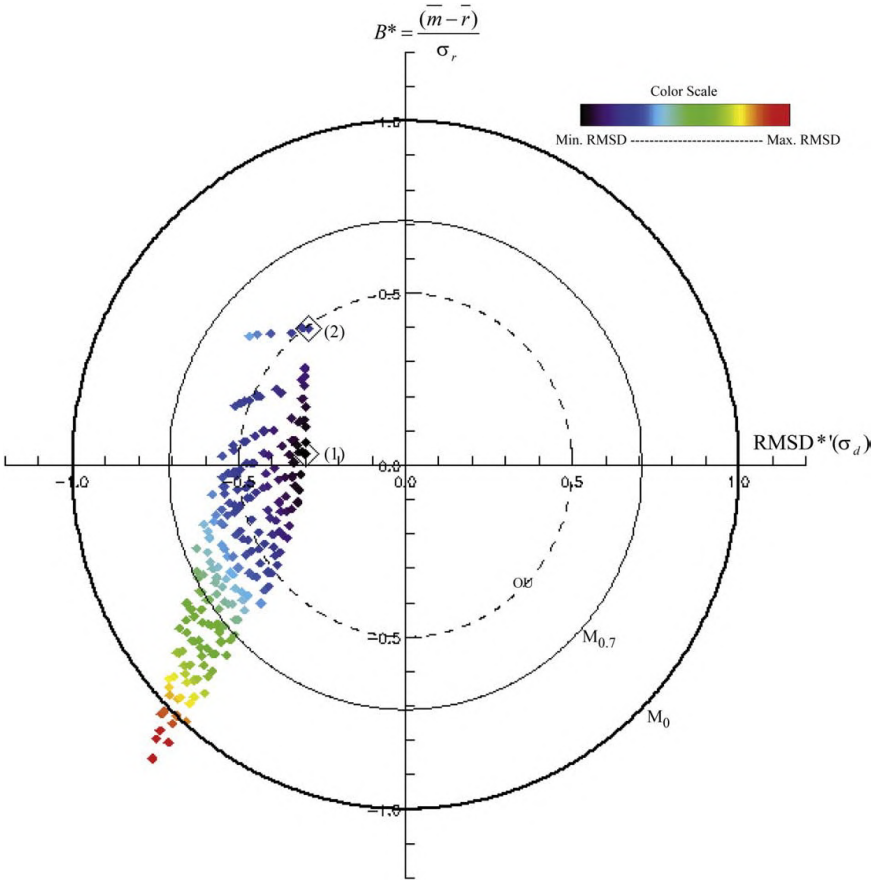

Figure 6.4: Normalized version of the target diagram from Jolliff et al. (2008): both metrics RMSD$'$ and B are normalized to the reference standard deviation, with the marker M_0 highlighted.

A practical and important addition to the target diagram is an explicit depiction of the *observational uncertainty* (OU) range. Jolliff et al. advocate showing an estimate of the average observational uncertainty as a dashed marker on the target diagram so that points falling between that marker and the origin may be regarded as within the estimated measurement/processing uncertainty and therefore not meaningfully improvable by further model tuning alone (Jolliff et al., 2008). This is done in two steps:

1. **Estimate the average absolute observational uncertainty.** If an average relative uncertainty α is expressed as a fraction (e.g. $\alpha = 0.15$ for $\pm 15\%$), then an estimate of the average absolute uncertainty for the reference time series is

$$\Delta_{OU} \;=\; \alpha\;\overline{o}, \tag{6.43}$$

where $\overline{o}$ is the temporal mean of the reference series. For instance, with $\alpha = 0.15$ and $\overline{o} = 0.2$ mg/m^3, one obtains $\Delta_{OU} = 0.03$ mg/m^3. If a model's total RMSD (in original units) is smaller than Δ_{OU} then the model–data misfit is within the average observational uncertainty and further reductions in RMSD may not be meaningful.

2. **Normalize and plot on the target diagram.** To place the OU threshold in the same normalized space used on the target diagram divide Δ_{OU} by the reference standard deviation σ_r:

$$\alpha^* = \frac{\Delta_{OU}}{\sigma_r} = \frac{\alpha\,\overline{o}}{\sigma_r}. \tag{6.44}$$

The OU is then visualized on the normalized target diagram as a dashed circle (or ring) centered at the origin with radius α^*. Points whose Euclidean distance from the origin $\sqrt{X^2 + Y^2}$ is smaller than or equal to α^* are thus inside the OU range and are likely indistinguishable from the observations given the assumed average measurement/processing uncertainty.

Jolliff et al. explicitly warn that this OU depiction is a pragmatic, conservative estimate rather than a full uncertainty quantification: observational uncertainty may be spatially and temporally heterogeneous and arises from multiple sources (sensor calibration/drift, atmospheric correction, algorithm errors for remotely-sensed products; sampling, preservation and laboratory methods for in-situ data). Thus the OU threshold shown as a single dashed circle is an *average* or *summary* indicator: it should be treated as a preliminary guide to whether observed model improvements are likely meaningful. The OU estimate is most defensible when it is grounded in empirical validation studies for the specific data product, or when it is derived from collocated in-situ/satellite match-ups. (Bailey and Werdell, 2006; McClain et al., 2006) Furthermore when observations are heterogenous (many stations or multiple regions) one may compute station- or region-specific OU values

$$\alpha_i^* = \frac{\alpha\,\overline{o}_i}{\sigma_{r,i}} \tag{6.45}$$

and either show multiple concentric rings, a shaded band, or adopt a robust summary (e.g. median or 90th percentile) to avoid misleading conclusions based on a single global value. Also, the OU estimate assumes the uncertainty is approximately unbiased and that an average relative uncertainty α is representative for the comparison set. If the observational errors are known to have significant bias or non-Gaussian structure, the OU circle is only a crude indicator and more detailed uncertainty propagation / hypothesis testing is recommended.

6.8 Spectral Analysis

Through a series of power spectrum analyses, the signal energy and its distribution across different periodic scales are quantified. A robust and widely used approach to estimate the power spectral density (PSD) is the *Welch method* (Welch, 1967), in which the series $x(t)$, sampled at frequency f_s, is divided into L segments of length M with an overlap D. This process is illustrated in the diagram shown in *Figure 6.5*.

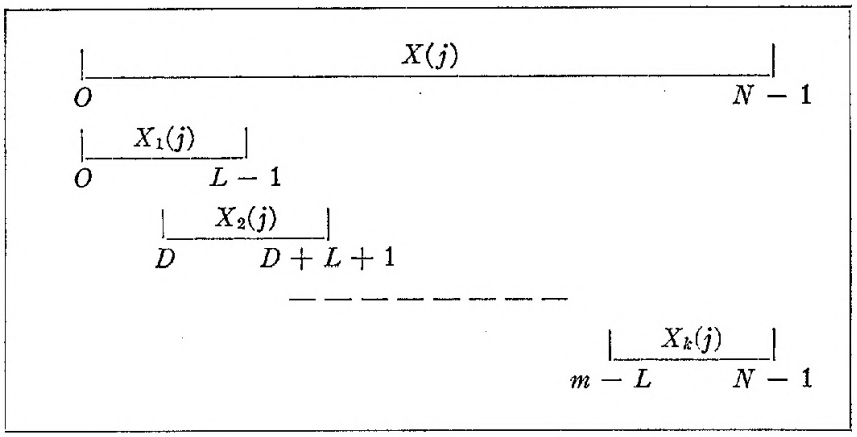

Figure 6.5: Partitioning of a time series $X(j)$ into overlapping segments for the estimation of the power spectral density using the Welch method (Welch, 1967). The complete sequence $X(j)$, of length N, is divided into K partially overlapping segments $X_k(j)$, each of length L, with an offset (overlap) D between consecutive segments. Each segment is used to compute a modified periodogram, and the results are averaged to reduce the variance of the spectral estimate.

For each segment $x_k(t)$, a preliminary *detrending* is performed by subtracting its climatological mean $\overline{x_k}$, then multiplied by a *window* $w[n]$ (e.g., Hanning or Hamming) and transformed using the discrete Fourier transform:

$$X_k(\nu) \;=\; \sum_{n=0}^{M-1} \left(x_k[n] - \overline{x_k}\right) w[n]\, e^{-2\pi i n\nu/M}, \tag{6.46}$$

from which the *periodogram* can be obtained:

$$P_k(\nu) \;=\; \frac{1}{M\,U} \left|X_k(\nu)\right|^2, \tag{6.47}$$

where

$$U = \sum_{n=0}^{M-1} w^2[n] \tag{6.48}$$

normalizes the window energy. The overall PSD estimate is obtained by averaging the periodograms of all segments, thereby reducing the variance of the estimate at the expense of spectral resolution (Welch, 1967).

To interpret spectral peaks in temporal terms, frequencies ν (Hz) are converted into periods T (days) as follows:

$$T = \frac{1}{\nu \times 86400}, \tag{6.49}$$

thus highlighting seasonal and interannual cycles in units of days or years (Percival and Walden, 1993).

The graphical representation used in this work adopts a double logarithmic scale, with the period on the horizontal axis and the PSD on the vertical axis. This choice allows both *"fast"* oscillations (daily or monthly) and *"slow"* oscillations (seasonal or multi-annual) to be simultaneously visible.

6.8.1 Butterworth Filters

A set of filtering procedures was also applied to the data using a digital *Butterworth* filter of order $n = 2$, chosen for its well-known frequency response characterized by a *"maximally flat"* behavior in the passband (Butterworth, 1930; Oppenheim and Schafer, 2014).
The normalized transfer function of an analog Butterworth filter of order n is defined as:

$$H(s) = \frac{1}{\sqrt{1 + \left(\frac{s}{\omega_c}\right)^{2n}}}, \tag{6.50}$$

where $\omega_c = 2\pi f_c$ represents the *cutoff angular frequency*.

For the digital domain implementation, the bilinear transform was adopted, which performs the mapping:

$$s \longrightarrow \frac{2}{T}\frac{1 - z^{-1}}{1 + z^{-1}}, \qquad T = \frac{1}{F_s}, \tag{6.51}$$

where F_s is the *sampling frequency*. This transformation preserves the shape of the analog response while minimizing phase distortion (Oppenheim and Schafer, 2014).

In this specific case, since the sea surface temperature (SST) data are sampled on a daily basis, we have:

$$F_s = \frac{1}{86400}\,\text{Hz}, \qquad f_{\text{Nyq}} = \frac{F_s}{2} \tag{6.52}$$

where f_{Nyq} is the Nyquist frequency. The cutoff frequencies are then expressed in normalized form:

$$W_n = \frac{f_c}{f_{\text{Nyq}}} \quad \text{for low-pass or high-pass filters} \tag{6.53}$$

or

$$W_n = \frac{[f_{\text{c,low}}, f_{\text{c,high}}]}{f_{\text{Nyq}}} \quad \text{for the band-pass filter.} \tag{6.54}$$

Through this normalization, it was possible to directly compute the digital coefficients (b, a) and apply bidirectional filtering, thereby eliminating residual phase delay and preserving signal integrity (Smith, 1997).

Three types of filtering were thus implemented on the daily data:

Low-pass filter: Normalized cutoff frequency

$$W_{n,\text{low}} = \frac{f_{\text{c,low}}}{f_{\text{Nyq}}}, \quad f_{\text{c,low}} = \frac{1}{225 \times 86400}\,\text{Hz} \tag{6.55}$$

corresponding to a period of about 225 days, aimed at isolating the low-frequency components.

High-pass filter: Normalized cutoff frequency

$$W_{n,\text{high}} = \frac{f_{\text{c,high}}}{f_{\text{Nyq}}}, \quad f_{\text{c,high}} = \frac{1}{90 \times 86400}\,\text{Hz} \tag{6.56}$$

corresponding to a period of about 90 days, useful for highlighting high-frequency variations.

Band-pass filter: Defined in the range $[f_{c,low}, f_{c,high}]$, i.e.:

$$f_{c,low} = \frac{1}{150 \times 86400}\,\text{Hz}, \quad f_{c,high} = \frac{1}{90 \times 86400}\,\text{Hz}, \tag{6.57}$$

corresponding to an intermediate variability window between approximately 90 and 225 days. An additional band-pass filter is defined in the range $[f_{c,low}, f_{c,high}]$, i.e.:

$$f_{c,low} = \frac{1}{105 \times 86400}\,\text{Hz}, \quad f_{c,high} = \frac{1}{125 \times 86400}\,\text{Hz}, \tag{6.58}$$

in order to isolate a specific window within the Sea Surface Temperature data for further analyses.

The use of a filter of order $n = 2$ allowed obtaining an adequate attenuation slope and, thanks to the bidirectional filtering, minimizing possible phase distortions while preserving a faithful representation of the temporal dynamics of the signal (Smith, 1997).

6.8.2 Spectral Decomposition

The spectral approach allows not only the exploration of the energy distribution as a function of frequency, but also the dynamic relationships between two time series in terms of phase, amplification, and coherence. Spectral decomposition is an extension of frequency-domain analysis which, in addition to quantifying the energy distribution through power spectral densities (PSD), enables the examination of dynamic relationships between two stochastic processes in terms of linear correlation, phase shift, and selective amplification across relevant time scales (Bendat and Piersol, 2010; Percival and Walden, 1993). Through the calculation of the cross-spectral density (CSD), this technique allows derivation of three fundamental quantities: coherence, which measures the strength of the linear dependence at each frequency; gain, which quantifies the amplitude ratio between the series; and phase, which expresses any temporal delays in the form of a phase angle (Bloomfield, 2000).

Let $x(t)$ be the time series produced by the model and $y(t)$ the one measured by satellite, both sampled at daily intervals ($F_s = 1/86400\,\text{Hz}$). After synchronizing the two series on a common time basis and removing any isolated zeros, a linear *detrend* is applied to remove the background component and focus the analysis on stationary fluctuations.

The spectral analysis uses Welch's method, with segments of length $N_{seg} = 1024$ samples, a Hann window and an *nfft* of 4096. This window, also known as a *raised cosine* or *cosine bell*, is defined as:

$$w[n] = 0.5\left(1 - \cos\left(\frac{2\pi n}{N-1}\right)\right), \quad 0 \le n \le N-1, \tag{6.59}$$

with 50% overlap (512 samples) for each segment.

Using the Hann window helps mitigate the effect of *spectral leakage*, caused by discontinuous jumps at the segment edges, significantly reducing the sidelobes of its

frequency response (about –31 dB), albeit at the cost of a wider main lobe compared to the rectangular window (Braun, 2001). This represents an effective compromise between frequency resolution and background noise attenuation.

For each segment $m = 1, \ldots, K$, the Fourier transforms $X_m(f)$ and $Y_m(f)$ are calculated, from which the following are derived:

Cross–Spectral Density (CSD)

$$P_{xy}(f_k) = \frac{1}{K} \sum_{m=1}^{K} X_m(f_k)\, Y_m^*(f_k)\,, \tag{6.60}$$

Auto–Spectral Densities (PSD)

$$P_{xx}(f_k) = \frac{1}{K} \sum_{m=1}^{K} |X_m(f_k)|^2, \quad P_{yy}(f_k) = \frac{1}{K} \sum_{m=1}^{K} |Y_m(f_k)|^2. \tag{6.61}$$

The CSD provides a complex measure of the energetic relationships between x and y at each frequency f_k, while the PSDs describe the unilateral energy of each series.

From these quantities, three fundamental spectral functions are derived:

Coherence $C_{xy}(f)$

$$C_{xy}(f) = \frac{\big|P_{xy}(f)\big|^2}{P_{xx}(f)\, P_{yy}(f)} \quad \big[0 \le C_{xy}(f) \le 1\big], \tag{6.62}$$

which quantifies the linearity and consistency of the signal–to–noise relationship between the two series at frequency f.

Gain $\Gamma(f)$

$$\Gamma(f) = \frac{\big|P_{xy}(f)\big|}{P_{xx}(f)}, \tag{6.63}$$

which expresses the amplification (or attenuation) factor of the model relative to the observation in terms of spectral power.

Phase $\phi(f)$

$$\phi(f) = \arg\big(P_{xy}(f)\big) \quad [\text{deg}], \tag{6.64}$$

which indicates the temporal phase shift between the series, expressed in degrees.

To interpret the phase in terms of time delay, the following relation is used:

$$\tau(f) = \frac{\phi(f)}{360}\, T(f), \tag{6.65}$$

where $\tau(f)$ is the lag time corresponding to frequency f, $\phi(f)$ is the phase in degrees, and $T(f) = 1/f$ is the period associated with the frequency. For daily time series, the

sampling frequency f_s is 1/86400 Hz (one sample per day), and the conversion from frequency in hertz to period in days requires multiplication by 86400:

$$\text{Period}[days] = \frac{1}{f\,[\text{Hz}]} \times \frac{1}{86400\ \text{s/day}}. \tag{6.66}$$

Applying this relation, the phase originally expressed in degrees is converted into a time delay $\tau(f)$ expressed in days, providing an intuitive indication of how much the simulated series leads or lags the observed one across different time scales.

Furthermore, to avoid numerical instabilities in low-power bands, the power spectrum $P_{xx}(f)$ of the reference series is replaced with

$$P_{xx}(f) \to \max\{P_{xx}(f), \varepsilon\}, \quad \varepsilon \ll 1, \tag{6.67}$$

ensuring greater robustness.

6.8.3 RMSE Spectra and Wavelets

The analysis of spectra and their components revealed specific phenomena that required further investigation. For this reason, in continuity with the spectral decomposition described in the previous section, a series of analyses focused on the *Root Mean Square Error* and *Wavelets* are introduced.

Let $m(t)$ be the *basin average* timeseries from the simulation and $o(t)$ its satellite counterpart. The *signed error* is defined as

$$e(t) = m(t) - s(t) \tag{6.68}$$

and the variable analyzed is its instantaneous magnitude

$$r(t) = |e(t)|. \tag{6.69}$$

Similarly to the analyses already carried out and presented in previous sections, the creation of the associated power spectrum required a constant sampling interval of $\Delta t = 1$ day (or sampling frequency $f_s = 1/86400$ Hz), and the energy distribution of $r(t)$ was obtained using the *Welch* method with a maximum period, and therefore resolution limit, equal to 3 years.

In parallel with the creation of these new spectra, a series of *Continuous Wavelet Transforms* (CWTs) were generated using the *Morlet* mother wavelet. Denoting the scale by $a > 0$ and the temporal translation by b, the *CWT* of $r(t)$ is

$$W_r(a,b) = \frac{1}{\sqrt{a}} \int_{-\infty}^{\infty} r(t)\, \overline{\psi\left(\frac{t-b}{a}\right)}\, \mathrm{d}t, \tag{6.70}$$

and the local scalogram is defined as $P_r(a,b) = |W_r(a,b)|^2$ (Torrence and Compo, 1998). The adopted scale–period relationship for the *Morlet* wavelet is

$$T(a) = a\,\Delta t / f_0, \tag{6.71}$$

where f_0 is the *central frequency* characteristic of the *mother wavelet* (expressed in cycles per unit time) and Δt is the sampling interval. To explore dynamics ranging

from oscillations of a few days to annual variability, a grid of periods between $T_{\min} = 2$ d and $T_{\max} = 365$ d was chosen, distributed over $N_a = 220$ scales, with the resulting mapping into scales according to the previous relation (Percival and Walden, 2000). The temporal average of the scalogram provides the *global wavelet spectrum*

$$\overline{P}_r(a) = \frac{1}{T_{\text{tot}}} \int_{t_0}^{t_0+T_{\text{tot}}} P_r(a,b)\,\mathrm{d}b, \tag{6.72}$$

which provides a multiscale measure of integrated energy and allows for direct comparison, after appropriate normalization, with the original spectrum obtained via the *Welch* method.

The significance of the wavelet power was evaluated following the protocol of Torrence and Compo (1998): from the empirical lag–1 autocorrelation $\alpha = \mathrm{corr}(r(t), r(t+\Delta t))$, the theoretical spectrum of an AR(1) process is constructed,

$$S_{\text{AR1}}(f) = \frac{1-\alpha^2}{1-2\alpha\cos(2\pi f \Delta t)+\alpha^2}, \tag{6.73}$$

which, multiplied by the sample variance σ_r^2, gives the expected background power; comparing $P_r(a,b)$ with the critical level

$$P_{\text{crit}}(a) = \sigma_r^2 S_{\text{AR1}}(f_a)\,\chi^2_{1-\alpha_s}(\nu)/\nu \tag{6.74}$$

with ν degrees of freedom typical of the Morlet wavelet (for this study $\nu \approx 2$) identifies regions where the observed energy exceeds the variability expected from red noise (Torrence and Compo, 1998). Regions close to the temporal boundaries are treated with the *cone of influence*, which delimits the zone where truncation effects make coefficients less reliable (Torrence and Compo, 1998).

A noteworthy result from the analysis is the presence of spectral content around the period $T_c = 114$ days. To isolate the local dynamics of this component, a relative band with width fraction $\delta = 0.20$ was defined, with period boundaries $T_\ell = T_c(1-\delta)$ and $T_u = T_c(1+\delta)$; converting to frequency via $f = 1/(T \cdot 86400)$ allowed the application of a *Butterworth* band–pass filter to extract the component $r_b(t)$, for which the *Hilbert transform* was then computed

$$\mathcal{A}(t) = r_b(t) + \mathrm{i}\,\mathcal{H}\{r_b(t)\}, \tag{6.75}$$

and the *instantaneous envelope*

$$A(t) = |\mathcal{A}(t)|, \tag{6.76}$$

which is useful for tracking temporal modulations of the quasi–periodic component (Mallat, 1999).

To explore the local relationship in the time–scale domain between model and observation, the complex CWTs $W_m(a,b)$ and $W_s(a,b)$ were computed, and the cross–wavelet defined as

$$W_{ms}(a,b) = W_m(a,b)\,\overline{W_s(a,b)} \tag{6.77}$$

(Grinsted et al., 2004); applying a separable smoothing in scale and time (numerically implemented as a *two-dimensional Gaussian filter* with parameters depending on scale) yields the *smoothed* terms that allow defining the *wavelet coherence squared*

$$R^2(a,b) = \frac{\left|S\{W_{ms}(a,b)\}\right|^2}{S\{|W_m(a,b)|^2\}\, S\{|W_s(a,b)|^2\} + \varepsilon}, \tag{6.78}$$

where ε is a small regularizing term.

The field $R^2(a,b)$ varies approximately between 0 and 1, and the complex argument of $S\{W_{ms}\}$ gives the local phase

$$\phi(a,b) = \arg(S\{W_{ms}\}), \tag{6.79}$$

which, translated into time lag by

$$\tau(a,b) = \phi(a,b)/(2\pi f_a) \tag{6.80}$$

allows estimating lead/lag at each scale (Grinsted et al., 2004; Torrence and Compo, 1998). Extracting the trajectory $b \mapsto R^2(a^\star, b)$ for the scale $a^\star$ closest to T_c provides the temporal coherence specific to the band and, together with the associated phase, allows interpreting any systematic delays between model and satellite (Grinsted et al., 2004).

6.9 Region of Fresh Water Influence

6.9.1 K-means Clustering for Po's ROFI Identification

To identify and map the *Region of Freshwater Influence* (**ROFI**) associated with the Po plume, an analytical strategy was adopted that combines deterministic criteria, allowing the most evident plume cores to be isolated, with an *unsupervised classifier* that explores the secondary structures present in the residual water mass. The analysis focuses on a composite signal, integrating a physical variable, the *sea surface salinity* $S(x,y,t)$, with a *biological tracer*, sensitive to terrestrial nutrient input, represented by the surface concentration of chlorophyll-a, $Chl(x,y,t)$. The choice of these variables is motivated by both theoretical considerations and empirical evidence: salinity allows a direct quantification of freshwater input and, when considering the anomaly relative to the monthly climatology, highlights the local riverine influence, as in the case of the Po and its tributaries (Cozzi and Giani, 2011); chlorophyll, on the other hand, serves as a well-established indicator of phytoplankton biomass and the potential *bloom* that often accompanies the plume, thus providing a complementary signature useful for distinguishing simple hydrodynamic mixing from areas of intense biological response (Ø'Callaghan and Stevens, 2017).

To formalize the concepts underlying the classification, we first define the salinity anomaly with respect to the monthly climatology $\overline{S}_m(x,y)$:

$$\Delta S(x,y,t) = S(x,y,t) - \overline{S}_{m(t)}(x,y), \tag{6.81}$$

which represents the local deviation of the salinity field from the expected value for month $m(t)$. For the biological field, given the strong asymmetry and the typical positive tail of bio-optical distributions, the variable Chl is stabilized using a logarithmic transformation:

$$\chi(x, y, t) = \log_{10}\big(\max\{Chl(x, y, t), 0\} + \varepsilon\big), \tag{6.82}$$

where ε is a small numerical constant that prevents issues at zero values, following common practice in optically complex waters (Campbell, 1995; Hu et al., 2012). The two primary fields $S(x, y, t)$ and $Chl(x, y, t)$, along with the two derived quantities ΔS and χ, constitute the biogeophysical feature vectors $\mathbf{f} = [S, Chl, \Delta S,\ \chi]^{\mathsf{T}}$ used in the clustering procedure. Prior to computing distances, each component is standardized to zero mean and unit variance:

$$\tilde{f}_j = \frac{f_j - \mu_{f_j}}{\sigma_{f_j}}, \qquad j = 1, 2, \tag{6.83}$$

where μ_{f_j} and σ_{f_j} represent the empirical mean and standard deviation of feature j calculated over all valid points. This normalization prevents the Euclidean metric from being dominated by numerically larger components and follows established practices in the application of machine learning methods (Pedregosa et al., 2011).

For the unsupervised partitioning of the data, the k-means algorithm was chosen, one of the most widely used clustering techniques in statistics and data analysis. The goal of the method is to divide a set of observations $\{\mathbf{x}_i\}_{i=1}^{N}$, represented in a multidimensional space, into K groups $\{C_k\}$, assigning each point to the cluster with the nearest centroid. The algorithm seeks to minimize the sum of squared Euclidean distances between the points and their respective centroids:

$$\mathcal{J}(\{C_k\}, \{\boldsymbol{\mu}_k\}) = \sum_{k=1}^{K} \sum_{\mathbf{x}_i \in C_k} \|\mathbf{x}_i - \boldsymbol{\mu}_k\|^2, \tag{6.84}$$

where $\boldsymbol{\mu}_k$ represents the centroid of cluster C_k, defined as the arithmetic mean of the vectors contained in it. The function $\mathcal{J}$, commonly referred to as *inertia*, provides a measure of the internal compactness of the clusters: the lower its value, the more homogeneous the resulting groups.

The algorithm proceeds iteratively through two main phases: assignment and update. During the assignment phase, each observation is assigned to the cluster whose centroid is closest, measured using the Euclidean distance in the space of the considered variables. In the update phase, each centroid is recalculated as the arithmetic mean of the observations assigned to it. This process repeats until convergence, that is, until the assignments no longer change between successive iterations or the relative change in the objective function $\mathcal{J}$ falls below a predetermined threshold. This procedure, originally introduced by MacQueen (1967) and later formalized by Lloyd (1982), constitutes a form of unsupervised optimization based on the principle of minimum intra-cluster variance.

Since the cost function $\mathcal{J}$ is not convex, the algorithm may converge to local minima, whose location strongly depends on the initial conditions. To mitigate this effect, an improved initialization method, known as k-means++ (Arthur and Vassilvitskii, 2007), is employed, which selects the initial centroids so as to maximize their

mutual distances. This strategy significantly reduces the probability of suboptimal convergence and increases the stability of the final result. Furthermore, the entire partitioning process is repeated multiple times with different initial conditions, ultimately selecting the solution that globally minimizes the inertia. In this way, the procedure ensures a consistent representation of the statistical structures of the analyzed field while preserving the intrinsic spatial and dynamic relationships of the considered variables.

Determining the optimal number of clusters K represents a crucial phase in the clustering process, as it directly affects the statistical coherence and the physical interpretability of the regions identified within the analyzed field. To ensure a robust estimate, the selection of K was performed using an adaptive procedure that combines multiple diagnostic metrics, capable of accounting for the significant spatial and seasonal variability of the hydrological characteristics of the basin.

The analysis pipeline considers, for each time step, a range $K \in [2, 6]$, performing for each value of K a new partition of the dataset $\mathbf{X} = \{\mathbf{x}_i\}_{i=1}^{N}$, composed of the pairs of normalized salinity and chlorophyll concentration variables, using the k-means algorithm. After standardizing the features via z-score transformation, each model produces a set of labels $\{C_k\}$ and an *inertia* value, computed as already reported in *Equation 6.84*, where $\boldsymbol{\mu}_k$ represents the centroid of cluster C_k. This quantity measures the internal compactness of the groups: lower values indicate higher cohesion, but the function tends to decrease monotonically as K increases, making a more nuanced evaluation necessary to identify the optimal number of clusters.

To identify the value of K beyond which adding new clusters does not produce a substantial structural improvement, the *elbow method* is applied, analyzing the relative change of Inertia(K) between two successive values of K:

$$\Delta\text{Inertia}_K = \text{Inertia}(K-1) - \text{Inertia}(K). \tag{6.85}$$

The inflection point of the curve, where the relative decrease becomes minimal, is taken as the initial estimate of K_{opt} (Rousseeuw, 1987). This approach allows identification of the threshold beyond which increasing the number of clusters yields only marginal improvements, avoiding over-partitioning of the domain that would limit interpretability in terms of actual physical structures.

In parallel, the silhouette coefficient is evaluated, which quantifies the geometric separability of the clusters by comparing the average distance of each point to its own centroid with that to the nearest other cluster centroid:

$$s_i = \frac{b_i - a_i}{\max(a_i, b_i)}, \tag{6.86}$$

where a_i is the average distance of $\mathbf{x}_i$ to the other points in its cluster, and b_i represents the minimum average distance to points in other clusters. The global silhouette value is the mean

$$\bar{s} = \frac{1}{N} \sum_i s_i, \tag{6.87}$$

ranging from -1 to 1: values close to 1 indicate compact and well-separated clusters, while values near zero suggest overlaps between groups (Rousseeuw, 1987).

In general, the optimal K maximizes the silhouette; however, in this context, the absolute maximum corresponds to a number of clusters that produces excessively fragmented and less physically interpretable partitions. For this reason, the *elbow point* of the silhouette curve is preferred, that is, the value of K beyond which adding clusters yields little improvement in group separability and the silhouette stabilizes. This criterion, analogous to the *elbow method* for inertia, balances cluster compactness and partition parsimony, preserving the domain's statistical structure. In our case, the elbow point is clearly at $K = 4$, confirming the chosen value and providing consistency between the two methods for estimating the optimal number of clusters.

The results are summarized in the diagrams shown in *Figure 6.6*, which display both the inertia curve and the mean silhouette coefficients for each K value.

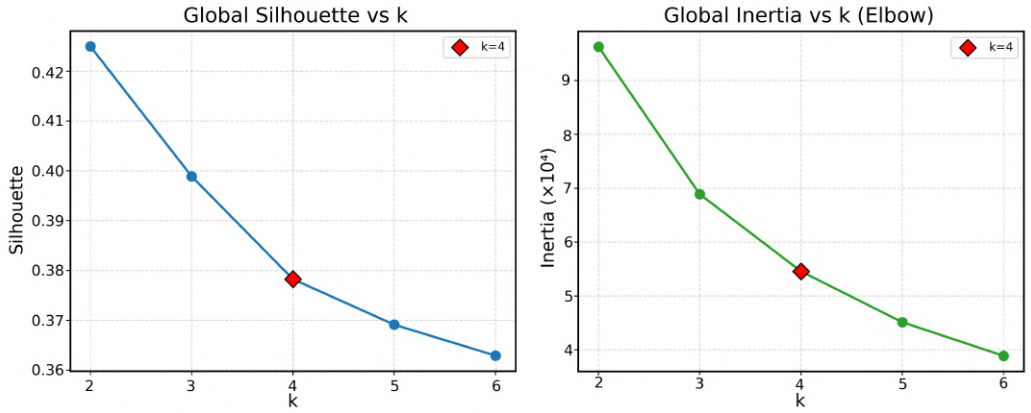

Figure 6.6: Graphs showing the *silouhette* and *inertia* values used to determine the ideal value of K. The red marker shows the chosen *K-value* per each method.

Once the optimal number of clusters K_{opt} was determined for each temporal interval, the water classification was guided by progressively applied physical constraints, rather than separating the partition from the statistical clustering. The first constraint focuses on the freshest waters, identifying the general riverine influence region using a salinity threshold of $S < 34$ PSU. This value, supported by previous studies on the Adriatic and the Po plume (Ø'Callaghan and Stevens, 2017; Babagolimatikolaei et al., 2025; Verri et al., 2022), robustly isolates continental waters, distinguishing them from the surrounding marine domain.

The second constraint concerns algal blooms, identified by applying a chlorophyll threshold based on the 85th percentile of the basin-wide values, corresponding to $Chl = 0.931\ mg/m^3$. This highlights areas with significantly elevated phytoplankton biomass, both within the Po influence region and in other parts of the domain. Simultaneously, the direct effect of the Po is isolated by considering the sign of the salinity anomaly relative to the climatological value at the Po delta; a minimum threshold of $|\Delta S| \geq 0.5$ PSU is then applied, above which the river's predominant signal is identified. This step is necessary because the Po signal anomalies, being one of the main hydrological drivers of the basin, change sign over time depending on discharge and other riverine factors.

By sequentially applying these constraints, three complementary and progressively segmented clusters are obtained, representing a physical hierarchy of freshwater and coastal waters:

1. the *general ROFI area* of the basin, identified by the first salinity constraint;
2. the *specific Po influence area*, isolated through the analysis of salinity anomalies;
3. the *bloom zones*, highlighted by elevated chlorophyll values, both within the Po influence area and in other regions identified as ROFI within the domain.

It is important to note that these areas do not constitute separate water families, but represent a progressive segmentation of the ROFI, initially identified based on salinity and subsequently refined by biological constraints.

The following are a series of plots reported here to show the performance of this clustering method and the criteria used to define the populations. The chosen plots will show the behavior of each population regarding their placements within the full variable fields and their respective anomalies.

To show the performance of this clustering methodology, the distributions of the populations based on the full salinity and chlorophyll fields for August 2000 are shown in *Figure 6.7*. The choice of this specific month is purely arbitrary.

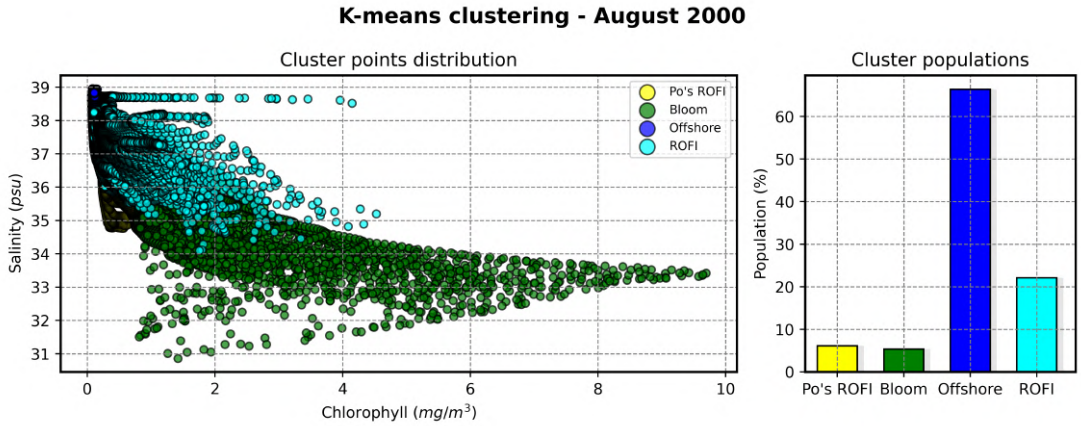

Figure 6.7: Graph showing the distribution of each population relative to the salinity/chlorophyll values (left) and their respective % within the domain.

The second distribution, computed using the anomaly fields, is presented in *Figure 6.8*, highlighting the differences compared to the full fields.

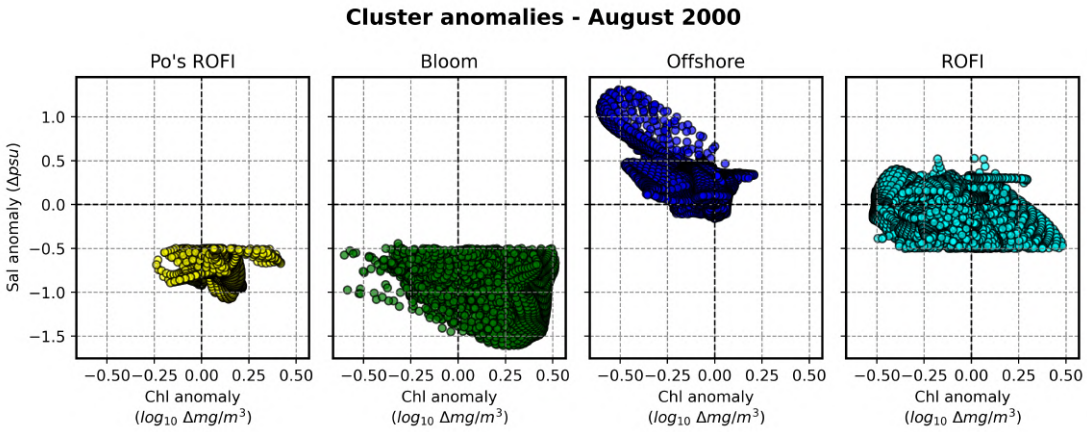

Figure 6.8: Graph showing the distribution of each population relative to the salinity and chlorophyll anomaly fields.

Finally, the spatial distribution of the populations is illustrated in *Figure 6.9*, providing a clear representation of their location within the domain.

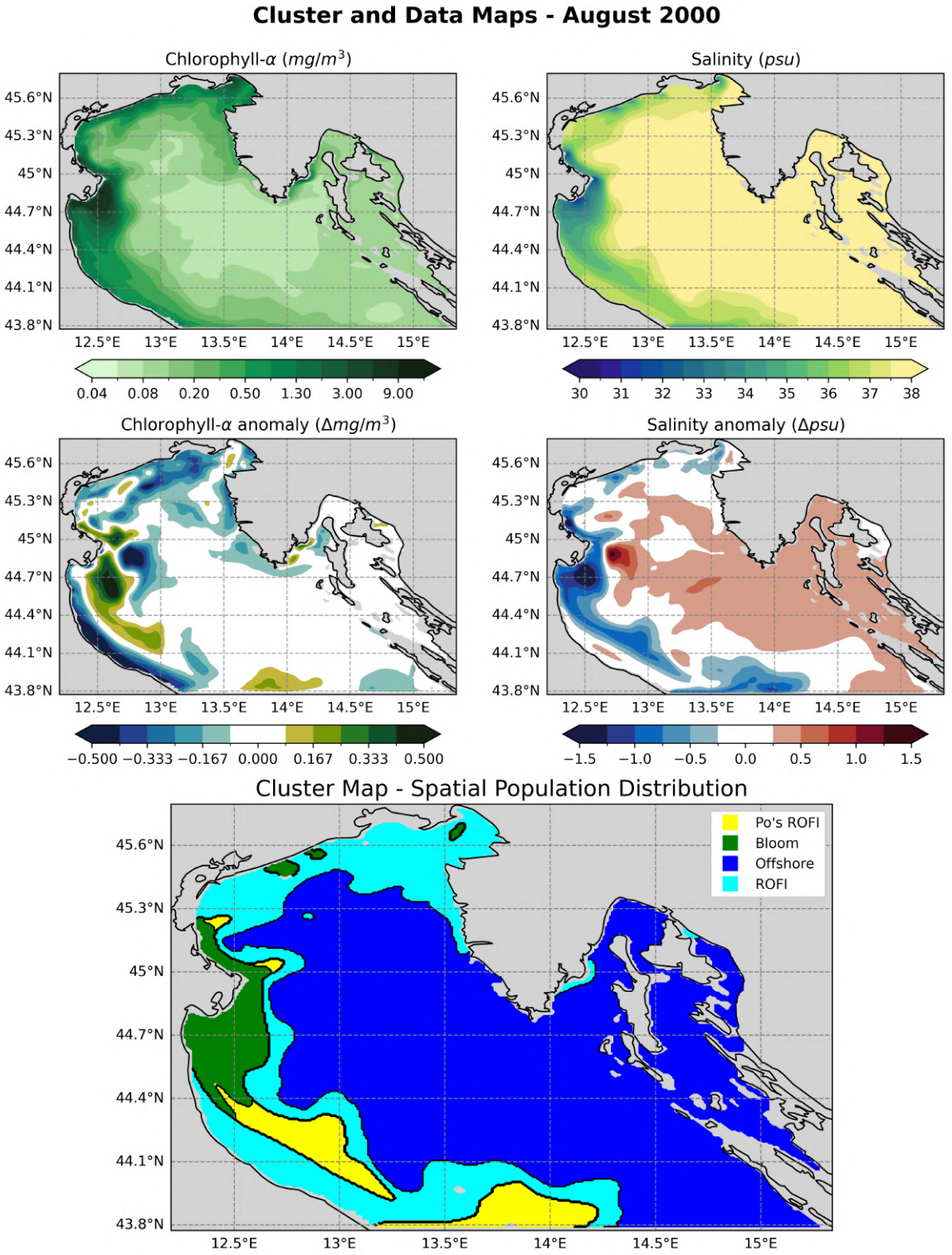

Figure 6.9: Comprehensive overview of the clustering results for August 2000. Top row: full fields for the month (chlorophyll on the left, salinity on the right); middle row: corresponding anomalies (chlorophyll anomaly on the left, salinity anomaly on the right); bottom row: spatial distribution of each cluster within the domain.

6.9.2 Po's Effect Using Chlorophyll as a Chemical Tracer

To assess potential differences in the behavior of the portion of waters originating from the Po River delta and entering the basin, the dynamics of the river *plume* were analyzed using a tracer available both from satellite observations and model outputs. In particular, the surface concentration of chlorophyll-a (Chl) was considered, recognized as a well-established indicator of phytoplankton biomass and particularly effective in delineating the spatial extent and dispersion of the incoming freshwater mass. The area of analysis is shown in *Figure 4.5*.

To make the dataset coherent and comparable, in view of the subsequent computation of the ROFI (*Region Of Freshwater Influence*), a three-phase pre-processing was applied, aimed at reducing non-significant variability and normalizing the statistical distribution of the observed field.

The first step consists of applying a *two-dimensional Gaussian filter* to each temporal level, intended to smooth spatial discontinuities due to noise or artifacts inconsistent with the physical dynamics of the water. This spatial smoothing operation can be formalized as a convolution:

$$\tilde{\mathrm{Chl}}(x,y) = \int_{-\infty}^{+\infty} \int_{-\infty}^{+\infty} \mathrm{Chl}(\xi,\eta)\, G(x-\xi, y-\eta; \sigma)\, d\xi\, d\eta \tag{6.88}$$

where $\tilde{\mathrm{Chl}}(x,y)$ represents the filtered field, $\mathrm{Chl}(\xi,\eta)$ is the observed value at point (ξ,η) of the original data grid, and $G(x-\xi, y-\eta;\sigma)$ is the Gaussian kernel centered at point (x,y) with standard deviation σ. The convolution acts as a linear operator that combines the values of surrounding points weighted according to the shape of the Gaussian bell curve, allowing the smoothing of local peaks and the reduction of noise without introducing undesired artifacts. Mathematically, convolution preserves system linearity, guarantees translation invariance, and, when applied with Gaussian kernels of increasing width, enables the analysis of the field at different spatial scales, consistent with the theory of *scale-space* (Witkin, 1983). The smoothing effect of the filter on a wave function is illustrated in *Figure 6.10*.

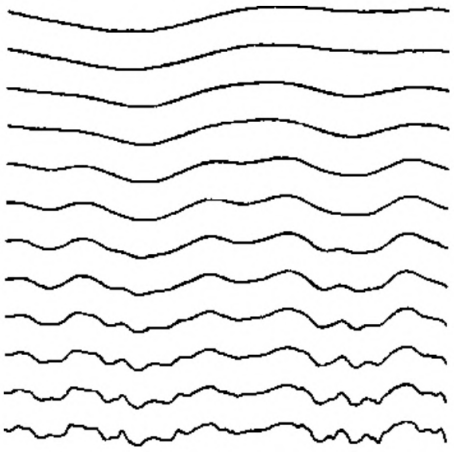

Figure 6.10: Application of Gaussian smoothing to a wave function. From top to bottom, a progressively decreasing value of σ is applied. (Witkin, 1983)

The Gaussian kernel is shown in *Figure 6.11* and is defined as:

$$G(x, y; \sigma) = \frac{1}{2\pi\sigma^2} \exp\left(-\frac{x^2 + y^2}{2\sigma^2}\right), \tag{6.89}$$

where x and y represent spatial coordinates relative to the filter center, and σ controls the width of the bell curve, determining the degree of smoothing. Normalization by the factor $1/(2\pi\sigma^2)$ ensures that the integral of the kernel equals one, preserving the mean amplitude of the filtered data. The choice of a Gaussian kernel is not arbitrary: it possesses mathematical properties that are particularly useful, such as separability into two one-dimensional convolutions, preservation of positivity, and infinite regularity, making it ideal for filtering continuous and discrete data in geophysical contexts.

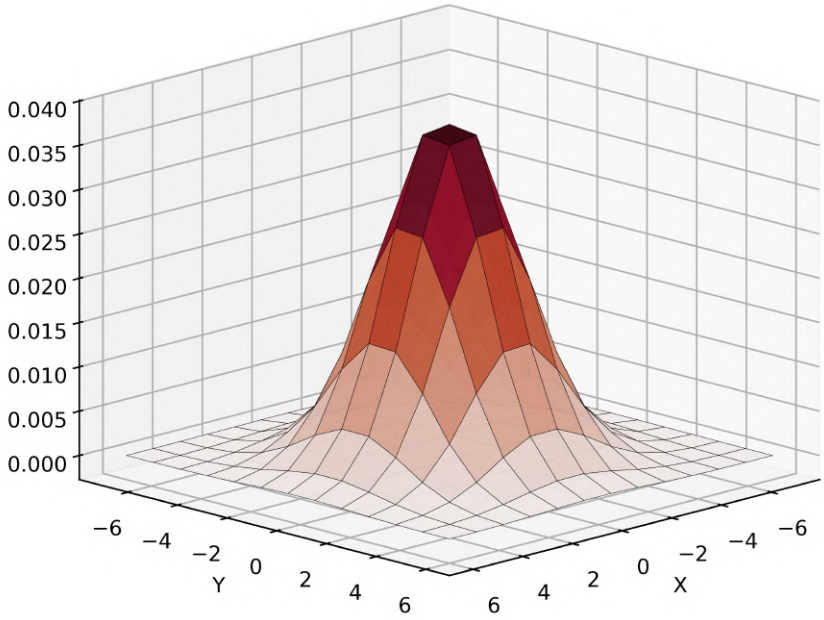

Figure 6.11: Graphical representation of the *two-dimensional Gaussian kernel* used in the filter. The imposed value of σ is 2.0, and the vertical axis shows the amplitude values obtained by evaluating the kernel.

Given the high spatial and temporal variability of chlorophyll-a data, in order to reduce noise and obtain a more stable representation of the surface distribution, a value of $\sigma = 2.0$ was imposed within the *Gaussian kernel*. This approach allows attenuation of local fluctuations while preserving the main structures of the river *plume*.

The second step involves applying a logarithmic transformation defined as $\log(1+\tilde{\text{Chl}})$, useful for mitigating the influence of the positive tails typical of biological distributions:

$$\tilde{\text{Chl}}_{\log}(x, y) = \log\big(1 + \tilde{\text{Chl}}(x, y)\big). \tag{6.90}$$

This operation emphasizes relative variations compared to extreme peaks, stabilizes variance, and produces a more symmetric distribution, facilitating subsequent statistical analyses. Adding unity to the logarithm argument avoids numerical issues

related to zero or near-zero values, and is a common practice in bio-optical analyses (Campbell, 1995).

Finally, if necessary, a *clipping* of values is applied to confine chlorophyll concentration within a physically plausible range $[c_{\min}, c_{\max}]$:

$$\tilde{\mathrm{Chl}}_{\mathrm{clip}}(x,y) = \min\big(\max(\tilde{\mathrm{Chl}}_{\log}(x,y),\ c_{\min}),\ c_{\max}\big). \tag{6.91}$$

This operation limits the influence of anomalous values or artifacts, ensuring that statistics of the filtered field and its spatial representation remain consistent. The lower bound $c_{\min}$ ensures no value falls below a physically plausible threshold, while $c_{\max}$ prevents excessive peaks caused by measurement errors or exceptional events, thus strengthening the reliability of the dataset for subsequent analyses.

To proceed with the analysis of the river *plume* dynamics, it is necessary to identify the predominant spatial position of the freshwater mass for each day, represented by the *centroid* of the *plume*. The definition of the *centroid* allows summarizing spatial information distributed over a larger area into a single point (Gonzalez and Woods, 2008), making it possible to track temporal evolution of the flow and quantify any deviations or dispersion along the coastal basin.

The first step in centroid computation consists in constructing a binary mask $\mathcal{M}(x,y)$ that identifies areas of significant chlorophyll concentration, considered representative of the incoming freshwater mass. This mask can be formalized as:

$$\mathcal{M}(x,y) = \begin{cases} 1 & \text{if } \tilde{\mathrm{Chl}}_{\mathrm{clip}}(x,y) \geq S, \\ 0 & \text{otherwise,} \end{cases} \tag{6.92}$$

where S represents a threshold defined according to the global percentile method p, and $\tilde{\mathrm{Chl}}_{\mathrm{clip}}(x,y)$ is the preprocessed chlorophyll field described above. Choosing a high global percentile, in this work $p = 85$, allows selection of the most significant regions, reducing the influence of background values or isolated peaks due to noise. Isolated pixels below a minimum area $A_{\min}$ are ignored, ensuring spatial and physical consistency of the mask.

Once the region of interest is defined, the weighted centroid of the chlorophyll concentration is calculated as the spatial average of the coordinates, weighted by the concentration values themselves:

$$\begin{aligned} x_c &= \frac{\sum_{x,y} x\, \tilde{\mathrm{Chl}}_{\mathrm{clip}}(x,y)\, \mathcal{M}(x,y)}{\sum_{x,y} \tilde{\mathrm{Chl}}_{\mathrm{clip}}(x,y)\, \mathcal{M}(x,y)}, \\ y_c &= \frac{\sum_{x,y} y\, \tilde{\mathrm{Chl}}_{\mathrm{clip}}(x,y)\, \mathcal{M}(x,y)}{\sum_{x,y} \tilde{\mathrm{Chl}}_{\mathrm{clip}}(x,y)\, \mathcal{M}(x,y)}, \end{aligned} \tag{6.93}$$

where (x_c, y_c) represent, respectively, the longitude and latitude of the centroid. This approach emphasizes areas of higher concentration, ensuring that the centroid truly reflects the dominant position of the freshwater mass rather than the simple geometric center of the mask.

To characterize the area of influence of the river *plume* along the coastal basin, it is necessary to go beyond the analysis of individual daily centroids by considering the

overall spatial distribution of positions calculated over multiple days or seasons. In this context, centroid density estimation proves to be a powerful tool for identifying regions of higher freshwater flow concentration and for delineating the main *corridors*. Such estimations allow not only quantifying the average position of the *plume*, but also the probability of its presence in surrounding areas, providing an indirect measure of the phenomenon's extent and variability (Lee and Park, 2021; Govorov, 2025).

One technique employed is the density estimation using hexbins (Lee and Park, 2021), which consists of dividing the area into hexagonal cells of uniform size and counting the number of centroids present in each cell. Formally, if N_i represents the number of centroids in cell i, the discrete density can be expressed as:

$$\rho_i = \frac{N_i}{A_{\text{hex}}}, \tag{6.94}$$

where A_{hex} is the area of each hexagon. This technique allows for an intuitive and easily interpretable visualization of zones of higher frequency, while reducing sensitivity to individual outliers (Lee and Park, 2021). In this study, a resolution of 50 hexagons along each axis was adopted, filtering cells with at least one centroid to avoid overestimating empty regions.

The fundamental difference between the two approaches lies in the discrete versus continuous nature of the representation. The hexbin method provides an aggregated and easily interpretable measure of density, but it strongly depends on the cell size and can introduce grid-related artifacts. KDE, on the other hand, generates a smooth continuous field that allows for more sophisticated probabilistic analyses, but requires careful selection of bandwidth parameters to avoid underestimating or overestimating local density.

Once the daily centroids of the *plume* are obtained, it is possible to describe the seasonal evolution of its mean trajectory along the coastal basin. To this end, a comprehensive representation of the *plume* propagation is constructed by combining monthly data and estimating an overall trajectory through non-parametric smoothing.

The first step consists of dividing the centroids according to the month of observation, thereby creating monthly data sets. For each month, the centroids are ordered from north to south and, when necessary, grouped into latitude bins of width $\Delta\phi = 0.01°$ in order to reduce local variability and improve the robustness of the estimate. Within each bin, the mean of the longitudinal and latitudinal coordinates of the centroids present is calculated. The application of this methodology is necessary for the correct reconstruction of the Po River plume trajectory, as the flow evolves along the Italian Adriatic coast from north to south.

Based on the aggregated monthly data, the seasonal trajectory is estimated using the **LOWESS** (Locally Weighted Scatterplot Smoothing) technique (Cleveland, 1979), which allows obtaining a representative curve of the *plume* path without assuming a predetermined functional form. Formally, given a set of points (x_i, y_i) ordered by latitude y_i, the smoothed estimate of longitude $\hat{x}(y)$ is calculated by locally weighting

nearby points:

$$\hat{x}(y) = \sum_i w_i(y)\, x_i,$$
$$w_i(y) = \left(1 - \left|\frac{y - y_i}{h}\right|^3\right)^3 \text{ for } \left|\frac{y - y_i}{h}\right| < 1, \text{ otherwise } 0, \tag{6.95}$$

where h is the smoothing parameter defining the width of the local neighborhood (set to 0.2 in the present study). The function used is the *tricubic kernel*, adopted as a decreasing weight with normalized distance.

For each month, in addition to the smoothed trajectory, an interquartile confidence band (25%-75%) on the observed longitudes is calculated, allowing the representation of the local variability of the centroids with respect to the mean trajectory.

The overall trajectory is finally estimated by interpolating the monthly trajectories over a common latitude interval and calculating the mean of the interpolated longitudes. This curve represents the mean trajectory of the *plume* over the entire period considered, providing a clear indication of the predominant paths and the main *corridors* of the freshwater flow. The **LOWESS** methodology also allows preserving local features without introducing artifacts due to predetermined geometric parameters (Cleveland, 1979; Bowman and Azzalini, 1997).

6.9.3 Bio-Geophysical Parameters Timeseries and Vertical Profiles

Once the area of the basin belonging to the ROFI of the Po River was identified, the validation of the main bio-geophysical parameters within the ROFI area involved the use of a series of in-situ observations provided by ARPAE. The arrangement of the stations within the analysis area is shown in *Figure 4.5*. For a description of the station characteristics, as well as their metadata, please refer to the information provided in section 4.2.

Studies conducted using the same stations (Fiori et al., 2016) propose a classification of these stations based on their distance from the Po River mouth area. In this study, however, a classification based on the distance from the coast was adopted for two main reasons: first, to assess potential *fall-off* effects of the model when approaching or moving away from the coast; second, to facilitate the construction of vertical profiles, since stations within each group record depths that are approximately consistent with each other.

Each station performs measurements at approximately regular depth intervals of 1 m until reaching the maximum available depth. The measured parameters include pressure, salinity, temperature, and dissolved oxygen. Additionally, near the surface, at 0.5 m depth, the stations measure chlorophyll concentration through fluorimetry.

A preliminary analysis of the field data revealed a key constraint: stations record data at irregular intervals and are not synchronized. Typically, each station samples at each depth step ($\sim$ 1 m) every 10–15 days, and measurements are not taken simultaneously across stations. This temporal irregularity limits data transformations, as they risk introducing artifacts. To ensure comparability with modeled and satellite

data, a conservative, reproducible approach was adopted, focusing solely on surface measurements at 0.5 m, the only depth with complete datasets required for analysis. Point-by-point comparison with model data was performed by matching station positions to model grid points and extracting the corresponding *time series*. This was not feasible for satellite data due to extensive missing data from cloud coverage (*Table 6.1*). Therefore, the analysis relied on the *basin average*, which offers a more complete and consistent representation of basin-wide behavior.

Group	**% of Missing Data**
300	82.84%
600	72.22%
1000	59.84%
2000	60.91%

Table 6.1: Percentage of missing satellate data in the location of each group of stations.

The construction of the reference time series, here referred to as *observation mean*, was formalized through a procedure of daily and spatial aggregation that preserves the intrinsic temporal discontinuities of the observational dataset. Let G be the set of station groups considered (identified by code classes 300, 600, 1000, and 2000), and for each group $g \in G$, let S_g be the set of stations belonging to g. For a given calendar day d and for a station $s \in S_g$, the set of observations at 0.5 m recorded on day d is defined as

$$\mathcal{X}_{s,d} = \{x_{s,d,1}, \ldots, x_{s,d,m_{s,d}}\}. \tag{6.96}$$

When a single station provides multiple samples on the same day, the information is summarized by the station's daily mean:

$$\bar{x}_{s,d} \;=\; \frac{1}{m_{s,d}} \sum_{k=1}^{m_{s,d}} x_{s,d,k}. \tag{6.97}$$

Let $S_g(d) \subseteq S_g$ denote the subset of stations in group g that have at least one observation on day d, and let $N_g(d) = |S_g(d)|$ be the number of such stations. The representative group measurement for day d is the arithmetic mean of the daily station means:

$$\mu_g(d) \;=\; \frac{1}{N_g(d)} \sum_{s \in S_g(d)} \bar{x}_{s,d}. \tag{6.98}$$

The intra-daily spatial variability is quantified through the population variance and standard deviation:

$$\begin{aligned} \sigma_g^2(d) \;&=\; \frac{1}{N_g(d)} \sum_{s \in S_g(d)} \big(\bar{x}_{s,d} - \mu_g(d)\big)^2, \\ \sigma_g(d) &= \sqrt{\sigma_g^2(d)}. \end{aligned} \tag{6.99}$$

In computational practice, the definition with denominator $N_g(d)$ was adopted, consistent with interpreting the values as the finite set of stations in the group: if there

is only one observation ($N_g(d) = 1$), the group mean coincides with the observed value and the standard deviation is zero; when $N_g(d) = 0$, the date is absent in that group's series, and no automatic temporal interpolation is performed, thus preserving the actual observational availability structure.

To ensure comparability between datasets and simplify interpretation of results, $Chlo-rophyll-a$ concentrations were expressed both in μg/L and mg/m^3. The adopted conversion is the physical relation

$$1\ \mu\text{g/L} \ = \ 1\ \text{mg/m}^3, \tag{6.100}$$

so the alternative scale is obtained by the conversion factor $C = 1$, i.e.

$$\tilde{\mu}_g(d) = C\,\mu_g(d), \quad \tilde{\sigma}_g(d) = C\,\sigma_g(d). \tag{6.101}$$

This dual representation allows for direct comparison with modeled and satellite products, which may have different units or alternative reporting conventions.

The methodological choice of not automatically interpolating observational gaps preserves the real information and coverage characteristics of the in situ dataset, avoiding the imposition of assumptions on un-sampled periods. However, this approach emphasizes the need for careful comparisons with *daily* products: such comparisons must be performed using agreed aggregation operators (for example, calculating the *basin average* of the modelled or satellite data limited to the observation dates) or explicitly stating the interpolation procedures and their effects on the results. The resulting *observation mean* therefore provides a reproducible reference basis for the validation of modelled and satellite fields, with a central representation $\mu_g(d)$ and a systematic quantification of the spatial dispersion $\sigma_g(d)$ observed on sampling days.

Once the reference *timeseries* (*observation mean*) were constructed, the validation was extended to the vertical structure of the main bio-geophysical parameters by building seasonal vertical profiles for each station group. From a computational perspective, the workflow consists of three steps: a) mapping stations to the model grid points, b) extracting the three-dimensional space-time model series at the grid point associated with each station and performing temporal aggregation by month/season, c) constructing and binning the monthly observed in situ profiles and homogenizing them spatially and vertically to allow direct comparison with modelled profiles.

Spatial mapping was performed using a *nearest-neighbour* method on the model grid: let (φ_s, λ_s) be the geographic coordinates (latitude, longitude) of a station s and $\{(\varphi_{i,j}, \lambda_{i,j})\}_{i,j}$ the set of grid points in the simulated basin. The station is assigned to the grid point (i_s, j_s) that minimizes the Cartesian distance on the local sphere. Formally:

$$(i_s, j_s) \ = \ \arg\min_{(i,j)} \ \text{dist}\big((\varphi_s, \lambda_s), (\varphi_{i,j}, \lambda_{i,j})\big). \tag{6.102}$$

The result is a discrete mapping $s \mapsto (i_s, j_s)$ that allows the unambiguous extraction of model samples corresponding to each observational station.

Let $F(t, z, i, j)$ denote the three-dimensional model fields (e.g., oxygen, temperature, salinity) with time index t, discrete vertical level z, and grid coordinates (i, j). The

extraction at the grid point associated with station s produces the vertical space-time series

$$\begin{aligned} F_s(t,z) \;&=\; F(t,z,i_s,j_s), \\ &t = 1,\ldots,T, \\ &z = 1,\ldots,Z, \end{aligned} \tag{6.103}$$

where T denotes the number of available time steps and Z the number of vertical model levels. In the dataset considered here, the vertical dimension of the model is defined by levels with constant thickness $\Delta z = 2$ m.

Temporal aggregation for the construction of seasonal profiles uses a simple definition of season: for each season $S \in \{\mathrm{DJF}, \mathrm{MAM}, \mathrm{JJA}, \mathrm{SON}\}$ we define the set of time indices

$$I_S \;=\; \{\, t \;:\; \mathrm{month}(t) \in M_S \,\}, \tag{6.104}$$

where M_S is the set of months belonging to the season (e.g., $M_{\mathrm{JJA}} = \{6,7,8\}$). The modelled seasonal profile for station s is then obtained as the temporal average of the values belonging to the season:

$$\Pi^{\mathrm{mod}}_{s,S}(z) \;=\; \frac{1}{|I_S|} \sum_{t \in I_S} F_s(t,z), \tag{6.105}$$

computed component-by-component along the vertical vector.

For the in situ observed time series, the approach accounted for two key aspects: variability in measurement depths and the need to produce homogeneous monthly profiles. Point observations were first converted into a monthly format by grouping samples by period and calculating, for each month, the mean of available readings at the same depth. Observed depths were rounded and bin-aggregated using the function

$$b(d) = \begin{cases} d, & d \le 1.0 \text{ m}, \\ \lfloor d \rfloor, & d > 1.0 \text{ m}, \end{cases} \tag{6.106}$$

so as to convert heterogeneous depth measurements into discrete comparable vertical columns. Columns with the same depth label were aggregated using the arithmetic mean to produce the monthly observed profile $\Pi^{\mathrm{obs}}_{s,m}(h)$, where h is the bin-aggregated depth and m the month.

Because the units of mean dissolved oxygen concentration differ between the model and observations, a physical conversion was applied for oxygen: data in mg/L were transformed into mmol/m^3 using the factor

$$\kappa \;=\; \frac{1000 \text{ mg/g}}{32 \text{ g/mol}} \;=\; 31.25, \tag{6.107}$$

so that $C_{\mathrm{mmol/m^3}} = \kappa\, C_{\mathrm{mg/L}}$. The same conversion was applied to the in situ monthly profiles before any seasonal averaging.

The construction of the observed seasonal profile follows the same logic as the modelling procedure: for a season S and station s, the monthly profiles $\{\Pi^{\mathrm{obs}}_{s,m}\}_{m \in M_S}$ are considered, and the seasonal vertical average is computed as

$$\Pi^{\mathrm{obs}}_{s,S}(h) \;=\; \frac{1}{|M_S|} \sum_{m \in M_S} \Pi^{\mathrm{obs}}_{s,m}(h), \tag{6.108}$$

During the multi-station assembly phase, differences in vertical extent between stations were addressed. To prevent artefacts from uncommon depths, group averages of observed profiles were truncated to the minimum common extent or, when appropriate, clipped to a maximum depth $H_{\max}$ defined for each group. Missing values due to empty bins or lack of observations were ignored in the averaging process.

The synthetic comparison between model and observations at the group level was obtained by stacking the seasonal profiles of all stations within each group and calculating the mean over all available realizations. Defining $\mathcal{S}_g$ as the set of stations in group g, the model group mean for season S is given by

$$\overline{\Pi}^{\text{mod}}_{g,S}(z) = \frac{1}{\sum_{s\in\mathcal{S}_g} |I_{s,S}|} \sum_{s\in\mathcal{S}_g} \sum_{t\in I_{s,S}} F_s(t,z), \tag{6.109}$$

where $I_{s,S}$ denotes the times available for station s in season S. The corresponding observed group profile was constructed by aggregating the observed monthly profiles across all stations and months of the season, applying vertical trimming to ensure homogeneity along the z-axis.

It should be noted that chlorophyll data were excluded from the vertical profiles, as measurements exist only at 0.5 m. The vertical assessment therefore refers exclusively to hydrodynamic and biogeochemical parameters (oxygen, temperature, salinity) for which observations are available at multiple depths.

6.10 Bottom Layer

To analyze the evolution of chemical species concentrations as well as the dynamics of *dense* and *hypoxic/anoxic* water masses near the *benthic layer*, the deepest layer of the simulated water column was extracted, corresponding to the layer closest to the seabed and effectively "simulating" a σ-equivalent at the same coordinates.

In a three-dimensional ocean numerical simulation based on σ coordinates, the water column is discretized along the vertical axis through normalized levels that follow the local bathymetry. This means each σ-layer dynamically adapts to the seabed depth, allowing finer resolution near continental margins and coastal areas (Song and Haidvogel, 1994), unlike z-layers defined at a fixed distance from a reference level $z = 0$, as illustrated in *Figure 6.12*.

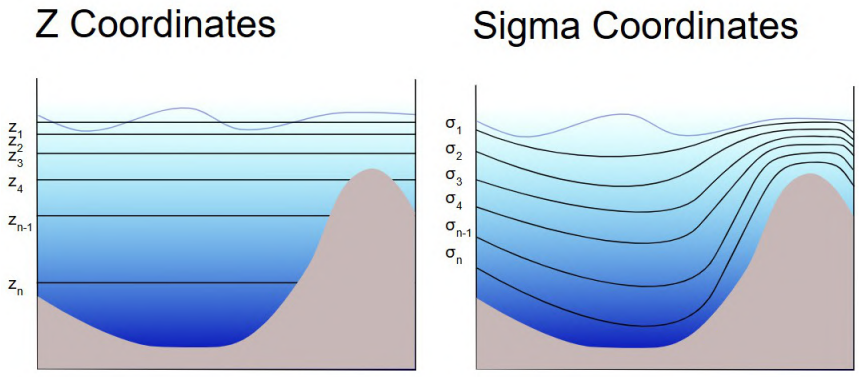

Figure 6.12: Example showing the difference in vertical coordinate representation in a numerical model. On the left, a basin using *z-coordinates*; on the right, the same basin with vertical discretization using *σ-coordinates*.

In the simulation used, 48 equidistant vertical levels in z coordinates were defined. To create the σ-layer equivalent necessary for the benthic analysis, it was necessary to identify, for each grid point (x, y), the deepest vertical level still immersed in water, excluding cells corresponding to bathymetry or with null values.
To this purpose, a custom mask was constructed by identifying, for each grid point, the first z-index such that:

$$V(x, y, z) = \texttt{NaN}, \tag{6.110}$$

where $V(x, y, z)$ represents the value of the physical variable (e.g., temperature, salinity, chemical concentration). The index of the layer immediately below is therefore:

$$z_{\text{bottom}}(x, y) = \max \{ z \mid \neg \texttt{isNaN}(V(x, y, z)) \} . \tag{6.111}$$

Applying this criterion to all variables of interest made it possible to extract a three-dimensional vertical layer $\sigma_{\text{bottom}}(x, y)$, corresponding to the layer closest to the seabed available.

6.10.1 Density Field and Dense Water Masses

To analyze the correct simulation of dense water mass formation within the study basin, the density field over the area of interest was calculated by combining temperature and salinity data at each z-layer of the domain. This was performed by applying the EOS-80 equation of state, integrating vertically across all z-layers to obtain a four-dimensional density field (time, depth, latitude, longitude).

Two different approaches were adopted for dividing the basin in this analysis: the first considers the entire basin as a single unit; the second defines a set of sub-areas following the methodology proposed by Pranić et al. (2024). The second approach enables a more detailed investigation of processes related to dense water mass formation by distinguishing regions with specific morphologies, allowing targeted analysis for each sub-domain. The sub-domains used in this study are shown in *Figure 6.13*.

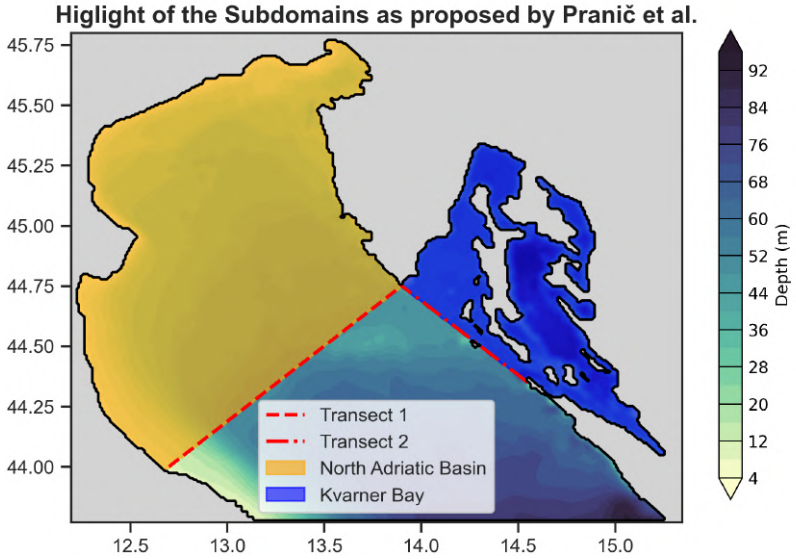

Figure 6.13: Subdivision into sub-domains for analysis according to the areas proposed by Pranić et al. (2024). Defined areas include the North Adriatic Basin (orange) and the Kvarner Bay (blue).

To ensure the reliability and validity of the data used in the density calculation and to exclude possible outliers inconsistent with the physical characteristics of Adriatic water masses, threshold values were applied to temperature and salinity fields. These limits were defined based on the climatological report of the Osservatorio Geofisico Sperimentale di Trieste (Giorgetti, 1999) and are reported in *Table 6.2*.

Depth (m)	**Temperature Range (°C)**	**Salinity Range (psu)**
$0 < z < 50$	$5 < T < 35$	$25 < S < 40$
$51 < z < 200$	$8 < T < 25$	$36 < S < 40$
$201 < z < 800$	$8 < T < 18$	$37 < S < 40$
$z > 800$	$12 < T < 15$	$38 < S < 40$

Table 6.2: Valid ranges of temperature and salinity for depth intervals in the water column, defined according to the climatological report of the Osservatorio Geofisico Sperimentale di Trieste (Giorgetti, 1999).

After filtering possible *outliers* according to the defined *thresholds*, the density field was calculated using the equation of state for seawater according to the $EOS - 80$ formulation (UNESCO - International Council for the Exploration of the Sea, 1980), which relates density, temperature, and salinity:

$$\rho(S, T, p) = \rho_0 + A(S, T) + B(S, T) \cdot p + C(S) \cdot p^2 \tag{6.112}$$

Where:

- $\rho(S, T, p)$ is the density of seawater (kg/m^3)
- S is practical salinity (PSU)
- T is temperature in °C (ITS-90)
- p is pressure in decibar (dbar)
- ρ_0 is the density of pure water at 0°C and 1 atm (approximately 999.8425 kg/m^3)
- $A(S, T)$ is a polynomial function of salinity and temperature (thermo-saline coefficient)
- $B(S, T)$ and $C(S)$ are correction terms for the effect of pressure

In the present case, the pressure p was computed from the depth z following the Gibbs Seawater (GSW) formulation, which accounts for the variation of gravity with latitude and depth. The pressure in decibars is obtained from

$$p = -\frac{\rho_0 g(\phi, z) z}{10^4}, \tag{6.113}$$

where ρ_0 is a representative seawater density (approximately 1025 kg/m^3), $g(\phi, z)$ is the local gravitational acceleration (m/s^2) that depends on latitude ϕ and depth z, and the factor 10^4 converts pascals to decibars. Depth z is taken positive downward.

For the analyses necessary to evaluate the formation of dense water within the basin, an additional *threshold* was applied to the density field, imposing a minimum value of

$$\rho \geq 1029.2 \quad \mathrm{kg/m^3}$$

in order to isolate the densest water masses (Oddo and Guarnieri, 2011).

The binary mask associated with this filter is defined as:

$$M(x,y,z) = \begin{cases} 1 & \text{if } \rho(x,y,z) \geq 1029.2\,\mathrm{kg/m^3} \\ 0 & \text{otherwise} \end{cases} \tag{6.114}$$

where $M(x,y,z)$ identifies the dense water cells within the three-dimensional domain, allowing the isolation and analysis of the formation and distribution of such masses within the basin.

Once all valid grid points according to the density *threshold* were identified, the number of corresponding cells was calculated. This was then multiplied by the volume of each cell, equal to $1\,\mathrm{km} \times 1\,\mathrm{km} \times 2\,\mathrm{m}$, thus obtaining the total volume, which can be analyzed over time to study its temporal evolution. Once the location of the dense water mass was identified via the corresponding mask, it was reused to analyze the evolution of other variables within the same area, such as temperature anomalies, salinity, or the mean concentration of chemical species.

In association with the identification of the mass exceeding the threshold, the value of the *Potential Density Anomaly* σ_θ is quantified within the basin, defined as the difference between the potential density of a water mass and the reference value of 1000 kg/m^3:

$$\sigma_\theta(S,T) = \rho(S,T,p_{\mathrm{ref}}) - 1000, \tag{6.115}$$

where $\rho(S,T,p_{\mathrm{ref}})$ is the potential density calculated from salinity S and temperature T, reduced to a reference pressure $p_{\mathrm{ref}} = 0\,\mathrm{dbar}$. Once this PDA is quantified within the water mass near the seafloor, it can be related to further anomalies such as temperature or salinity anomalies.

To finally evaluate the outgoing movement of the *dense water mass* from the basin of analysis, a *Hovmöller diagram* is constructed. In this case, the diagram was used to analyze the fraction of dense water at the lower boundary of the domain, monitoring its horizontal distribution month by month. Starting from the two-dimensional density field $\rho(x,y)$, a reduced vertical spatial section of thickness 5 km is defined and extracted, located near the lower boundary; on this section, the vertical fraction of points that satisfy the condition of high density is calculated column by column. Formally, defining $N(x)$ as the total number of available vertical levels for column x, and $N_{\mathrm{dense}}(x)$ as the number of levels such that $\rho(x,y) \geq \rho_{\mathrm{thr}}$, the fraction is defined as:

$$f(x,t) = \frac{N_{\mathrm{dense}}(x,t)}{N(x)}. \tag{6.116}$$

This allows quantifying the vertical portion occupied by the dense water mass in the column corresponding to the horizontal coordinate x at time t.

The result is thus a two-dimensional matrix $f(x,t)$, where the temporal axis is discretized on a monthly basis and ordered chronologically, while the horizontal axis x follows the *longitudinal* domain of the analysis area. In this way, it is possible to analyze the signal associated with the *dense water mass* passing through the lower boundary of the basin.

6.10.2 Bottom Oxygen and other Bio-Geochemical Data

Applying the same methodology, it was possible to isolate and analyze the evolution of the simulated *Oxygen* values within the water mass. Alongside the general analysis of the variable and subsequent validation, an oxygen threshold O_{2o} was also set at approximately 30% of the range of observed values in the basin, corresponding to a concentration of 62.5 mmol/m^3:

$$A(x,y,z) = \begin{cases} 1 & \text{if } O_{2o} \leq 62.5\,\text{mmol/m}^3 \\ 0 & \text{otherwise} \end{cases} \tag{6.117}$$

where $A(x,y,z)$ identifies the cells in the domain that satisfy an *hypoxia/anoxia* condition to analyze the extent of these events within the simulation. The total number of such cells is then multiplied by the area (m^2) and the volume (m^3) of each cell, thus obtaining the total volume, which can be analyzed over time. This is also accompanied by the study of the evolution of the front of these *hypoxic* masses by using the section obtained using the transects illustrated in *Figure 6.14*.

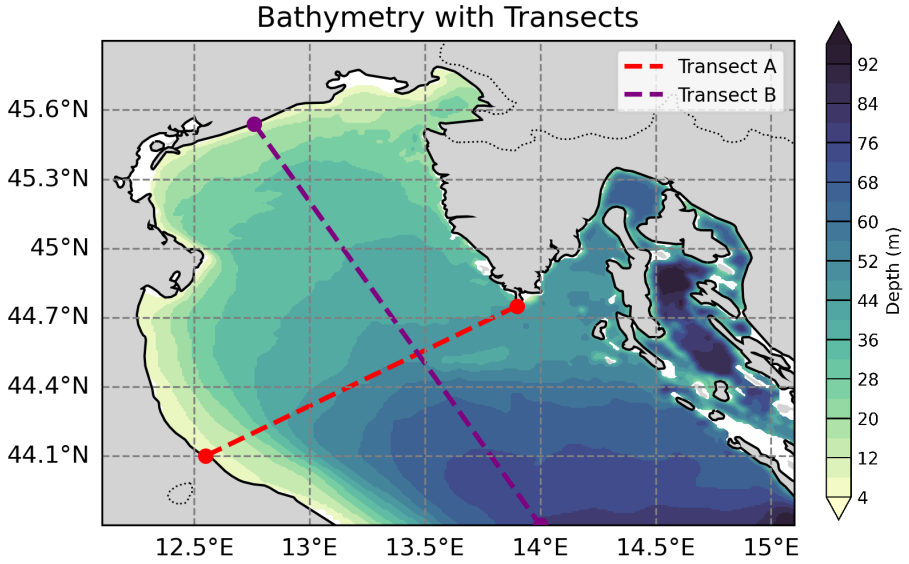

Figure 6.14: Location of the Transect A (red) and B (purple) within the basin used to create the oxygen sections.

In order to evaluate the evolution of stratification following the occurrence of *anoxia* conditions, a *stratification index SI* was introduced to define the intensity of stratification or mixing conditions within the column. This index is directly based on the *vertical density gradient* and therefore on the calculation of the *Brunt–Väisälä frequency*, a physical quantity describing the resistance of a water column to vertical disturbances (Dunić et al., 2018).

The procedure for estimating this index begins with the estimation of the potential density $\rho(z)$, obtained from the temperature T and salinity S fields along the water column according to the equation of state $EOS-80$ (2.5). Once the density field is constructed, its *vertical gradient* is estimated as:

$$\frac{\partial \rho}{\partial z}(z) \approx \frac{\rho(z+\Delta z)-\rho(z)}{\Delta z}, \tag{6.118}$$

where Δz represents the characteristic vertical thickness of the model layers, set to 2 m.

From this gradient, the *Brunt–Väisälä frequency* N^2 is defined as:

$$N^2(z) = \frac{g}{\rho_0}\frac{\partial \rho}{\partial z}(z), \tag{6.119}$$

where g is the *acceleration due to gravity* and ρ_0 is the reference density. This quantity provides a measure of static stability: positive values indicate that the stratification tends to resist vertical displacements, while values close to zero reflect neutral conditions or possible vertical mixing.

To obtain the stratification index, the vertical integration of N^2 values, weighted by depth, is considered up to a maximum depth H. The index SI at a given spatial position (x, y) and time t is then defined as:

$$SI(t,x,y) = \sum_{k=1}^{K(H)} N^2(t, z_k, x, y)\, z_k\, \Delta z, \tag{6.120}$$

where z_k represents the considered vertical levels, Δz the layer thickness, and $K(H)$ the number of layers within the maximum depth H.

The obtained value provides a scalar measure of columnar stratification, which is then spatially averaged to produce a monthly index representative of the entire basin:

$$\overline{SI}(t) = \frac{1}{A}\iint_{\Omega} SI(t,x,y)\, dA, \tag{6.121}$$

where Ω indicates the horizontal surface of the basin and A its total area.

In this way, the temporal trend of $\overline{SI}(t)$ allows evaluating the average intensity of stratification in the basin and following its evolution during and after critical events such as the formation of anoxic waters, providing a synthetic but physically consistent indicator of the vertical stability of the water column.

Chapter 7
Results and Discussion

The discussion of the results begins with a systematic comparison between numerical simulations and observations, both satellite-based and *in-situ*. This comparison made it possible to highlight the model's ability to reproduce the main variables characterizing the dynamics of the Northern Adriatic Basin, a basin well known for the complexity of its biogeophysical features and for the frequent occurrence of peculiar processes. The analysis primarily took the form of a series of validation exercises, aimed at assessing the model's accuracy in representing both the fundamental parameters and the phenomena emerging from their interactions.

In particular, the comparison allowed for the observation of the main processes within the basin, such as the formation of *dense water masses*, a crucial element for the ventilation of deep waters, the spatial distribution of the main *phytoplanktonic* groups at the surface and the establishment of recurrent *anoxic* conditions that significantly influence the ecological balance of the region.

7.1 Sea Surface Temperature

The first field examined for validation purposes was the simulated *Sea Surface Temperature* (SST), compared with the corresponding satellite observations obtained from the *level 3* (**L3s**) datasets provided by CMEMS through the product `SST_MED_PHY_L3S_MY_010_042` E.U. Copernicus Marine Service Information (CMEMS) (2024). Both datasets underwent the pre-processing procedures described in Chapter 5, in order to ensure data homogeneity and the reliability of the comparative analysis.

7.1.1 Timeseries and Outliers

The first step in the validation analysis of this field concerned the comparison of daily basin-scale time series (*Basin Averages*), obtained through the spatial averaging of values distributed across the entire study area. This procedure allowed the derivation of a single representative value of surface temperature for each day, thereby summarizing the information into an overall indicator of the system's variability. The procedure, detailed in Section 6.1, was applied uniformly to both the model and satellite datasets, ensuring the possibility of a direct and consistent comparison between the two data sources.

The results, shown in *Figure 7.1*, where the top panel shows the timeseries and the bottom shows the bias, highlight a general agreement between simulation and observation, both in terms of the model's ability to reproduce the *seasonal cycle* and the amplitude of seasonal variations. The most evident discrepancies appear at the extremes of the annual distribution, particularly during February–March and July–August, when the

amplitude of the modelled signal tends to exceed that observed in the satellite data. This results in a slight overestimation during the summer season and, conversely, an underestimation in the winter period, as reflected by the *mean bias* computed between the two datasets whose values range between $\sim \pm 2°C$ ($-2.309°C$ to $+2.155°C$ to be precise). This aspect, alongside the values of the peaks of such biases, will be further investigated in the following sections.

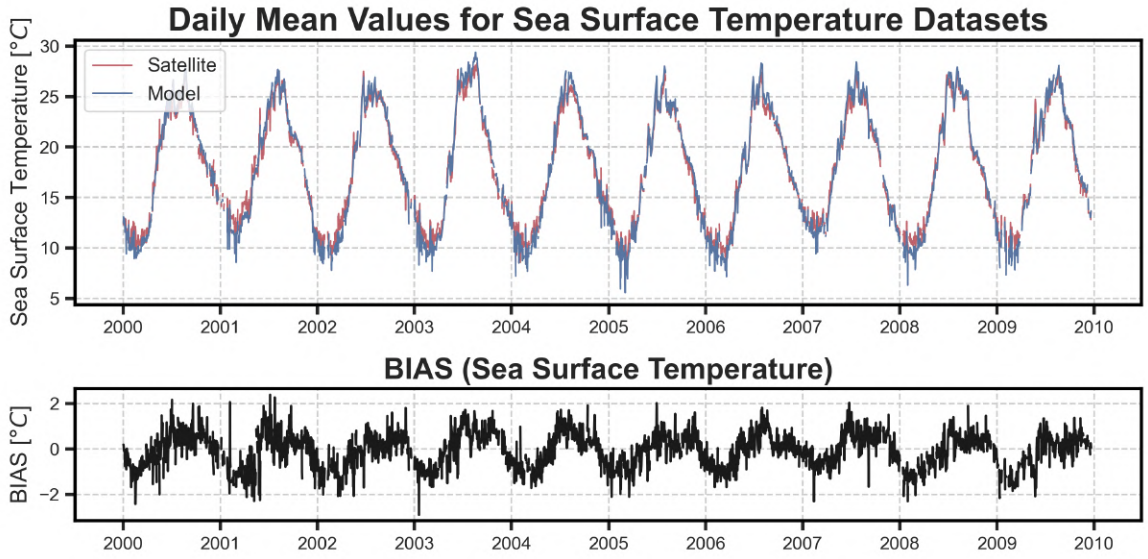

Figure 7.1: Time series of *Sea Surface Temperature* (SST). From top to bottom: *daily basin-mean* values, with the blue curve representing model data and the red curve satellite observations; and the corresponding *daily mean bias* between the two datasets.

A more detailed analysis of the values from the two datasets was conducted through a series of *boxplots*, derived from the *basin average timeseries*, as described in Section 6.1 which highlights the characteristic mean values of the two datasets the associated months with a higher number of *outliers*, thus providing further elements useful for comparative evaluation.

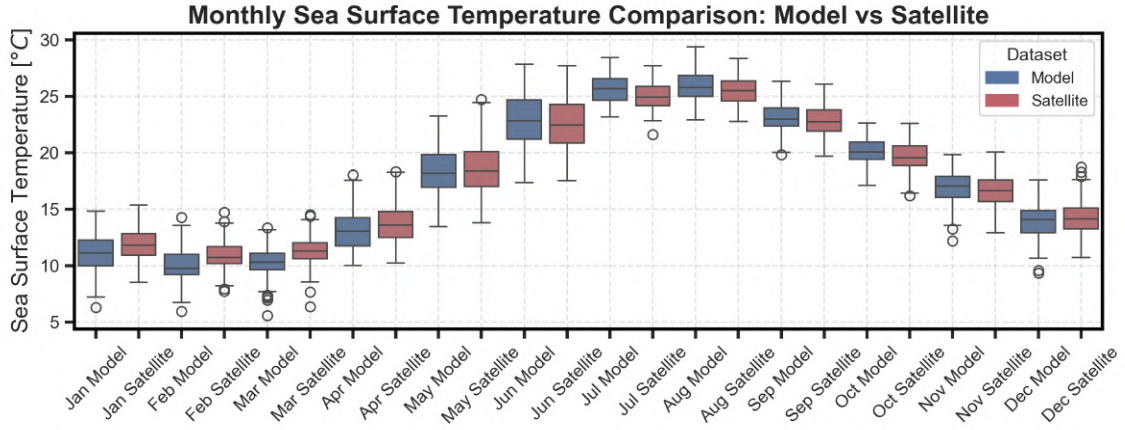

Figure 7.2: Boxplot of *Sea Surface Temperature* (SST). Model data are shown in blue and satellite data in red. Each box summarizes the distribution of monthly values: the rectangle represents the *Interquartile Range* (**IQR**), the horizontal line indicates the *median*, whiskers extend up to 1.5σ, and white dots mark the *outliers*.

The plot shown in *Figure 7.2* confirms, through the median trend, the tendency already observed: the model tends to overestimate the values during the summer months and underestimate them during the winter period. This aspect, too, will be revisited and examined in greater detail in the following analyses. The median and **IQR** (as explained within *Section 6.1*) values recorded for the months mentioned above are reported in *Table 7.1*.

Month	**Median**		**IQR**	
	Model	**Satellite**	**Model**	**Satellite**
February	9.743	10.729	1.766	1.467
March	10.303	11.289	1.444	1.413
July	25.669	24.923	1.928	1.711
August	25.778	25.489	1.846	1.779

Table 7.1: Median and interquartile range (IQR) values of temperature for February, March, July, and August, comparing model and satellite data.

The analysis of the *outliers* shows that, although their presence is more evident during the winter months, particularly between February and March, their overall number remains limited when compared to the total data points, highlighting how the mean value is the main driver of the differences between the two datasets. In the remaining months, *outliers* occur only sporadically and with reduced intensity. Moreover, the frequency and distribution of these anomalous values are comparable to those identified in the satellite dataset as reported in *Table 7.2*.

Month	**Model Outliers**	**Satellite Outliers**
February	2	4
March	6	5

Table 7.2: Number of outliers identified in temperature data for February and March, comparing model and satellite time series.

7.1.2 Seasonal Decomposition

To validate the model results and highlight possible discrepancies between the two datasets, a *seasonal decomposition* procedure based on an additive approach was applied. This method allowed the original signals to be decomposed into three main components: the *trend*, obtained through a linear fit; the *seasonal* component, calculated using a centered 30-day centered moving average; and finally, the residuals. This procedure, described in more detail in Section 6.3, enabled a more targeted analysis of the structural differences between the two datasets.

The results, graphically represented in *Figure 7.3*, confirm good agreement between the two datasets. As also shown by the values reported in *Table 7.3*, there is an almost perfect correspondence in both the linear *trend* and the amplitude of the seasonal and residual components, although this second element records an absolute difference of $\sim 1.5°C$.

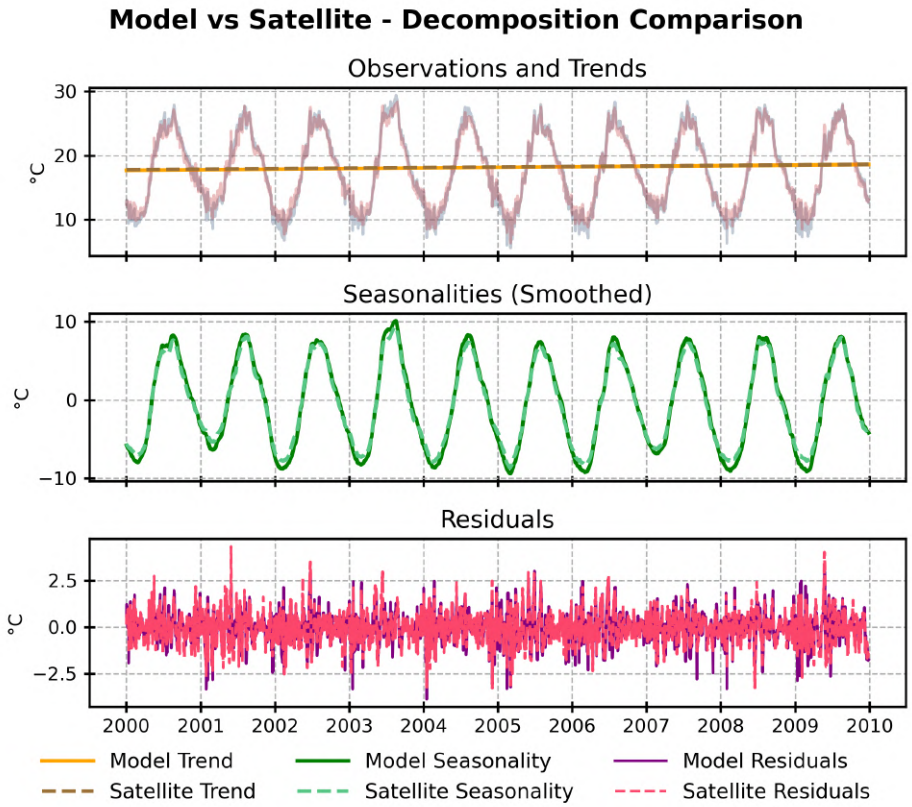

Figure 7.3: *Seasonal Decomposition* results obtained with the *additive method* using model data (solid lines) and satellite data (dashed lines). From top to bottom: the first panel shows the raw data (blue for model, red for satellite) with the trend estimated by linear fit; the second shows the seasonal component derived from a centered moving average; the third displays the residuals.

Series	**Trend** ($°C/yr$)	**Seasonality** ($°C$)	**Residuals** ($°C$)
`Model`	+0.091	16.508	1.866
`Satellite`	+0.081	15.035	1.776

Table 7.3: Table of values obtained from the *seasonal decomposition* of the *Sea Surface Temperature* field. Reported are the amplitudes of the linear component ($°C/yr$), the seasonal component, and the residuals, each accompanied by its respective standard deviation.

7.1.3 Scatterplots

A further validation step involved creating scatterplots of monthly values, color-coded by season, to compare regression lines with the *ideal fit* and identify discrepancies between datasets. Two types of scatterplots were generated: the first, shown in *Figure 7.4*, displays *basin-scale* monthly averages in a single plot; the second, in *Figure 7.5 a)-d)*, presents separate plots for each season, allowing a more detailed examination of model–observation relationships.

Two regression methods were applied: the *Huber* regression, robust to outliers, and the *LOWESS* (*Locally Weighted Scatterplot Smoothing*) regression, which captures local nonlinearities. Further details are provided in Section 6.2.

The analysis confirms a good agreement between model and satellite data. As shown in *Figure 7.4*, the slopes from both *Huber* and *LOWESS* regressions closely match the *ideal fit* line. The differences found within these results align with previous findings: minimum values tend to be slightly underestimated by the model, while maximum values show a mild overestimation.

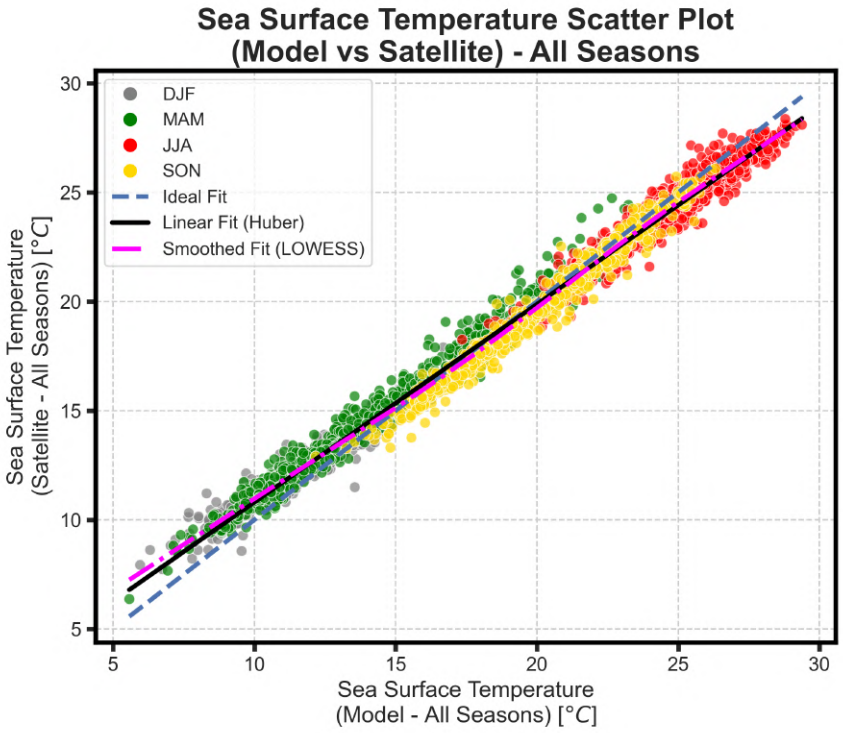

Figure 7.4: Scatterplot of *Sea Surface Temperature* (SST) by season: gray for **DJF** (winter), green for **MAM** (spring), red for **JJA** (summer), and yellow for **SON** (fall). The plot shows three reference lines: the *Ideal Fit* $y = x$ (blue dashed), the *Huber* regression (black), and the *LOWESS* regression (pink).

The decomposition into four scatterplots, one for each season, allows for further analysis of the model's behaviour. As shown in the plots presented in *Figure 7.5 a)-d)*, during winter the model's underestimation concerns all values below 15°C, while above this threshold, the *LOWESS* curve aligns with the *best fit* line. A similar behavior is observed in spring, although the deviation of the *LOWESS* curve occurs at higher values, around 17.5°C. These results suggest that, despite an overall tendency of the model to underestimate satellite data during the winter and spring seasons, the simulated extreme values of *Sea Surface Temperature* show a closer agreement with satellite observations.

During summer, an opposite behavior is observed: the *LOWESS* curve aligns more closely with the markers corresponding to the lower values, which represent the less populated region of the dataset. Conversely, for higher values, starting around 20°C and becoming particularly evident above 24°C, the overestimation phenomenon already identified in previous analyses becomes more apparent. Finally, the fall season shows regression curves with a slope overall more consistent with the *best fit* line, although a systematic bias persists, suggesting a slight discrepancy between the model and the observational data.

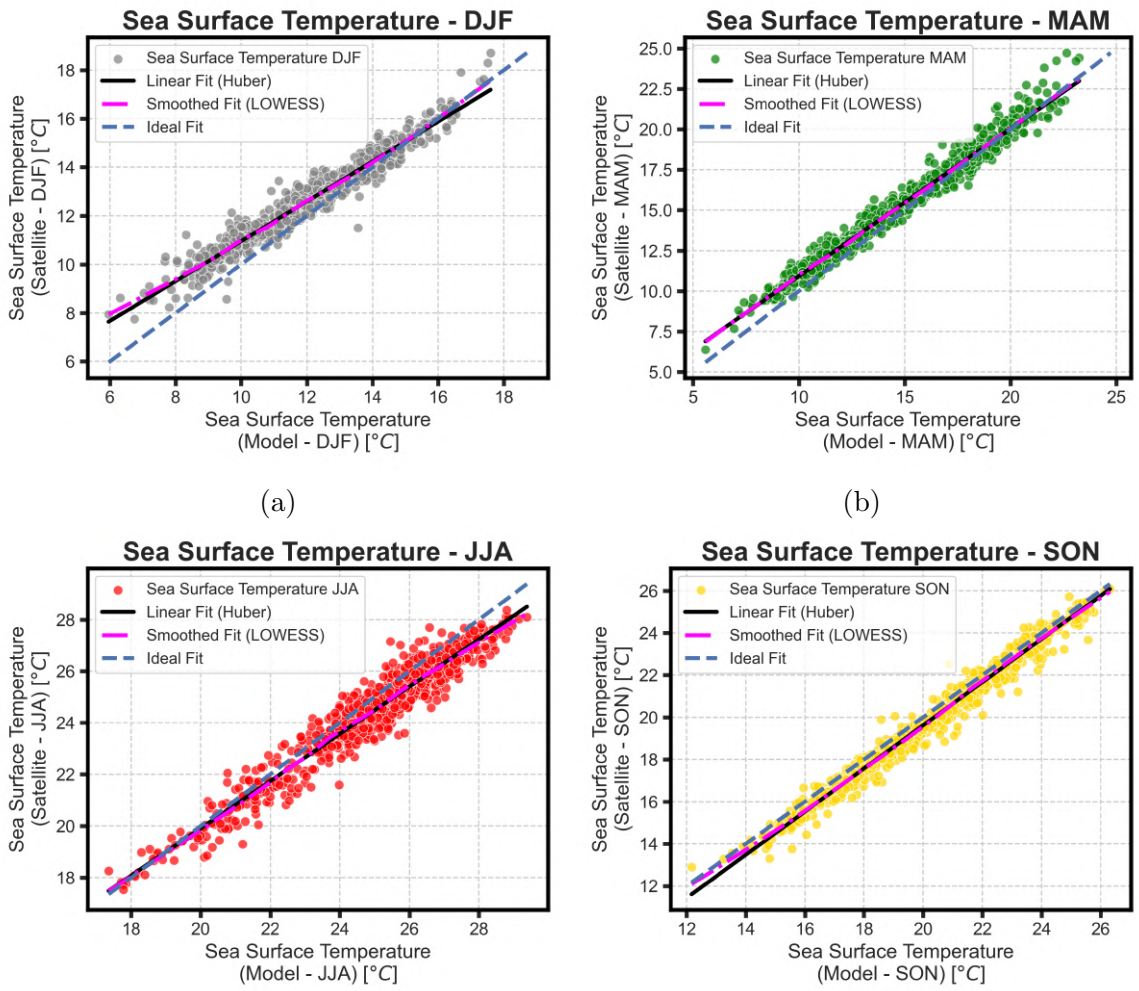

Figure 7.5: Collection of *Sea Surface Temperature* (SST) scatterplots by season: a) **DJF** (winter), b) **MAM** (spring), c) **JJA** (summer), and d) **SON** (fall). Each plot shows the *ideal fit* (blue dashed), the *Huber* regression (black), and the *LOWESS* regression (pink).

The slope and intercept values of the regression lines and curves are reported in *Table 7.4*. To ensure comparability of the results, the nonlinear regressions have been approximated by a straight line.

Series	**Huber**		**Lowess**	
	Slope	**Intercept** ($°C$)	**Slope**	**Intercept** ($°C$)
All	0.9069	7.1083	0.9073	7.0911
DJF	0.8210	12.5710	0.8221	12.5605
MAM	0.9112	12.7775	0.9099	12.7901
JJA	0.9156	22.2357	0.9141	22.2782
SON	1.0230	23.7387	1.0226	23.7559

Table 7.4: Slope and intercept values obtained from the robust (*Huber*) and smoothed (*Lowess*) fits on the seasonal and overall scatterplots of the *Sea Surface Temperature* field.

7.1.4 Efficiency Results

To quantify the degree of correlation between the simulated data and the satellite observations, a series of efficiency indices were calculated following two approaches: on a monthly basis, in order to obtain a characteristic value representative of each month, and on an *overall* value, relative to the entire simulation period. The choice to use monthly values allows summarizing the typical behavior of the model for each period of the year into a single indicator, avoiding direct comparisons between individual instances (monthly or annual) that could be influenced by interannual variability not strictly related to model performance, such as the spatial distribution of the data. The *overall* value, instead, provides a global measure of the model's ability to reproduce the observed conditions throughout the entire considered time interval.

Coefficient of Determination (R^2)

The results of the coefficient of determination, and its weighted version, are shown in *Figure 7.45b a) and b).*

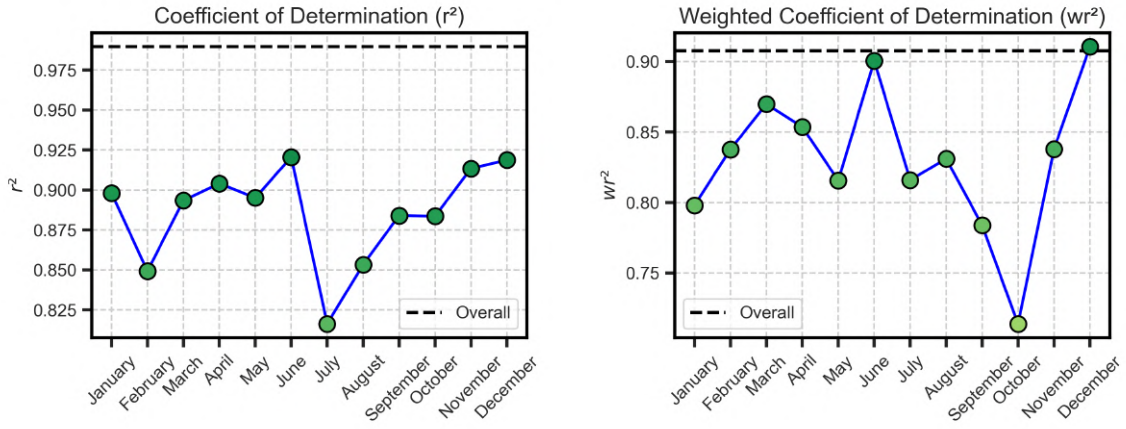

(a) (b)

Figure 7.6: Monthly results of the Coefficient of Determination calculated from Sea Surface Temperature (SST) data: a) classic version R^2, b) weighted version wr^2. Each circular marker indicates the global value for the month, with a color coding reflecting proximity to the ideal value (green = 1, red = 0). The dashed black line represents the overall simulation value.

The monthly trend generally shows high values for both metrics, indicating good agreement between simulated and observed data, though notable discrepancies appear in some months.

In the *Coefficient of Determination* (R^2) graph, February, July, and August record the lowest values, confirming the patterns already highlighted in previous sections, where these periods show the largest model–observation differences. Overall, however, the values remain clearly positive, indicating the model's solid ability to reproduce observations. In the *weighted* version, both individual and overall values slightly decrease yet remain positive. Some months show larger variations, with relative improvements or deteriorations, though the indices stay generally high.

The most notable case is October, where the weighted version shows a marked drop compared to the classic coefficient. This suggests that major model–observation devi-

ations occur in cells or conditions with higher weights, meaning performance degradation is localized in key areas. Conversely, June, November, and December show strong agreement between r^2 and wr^2, indicating robust consistency across the domain, with errors not concentrated in the most relevant cells. March and April, instead, show a slight increase in wr^2 over r^2, implying greater model accuracy in high-weight observations; in other words, outliers degrading the unweighted coefficient lie mostly in less relevant areas, reducing their effect on the index.

Nash-Sutcliffe Efficiency (NSE)

Subsequently, the same analytical approach was applied to an additional performance indicator, the *Nash-Sutcliffe Efficiency* (NSE), with the results of this analysis presented in *Figure 7.7 a)-d)*.

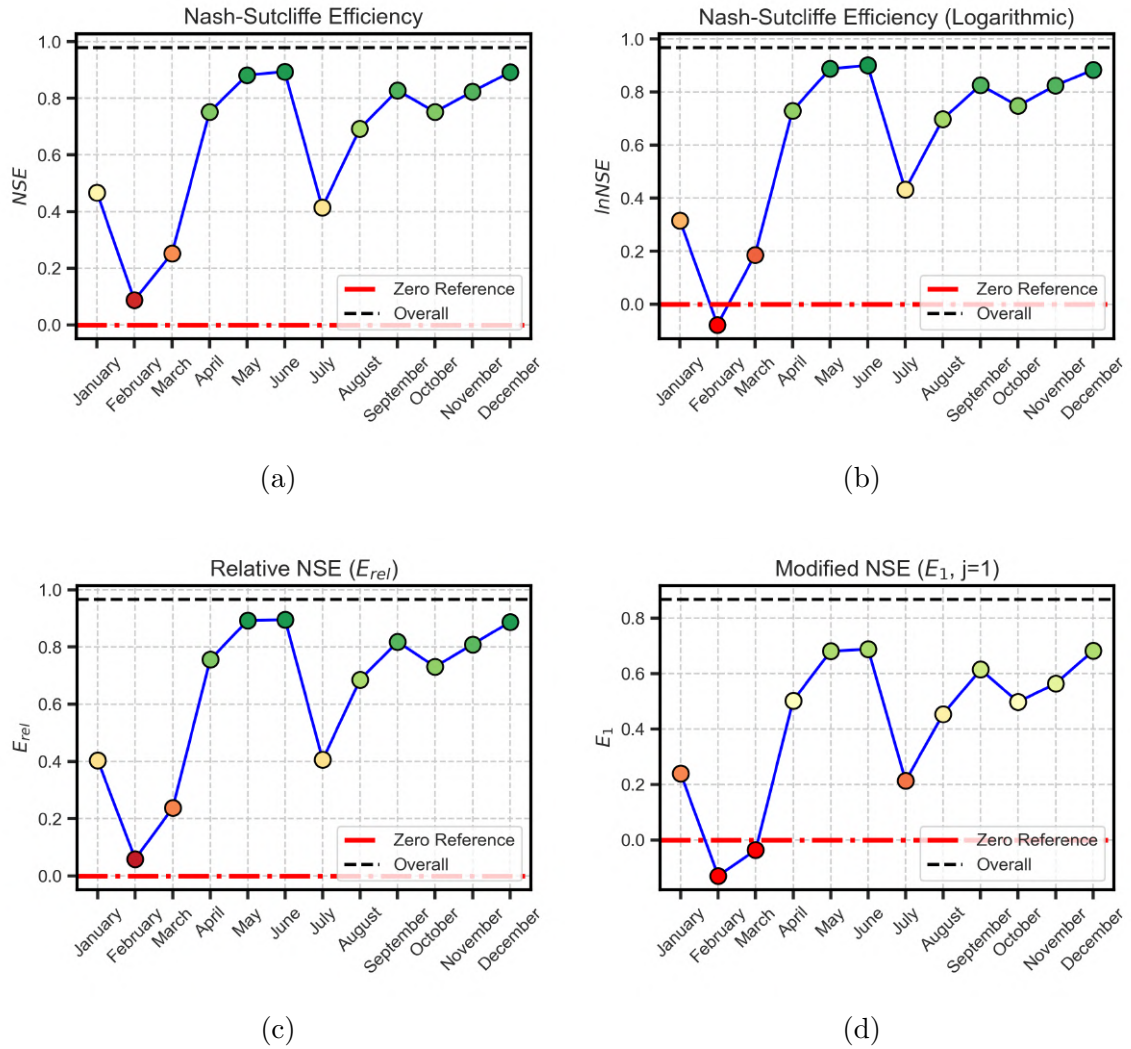

Figure 7.7: Monthly *Nash–Sutcliffe Efficiency* results from *Sea Surface Temperature* (SST) data: a) classic, b) logarithmic, c) relative, and d) modified versions. Each circular marker represents the monthly global value, color-coded by proximity to the ideal (green = 1, red = 0). The dashed black line shows the overall simulation value, while the red line marks the performance threshold: markers below it indicate cases where climatological averages outperform the simulation.

The analysis based on the NSE index further confirms the trends observed previously, clearly highlighting that the months of February–March and July are characterised

by the lowest values of the index. This pattern is consistent with the discrepancies between observed and simulated data already discussed in the preceding sections.

In particular, the analysis reveals that in both the logarithmic version (NSE_{log}) and the modified version (E_1) of the index, February and March (specifically in the case of E_1) exhibit values below the efficiency threshold of 0.0. As discussed in Section 6.4.2, whenever a marker falls below this limit, substituting it with climatological mean values produces results that are superior to those obtained through the simulation. In contrast, in the classic version and the relative version (NSE_{rel}) of the index, the markers for these same months exceed the efficiency threshold. Nevertheless, the values remain relatively low, confirming the critical issues that have already been highlighted for these specific periods of the year and pointing to recurring seasonal limitations in the model performance.

Index of Agreement (d)

Finally, the same analyses were extended to the *Index of Agreement* (d), with results shown in *Figure 7.8 a)-c)*.

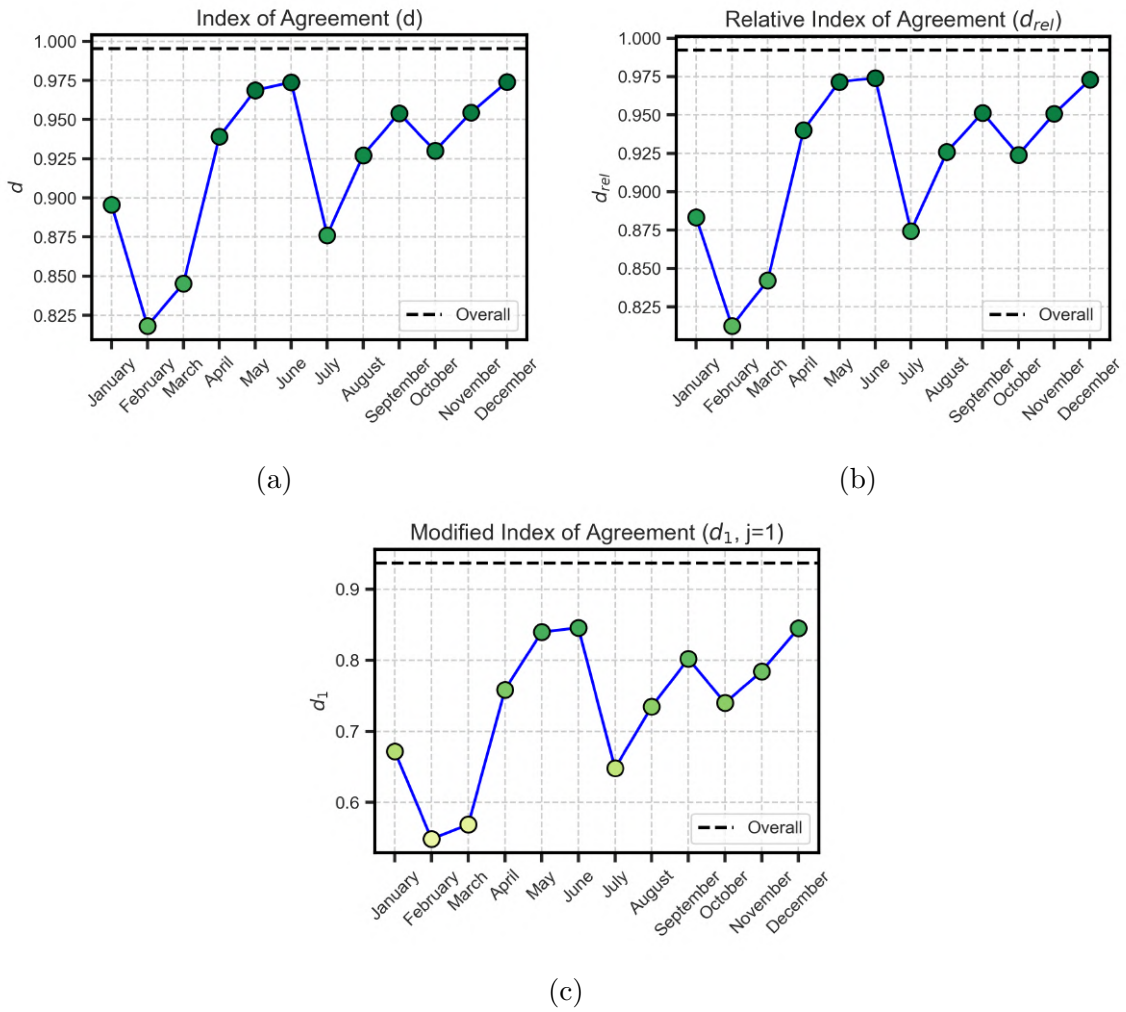

Figure 7.8: Monthly results of the Index of Agreement calculated from Sea Surface Temperature (SST) data: a) classic version, b) relative version, and c) modified version. Each circular marker represents the global value for the month, with a color code reflecting proximity to the ideal value (green = 1, red = 0). The dashed black line represents the overall simulation value.

The results of the *Index of Agreement*, considered across all its different versions (classic, relative, and modified), reveal a similar pattern of agreement between the observed and simulated data. In all cases, the graphs consistently report positive values for both the individual markers and the *overall* index value, indicating generally satisfactory model performance. February, March, and July stand out as the months exhibiting the lowest values of the index, corresponding to periods in which critical discrepancies were identified in the previous analyses, thereby highlighting the particular challenges of simulating observed conditions during these months. Notably, the shape of the resulting markers closely resembles that obtained with the Nash–Sutcliffe efficiency, likely because both metrics are sensitive to the magnitude and timing of deviations between observed and simulated values, emphasizing periods with larger model–observation differences.

7.1.5 Error Components and Spatial Efficiency

As the temporal validation of the model has been performed the analysis now shifts its focus on evaluating the spatial efficiency. This is done via an analysis of the spatial distribution of the error components described in section 6.5.

Similarly to the approach used for the efficiency indices, the analysis involves constructing a map that represents the spatial pattern of the model behaviour. Subsequently, this map is decomposed on a monthly basis to obtain maps of monthly averages, in order to highlight the intra-annual variations of the main signals. Unlike the previous analyses, annual maps are also produced, which are useful for assessing the inter-annual variations of the model.

Mean Bias

The first result presented concerns the spatial distribution of the mean bias, which is shown in *Figure 7.9*.

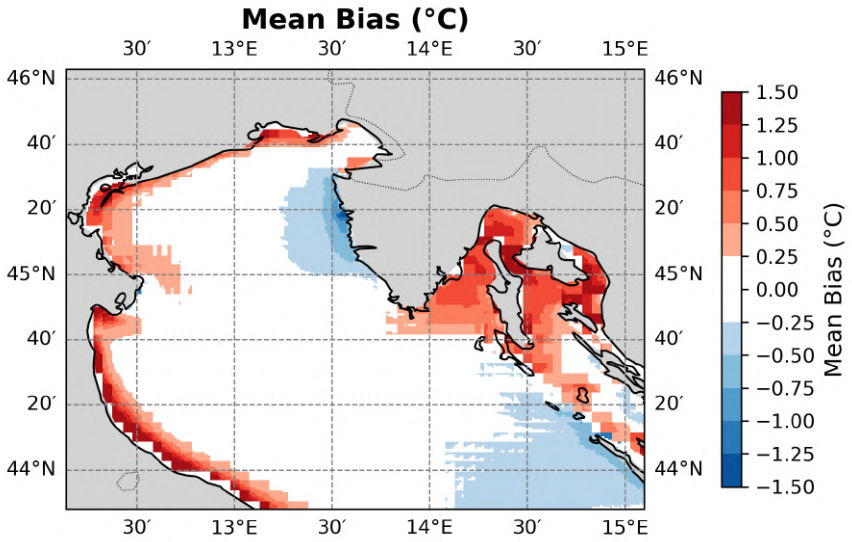

Figure 7.9: Map of the *Mean Bias* of the model with respect to the observed data for the *Sea Surface Temperature* field over the entire simulation period. Values within the range of ±0.25 are shown in white, in order to exclude marginal signals.

The analysis of the spatial distribution of the mean bias shows that most of the open basin exhibits negligible values, represented in white. The most significant positive signals are concentrated in two main areas: along the northern and western coasts of the basin, as well as in the Kvarner Bay. In contrast, negative biases appear in the southeastern portion of the basin, with a particularly pronounced signal at the outlet of the Mirna Bay, alongside the Istrian coast.

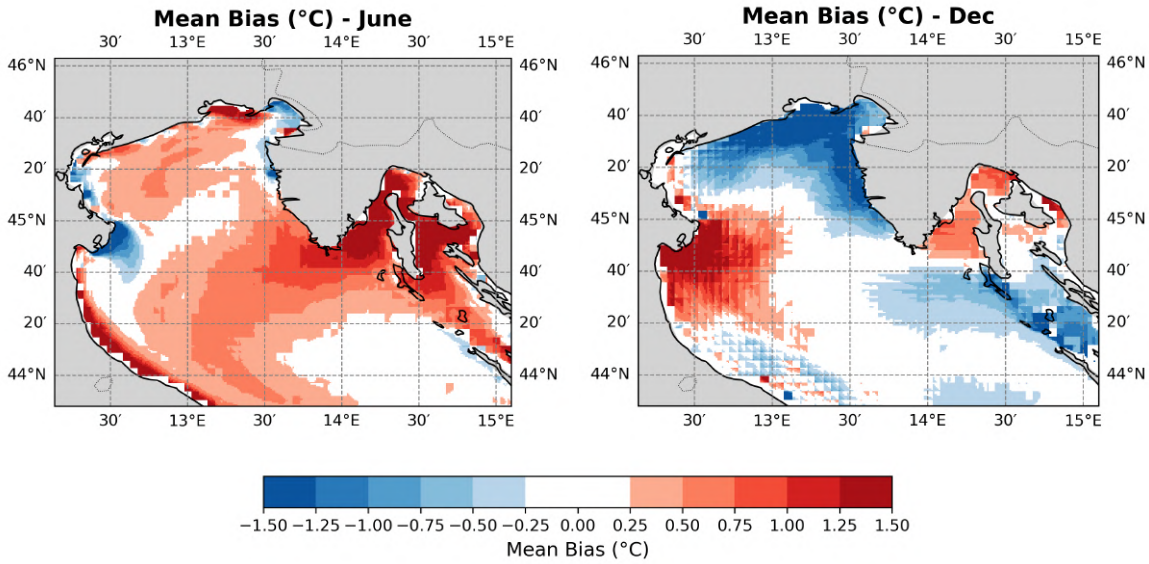

Figure 7.10: Comparison of the *mean bias* maps relative to the months of June (left) and December (right) of the Sea Surface Temperature field. Values within the range of ±0.25 are shown in white, in order to exclude marginal signals.

The monthly maps confirm the reappearance of the biases highlighted in the previous sections, reinforcing the patterns identified earlier in the analysis. However, a particular feature related to the effect of the Po River emerges, not evident in the overall map shown in *Figure 7.9*. In the transitional months preceding the bias peaks, as exemplified for June and December in *Figure 7.10*, it is observed that the signal associated with the Po River exhibits a bias of opposite sign compared to that recorded in the rest of the basin, suggesting the presence of a distinct seasonal dynamic in the influence of the Po River between the two datasets.

The analysis of the annual maps, not shown here, highlights a slight variability in the sign of the bias over the course of the year. This variability, while detectable, remains limited in magnitude and does not substantially alter the general pattern observed. Overall, the bias values at these temporal scales are relatively small, indicating that the model maintains a consistent level of accuracy when considered on an annual basis.

Standard Deviation Error

The overall result of the spatial performance, evaluated using the standard deviation error measure, is shown in *Figure 7.11*.

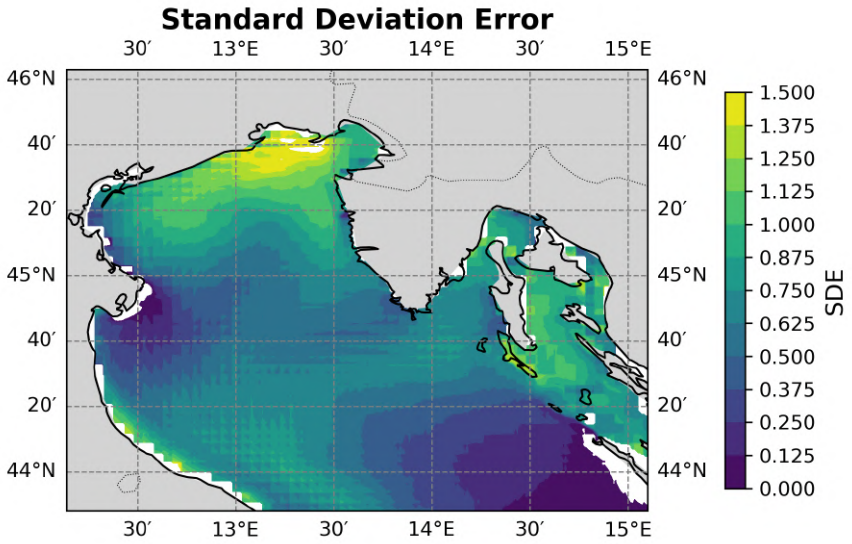

Figure 7.11: Map of the *Standard Deviation Error* of the model with respect to the observed data for the *Sea Surface Temperature* field over the entire simulation period.

Overall, the *standard deviation error* is higher along the northern coast and at the outlet of the Marano Lagoon, indicating greater variability in model performance. Positive signals also appear along the western coast, particularly near Kvarner Bay, suggesting localized regions of increased deviation. For this error component, the Po River influence is negligible due to the compensation of opposite signs in the *standard deviation* of the two datasets. Analysis of monthly and annual maps (not shown) likewise confirms the absence of significant intra- or interannual variability in the spatial distribution of the standard deviation error.

Cross-correlation

The results of the cross-correlation are shown in *Figure 7.12*.

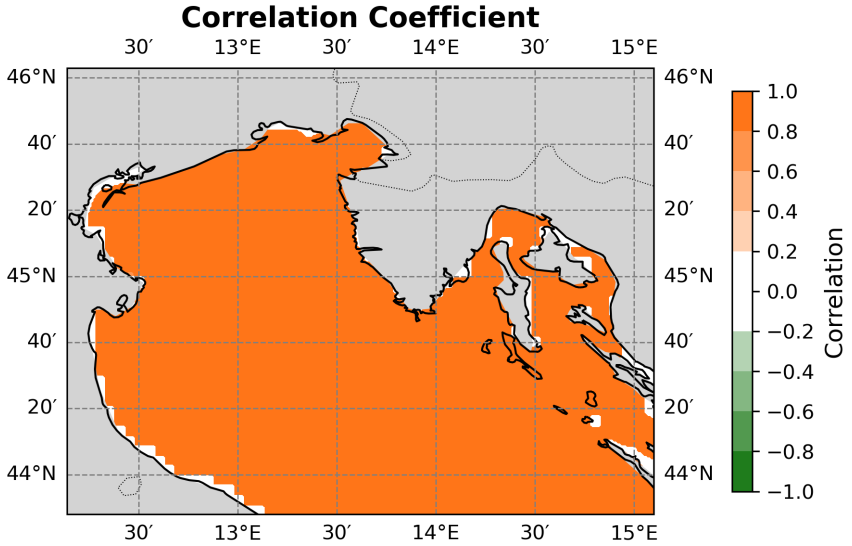

Figure 7.12: Map of the *Cross Correlation* of the model with respect to the observed data for the *Sea Surface Temperature*. Values within the range of ±0.2 are shown in white.

The general cross-correlation map shows near-perfect values throughout the basin,

confirming high spatial coherence between the datasets. This strong correspondence is supported by the monthly and annual maps (not shown), which display no significant deviations from the overall pattern.

Unbiased RMSE

Finally, the results of the unbiased RMSE are shown in *Figure 7.13*.

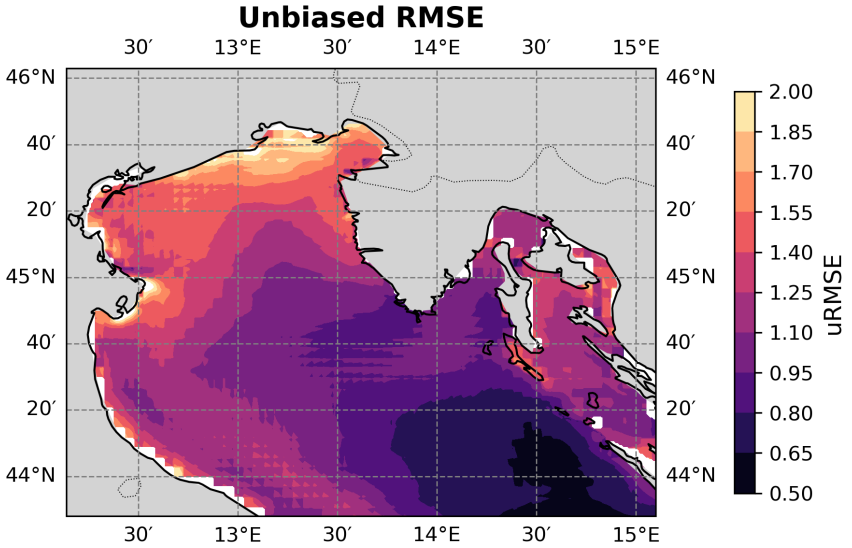

Figure 7.13: Map of the *Unbiased RMSE* of the model with respect to the observed data for the *Sea Surface Temperature* field over the entire simulation period.

The unbiased RMSE largely mirrors the standard deviation error, showing high values at the outlet of the Marano Lagoon and a weaker positive signal in Kvarner Bay. A positive signal also appears near the Po River delta, more evident in the monthly components, particularly in December and June, as shown in *Figure 7.14*.

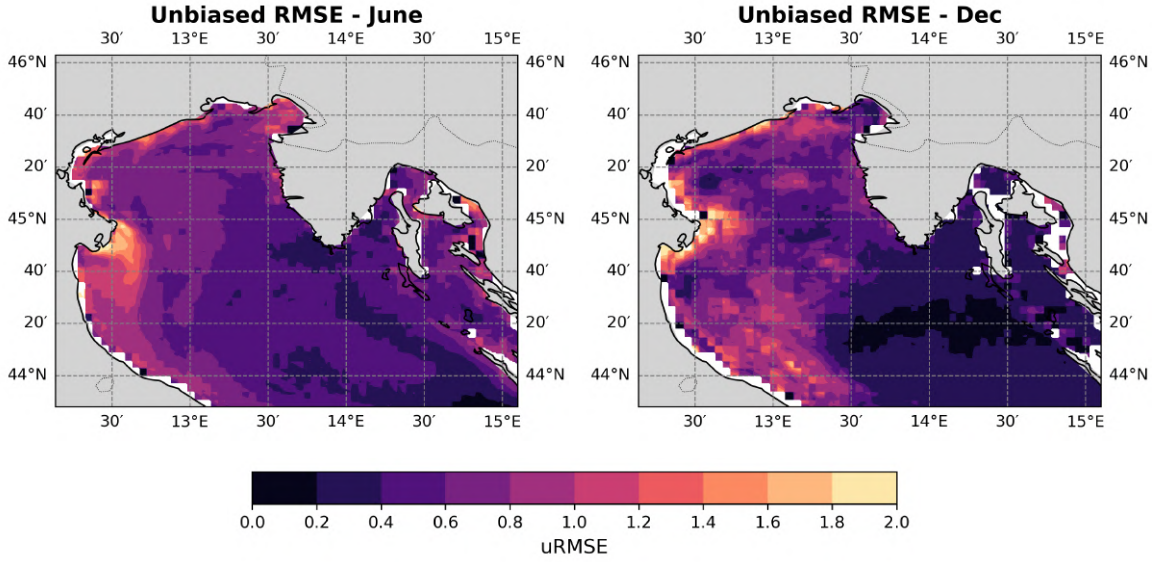

Figure 7.14: Comparison of the *unbiased RMSE* maps relative to the months of June (left) and December (right) of the Sea Surface Temperature field.

The annual analysis highlights a slight interannual variability of this signal, with a particularly marked peak in the year 2002, as shown in the corresponding map in *Figure 7.15*. This trend suggests that, while maintaining a certain consistency over time, the magnitude of the error in the area of the Po River delta may be influenced by oceanographic and seasonal conditions that vary from year to year.

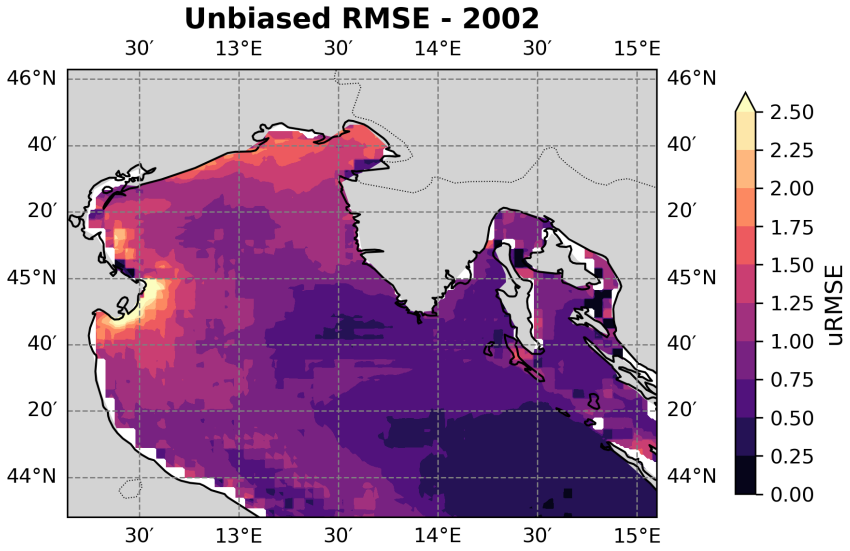

Figure 7.15: Map of the *Unbiased RMSE* of the model with respect to the observed data for the *Sea Surface Temperature* field for the year 2002.

7.1.6 Target Plots

To comprehensively evaluate the model's performance, a series of summary plots were produced to represent both the performance trends across individual years and months, allowing for a more detailed and structured analysis of the model's behavior over time.

The first group of proposed graphs consists of target plots, in which the statistics were appropriately normalized to enable a direct and consistent comparison between different temporal instances. The results of this analysis are shown in *Figure 7.16 a) and b)*.

By first examining the annual performance, it is evident that the recorded values are overall quite small, indicating a good ability of the model to reproduce the mean annual behavior of the system. This finding is consistent with what was previously observed through the efficiency indices, whose overall values were high, confirming the robustness of the model on an extended temporal scale.

Particularly interesting is the behavior of the *Bias*, whose annual mean value appears to be nearly zero. However, this result must be interpreted with caution: as shown in previous analyses (see *Figure 7.1*), significant seasonal biases are present, both positive and negative. The mean value close to zero therefore results from the compensation between these opposing patterns, a phenomenon clearly visible also in the markers of individual months represented in the monthly *target plot* in *Figure 7.16 b)*.

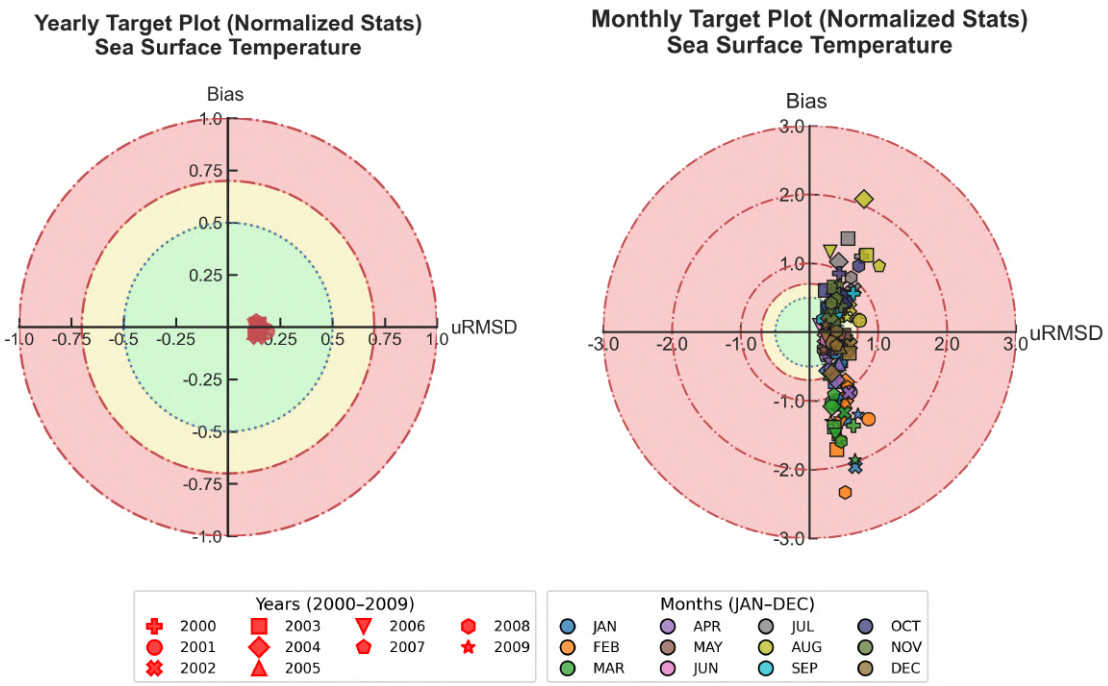

Figure 7.16: Target plots of the Sea Surface Temperature (SST): a) annual performance of the simulation, b) monthly performance. The values were normalized to allow comparison between different months. Each area is associated with a color indicating performance, with regions closer to the origin of the plot corresponding to better performance.

Examining the monthly *target plot*, it is evident that while the normalized unbiased RMSE ($uRMSD'$) generally remains within the $\sim$ 1.0 threshold across all months, indicating a consistently acceptable overall model performance, the bias exhibits a much larger spread and a pronounced seasonal pattern. February (orange marker) and March (green) show particularly strong negative biases, sometimes exceeding $\sim$ 2.0, whereas summer months, like July (gray) and August (yellow), display positive biases of comparable magnitude. This cyclic behaviour highlights that, despite the model maintaining low overall error, systematic over- or underestimation varies seasonally, reflecting the challenges in capturing specific month-to-month dynamics.

7.1.7 Taylor Diagrams

As an additional tool for the evaluation and comparison of model performance, the results of the *Taylor diagrams* are presented here and shown in *Figure 7.17 a) and b)*. In this case as well, the statistics have been normalized to allow for a direct and consistent comparison among the different temporal instances analyzed.

The analysis of annual performance highlights extremely high correlation values, with most markers positioned within the 99th percentile, and generally low RMSD values. A particularly noteworthy aspect concerns the standard deviation, which is almost always higher than that of the reference, obtained using satellite data only and representing a perfectly coincident performance with the observed data. This phenomenon can once again be attributed to the presence of previously identified biases, which induce a slightly larger amplitude in the simulated seasonal cycle compared to the observed counterpart, thereby increasing the standard deviation.

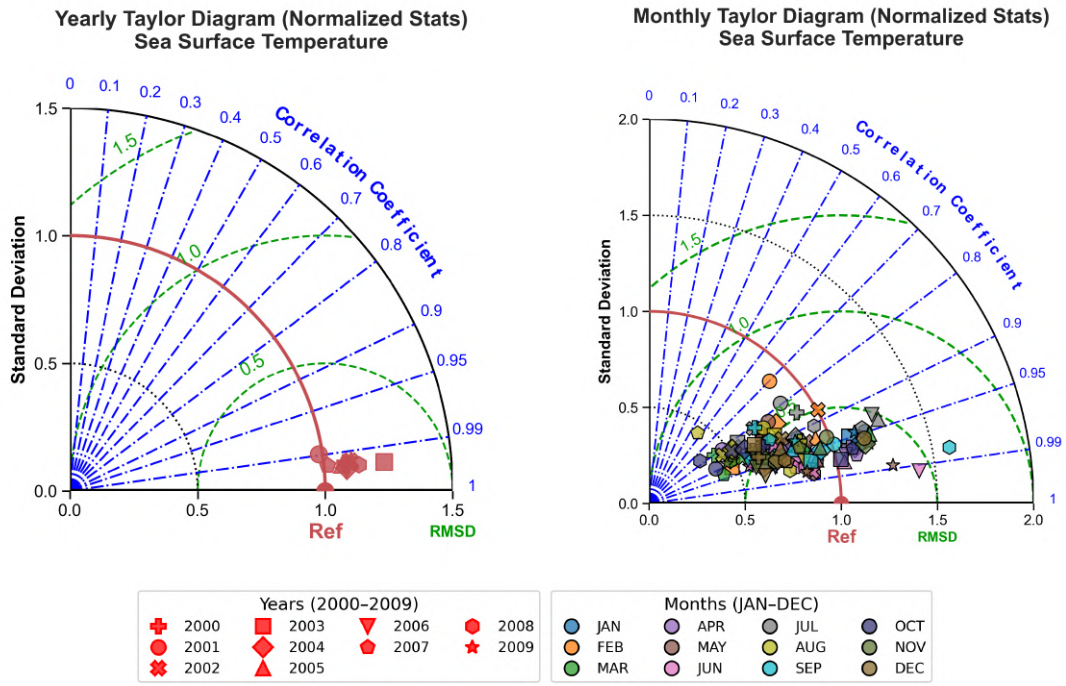

Figure 7.17: Taylor diagrams of the Sea Surface Temperature (SST): a) annual performance of the simulation, b) monthly performance. The values have been normalized to allow comparison between different months. The performance of each instance is defined based on the distance of the marker from the reference value, indicated by the red-colored **Ref** marker.

In the case of monthly performance, an opposite trend is observed: the cloud of markers tends to position itself at lower values, ranging between approximately 0.5 and 1.0. However, there are instances that exceed this range, particularly above the reference value. This aspect causes some markers to surpass the RMSD = 0.5 threshold, indicating a slight decrease in monthly performance. On the correlation front, however, almost all markers exhibit values equal to or greater than 0.8, confirming the model's strong ability to represent the temporal variability of SST.

7.1.8 Spectral Analysis

As an additional method to investigate discrepancies between simulated and observed data, a series of power spectra were calculated and compared. The resulting *power spectra* are shown in *Figure 7.18*.

Similar to the analyses conducted in previous sections, the *power spectra* show substantial consistency between simulated and observed data, indicating a high degree of agreement between the model and our reference. In particular, the main power peak is associated with periods between approximately 300 and 365 days, consistent with the accurate reproduction of the *seasonal cycle*. Peaks in intensity also occur around periods of 170–180 days and 80–90 days that end up being in phase and with equal power. Finally, elevated power values are also visible for longer periods ($>\sim$ 2.5 *years*), attributable to interannual variability in the basin; however, these aspects were not explored further in this study.

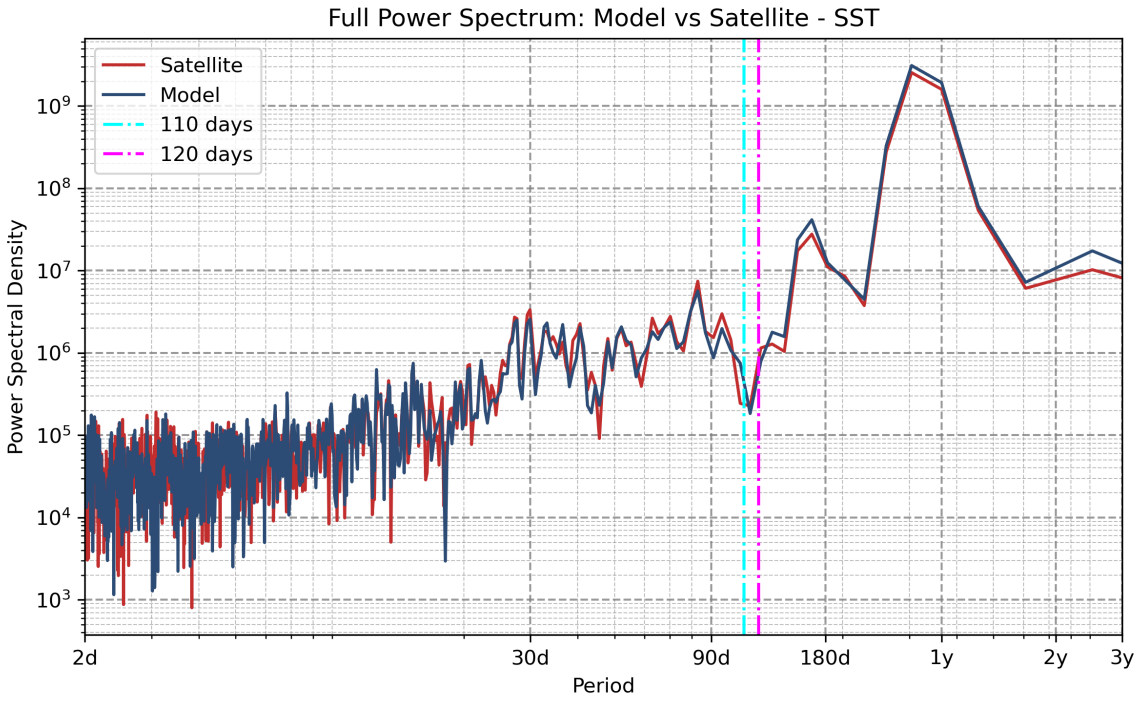

Figure 7.18: Power spectra of *Sea Surface Temperature* (SST) from model (blue) and satellite (red) data, shown on a double-logarithmic Power–Period scale (period in days). The vertical dashed lines in magenta and cyan mark periods of 108 and 114 days, highlighted for detailed analysis in the spectral decomposition and wavelet sections.

Despite the overall agreement, some differences emerge at periods of approximately $\sim$ 43, $\sim$ 45, and $\sim$ 59 days. While linked to less significant phenomena, these discrepancies are visible in the spectral analysis, as such they'll be studied further in a later analysis. At the $\sim$ 43-day period, coherence drops in the observed spectrum, a feature not seen in the simulated data; similar patterns appear at $\sim$ 45 and $\sim$ 59 days. A zoom of he power spectrum around these periods is shown in *Figure 7.19*.

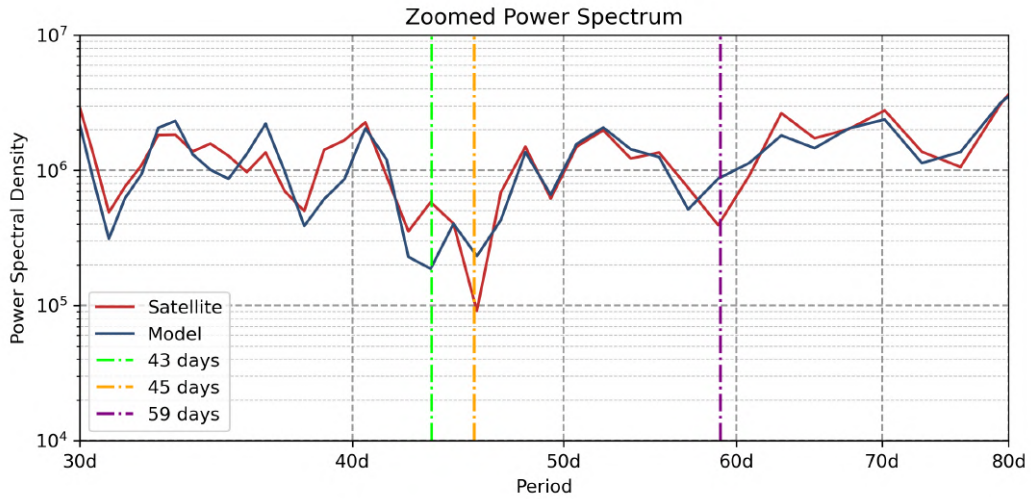

Figure 7.19: Zoom of *Sea Surface Temperature* (SST) power spectra in the 30–80 day range. Model spectra are shown in blue, satellite spectra in red, with highlighted periods of coherence reduction at 43 days (lime), 45 days (orange), and 59 days (pink).

More pronounced discrepancies are instead observed at periods of approximately $\sim$ 110 and $\sim$ 120 days. Among these, the feature at $\sim$ 110 days is particularly noteworthy: although it appears only marginally evident in the overall *power spectra*, it stands out as a potentially significant component of the system's variability. For this reason, it will be the focus of a dedicated analysis, with special attention given to the corresponding *phase* and *coherence* values identified within these temporal windows.

In *Figure 7.20 a) and b)* the power spectra filtered according to the *Butterworth* filters described in section 6.8.1 are presented. Unfortunately, the analysis of these filtered spectra does not highlight new phenomena.

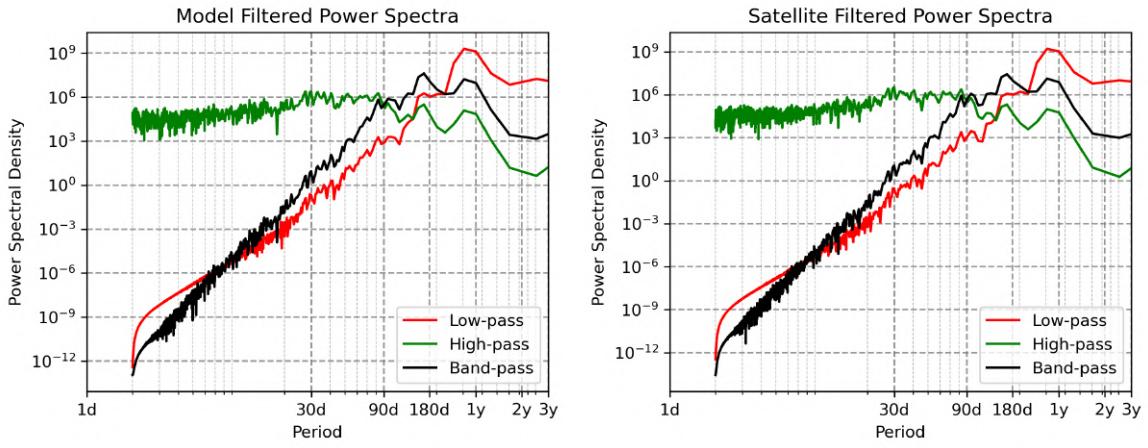

(a) (b)

Figure 7.20: Power spectra of Sea Surface Temperature data filtered using *Butterworth* filters: a) model data, b) satellite data. Three types of filters were applied: *low-pass* (225 days), *band-pass* (90–225 days), and *high-pass* (90 days).

As a further extension of the spectral analysis related to *Sea Surface Temperature* (SST), a detailed decomposition of the *power spectra* into their main constituent components, namely *gain*, *phase*, *coherence*, and *cross-spectral density magnitude*, was performed. This approach allows for a more thorough characterisation of the relationships between observed and simulated SST variability across different temporal scales. The detailed results of this decomposition are presented and illustrated in *Figure 7.21*.

The analysis of the *phase* and *coherence* components reveals slight but notable decreases in coherence at periods around 43, 45 and 59 days, corresponding directly to the discrepancies already identified in the *power spectra* and clearly visible in *Figure 7.18*. These decreases suggest specific temporal ranges in which the agreement between observed and simulated datasets is reduced, indicating areas for further examination. The main drop in *coherence* however can be seen at a period of $\sim$ 110 *days* with values dropping as low as $\sim$ 0.35. Notably this major drop in coherence is accompanied by a *phase* of ~ -5 *days*, the 2nd lowest recorded *phase* of the whole spectra. To ensure the validity of this observed *coherence* drop and to better understand its impact on the basin, this event will be further investigated in a dedicated section.

The graphs further illustrate a marked shift in *phase* between the periods of $\sim 110 \div 120$ days, which changes between a $\sim \pm 5$ *day lag* for these periods (-4.78 to 6.31 to be precise). Due to the proximity in period of these two phenomena it is hypothesized

that they share the same origin, hence why this shift in phase will be analyzed further in a subsequent section, alongside the main *coherence* drop.

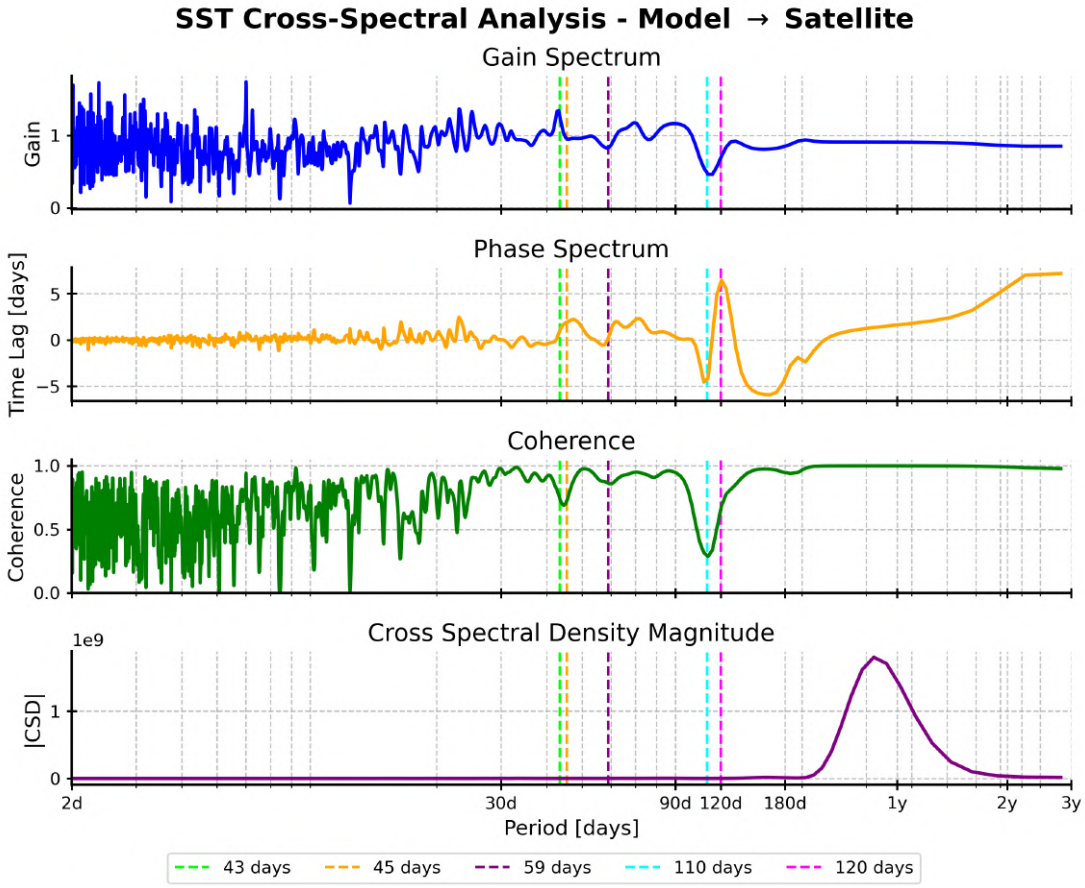

Figure 7.21: Spectral decomposition of the power spectra of Sea Surface Temperature (SST) data. From top to bottom: *Gain*, *Phase*, *Coherence*, and *Cross-Spectral Density Magnitude*. Dashed lines indicate key periods as shown in the legend.

7.1.9 Cross-Wavelet Analysis to Confirm the Coherence Drop

To verify the actual presence of the observed *coherence drop* in the Sea Surface Temperature (SST) data, and to exclude the possibility that it is an artifact arising from the decomposition using Welch's method for power spectrum estimation, a *wavelet* analysis was conducted. The first step focused on the behavior of the RMSE calculated from the surface temperature data.

The wavelet estimate of the RMSE is shown in *Figure 7.22*, together with the corresponding power spectrum. The analysis reveals the presence of a partial signal at the key period of 110 days under investigation. However, this signal appears preceded by a component of equivalent power located within the range $\sim 100 \div 120$ days, and masked by a stronger signal with a period of $\sim 160 \div 170$ days, which hinders its clear identification. Furthermore, the dominant contribution in the wavelet is not located at 11o days, but rather at a significantly longer period around 300 days. The use of an AR(1) model to construct an alternative spectrum did not allow a clear isolation of the 114-day component, instead producing a spectrum characterized by a *power plateau* for periods greater than 30 days.

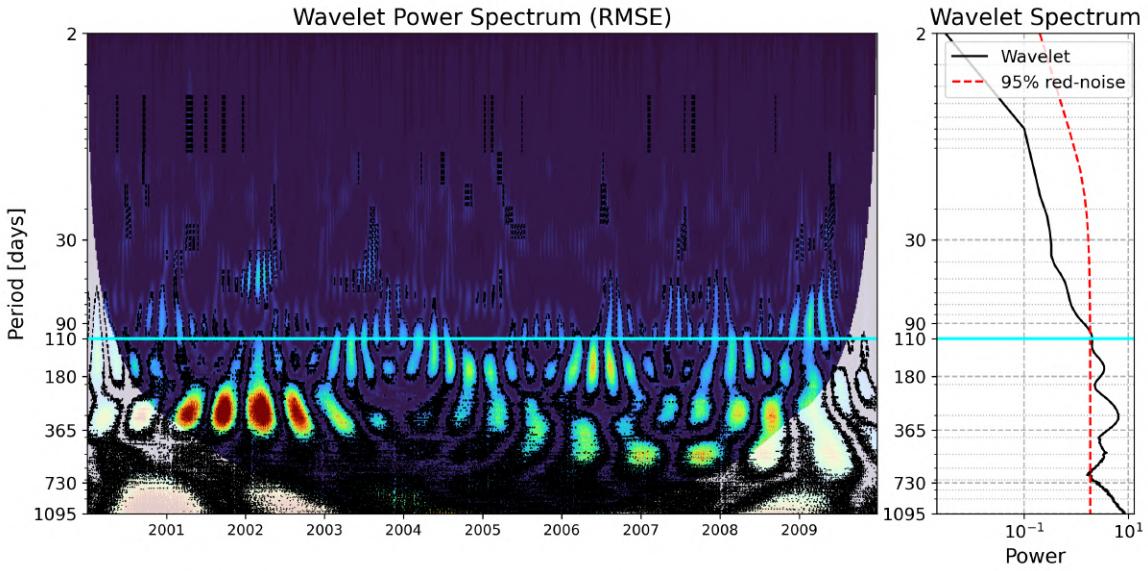

Figure 7.22: Wavelet analysis of RMSE. Left: wavelet of the RMSE; right: corresponding spectrum including the AR(1) model estimate of the original data. The cyan line marks the 110-day period under investigation.

To further investigate and confirm the presence of the coherence drop, a power spectrum was computed directly from the RMSE data rather than its wavelet transform. The spectrum, together with the RMSE time series, is shown in *Figure 7.23*. This analysis highlights several spectral peaks consistent with those revealed by the wavelet: a peak in the $\sim 160 \div 170$ day range and a dominant peak around 300 days. Additionally, the RMSE power spectrum shows another peak of comparable intensity located at a period of ~ 110 days, which matches the *coherence* drop period already identified in the previous analysis.

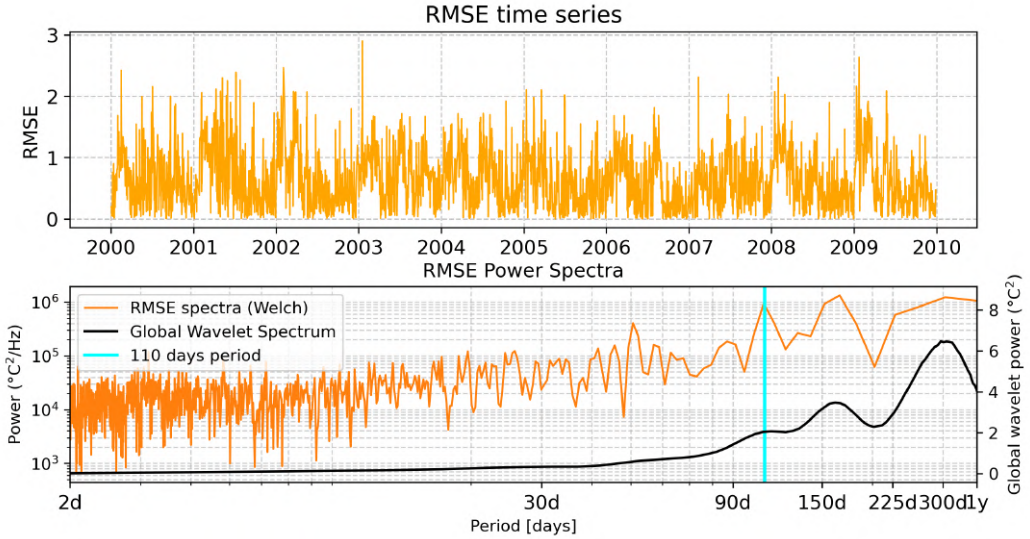

Figure 7.23: RMSE analysis. Top: RMSE time series from *Sea Surface Temperature* data; bottom: corresponding power spectrum including the AR(1) model estimate. The cyan line marks the characteristic 110-day period.

To conclude the analysis and verify the observed *coherence drop*, a *cross-wavelet* analysis was performed, enabling the extraction of coherence as a function of period. In *Figure 7.24*, both the resulting coherence wavelet and the time series at the 110-day period are shown, which highlight the systematic presence of a *coherence drop* at the 110-day period.

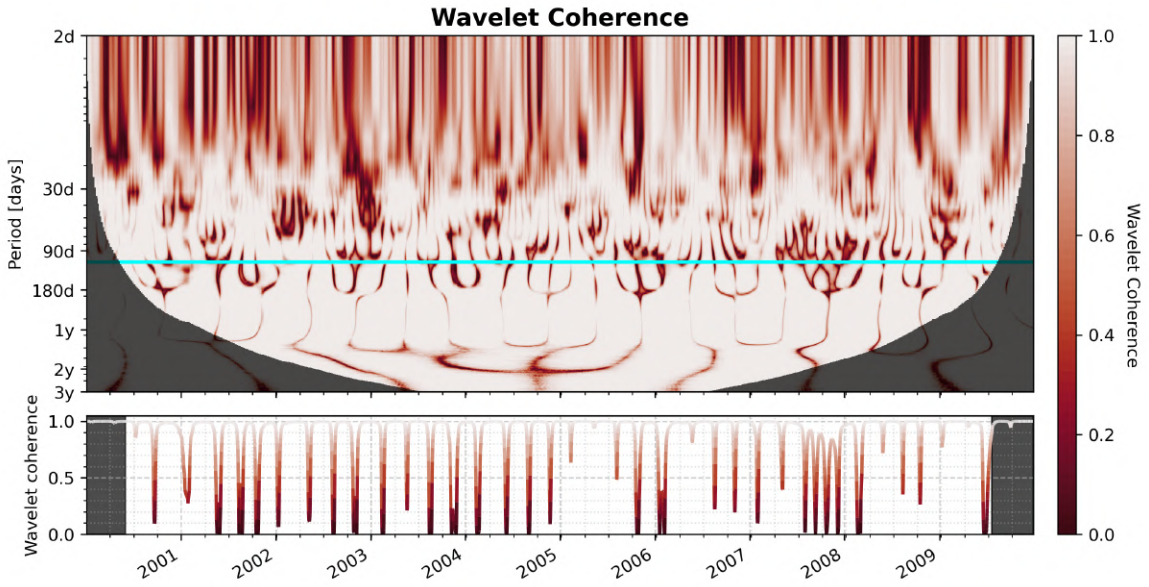

Figure 7.24: Wavelet coherence from the cross-wavelet of model and satellite data. Coherence values are color-coded, with 1.0 in gray and 0.0 in red, highlighting minimum coherence. From top to bottom: the coherence wavelet (cyan line at the 110-day period) and the temporal evolution of coherence within the simulation. Areas outside the COI are shown in black.

7.1.10 The Coherence Drops and Phase Shifts Effects Within the Basin

These analyses thus confirm the existence of systematic coherence drops at a 110-day period and a phase shift at 120 days, excluding the possibility that they are artifacts introduced by Welch's method for power spectrum estimation. To investigate the causes and effects of this phenomena on the dataset, a series of band-pass Butterworth filters were applied to the time series. In this case, the selected period for filtering corresponds to the periods at which the previously identified coherence drop and phase shifts occur; a windows whose period is $\sim 105 \div 125$ *days*. The filtered timeseries can be seen in *Figure 7.25*.

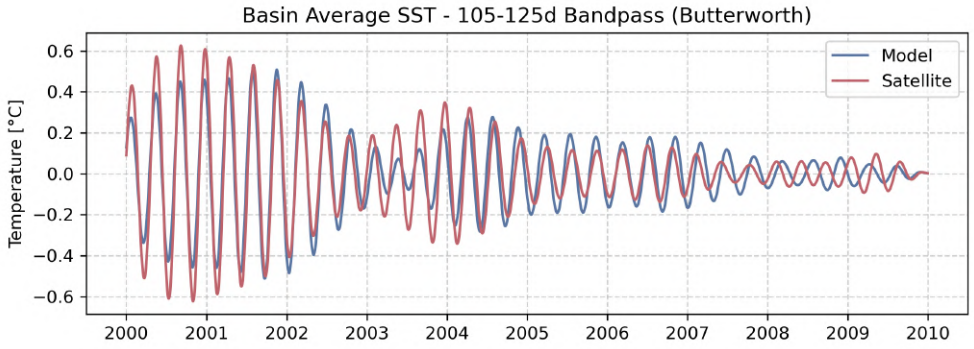

Figure 7.25: Timeseries of the *Sea Surface Temperature* (SST) filtered using a band-pass filter with a selected period of $105 \div 125$ days. Model data is shown in blue and satellite data in red.

Observing the timeseries, it is possible to notice that after the last third of 2002 a slight phase shift emerges, gradually intensifying until mid-2003, when the model begins to exhibit a small delay. This phase difference is partially mitigated during

the first half of 2003 but reappears as the timeseries approach 2004. From this point onward, the phase discrepancy becomes always present, with alternating situations in which the model either anticipates or lags behind the satellite signal. Up to 2007, these variations remain relatively minor, within lag values of approximately ± 5 *days*. However, after this threshold, the phase shift becomes more pronounced, culminating in a strong divergence between the two series from $Q2$ 2008 to $Q1$ 2009, when they become nearly anti-correlated for about a year.

It is also noteworthy that the amplitude of this component progressively decreases over time. The maximum amplitude is observed up to 2002, with satellite values reaching approximately $\sim \pm 0.6\ ^{\circ}C$, while the model exhibits only slightly lower amplitudes. Following this period, a gradual reduction and subsequent increase can be observed, leading to a second local maximum at the beginning of 2004 for the satellite and during the summer of 2004 for the model, with amplitudes that are nearly identical. After this event, the amplitude remains relatively stable, around $\sim \pm 0.2\ ^{\circ}C$, until 2007, when, alongside the marked phase shift, a further decrease in amplitude becomes evident.

To further analyze this phenomenon, a sliding correlation with the same filter was applied. The analysis employs a 115-day rolling window to compute the temporal correlation between the two datasets and is used for all subsequent sliding correlation analysis. The results of this analysis are presented in *Figure 7.26*.

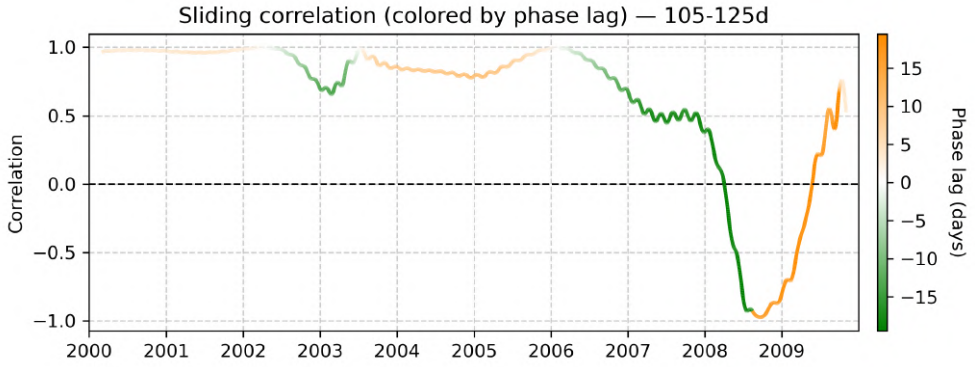

Figure 7.26: Graph of the *sliding correlation* obtained with a $105 \div 125$ *days* band-pass filter. The colorscale represents the instantaneous phase computed at each times step: green indicates a leading satellite-lagging model while orange indicated the opposite.

This analysis clearly encapsulates and reinforces all the phenomena previously discussed. In particular, two distinct and well-defined drops in correlation can be identified: the first occurring around $Q1$ 2003, and the second during the transition between 2004 and 2005. Both events are indicative of temporary disruptions in the correspondence between the modelled and observed signals. The most significant feature, however, is the marked and persistent decline in correlation that begins after 2006. This downward trend continues steadily, culminating in a phase of clear anticorrelation emerging shortly after $Q1$ 2008 and extending through to $Q1$ 2009.

In order to further refine and better characterize these behaviors, two additional band-pass filters were applied, each specifically designed to isolate the main patterns of *coherence* reduction and *phase* displacement. More precisely, periods of 110 *days* and 120 *days* were selected for the *coherence* and *phase* analyses, respectively.

The first filter applied corresponds to the main *coherence* drop period, set at 110 *days*; the results are presented in *Figure 7.27*.

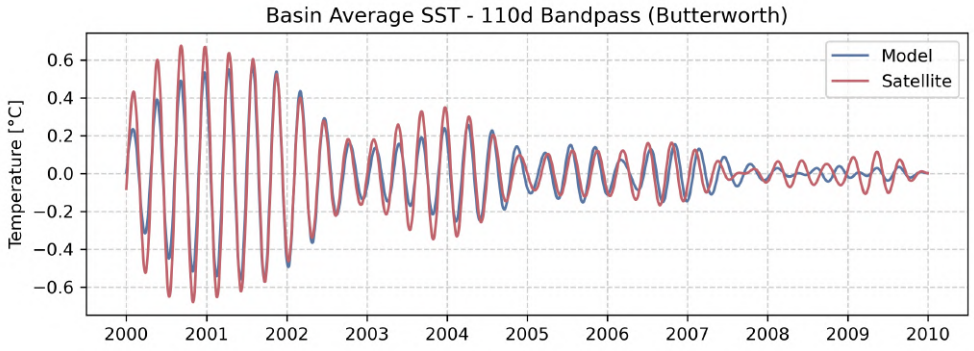

Figure 7.27: Timeseries of the *Sea Surface Temperature* (SST) filtered using a band-pass filter with a selected period of 110 days. Model data is shown in blue and satellite data in red.

The main effects of this filtering reproduce the same phase pattern observed in the previous analyses, maintaining the overall behaviour already discussed. However, it is worth noting that, under this specific filtering, the phenomenon observed during the summer of 2003 does not appear, with the two series exhibiting a more regular trend, albeit with a slight phase shift. The most significant event emerges starting from 2007, when, following a progressive phase divergence between the two series, a marked drop in both amplitude and coherence can be observed. This behaviour is further corroborated by the *sliding correlation* analysis, presented in *Figure 7.28*.

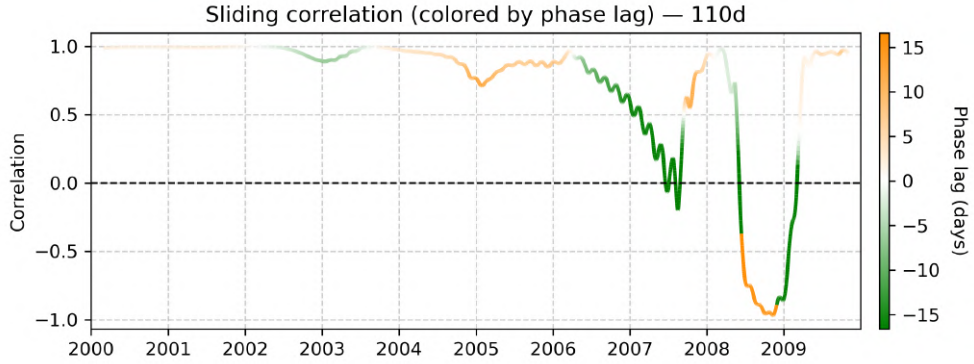

Figure 7.28: Graph of the *sliding correlation* obtained with a 110 *days* band-pass filter. The colorscale represents the instantaneous phase computed at each times step: green indicates a leading satellite-lagging model while orange indicated the opposite.

The main correlation drop extends from $Q2$ 2008 to $Q1$ 2009. A notable decline also begins around the previously identified decrease in 2006, intensifying throughout the summer of 2007, which marks a *critical tipping point* within the simulation, as confirmed by subsequent analyses. After this period, correlation briefly improves before deteriorating again, leading to the major decline observed thereafter.

The final set of results, corresponding to the *phase* component, is presented in *Figure 7.29*.

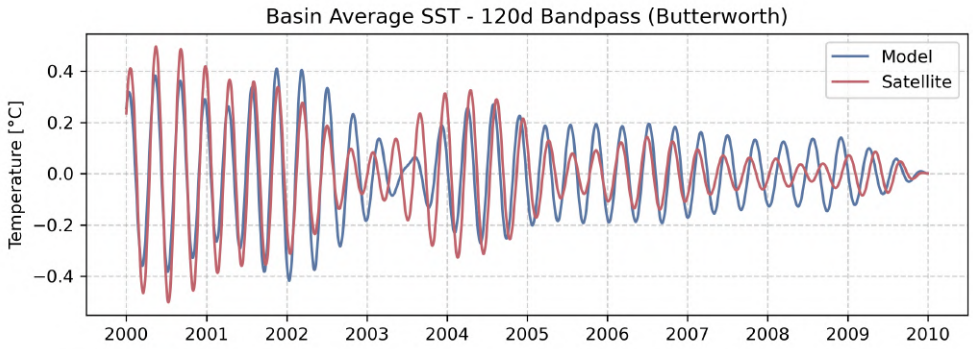

Figure 7.29: Timeseries of the *Sea Surface Temperature* (SST) filtered using a band-pass filter with a selected period of 120 days. Model data is shown in blue and satellite data in red.

In this time series, a phase shift comparable to that observed in *Figure 7.25* can be identified. However, two additional features emerge. Firstly, the model time series maintains a nearly constant amplitude after 2007, with a further reduction only after 2009, a behavior differing from the progressive decrease seen in *Figure 7.25*. The satellite signal, by contrast, preserves a pattern consistent with the previous filter analysis. Secondly, during the summer of 2003, the model becomes completely out of phase with the satellite, effectively missing an entire peak. This results in a pronounced phase shift that persists until a realignment occurs in 2004. The sliding correlation for this filter is shown in *Figure 7.30*.

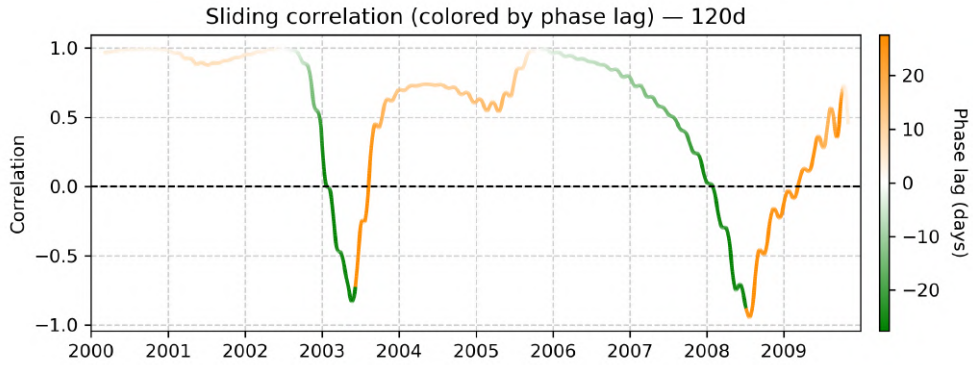

Figure 7.30: Graph of the *sliding correlation* obtained with a 120 *days* band-pass filter. The colorscale represents the instantaneous phase computed at each times step: green indicates a leading satellite-lagging model while orange indicated the opposite.

The sliding correlation analysis once again highlights the main events discussed earlier, showing a minor decline in early 2005 and two major drops during the summers of 2003 and 2008. The effects of the latter are already evident by early 2006, when a steady decrease in correlation begins.

Across all time series and *sliding correlation* plots, two recurrent behaviors emerge. Firstly, each correlation drop begins with a pronounced negative lag, indicating that the model initially trails the satellite signal, a pattern consistently observed during all major events. As each event progresses, a rapid phase inversion occurs, with the model shifting from lagging to leading the satellite, which then falls behind. This cyclic phase inversion repeats throughout all major correlation drops, except for the JJA 2008 event computed using the 110-day band-pass filter. In this case, the event again begins with a model lag (negative phase), but the inversion occurs before the correlation minimum is reached. The lowest correlation instead coincides with a model lead, followed by a second inversion that restores a persistent negative phase.

Secondly, the major correlation drop observed during the second half of 2008 appears consistently across all filters and *sliding correlation* analyses. To evaluate its basin-scale impact, the summer season (**JJA**) of 2008 was selected, as it represents a common period of anticorrelation across all tested band-pass filters. The first analysis applies the 105–125 day filter. As a starting point, the mean temperature fields and corresponding anomaly maps for this season are presented in *Figure 7.31*.

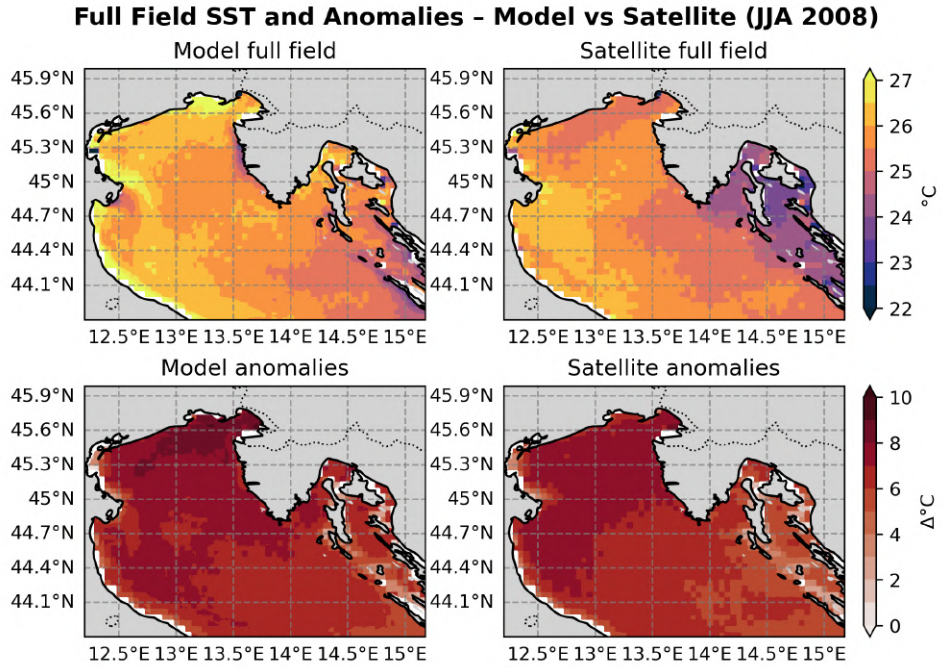

Figure 7.31: Maps of the *Sea Surface Temperature* for the model data (left) and the satellite data (right). The top row shows the full field while the bottom row the anomalies.

The anomaly maps reveal a widespread positive temperature anomaly extending across the entire basin, with peak values of up to 9–10 °C, consistently captured by both datasets. The only notable deviation is a slightly cooler region within Kvarner Bay in the observed dataset, whereas the model shows values comparable to those in the surrounding areas. Overall, the maps do not indicate any pronounced or localized effects within the basin.

The next step focuses on analyzing the temperature anomalies after applying the band-pass filter, whose results are shown in *Figure 7.32*.

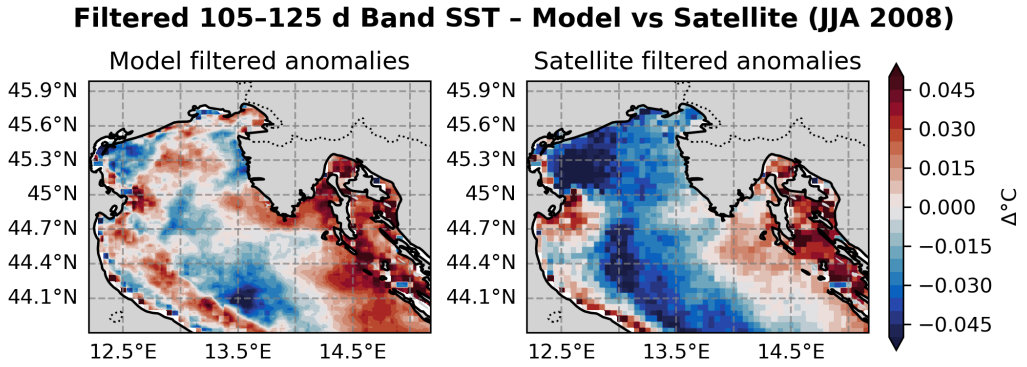

Figure 7.32: *Sea Surface Temperature* anomaly fields computed after applying the band-pass filter with a $105 \div 125$ *days* window. Left: model anomalies; right: satellite anomalies.

Observing the maps, the cause of the discrepancy between the two datasets, and the resulting drop in correlation, can be identified in the presence of a pronounced negative anomaly within the filtered satellite dataset, which covers most of the basin. Within the numerical simulation this anomaly appears significantly weaker and more spatially confined, with the main signal being located in the southern area of the basin.

A similar phenomenon can also be observed by investigating the drop in the *sliding correlation* obtained by applying the 110 *days* filter. By examining the maps shown in *Figure 7.33*, it can once again be inferred that the cause of the correlation drop is likely linked to the presence of another negative temperature anomaly.

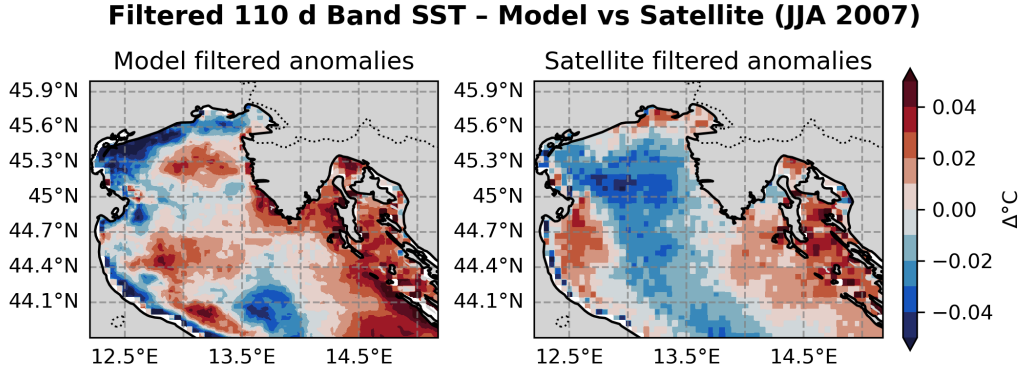

Figure 7.33: *Sea Surface Temperature* anomaly fields computed after applying the band-pass filter with a 110 *days* window. Left: model anomalies; right: satellite anomalies.

Finally, investigating the drop in correlation visible in the *sliding correlation* graph for the 120 *days* band-pass filter reveals that the minimum occurs in May 2003. The anomaly maps, shown in *Figure 7.34*, indicate an opposite behavior compared to the previous cases, with the satellite dataset displaying a pronounced positive temperature anomaly, not present within the simulation.

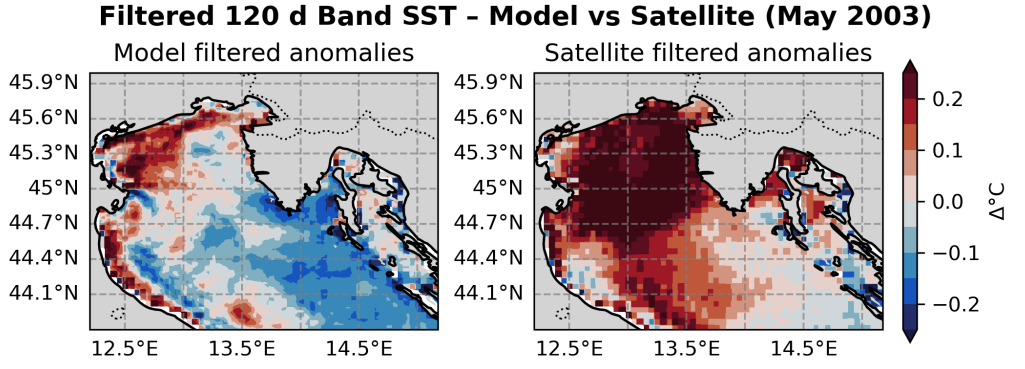

Figure 7.34: *Sea Surface Temperature* anomaly fields computed after applying the band-pass filter with a 120 *days* window. Left: model anomalies; right: satellite anomalies.

7.2 Chlorophyll-a

The second field analyzed for validation concerned the concentration of $Chlorophyll - a$, compared with the corresponding satellite observations provided by the CMEMS L3s datasets through the product `OCEANCOLOUR_MED_BGC_L3_MY_009_143` E.U. Copernicus Marine Service Information (CMEMS) (2023). In this case as well, both observational and model data were subjected to the pre-processing procedures described in Chapter 5, in order to ensure statistical consistency and spectral compatibility between the two series.

7.2.1 Timeseries and Outliers

Similarly to what was presented for the sea surface temperature results, the first result shown here is the *daily mean basin average* timeseries of the two datasets, presented in *Figure 7.35*.

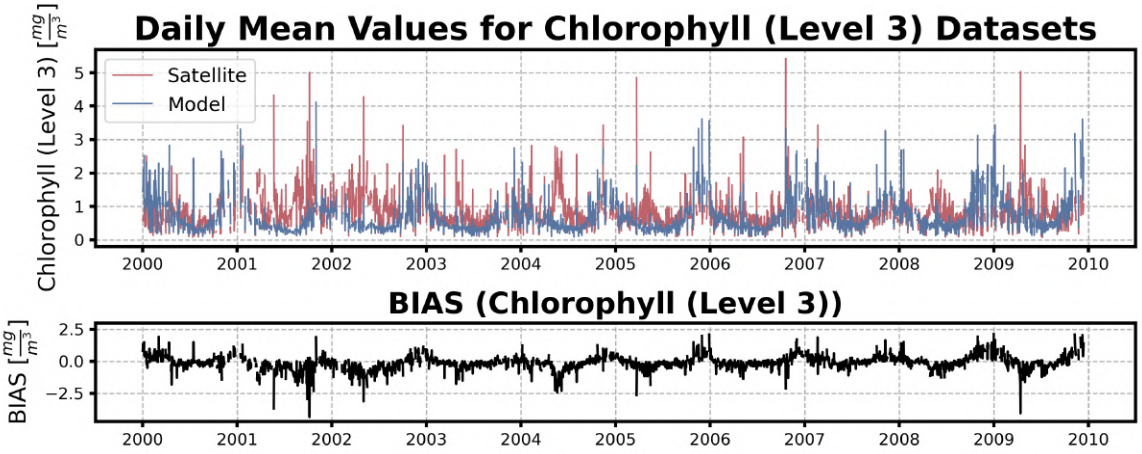

Figure 7.35: Timeseries of $Chlorophyll - a$. From top: first panel, *daily mean basin average*, with the blue curve representing model data and the red curve representing satellite observations; second panel, timeseries of the *mean bias daily mean* between the two datasets.

The Northern Adriatic typically shows a bimodal seasonal cycle of surface phytoplankton biomass: a late spring bloom that often initiates already in mid–late winter if we move towards the coast, and a weaker, more patchy late-summer/early-autumn open sea increase sustained mainly by regenerated production and microbial-loop processes. Coastal spring blooms begin earlier nearshore where winter mixing and immediate riverine nutrient inputs (notably from the Po) replenish the surface nutrient pool and, as light conditions recover, drive rapid phytoplankton growth (Penna et al., 2004; Polimene et al., 2006). The magnitude and timing of this spring events depend on the interplay between the winter mixing depth, the timing and strength of Po-driven nutrient pulses, and the rapid establishment of stratification on the shelf (Polimene et al., 2006). By contrast, late-summer biomass increases are typically smaller in amplitude, spatially patchy and largely supported by recycling of organic matter through bacterial pathways and grazing dynamics rather than by large new nutrient inputs (Vichi et al., 1998; Polimene et al., 2006).

Comparing these expectations with the time series shows partial agreement and specific mismatches: the model tends to capture better the broad winter behavior seen

near the coast, whereas the satellite data record chlorophyll peaks, notably the late-spring bloom, that the simulation fails to reproduce (negative bias at those times). This suggests a bias of the model to over-represent the dynamics seen in the near-shore regimes while failing to reproduce the recycled/microbial-loop production and grazing characteristic of the open-sea regimes. The satellite, on the other hand, tends to see a pattern more similar to the open sea bloom cycle, as confirmed by the timing of the observed chlorophyll concentration peaks.

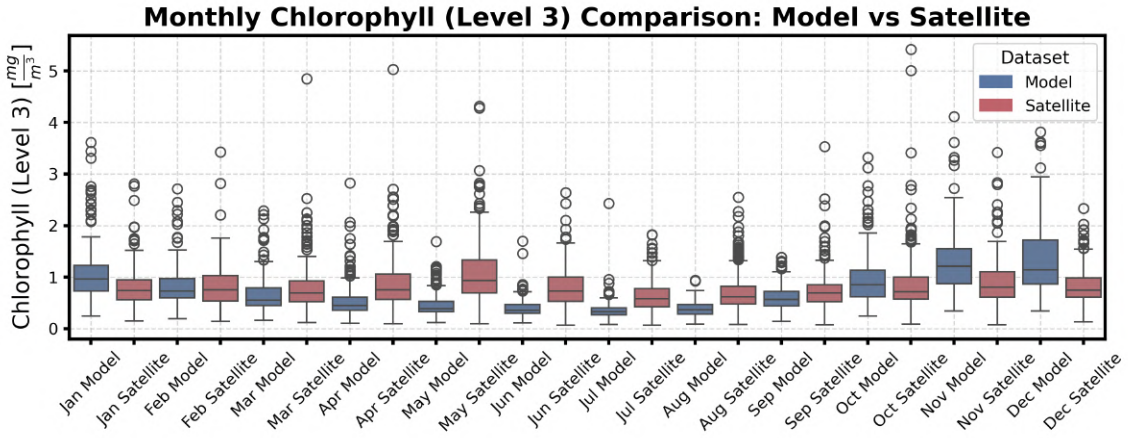

Figure 7.36: Boxplot of *Chlorophyll − a*. Model data are shown in blue, while satellite data are shown in red. Each box summarizes the distribution of monthly values: the rectangle corresponds to the *Interquartile Range* (**IQR**) and the horizontal line inside it indicates the *median*. The *whiskers* extend the range up to 1.5σ, while white points identify *outliers*.

The analysis of the boxplots, shown in *Figure 7.36*, confirms the patterns already highlighted in the timeseries. Considering only the boxes and excluding the *outliers*, which can be attributed to the high interannual variability of the data, a clear model overestimation emerges during the November–January period. Conversely, the lack of reproduction of the *bloom* between April and June is evident from the underestimation of the simulated data. The exact values of the median and IQR for the aforementioned months are reported in *Table 7.5*.

Month	**Median**		**IQR**	
	Model	**Satellite**	**Model**	**Satellite**
November	1.210	0.808	0.674	0.495
December	1.142	0.752	0.853	0.373
January	0.965	0.743	0.496	0.391
April	0.449	0.753	0.254	0.490
May	0.389	0.933	0.208	0.636
June	0.363	0.763	0.173	0.474

Table 7.5: Median values and interquartile range (IQR) of *Chlorophyll − a* for the months affected by *bloom* events. The table reports months corresponding to the winter bloom (Nov–Dec–Jan) and the late spring bloom (Apr–May–Jun).

7.2.2 Chlorophyll-*a* Distribution within the Basin

After identifying the main features of the temporal evolution of the two datasets, a brief spatial analysis was conducted to examine the location and extent of the *blooms*. The selected months, January, May, and October, correspond to the principal seasonal events identified in the previous sections.

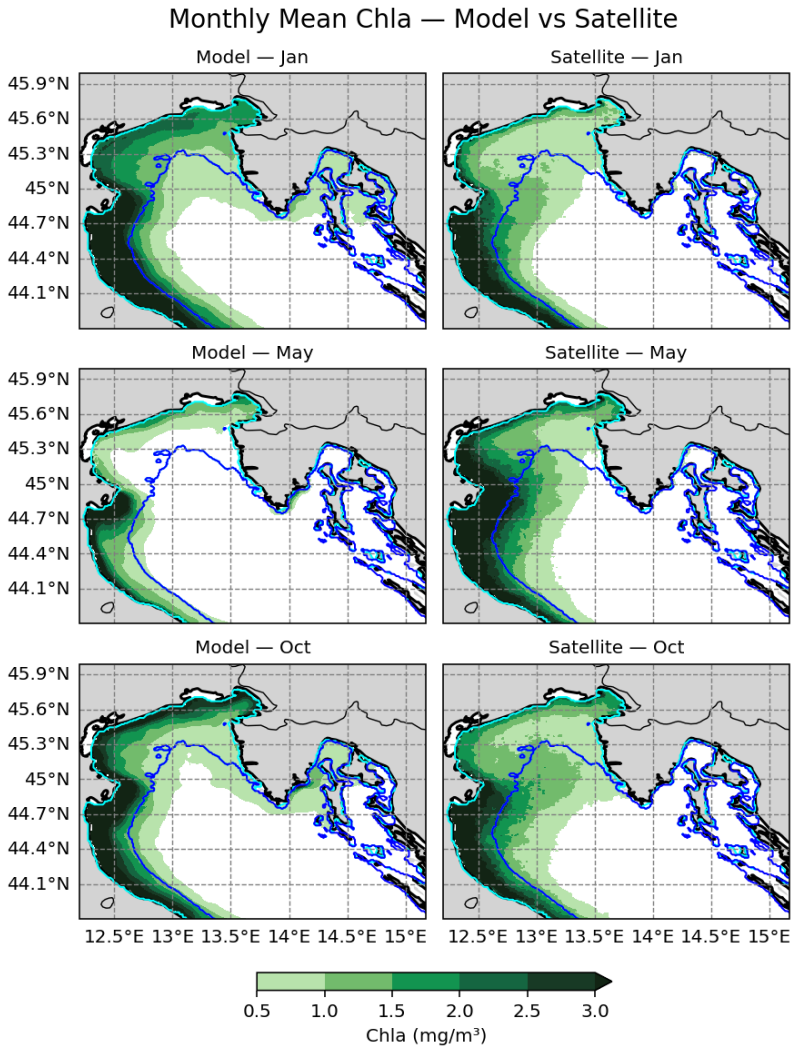

Figure 7.37: Distribution of chlorophyll concentration for January, May, and October. Contours delineate the boundaries of the *nearshore* environment (light blue) and the *open sea* (blue) chosen when the basin's depth surpasses 30m.

The January map shows that the model tends to overestimate surface phytoplankton production in late winter, as indicated by the broader > 3.0 mg/m^3 area. In contrast, satellite scenes display higher offshore concentrations, consistent with the established spatial partitioning of the Northern Adriatic, where river-influenced coastal waters host larger, often diatom-rich phytoplankton, while offshore waters are dominated by smaller cells and stronger microbial-loop activity (Vichi et al., 1998; Polimene et al., 2006).

The May maps reveal marked discrepancies: the model confines biomass mainly to the coast, whereas satellite data show elevated values extending offshore. This contrast reflects the basin's seasonal cycle, in which coastal spring blooms typically start earlier and more intensely nearshore, driven by winter mixing and riverine nutrient

inputs that replenish the surface layer and, with early stratification, trigger rapid phytoplankton growth (Penna et al., 2004; Polimene et al., 2006).

These patterns indicate that the model accentuates a coastal, large-phytoplankton signal with bloom timing biased toward mid-to-late winter, while the satellite emphasizes offshore dynamics linked to microbial-loop and regenerated-production processes peaking later in the season. Model and field studies consistently show that the coastal shelf (ROFI region) acts as an ecological front: larger phytoplankton dominate nearshore, while smaller cells and microbial processes prevail offshore (Zavatarelli et al., 2000; Vichi et al., 1998; Polimene et al., 2006).

Further evidence of these contrasting behaviors emerges in the October bloom. Observations and model results agree that autumn blooms can rival spring events in magnitude but differ mechanistically, being driven by stratification breakdown and upward nutrient fluxes. Here, the model again shows a strong coastal signal, while the satellite reveals a pronounced open-sea bloom, consistent with the coexistence of coastal, diatom-dominated regimes and offshore, microbial-loop-dominated regimes described in prior studies (Vichi et al., 1998; Polimene et al., 2006).

7.2.3 Seasonal Decomposition

The analysis of the results obtained through the *seasonal decomposition* are shown in *Figure 7.38*.

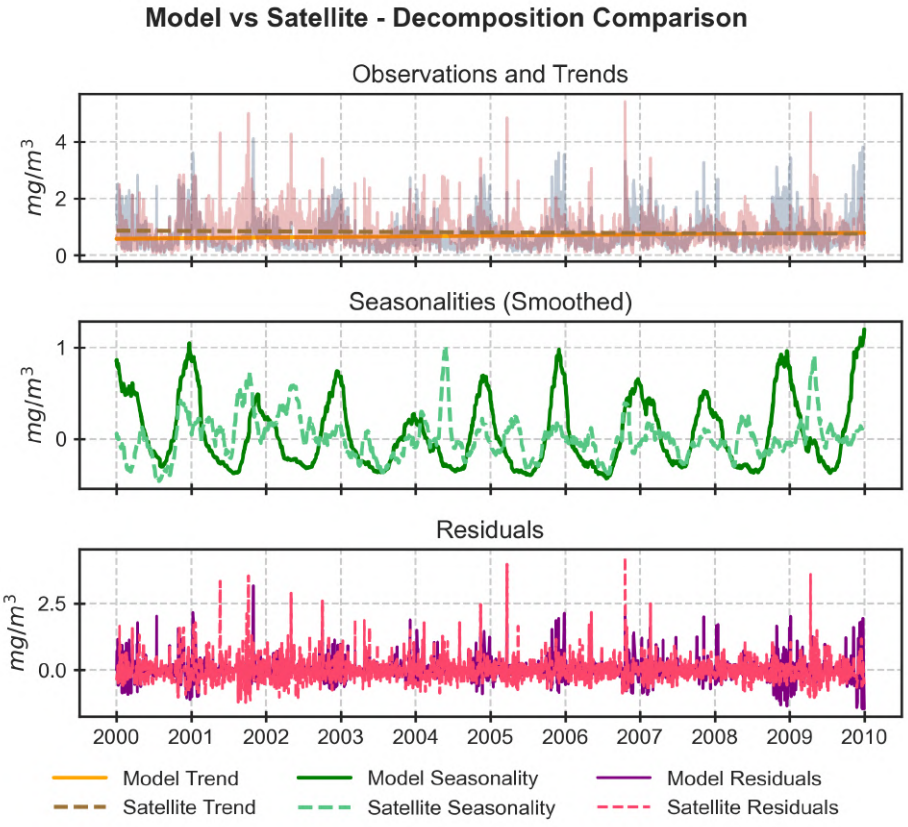

Figure 7.38: *Seasonal Decomposition* results obtained with the *additive method* using model data (solid lines) and satellite data (dashed lines). From top to bottom: raw data (blue for model, red for satellite) with the trend estimated by linear fit; seasonal component derived from a centered moving average; finally the residuals.

The most evident difference between the two datasets concerns the *seasonality* signal. In the modelled data, there is a marked cyclic pattern, characterized by a single main peak during the winter months, particularly between November and January, with occasional extensions into February, while the satellite data behaviour is notably more erratic. These discrepancies confirm the difference in the timings of the *blooms* discussed in the previous sections.

Substantial differences also emerge in the analysis of the residuals: in the simulated data, they show greater amplitude corresponding to the *bloom* phenomenon reproduced by the simulation. The observed data, on the other hand, does not exhibit such cyclicity, showing a more uniform residual amplitude across all time steps.

Finally, another significant difference concerns the trend, whose values are reported in *Table 7.6*. Although the variation is only slightly evident in the graphs due to the small magnitude of the values, the table data show that the model predicts an increasing trend in basin-averaged chlorophyll while the satellite shows a clear decrease, aligning with the main hypothesis presented in modern literature of an oligotrophication of the basin (Giani et al., 2012; Ricci et al., 2022; Marini and Grilli, 2023). This discrepancy required further investigation, which is reported in the following sections.

Series	**Trend** $(mg/m^3/yr)$
`Model`	$+0.021125$
`Satellite`	-0.011761

Table 7.6: Table of the trend values from modelled and satellite data obtained via *seasonal decomposition* of the basin average timeseries of $Chlorophyll-a$ data.

7.2.4 Trend Analysis

To identify the causes of the discrepancy between the trend of the modeled chlorophyll data and that observed from satellite data, a deeper analysis of the *trend* was conducted.

To this end, a second-degree polynomial regression was applied to both datasets, allowing the identification of potential inflection points that could indicate a change in the long-term trajectory of the chlorophyll signal. For the model data, the analysis revealed a clear turning point occurring in late 2006, precisely on June 26, marking a distinct alteration in the trend around that date. The corresponding polynomial curvature and the derived *breakpoint* of the linear regression segments are illustrated in *Figure 7.39*.

A similar pattern was observed in the satellite dataset, where an analogous turning point was detected in the same period, specifically on November 15, 2006. The near-simultaneous occurrence of these inflection points in both datasets provides strong evidence of a genuine transition in the temporal evolution of the chlorophyll field, rather than an artifact arising from individual data sources or model behavior.

In light of these findings, the dataset was subsequently reanalyzed within a spatio-temporal framework, dividing the time series into two distinct intervals: the first extending from the beginning of the record up to the identified *breakpoint*, and the

second covering the period from the *breakpoint* to the end of the simulation. This segmentation allows a more accurate characterization of the temporal evolution of chlorophyll trends and a clearer comparison between modeled and observed behaviors before and after the detected transition.

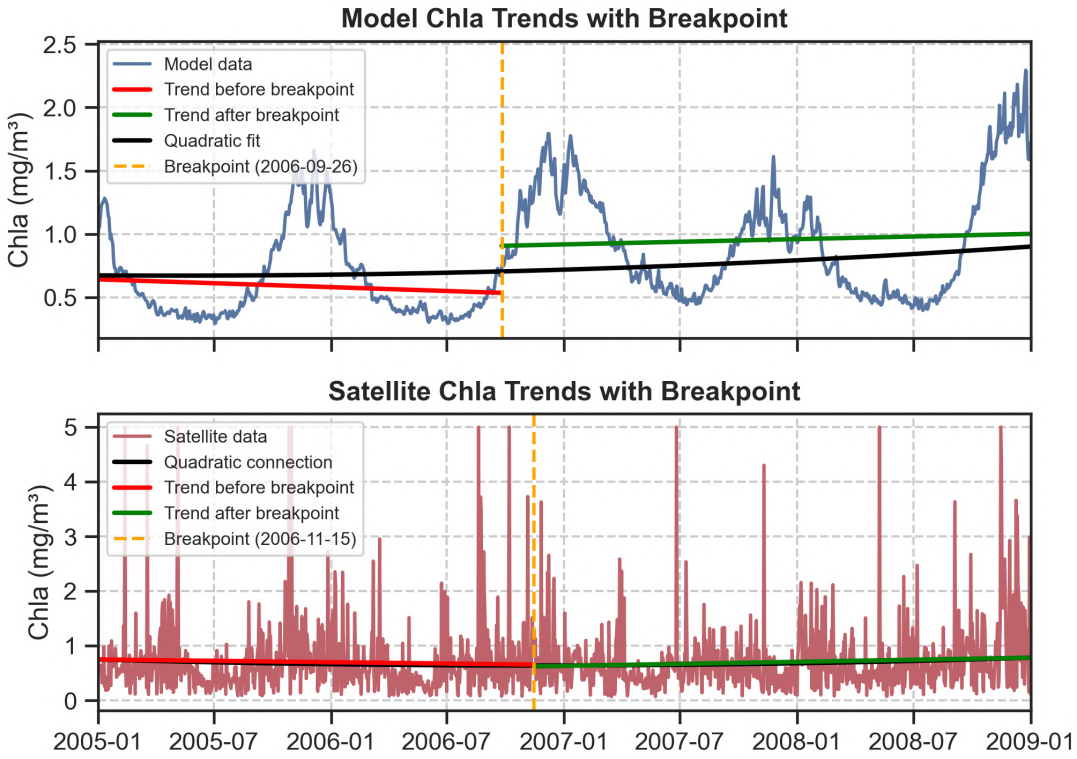

Figure 7.39: Highlight of the 2005–2009 time window for the *Chlorophyll − a* datasets. The top panel shows the model data results while the bottom the satellite data ones. Linear regressions (trends) are shown in red for the period before the *breakpoint* and in green for the period after; the black line indicates the second-degree polynomial regression, while the orange vertical line marks the inflection point (*breakpoint*).

Since the turning points identified in the two datasets do not exactly coincide, an operational choice was necessary to unify the analysis. The decision to fix the *breakpoint* at 01-01-2007 is based on two main reasons: first, the modeled data show a significant change in the minimum values between 2006 and 2007 (0.2841 mg/m^3 in 2006 as opposed to 0.4244 mg/m^3 in 2007), suggesting a real transition in the behavior of the series within this time frame; second, this date is close to the turning point identified in the satellite dataset, thus ensuring temporal consistency in the comparison between the two datasets.

It is important to emphasize that the choice of 01-01-2007 remains somewhat arbitrary: it was adopted as a methodological compromise to simplify the analysis and create a common comparison basis, minimizing the effect of slight temporal discrepancies while maintaining the robustness of the analysis. This approach allows focusing on long-term trend changes, reducing the impact of local or episodic fluctuations and improving the interpretative clarity of the results.

The time series and the corresponding trends, divided according to this criterion, are shown in *Figure 7.40*.

The first computed trend, corresponding to the period 2000–2006, reveals an overall negative behaviour, which is consistent both with the general tendency observed in the empirical data and with the findings reported in the relevant scientific literature (Giani et al., 2012; Ricci et al., 2022; Marini and Grilli, 2023). This indicates that, during this initial phase, the system underwent a gradual decrease in the variable under consideration. The second trend, which covers the subsequent period 2007–2010, exhibits a distinctly positive value, suggesting a reversal in the direction of change compared to the earlier interval.

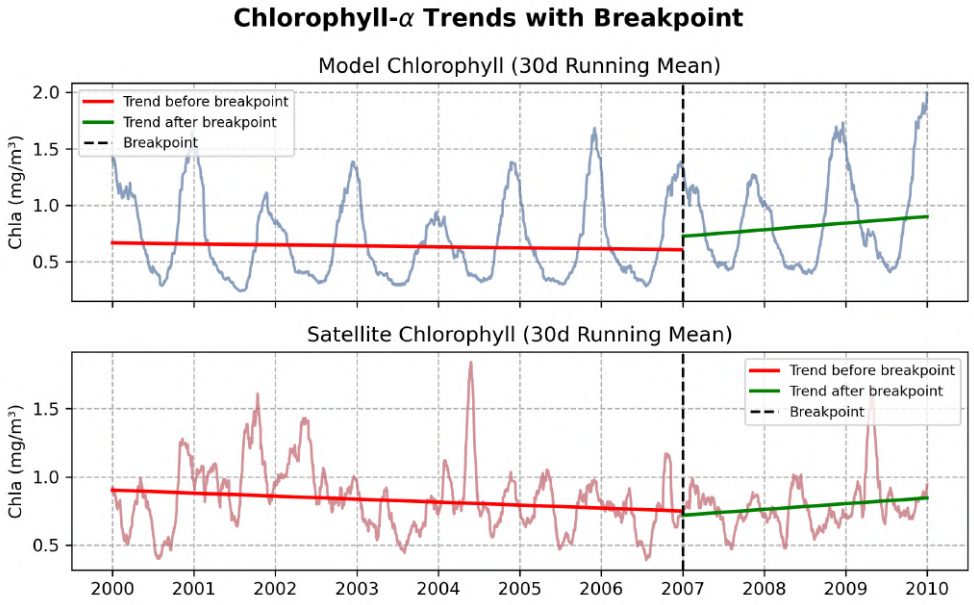

Figure 7.40: Timeseries of the *daily mean Chlorophyll − a* data, with trends calculated for the periods 2000–2007 (red) and 2007–2010 (green). The top plot shows the model data and trends while the bottom one the satellite data and trends. The chosen *breakpoint* is marked in black

As illustrated in *Table 7.7*, it is this second positive trend, combined with the shift in the overall minimum, that ultimately dominates the model trend, thereby producing an overall long-term positive trend in the model results.

Series	**2000–2006** $(mg/m^3/yr)$	**2007–2009** $(mg/m^3/yr)$	**2000–2009** $(mg/m^3/yr)$
`Model`	-0.008486	$+0.060607$	$+0.021125$
`Satellite`	-0.021507	$+0.041985$	-0.011761

Table 7.7: Trends of *Chlorophyll − a* values calculated over three periods.

In the satellite-derived data, a similar behaviour can be identified across the same two time windows. However, in this case, the overall decrease in mean concentration within the first timeframe is of greater magnitude and thus prevails over the subsequent positive phase. As a result, the combined effect leads to an overall negative trend for the entire analysis period, indicating a general decline according to the satellite observations.

The subsequent analysis involved the creation of a series of two-dimensional maps designed to assess in greater detail the spatial variability of the identified trends across

the study area. The results corresponding to the first time window are presented in *Figure 7.41*.

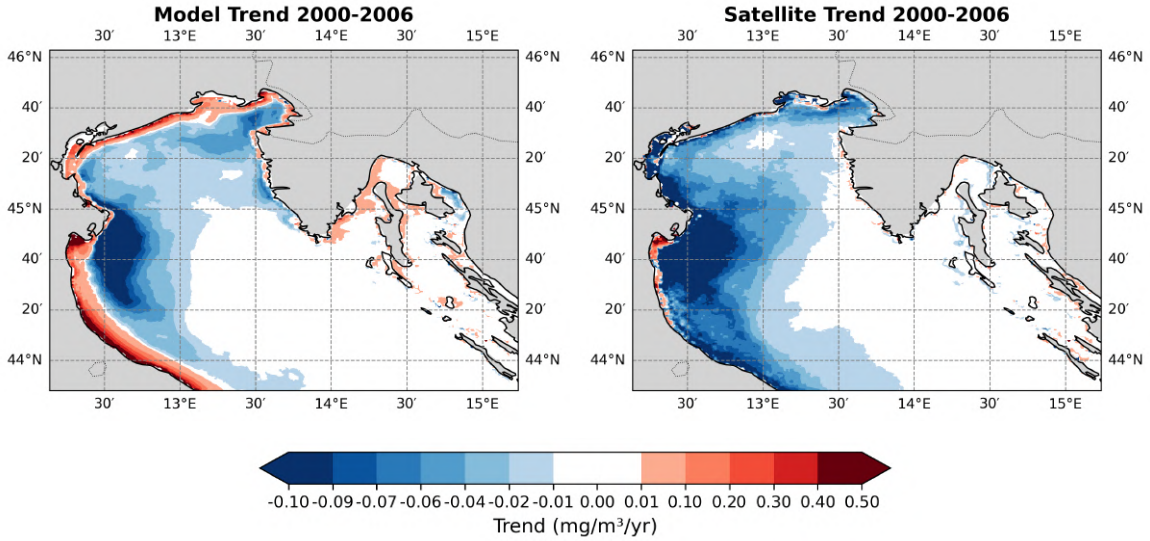

Figure 7.41: Two-dimensional maps of the basin trend distribution for the period 01/01/2000–31/12/2006. Left: trends calculated from modelled data; right: corresponding trends from satellite data. Trend values within the range ±0.1 are shown in white.

From inspection of these maps, it becomes evident that a large portion of the basin shows a negative trend, indicating a general decrease in the studied variable during this period. This negative signal is particularly pronounced near the Po River delta and in the area corresponding to the ROFI (Region of Freshwater Influence), where spatial gradients are strongest.

The main difference between the two result sets, and the most probable cause of the discrepancies in trend values highlighted in the timeseries analysis, lies in the behaviour along the coastline. In the satellite-derived data, this coastal zone consistently displays a pattern of eutrophication, characterised by a distinct negative trend. In contrast, the model data reveal the opposite tendency in the same area, showing a markedly positive trend. Consequently, although much of the basin in the model data is dominated by a negative trend, the strong positive signal along the coastal fringe counteracts part of that effect. This interaction attenuates the overall basin-wide signal, producing a *basin average* trend that remains negative but with noticeably smaller magnitude compared to the satellite observations.

Examining results for the second time window, shown in *Figure 7.42*, reveals that spatial differences between the two datasets extend beyond the coastal region into the basin interior. This broader divergence results in only partial agreement between the datasets for this period.

From a closer inspection of the two maps, it becomes apparent that during this time window both datasets display an overall positive trend, indicating a general increase in the studied variable across much of the basin. Nonetheless, while the satellite data show a relatively consistent and spatially coherent positive pattern at the basin scale, the model results exhibit a higher degree of spatial variability. In particular, pronounced negative signals are evident in the ROFI area of the Po River and within the Gulf of Trieste, together with a distinct negative strip that extends from the northern sector of the basin toward the northern entrance of the Kvarner Bay.

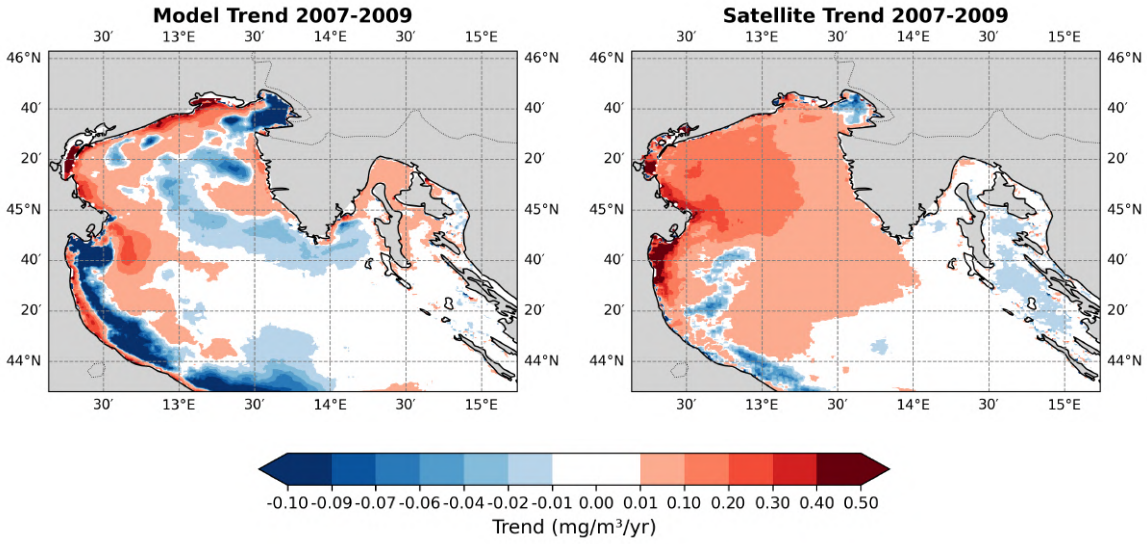

Figure 7.42: Two-dimensional maps of the basin trend distribution for the period 01/01/2007–31/12/2009. Left: trends calculated from modelled data; right: corresponding trends from satellite data. Trend values within the range ±0.1 are shown in white.

7.2.5 Scatterplots

The scatterplot analysis also highlights differences in the behavior of the two datasets. The main scatterplot is shown in *Figure 7.43*.

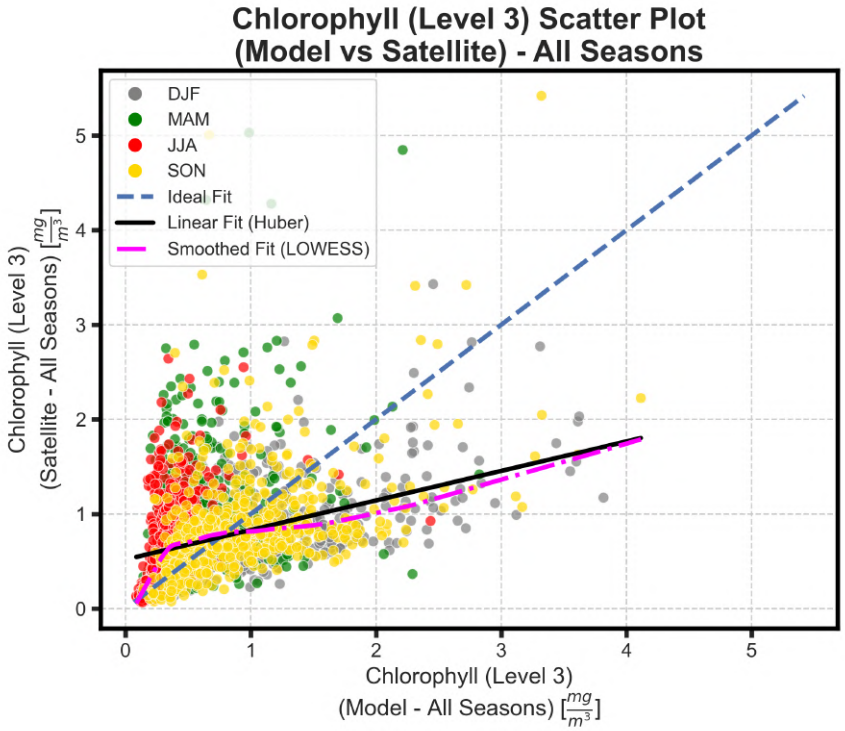

Figure 7.43: Scatterplot of *Chlorophyll* − *a*, divided by season: gray for **DJF**, green for **MAM**, red for **JJA**, and yellow for **SON**. Within the plot, three reference lines are shown: the *Ideal Fit* $y = x$ (blue dashed line), the regression line estimated using the *Huber* method (black), and the regression curve obtained via *LOWESS* (pink).

From the analysis of the scatterplot, it can be observed that the regression lines obtained do not perfectly follow the ideal *best fit* line, exhibiting a general deviation that systematically tends to favour the modelled values over the corresponding satellite observations. This discrepancy suggests a slight but consistent bias in the model results. However, it is important to note that this apparent behaviour may, at least in part, be attributed to the high concentration of data points located near the origin of the plot, which can create an artificial visual effect and give rise to an apparent bias. In order to investigate this dynamic more thoroughly and to better understand its seasonal characteristics, seasonal scatterplots are presented and discussed in *Figure 7.44*.

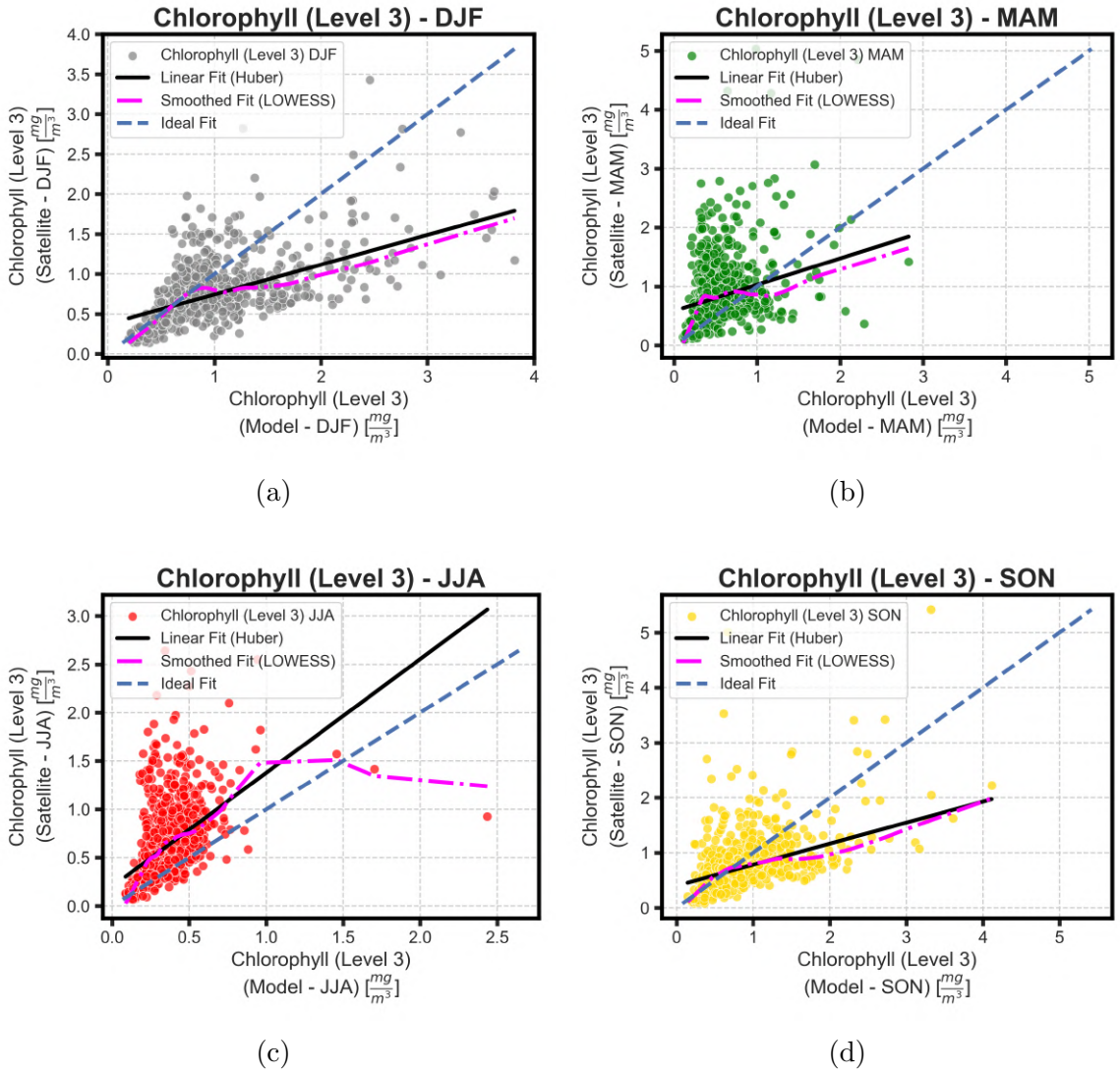

Figure 7.44: Collection of scatterplots of $Chlorophyll - a$, divided by season: a) **DJF**, b) **MAM**, c) **JJA**, and d) **SON**. Each plot shows the *ideal fit* (blue dashed line), the regression line estimated using the *Huber* method (black line), and the regression curve obtained via *LOWESS* (pink curve).

The seasonal analysis based on these scatterplots further emphasizes the presence of specific, seasonally dependent biases. In the SON and DJF seasons, an evident model bias can be identified, manifested as a systematic deviation of the regression lines and curves toward the simulated values. This behaviour reflects the model's

tendency to overestimate the magnitude of the winter *bloom* during the NJF window (Nov–Jan–Feb), a feature that had already been noted in the previous analyses and is confirmed here by the scatterplot distribution.

During the JJA season, on the other hand, a distinct satellite bias becomes apparent, which is also partially evident during the MAM season, although with a noticeably lower intensity. This pattern is consistent with the model's documented limitation in reproducing the late spring *blooms* observed in the AMJ window (Apr–May–Jun), highlighting a persistent underestimation of chlorophyll concentrations during this period.

It should be noted, however, that the use of regression lines and fitted curves for this type of dataset presents certain limitations that need to be considered when interpreting the results. The high density of data points concentrated near the origin tends to influence the shape of the LOWESS curves, shifting them toward the modelled values and thereby affecting the perception of the bias. Likewise, the regression lines obtained through the robust Huber method exhibit a slope that generally favours the simulated data over the satellite observations. An exception is found in the JJA season, where this deviation appears less pronounced; however, a residual effect remains, slightly reducing the ability to accurately represent the satellite bias during this period.

7.2.6 Efficiency Results

Similarly to the analysis performed for the Sea Surface Temperature data, a monthly and overall estimation of various efficiency indices was carried out for $Chlorophyll - a$. This approach allows for a quantitative and detailed assessment of the model's performance, providing a more complete and in-depth view of its ability to reproduce the observed behavior.

Coefficient of Determination (R^2)

Figures *7.45 a) and b)* illustrate the results of the determination coefficients obtained for the $Chlorophyll - a$ data.

From the graphs, it emerges that the overall model performance is almost negligible, with both monthly and *overall* values being very low and close to zero for both indices (weighted and standard versions). This outcome indicates a limited capacity of the model to fully capture the observed temporal variability of $Chlorophyll - a$. However, there are some noteworthy exceptions to this general pattern: in particular, the winter months of December and January stand out, showing values around 0.40.

This slight improvement can be attributed to the presence of a winter *bloom* in both datasets, although the relatively contained values suggest that this feature is not reproduced with the same intensity in the two cases, thus confirming observations made in the previous sections regarding the spatial and temporal distribution discrepancies of the blooms between the datasets.

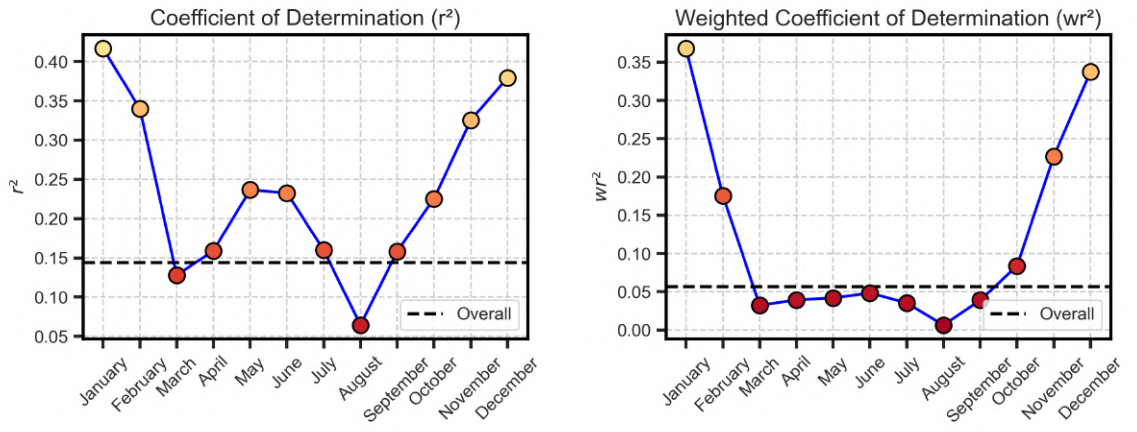

(a) (b)

Figure 7.45: Monthly results of the Coefficient of Determination calculated from $Chlorophyll-a$ data: a) classic R^2 version, b) weighted wr^2 version. Each circular marker represents the overall value for the month, with a color code reflecting proximity to the ideal value (green = 1, red = 0). The black dashed line represents the overall simulation value.

In the standard version of the index, a partial increase is also observed in May and June, suggesting a possible, albeit limited, presence of the late-spring *bloom* within the simulation, aspect confirmed by previous findings. Nevertheless, the contained values indicate that this phenomenon does not reach the same magnitude observed in the satellite data, pointing to persistent limitations in the model's capacity to represent these events with sufficient accuracy.

Nash-Sutcliffe Efficiency (NSE)

Figures *7.46 a) - d)* show the results obtained for the Nash-Sutcliffe Efficiency index.

From the results of all index versions, it can be observed that in nearly all cases the recorded values are close to or below the efficiency threshold, indicating limited agreement between the observed and simulated datasets. Even the use of modified or relative versions of the index, which are designed to be less sensitive to sporadic peaks and extreme variability in the data, does not yield substantially better efficiency values. Although this result is not promising, it is not entirely unexpected. The $Chlorophyll-a$ data, as shown in the time series in *Figure 7.35*, are characterized by daily fluctuations that range from relatively low chlorophyll concentration values to occasional very high peaks, as well as intermittent gaps caused by cloud cover or other observational limitations.

This extremely erratic nature of the chlorophyll data makes the NSE particularly sensitive to small differences in both magnitude and temporal patterns within the time series. As a result, the efficiency values observed in the analyses of the simulation remain consistently low, reflecting the inherent variability of the data.

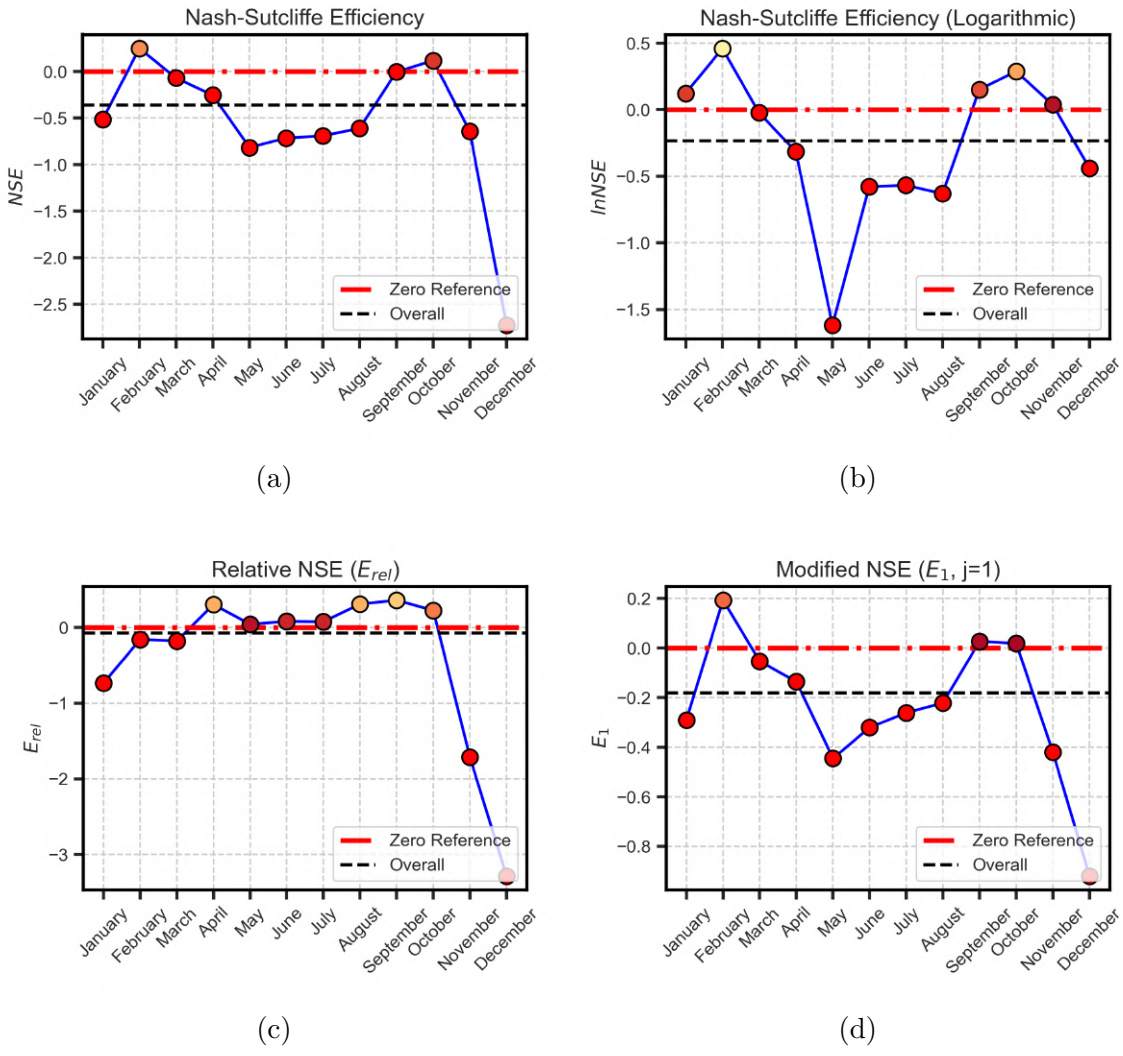

Figure 7.46: Monthly results of the Nash-Sutcliffe Efficiency calculated from *Chlorophyll − a* data: a) classic version, b) logarithmic version, c) relative version, and d) modified version. Each circular marker represents the overall monthly value, with a color code reflecting proximity to the ideal value (green = 1, red = 0). The black dashed line indicates the overall simulation value, while the red line represents the performance threshold: markers below this line indicate cases where climatology performs better than the simulation.

Index of Agreement (d)

Figures *7.47 a)–c)* present the results obtained using the *Index of Agreement* which, across all its formulations, show significantly better performance compared to the indices previously analyzed.

Considering the standard version, the index highlights an overall positive behavior, with particularly high values in January and February, which can be interpreted as a direct consequence of the agreement of the winter bloom between the two datasets. Additional positive signals are observed in temporal windows where the presence of secondary blooms has already been hypothesized: specifically, between October and November and, albeit with reduced intensity, during the summer period between June and July.

When analyzing the relative version of the index, however, an inversion of the general

behavior emerges. In this case, the highest values are concentrated in the period between April and October, with values around 0.75. January also shows positive performance, though slightly lower, with a value of about 0.7.

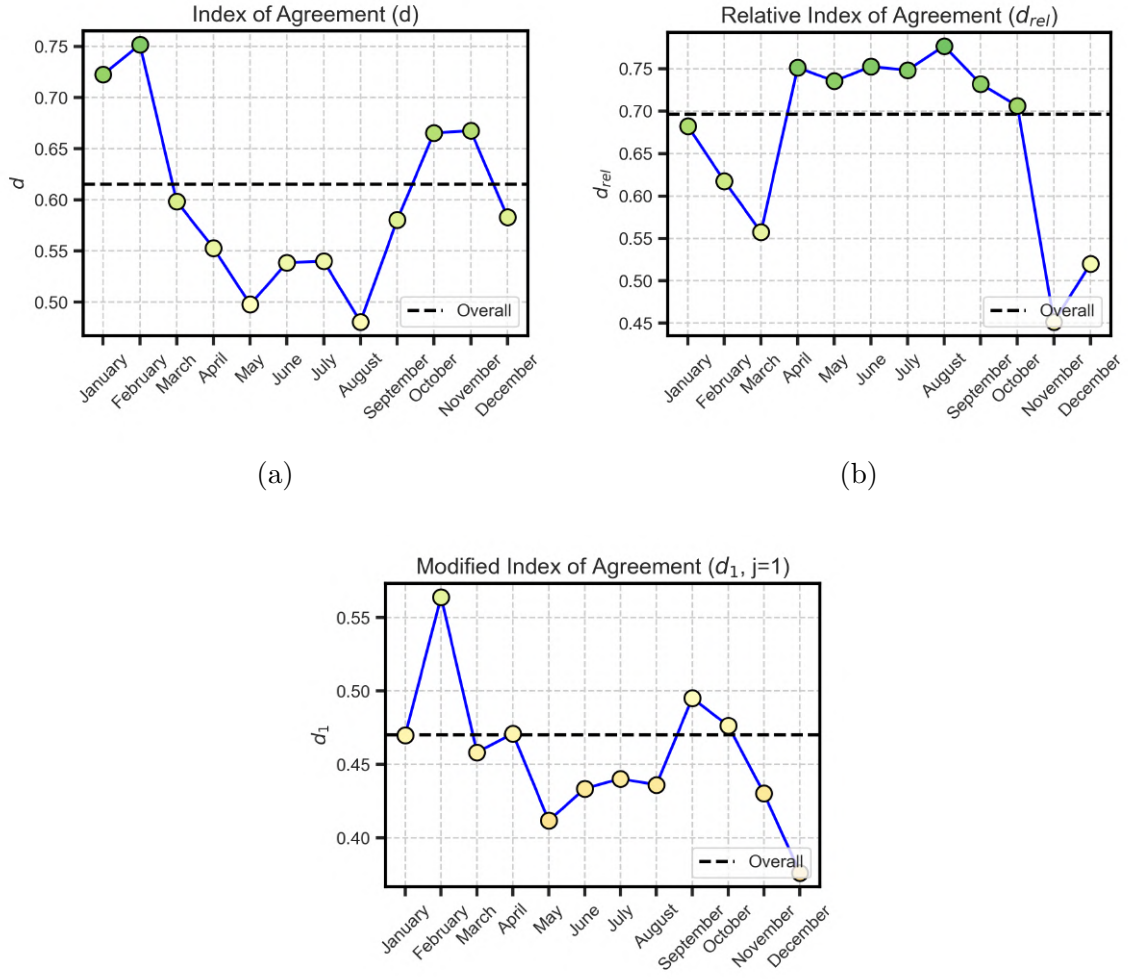

Figure 7.47: Monthly results of the *Index of Agreement* calculated from *Chlorophyll* − *a* data: a) standard version, b) relative version, c) modified version. Each circular marker represents the global value for the month, with color coding indicating proximity to the ideal value (green = 1, red = 0). The dashed black line represents the global simulation value.

This inversion can be explained by the different sensitivities of the two formulations: the standard version rewards absolute agreement and therefore performs better when both datasets capture high-magnitude events (e.g., the winter bloom), while the relative version normalizes deviations and evaluates agreement proportionally. If the satellite product tends to saturate, smooth peaks, or underestimate high concentrations, relative errors during blooms become larger even in the presence of small absolute differences. Conversely, during periods with moderate signal levels (April–October), the same absolute differences represent a smaller fraction of the observed value, and relative performance improves.

The modified version of the *Index of Agreement* exhibits nearly uniform values throughout the entire period, with only a slight increase limited to the month of February.

7.2.7 Error Components and Spatial Efficiency

Alongside the efficiency indices, which are primarily used for evaluating the temporal component, the different error components are analyzed to assess the spatial efficiency of the *Chlorophyll-a* data. The methods applied follow an approach analogous to that adopted for the *Sea Surface Temperature*, thus allowing for a direct and consistent comparison between the two simulated fields.

Mean Bias

At an attempt to highlight any systematic over- or underestimation by the model compared to the observed data the first component analyzed is the mean bias, the general map of which is shown in *Figure 7.48*.

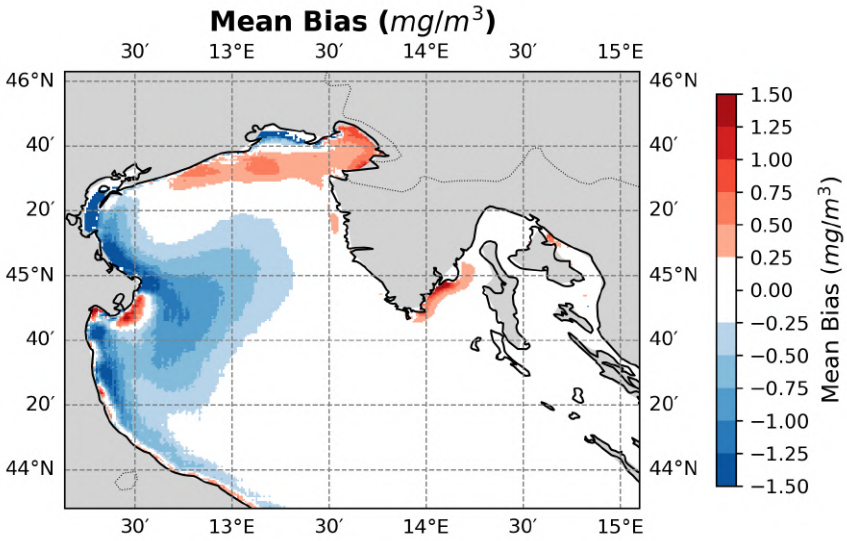

Figure 7.48: Map of the *Mean Bias* of the model with respect to the observed data for the *Chloropyll − a* field over the entire simulation period. Values within the range of ±0.25 are shown in white, in order to exclude marginal signals.

By examining the overall performance map, it is possible to identify the presence of strongly positive and negative signals, particularly concentrated along the coastline and near river mouths. In the eastern sector of the basin, two areas characterized by marked positive values can be distinguished: one located in the Gulf of Raša and the other in the Gulf of Trieste, with the latter extending over a significant portion of the northern basin. In proximity to this area, a negative signal can be observed within the Marano Lagoon.

On the western side of the basin, the bias distribution predominantly exhibits negative values, except for a few localized areas showing positive signals of limited spatial extent but considerable intensity, the most evident of which occurs at the outlet of the Sacca degli Scardovari.

The monthly maps, exemplified by those for January and May shown in *Figure 7.49*, reveal the reappearance of the biases already identified in previous analyses. Specifically, a strongly positive signal is observed during the winter months, attributable to the winter *bloom* reproduced by the model, along with an equally pronounced but opposite signal in late spring. The latter confirms the model's inability to reproduce the late-spring *bloom* that is instead detected in the satellite data.

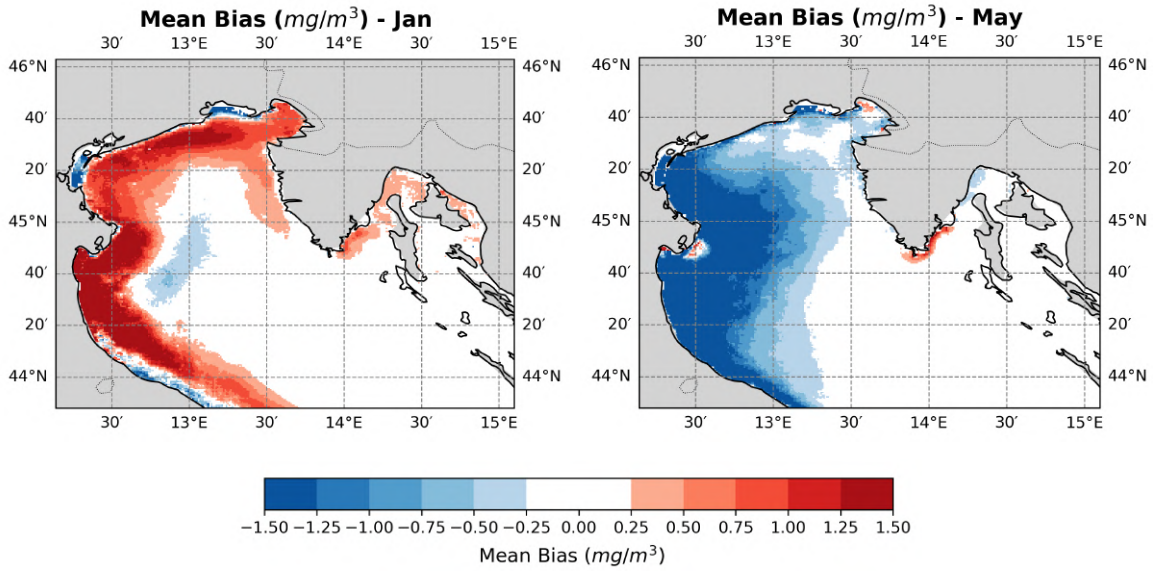

Figure 7.49: Comparison of the *mean bias* maps relative to the months of January (left) and May (right) of the $Chlorophyll - a$ field. Values within the range of ± 0.25 are shown in white, in order to exclude marginal signals.

The annual maps also highlight the presence of biases, which in this case are more pronounced than those observed for sea surface temperature. Considering, for instance, the years 2002 and 2007, shown in *Figure 7.50*, a clear interannual variability of the chlorophyll field emerges, with no complete agreement between the two datasets. In 2002, a strongly negative signal is observed along the coastal zone, indicating an underestimation of *Chlorophyll-a* concentrations by the model, whereas in 2007 the trend is reversed, with a general overestimation of the simulated data compared to the observations.

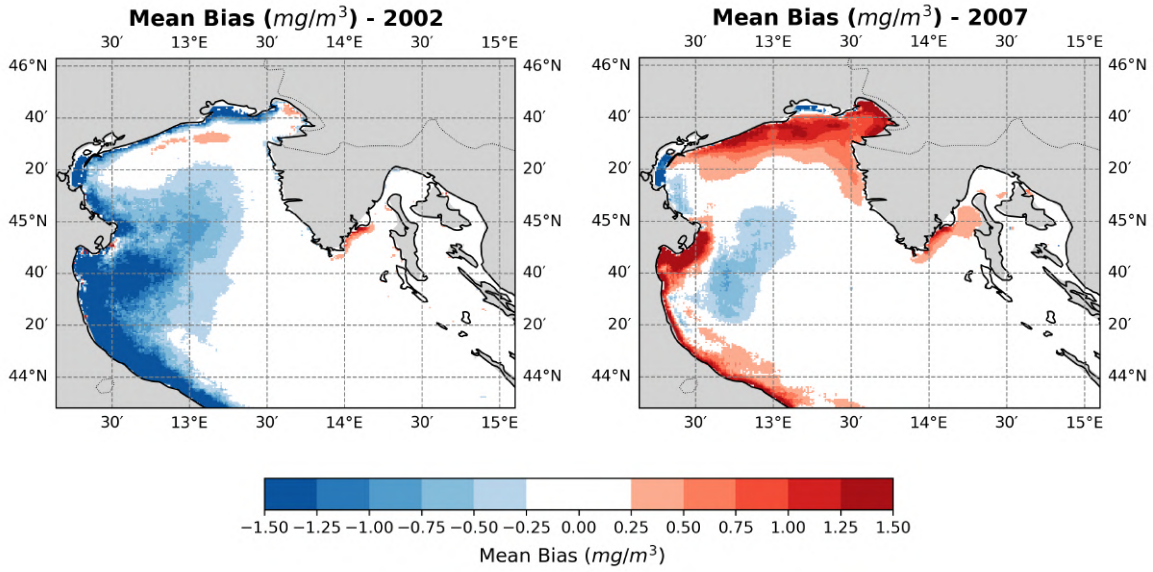

Figure 7.50: Comparison of the *mean bias* maps relative to the years 2002 (left) and 2007 (right) of the $Chlorophyll - a$ field. Values within the range of ± 0.25 are shown in white, in order to exclude marginal signals.

Standard Deviation error

The standard deviation error (SDE) is analyzed next, the overall result of which is shown in *Figure 7.51*.

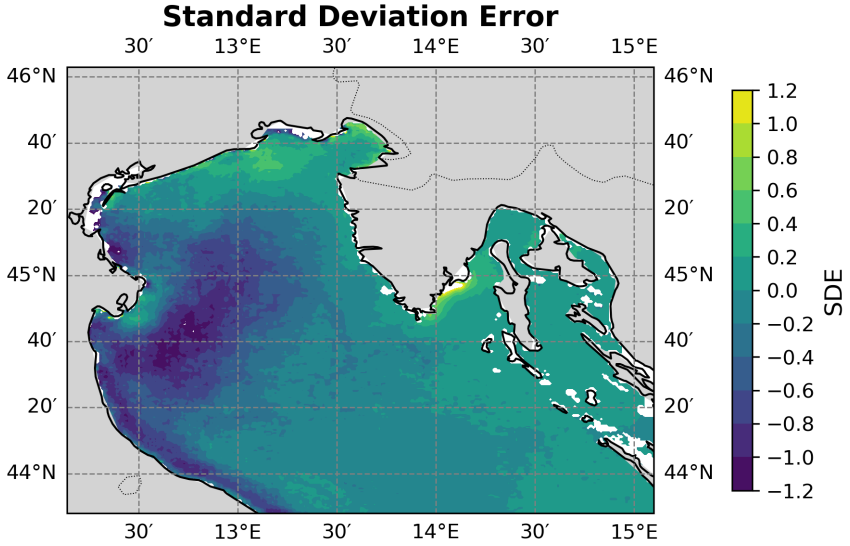

Figure 7.51: Map of the *Standard Deviation Error* of the model with respect to the observed data for the $Chloropyll - a$ field over the entire simulation period.

From the general map, two main signals can be identified. The first appears at the mouth of the Gulf of Raša, characterized by predominantly positive values, indicating an overestimation of chlorophyll concentrations by the model relative to the observations. The second concerns the western basin, where negative values of similar magnitude are recorded, with a spatial distribution resembling the bias patterns previously noted in earlier analyses.

As observed for the *mean bias*, the Po influence area also exhibits marked intra-annual variability in the case of the *standard deviation error*, particularly evident in December and August, shown as examples in *Figure 7.52*.

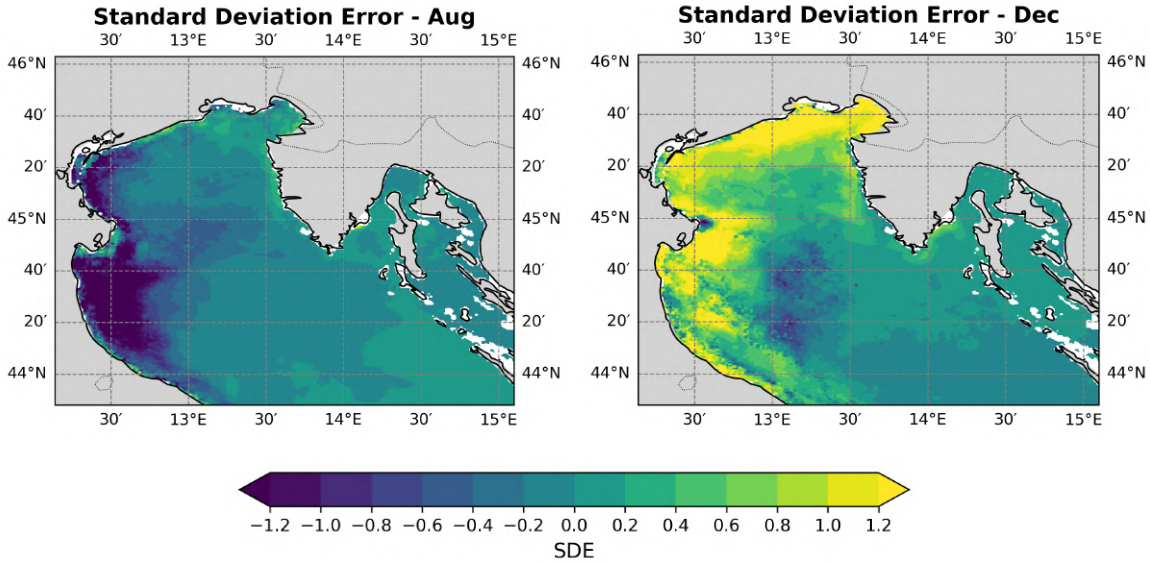

Figure 7.52: Comparison of the *standard deviation error* maps relative to the months of December (left) and August (right) of the $Chlorophyll - a$ field.

It is interesting to note that during transitional periods such as May, a month characterized by the presence of the late spring bloom observed by satellite but not reproduced by the model, as previously discussed, the western area of the basin shows a predominantly negative signal, which, however, becomes positive near the Po delta, where markedly higher values are recorded. The plot illustrating this behavior is shown in *Figure 7.53*.

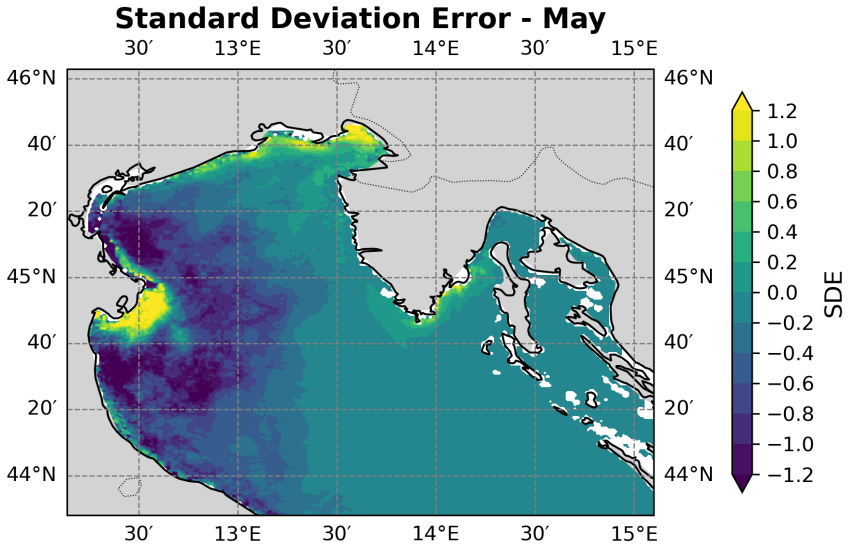

Figure 7.53: Map of the *Standard Deviation Error* of the model with respect to the observed data for the $Chloropyll - a$ field for the month of May.

Observing the annual trend, no particular or noteworthy signals emerge. The only significant phenomenon is a sharp increase in the *sde* values near the western and northern coasts, starting in 2008 and continuing until the end of the simulation. The plot corresponding to the year 2008 is shown in *Figure 7.54*.

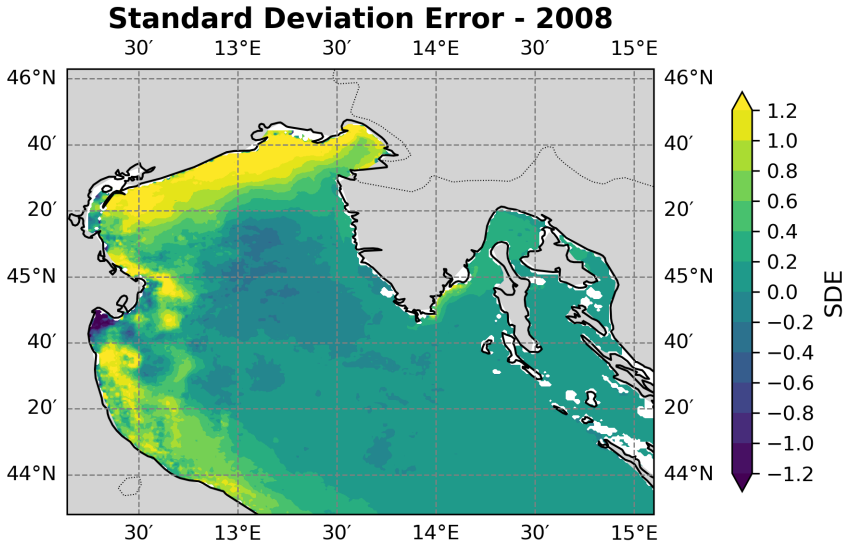

Figure 7.54: Map of the *Standard Deviation Error* of the model with respect to the observed data for the $Chloropyll - a$ field for the year of 2008.

Cross Correlation

The analysis of the cross-correlation is shown in the general map in *Figure 7.55*.

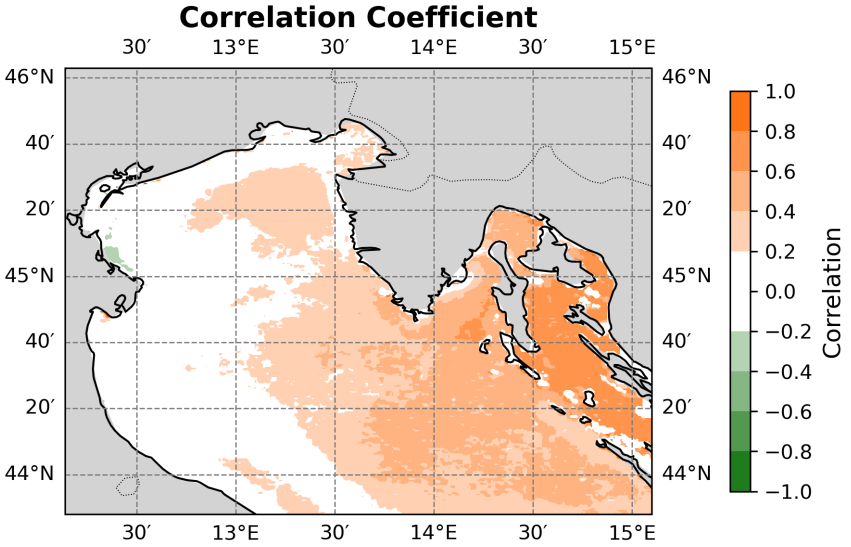

Figure 7.55: *Cross Correlation* of the model with respect to the observed data for the *Chloropyll − a* field over the entire simulation period. Values within the range of ±0.2 are shown in white.

The cross-correlation map reveals two distinct areas within the basin. The eastern sector shows strong positive correlations, indicating good spatial agreement between simulated and observed data. In contrast, the western sector displays near-zero correlations, highlighted in white, denoting poor agreement. North of the Po River mouth, a small anti-correlated signal appears, suggesting an inverse relationship.

Monthly patterns are more complex, with correlation values and signs varying markedly through the year. The maps for March and December, shown as examples in *Figure 7.56*, reveal a clear inversion of correlation near the Po River ROFI and at the outlets of Mirna Bay and Limski Fjord. December shows generally high correlations across the basin, especially along the north-western coast, where a winter bloom is hypothesized.

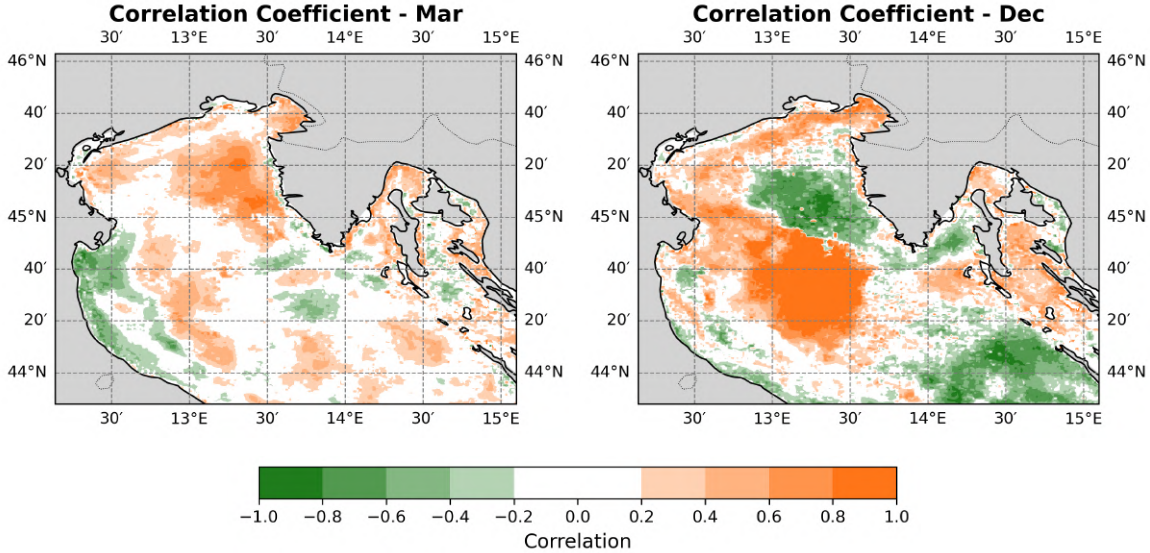

Figure 7.56: Comparison of the *cross correlation* maps relative to the months of March (left) and December (right) of the *Chlorophyll − a* field. Values within the range of ±0.2 are shown in white.

Observing the interannual variability, there is a consistent signal of anti-correlation along the western coast of the basin, with particular intensity near the mouth of the Po River. This signal, although showing variations in intensity over the years, as evident in the examples of 2002 and 2006 reported in *Figure 7.57*, remains persistent, confirming a recurring feature in the basin's dynamics.

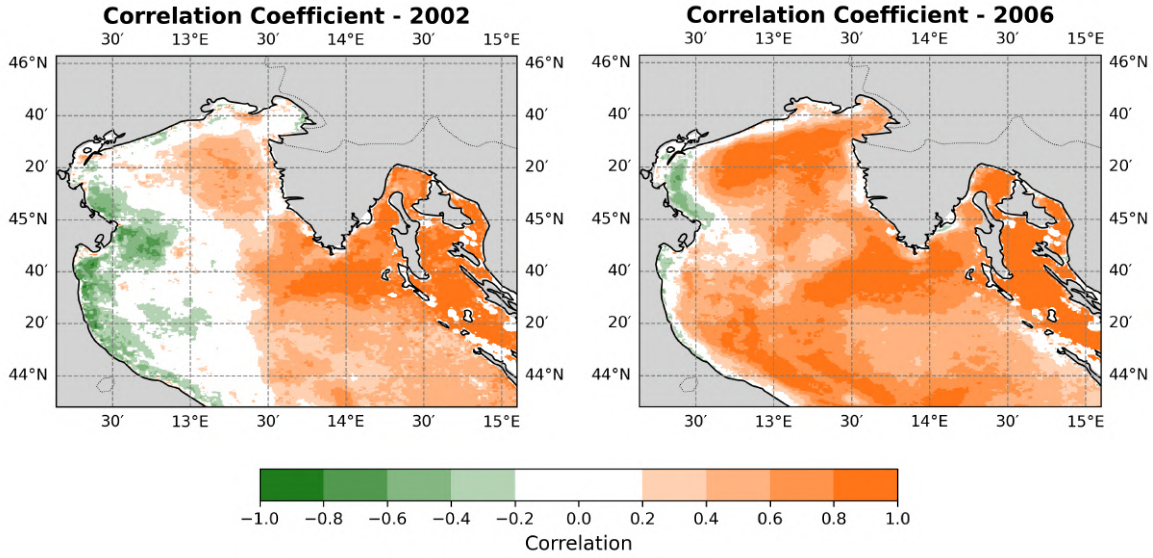

Figure 7.57: Comparison of the *cross correlation* maps relative to the years 2002 (left) and 2006 (right) of the $Chlorophyll - a$ field. Values within the range of ± 0.2 are shown in white.

Unbiased RMSE

Finally, the last component analyzed is the uRMSE, whose overall behavior is shown in *Figure 7.58*.

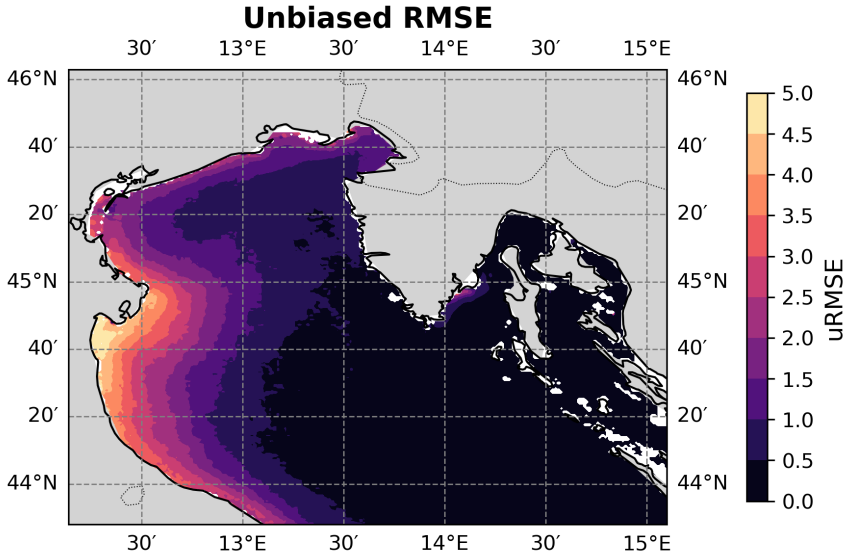

Figure 7.58: Map of the *Unbiased RMSE* of the model with respect to the observed data for the $Chloropyll - a$ field over the entire simulation period.

Observing the general map of the unbiased RMSE, it is confirmed that the main

discrepancies are concentrated along the western coast of the basin, particularly in the areas near the Po delta and immediately to its south.

The analysis of the monthly maps also highlights an intra-annual variability of this signal, with values peaking in March and reaching minima during the month of September. As an example, these two months are shown in *Figure 7.59*.

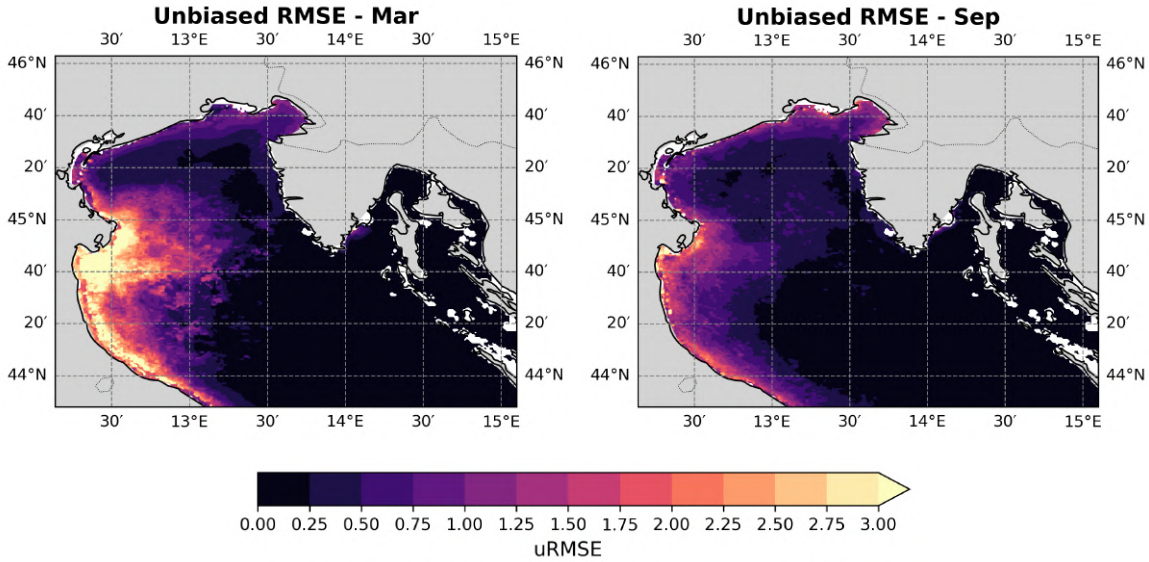

Figure 7.59: Comparison of the *unbiased RMSE* maps relative to the months of March (left) and September (right) of the $Chlorophyll - a$ field.

Finally, the interannual analysis reveals a behavior similar to that observed for the annual cross-correlation signal: the signal remains consistently present along the western edge of the basin, although its intensity varies over time. This variability is clearly visible in the years 2002 and 2006, shown as examples in *Figure 7.60*.

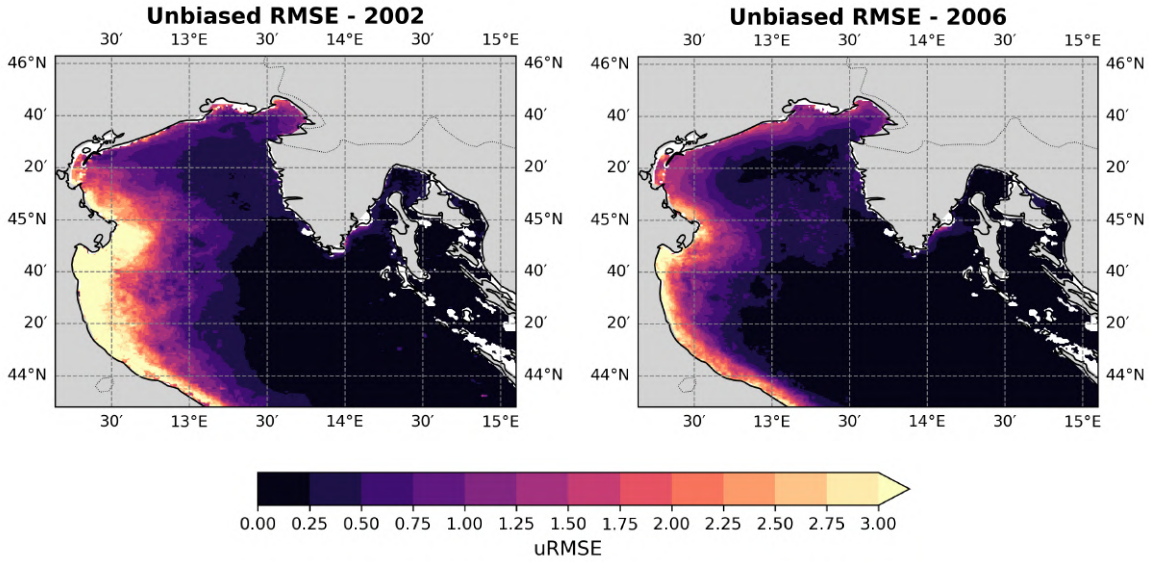

Figure 7.60: Comparison of the *unbiased RMSE* maps relative to the years 2002 (left) and 2006 (right) of the $Chlorophyll - a$ field.

7.2.8 Target Plots

Similarly to what was done for sea surface temperature, a series of *summary plots* have also been introduced for chlorophyll in order to evaluate the model's performance. The first type of these plots are the target plots, shown in *Figure 7.61 a) and b).*

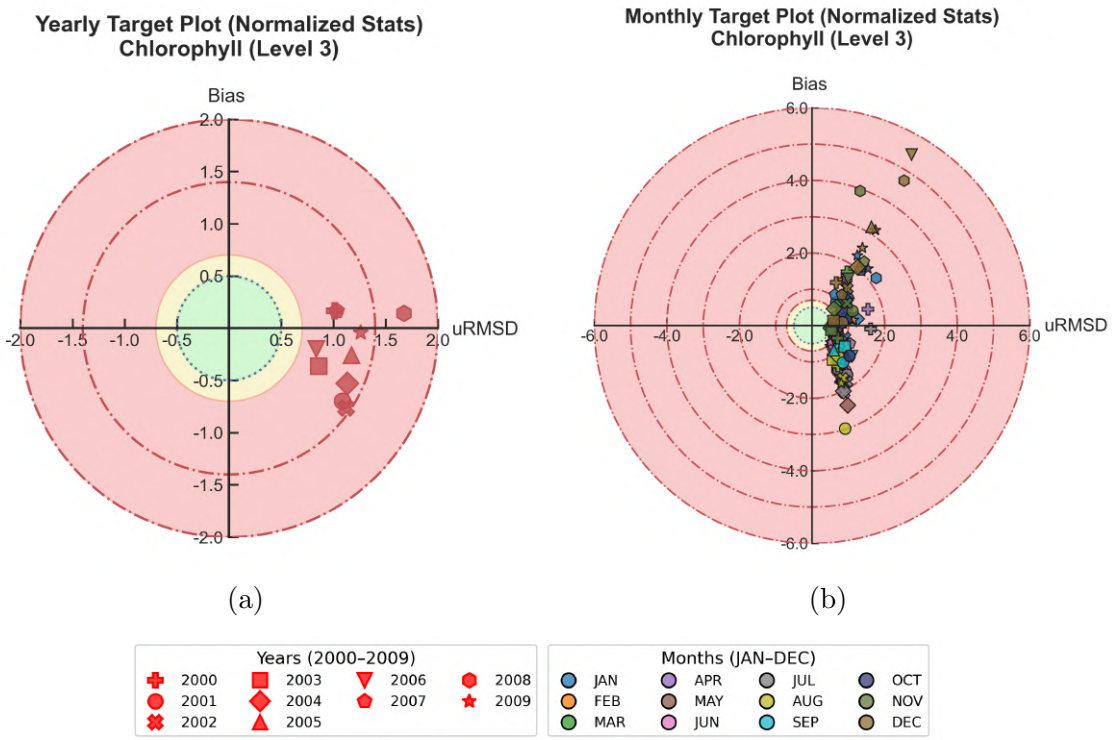

Figure 7.61: Target plots of the *Chlorophyll* − *a*: a) annual performance of the simulation, b) monthly performance. The values were normalized to allow comparison between different months. Each area is associated with a color indicating performance, with regions closer to the origin of the plot corresponding to better performance.

Analyzing the results reported in the annual target plot, it emerges that the model's performance is generally below the optimal threshold, with uRMSD values oscillating on average between approximately ~ 0.75 and 1.25. Bias values are also overall higher compared to those observed for temperature, as shown in *Figure 7.16*. In particular, it is evident that in most instances the biases assume negative values, reaching a normalized magnitude of about ~ 1.0, which highlights a systematic underestimation by the model in these conditions.

Monthly performance does not show significant improvements compared to the annual scale, although some peculiar behaviors emerge when analyzing the relationship between bias and uRMSD in greater detail. In particular, it is observed that markers associated with negative bias tend to maintain uRMSD values similar to those found in the annual assessments, suggesting a persistent model characteristic across different timescales. Conversely, for markers with positive bias, a different trend becomes evident: near a bias value of approximately ~ 2.0, there is a noticeable increase in uRMSD, which continues to grow for markers that exceed this threshold. This indicates that, in such cases, not only does the magnitude of the bias increase, but the overall variability of the model error also intensifies.

7.2.9 Taylor Diagrams

Similarly, the Taylor diagrams, shown in *Figure 7.62 a) and b)*, are presented.

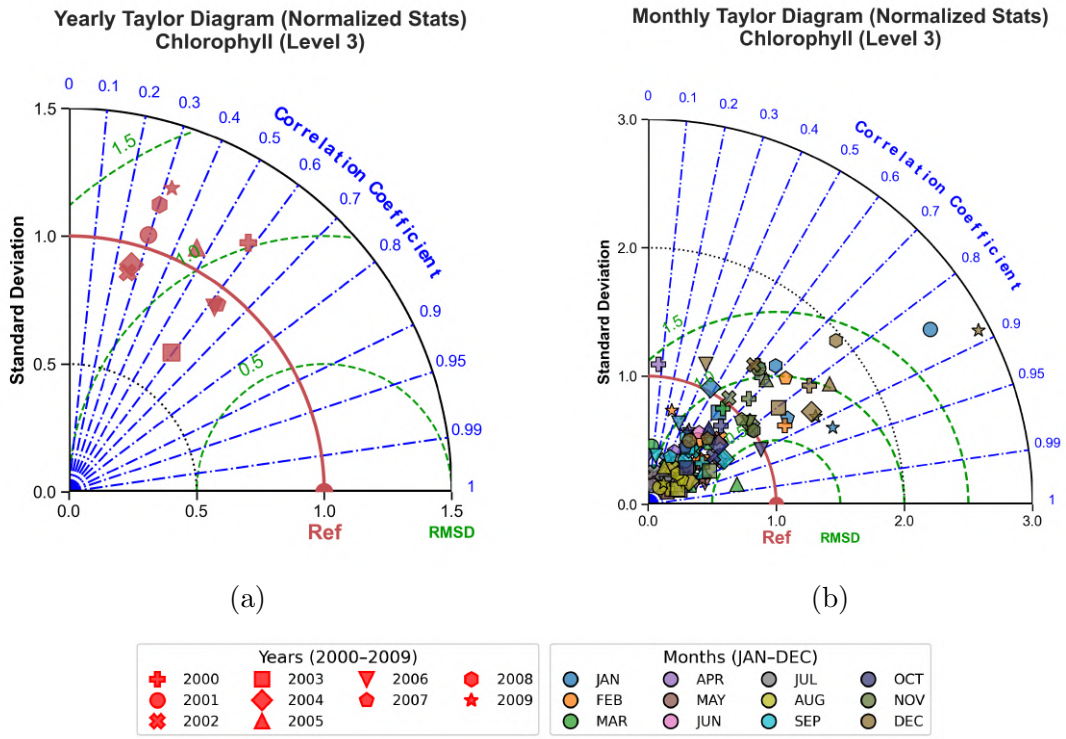

Figure 7.62: Taylor diagrams of the *Chlorophyll* − *a*: a) annual performance of the simulation, b) monthly performance. The values have been normalized to allow comparison between different months. The performance of each instance is defined based on the distance of the marker from the reference value, indicated by the red-colored **Ref** marker.

Observing the behavior of the annual markers reveals an unusual characteristic: almost all are distributed along varying values of standard deviation, yet correlations appear clustered around distinct levels, specifically near ~ 0.3 or ~ 0.6. The only notable exception is the marker for the year 2005, which records a correlation value of about ~ 0.45. This clustering suggests the presence of consistent underlying factors affecting the correlation patterns, possibly linked to interannual variability or specific climatic conditions during certain years.

The monthly markers, in contrast, show a more heterogeneous distribution, reflecting greater variability on shorter timescales. However, they are generally characterized by standard deviations lower than those of the reference marker, indicating improved relative performance at the monthly scale. In this case, the data cloud appears concentrated towards standard deviation values below ~ 0.5, which points to more consistent monthly agreement. Regarding correlation, the monthly markers also exhibit some variability, but they show an overall improvement compared to the annual scale, with most values falling within the range of ~ 0.4 to ~ 0.9. This broader correlation range indicates a more nuanced relationship between the modeled and observed data at the monthly level, likely reflecting seasonal dynamics and variability in model performance.

7.2.10 Spectral Analysis

To further investigate and better characterize the differences between the observed and simulated $Chlorophyll-a$ datasets a spectral analysis was conducted. The results are presented and illustrated in detail in *Figure 7.63*.

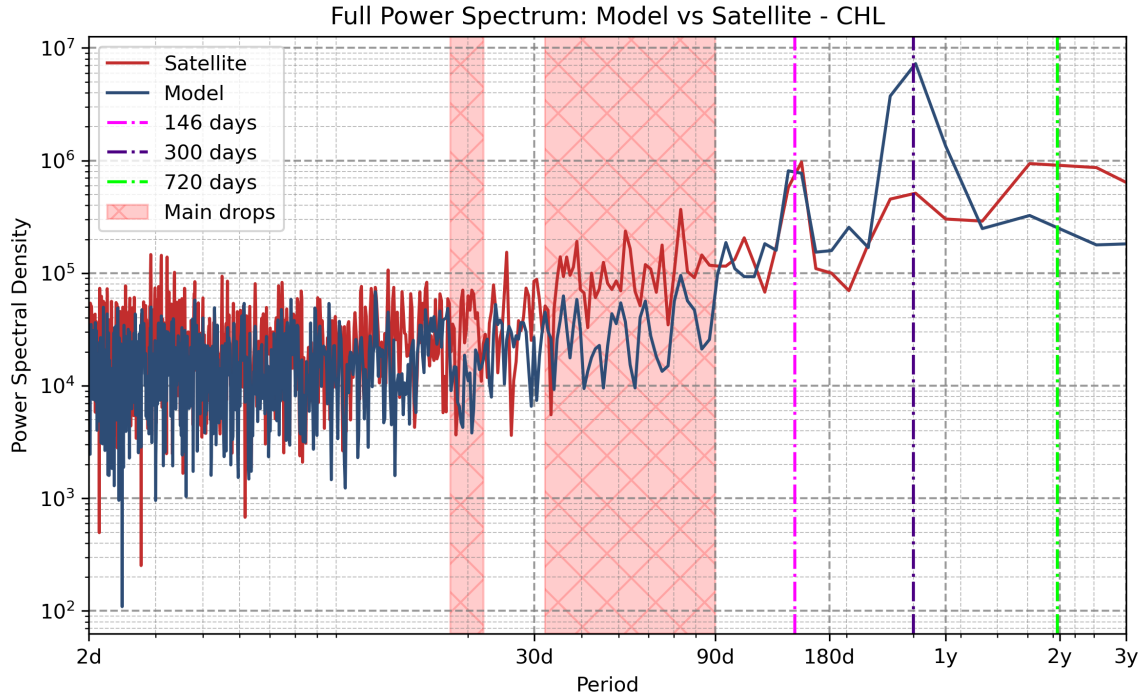

Figure 7.63: Power spectra of *Chlorophyll-a* from model (blue) and satellite (red) data, displayed on a double-logarithmic Power/Period scale (period in days). Key periods are highlighted in different colors, together with the regions where the model exhibits a power drop.

The analysis reveals significant differences between the observed and modeled data. Focusing on the medium-to-long term, it is observed that starting from a period of $\sim$ 18 to $\sim$ 22 days the model shows a reduction in spectral power, a phenomenon that becomes particularly pronounced from $\sim$ 32 days and persists up to about $\sim$ 90 days. Subsequently, within this time window, the two spectra show good agreement again, characterized by similar power values and a clear peak whose maximum value is found around $\sim$ 146 days.

Beyond this period, however, the two spectra diverge again, with an order-of-magnitude difference corresponding to a peak around $\sim$ 300 days, where the modeled data exhibits a markedly higher power compared to the observed data. This behavior appears specific to this peak: for longer periods, the modeled data tends to show lower power compared to the satellite data.

These findings align with those of previous sections. Simulated data display a winter bloom with an annual periodicity, along with a secondary peak at semiannual frequency, likely reflecting the model's attempt to reproduce late-spring and autumn blooms. In contrast, satellite data exhibit greater power around a period of $\sim$ 146 days, indicating a higher ability to capture these secondary events. However, the power associated with the winter bloom is lower than in the model, supporting the hypothesis that satellite observations cannot fully capture this peak. Furthermore, the observed data shows a peak around $\sim$ 720 *days*, with power comparable to that of the main cycle, suggesting the presence of multi-year oscillations not present within the simulation.

Within *Figure 7.64 a) and b)* are reported the filtered spectra, which show no additional phenomena.

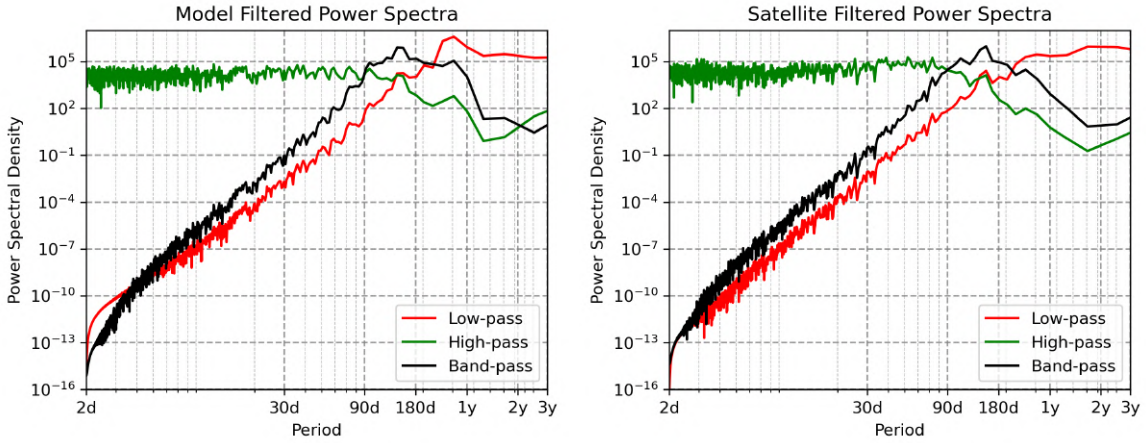

(a) (b)

Figure 7.64: Filtered power spectras of *Chlorophyll-a* data: a) model data, b) satellite data. Three filters are shown: *low-pass* (225 days), *band-pass* (90–225 days), and *high-pass* (90 days).

The analysis proceeds with the decomposition of the spectrum, the results of which are shown in *Figure 7.65*.

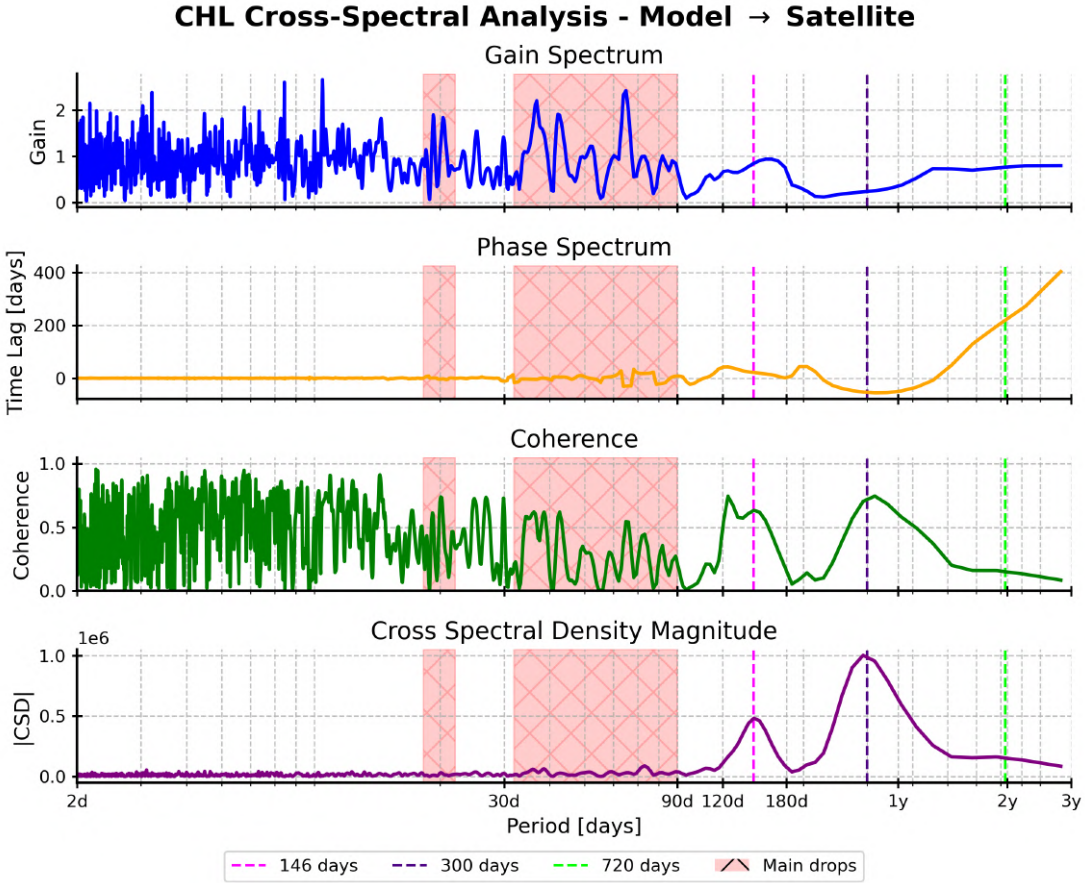

Figure 7.65: Spectral decomposition of the power spectra of the $Chlorophyll-a$ data. From top to bottom, in order: *Gain*, *Phase*, *Coherence*, and *Cross-Spectral Density Magnitude*. Key periods are marked with colored line, the colored areas match the ones plotted in the full spectra.

The analysis of the decomposition elements highlights several relevant and noteworthy phenomena. Firstly, there is a marked increase in the cross-spectral density at a period of approximately $\sim$ 146 days, which can be attributed to the power peak already identified and discussed in the earlier power spectrum analysis. Notably the gain for this period is close to 1.0, indicating the matching power of this peak between the datasets.

An increase in both coherence and cross-spectral density at longer periods, close to $\sim$ 300 days, can be attributed to the presence of a shared spectral peak in both the model and satellite datasets. Although this peak also appears in the satellite spectrum, it shows a noticeably lower power amplitude compared to the model output, thereby confirming and strengthening the findings of the previous spectral analysis. This difference indicates that the model tends to overrepresent annual or near-annual variability, while still maintaining a coherent signal with the observations, this is highlighted by the lower gain values meaning that the power of the model data is significantly higher than that of the satellite.

Furthermore, for the 720 *days* period peak, a higher gain can be observed, suggesting the presence of a multi-year component within both datasets. However, the *coherence* corresponding to this period is close to 0.0, indicating a mismatch between the peaks recorded in the two spectra. This interpretation is further supported by the pronounced increase in phase, which highlights how the model fails to correctly simulate and represent the multi-year variability of the chlorophyll within the basin.

It is also important to emphasize that the red-marked regions, which indicate areas where the model exhibits a relative loss of power in the full spectra, coincide with zones of increased gain, reflecting cases where the satellite data displays stronger spectral energy than the model. Interestingly, these same regions also show slightly elevated coherence values, suggesting that despite the difference in amplitude, the phase relationship between the two datasets remains relatively stable. This behavior points to a consistent underlying dynamic between modeled and observed processes, even when the magnitude of variability diverges.

7.3 Po's ROFI Area

7.3.1 Bio-physical Parameters Comparison to In-Situ Data

The validation of the biogeophysical parameters within the Po's River Plume was performed through two complementary distinct approaches. The first consisted of an integrated temporal analysis based on long-term historical time series of the main physical and biogeochemical variables. For this purpose, the observational stations were grouped into homogeneous classes according to their relative distance from the coastline (Section 4.2; *Figure 4.5*) hence building a gradient from the nearest coastal regimes for the ID 300 stations (300 m from the coast) up to an open sea regime with the ID 2000 (2 km from the coastline). The second focused instead on a point-by-point comparison between in situ measured vertical profiles and the corresponding profiles extracted from the model outputs. This method was aimed at evaluating the model's capability not only to reproduce the observed mean values but also to capture the vertical structure and stratification patterns that characterize the area's dynamics.

The first component of the analysis focused on reconstructing the surface field of Chlorophyll-a using in situ observations collected at an average depth of approximately 0.5 m below the surface. The resulting dataset was expressed in both the ARPAE measurement scale ($\mu g/L$) and the model's native scale (mg/m^3), ensuring consistency and comparability between datasets. It is important to emphasize that the reported values correspond to *observation means* rather than daily means, as the monitoring campaigns were conducted at irregular intervals, typically every 10–15 days. Consequently, the temporal distribution of the data was preserved in its original form, without interpolation, in order to maintain the integrity and fidelity of the actual sampling chronology. The time series derived from this analysis are presented in *Figure 7.66 (a–d)*.

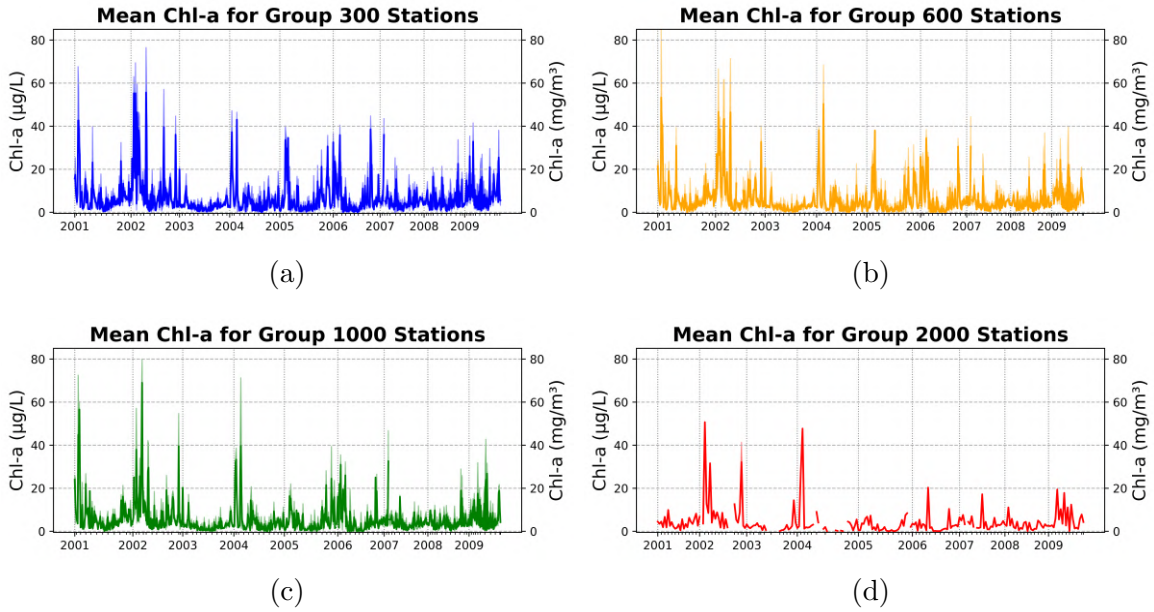

Figure 7.66: Time series of the *observation mean* of $Chl-a$ data obtained from the four groups of stations, grouped according to their distance from the coast: a) group 300 (3 km); b) group 600 (6 km); c) group 1000 (10 km); d) group 2000 (20 km). The lighter shaded area represents the standard deviation range associated with each observation.

The comparison with the *basin average time series* of the modelled and satellite data, originally presented in section 7.2.1 as *Figure 7.35*, highlights that the values recorded by the in-situ stations are significantly higher than those provided by both the model and the satellite. Despite this clear discrepancy in absolute terms, it is possible to observe that the series derived from the observations exhibit a similar cyclicity to that simulated, particularly characterized by a pronounced winter peak.

To further investigate this aspect, a *seasonal decomposition* was carried out with the aim of extracting the *trend* component (*linear fit*) and the seasonal component (30-day centered moving average) from the observed time series, in order to compare their behaviour with those of the satellite and simulated datasets. The results of the seasonal decomposition are shown in *Figure 7.67*. Since the phenomenon is particularly evident during the period between 2003 and 2007, the graphical representation has been limited to these years to highlight the most relevant features of the signal.

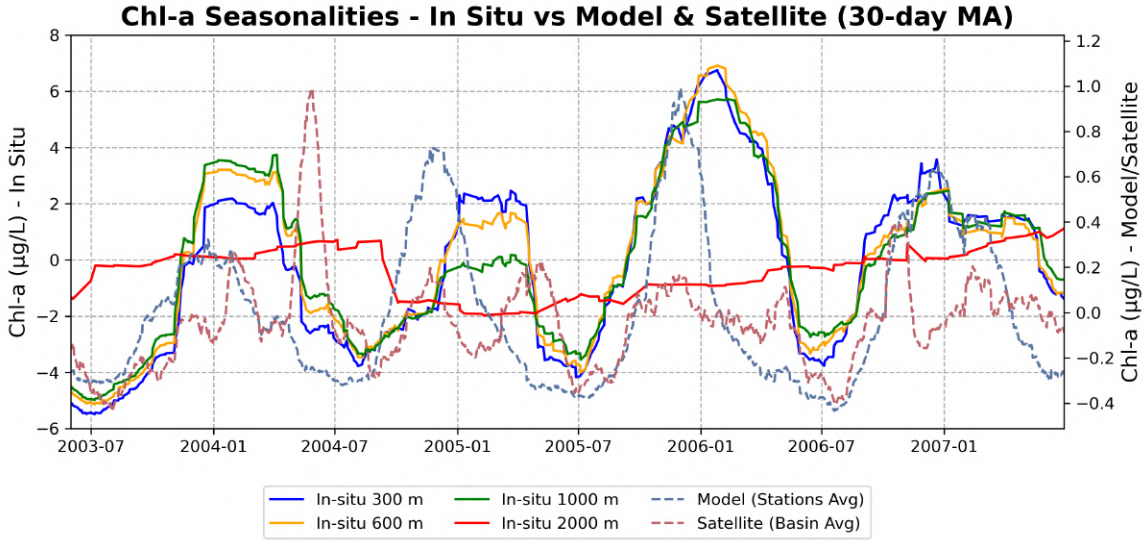

Figure 7.67: Results of the *seasonal decomposition* applied to satellite, observational, and simulated data. The graph is restricted to the years 2003–2007 to highlight the matching seasonalities between model and stations data. The observed data is shown using solid lines, with a color-coding that matches the already defined groups (300 blue; 600 orange; 1000 green and 2000 red) while the other datasets are shown as dashed lines. The model data is created by extracting the chlorophyll values at the exact location of the in-situ stations.

The results of the *seasonality* clearly reveal the presence, within the in-situ observations, of a dominant winter peak, which gives the chlorophyll cycle a pattern much more similar to the simulated one than to that derived from the satellite data. However, a slight phase shift between the two series can be observed: while the model places the main peak between December and January, the in-situ observations record it between January and February.

The analysis of lag-correlations between the two *time series* further confirms this difference, clearly indicating a temporal shift in the model's ability to reproduce the observed variability. The highest correlation values are obtained when a lag of +1 month is applied to the simulated seasonal component, suggesting that the model tends to reproduce the observed signal with a slight temporal delay.

The quantitative results of the correlation analysis are reported in *Table 7.8*.

Series	2001–2009		2003–2007	
	Group	**Correlation**	**Group**	**Correlation**
`Model`	300	0.457	300	0.562
	600	0.470	600	0.506
	1000	0.481	1000	0.495
	2000	−0.10	2000	−0.016
`Satellite`	300	0.364	300	0.396
	600	0.372	600	0.455
	1000	0.401	1000	0.478
	2000	0.360	2000	0.199

Table 7.8: Correlation between the model and the in-situ observations, divided into groups 300, 600, 1000, and 2000 m, for the full period 2001–2009 and the sub-window 2003–2007. Correlation values for the satellite–observations comparison for the same groups and time windows are also reported.

Analyzing the correlation values obtained using the *Pearson* index, it is observed that, both when considering the entire available observation period (2001–2009) and when restricting the analysis to the sub-window (2003–2007), the model generally exhibits slightly better performance compared to the satellite data for groups 300, 600, and 1000. This indicates that, for these groups, the model is able to capture the temporal variability of the observed signal with a higher degree of consistency.

A different behaviour is observed for group 2000: in this case, the model data show an almost negligible correlation with the *in-situ* observations, suggesting a limited capability of the simulation to represent the dynamics at that specific depth or location. Conversely, the satellite product displays a positive, albeit modest, correlation that tends to slightly decrease (by approximately ~ -0.1) in the 2003–2007 sub-window.

These results suggest that the model's *basin average* data are able to represent more realistically the seasonal dynamics of $Chlorophyll - a$ concentration in areas close to the coast. As the distance from the coast increases, and in particular beyond a threshold presumably between $10 \div 20$ km, the satellite representation appears instead to be a more suitable proxy for basin-scale phytoplankton dynamics.

The correlation values for the lag case are presented separately in *Table 7.9*.

Series (2003-2007)	**Lag 0**	**Lag +1**	**Lag +2**
`Model -- Group 300`	0.562	0.669	0.621
`Model -- Group 2000`	−0.016	0.081	0.032
`Satellite -- Group 300`	0.396	0.213	0.013
`Satellite -- Group 2000`	0.199	0.298	0.252

Table 7.9: Time-lagged correlation between the model and satellite compared to the in-situ observations for groups 300 m and 2000 m. Values are reported for lags of 0, +1, and +2 months.

Assuming a temporal lag of the model and satellite data between 0 and +2 months, a clear and progressive improvement in the correlation values produced by the model

is observed for the groups located closest to the coast. In particular, the correlation reaches its maximum at a lag of +1 month, suggesting that the simulated seasonal dynamics occur slightly later than those observed. At a lag of +2 months, a marginal decrease in correlation is observed, although the values remain higher than those recorded in the absence of any temporal shift, thereby confirming the presence of a consistent phase delay in the model's reproduction of chlorophyll variability.

Conversely, the satellite data show a distinctly different behaviour. For the coastal group (300), the correlation values deteriorate markedly as soon as a lag is introduced, both at +1 and +2 months, indicating that the satellite-derived product tends to be more temporally aligned with the observations. For the offshore group (2000), however, the satellite dataset shows a modest increase in correlation at a lag of +1 month, suggesting a limited phase shift in this sector, though for longer lags the correlation values again decline.

To complete the validation analyses of the chlorophyll field, temporal trends (*linear fits*) were estimated for each station group using both the model and satellite datasets. These trends provide an additional diagnostic measure of the model's ability to capture long-term variations in chlorophyll concentration. The resulting values are reported in *Figure 7.68*, where a dual vertical scale was adopted to facilitate the visualization and comparison of the model and satellite trends, whose magnitudes are particularly small following conversion to $\mu g/L/yr$.

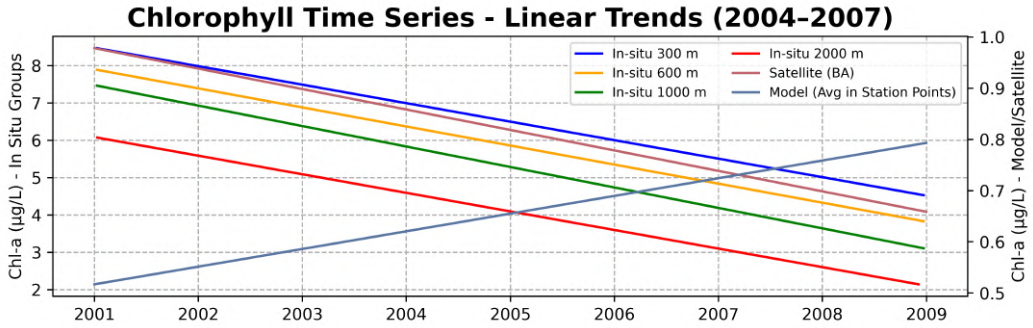

Figure 7.68: Graph of trends calculated from the *basin average* time series of the satellite data and the station's locations for both the model data and the *in-situ* stations. Two vertical scales with different intervals ($\mu g/L$) are shown to facilitate the reading of the model and satellite trends.

Upon examining the results, a discrepancy can be seen between the trend estimated from the model data and those derived from both the in situ observations and the satellite-based time series. Specifically, the observational and satellite datasets display an overall negative trend in the basin-wide mean concentration of *Chlorophyll–a*. This coherent downward tendency has been widely interpreted in the regional scientific literature as indicative of a gradual reduction in the eutrophic conditions observed along the coastal zones of the Northern Adriatic (Giani et al., 2012; Ricci et al., 2022; Marini and Grilli, 2023). Such a trend is often associated with a broader, long-term process of *oligotrophication* within the basin, reflecting improvements in nutrient management and a corresponding decline in primary productivity.

In contrast, the model exhibits a markedly different behavior, displaying a counter-trend characterized by an overall increase in the simulated mean concentration of

chlorophyll across the analyzed period. This opposing tendency suggests that the model may overestimate phytoplankton biomass or insufficiently capture the mechanisms driving nutrient reduction and trophic decline observed in situ. The quantitative slopes of the linear regressions computed for each group and dataset are presented in *Table 7.10*, confirming the consistency of this divergence across the different datasets.

Element	**Slope** ($\mu g/L/yr$)
`Model`	$+0.2829$
`Satellite`	-0.1950
`Group 300`	-0.5743
`Group 600`	-0.5761
`Group 1000`	-0.6353
`Group 2000`	-0.5624

Table 7.10: Slope of the linear trend (*linear fit*) for the Model, Satellite, and each station group. The values refer exclusively to the period from 01-01-2001 to 31-12-2007.

Following the comparative analysis of the $Chlorophyll-a$ field against satellite and model datasets, the validation of the simulation was extended to other key physical and biogeochemical parameters: mean dissolved oxygen concentration, temperature, and salinity. For each variable, the *in-situ* station data were analyzed through their respective *time series*, anomalies relative to climatological values, and vertical profiles, and subsequently compared with the corresponding model outputs.

The first phase of the analysis consisted of a direct comparison between the modelled *time series* and those derived from *in-situ* measurements. The results of this comparison are presented in *Figure 7.69 (a–d)*.

Starting with the salinity field, a general agreement between simulated data and observations can be noted, although the model tends to reproduce variations of smaller amplitude than those measured at the monitoring stations.

For the temperature field, the agreement is also generally satisfactory; however, the model systematically exhibits a lag of approximately +1 month with respect to the observations across the entire simulation period. This behaviour is the inverse of what was identified for the $Chlorophyll-a$ parameter, where the model anticipated the seasonal cycle by roughly one month relative to the *in-situ* data.

In the case of dissolved oxygen, the seasonal dynamics display more pronounced discrepancies. During the first years following model initialization, the onset of the annual oxygen peak occurs almost simultaneously in both the observations and the simulation. Over time, however, the model tends to reproduce longer-lasting high-concentration phases, with elevated oxygen levels persisting for up to two months beyond those recorded by the stations. This behaviour progressively leads to the accumulation of a lag in the cyclicity of the phenomenon, becoming particularly evident from 2007 onward, when the simulated oxygen maxima occur with delays of up to six months compared to the observations.

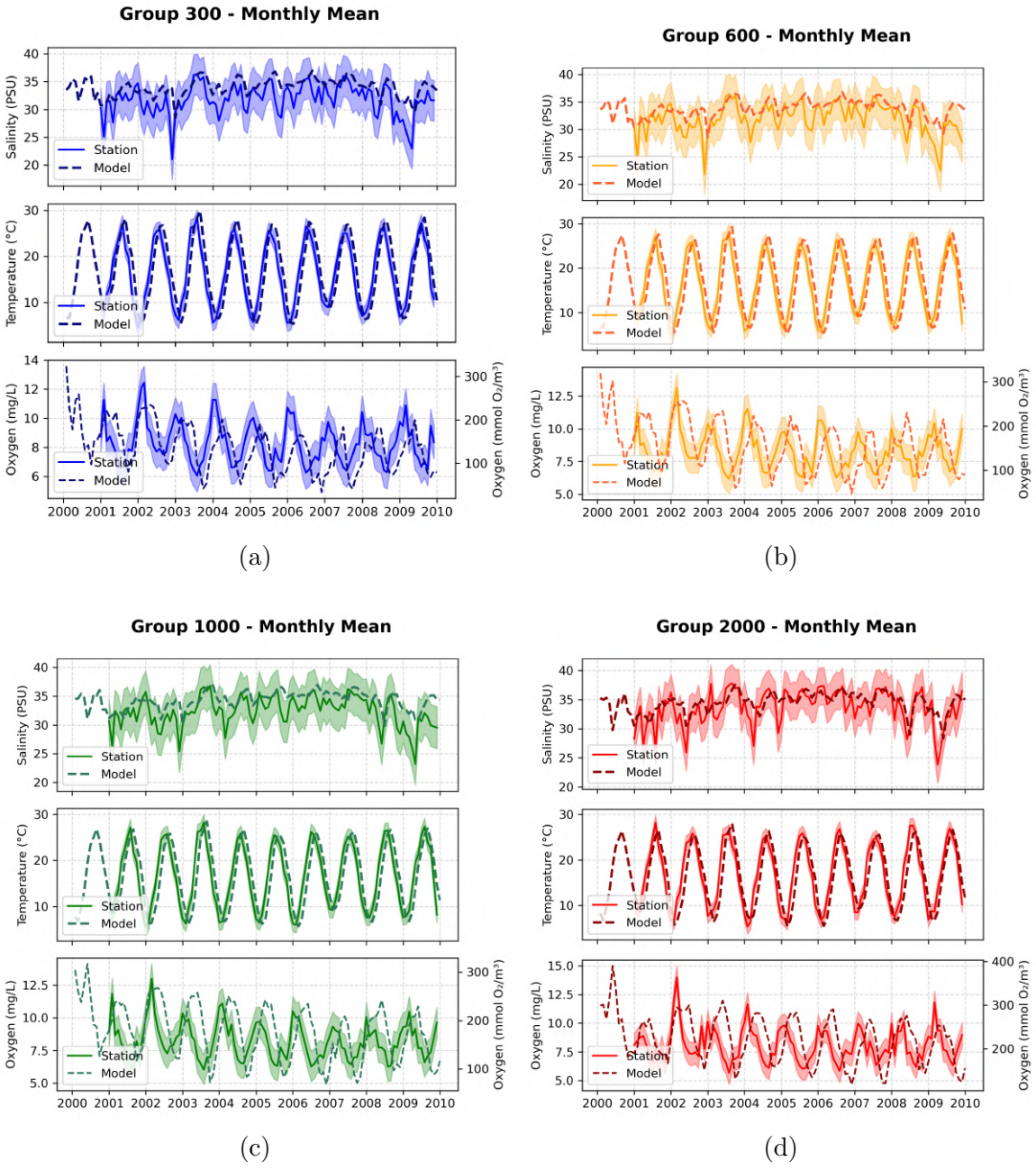

Figure 7.69: Series of comparison plots between the *monthly mean timeseries* of model data and *in-situ* observations. Each panel, from top to bottom, shows: salinity (psu), temperature ($°C$), and dissolved oxygen concentration. Dissolved oxygen is represented using two different scales: the native observational scale (mg/L) and the model scale ($mmol/m^3$). For each plot, observations are shown as solid lines with shaded areas indicating the standard deviation, while model data are shown as dashed lines. Panels correspond to station groups as follows: a) 300 m; b) 600 m; c) 1000 m; d) 2000 m.

The subsequent analysis revolved around the study of the anomaly timeseries, shown in *Figure 7.70 a) to d).*

Analyzing the salinity anomaly field, a good agreement emerges between the simulated and observed anomalies: although the amplitude of the modelled anomalies is generally lower than that measured in situ, the interannual pattern appears to be well reproduced.

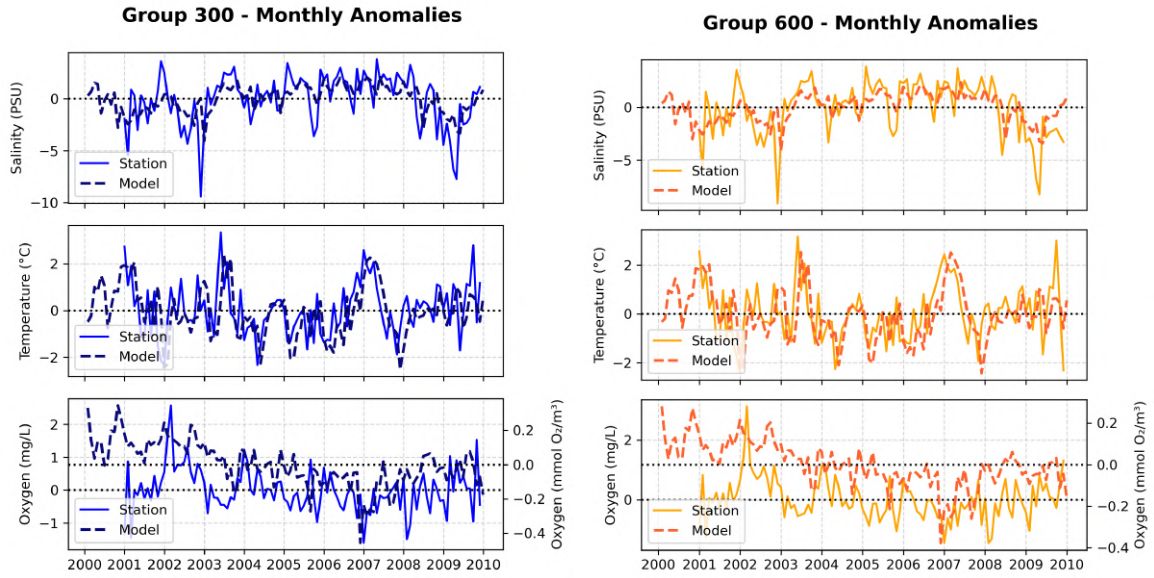

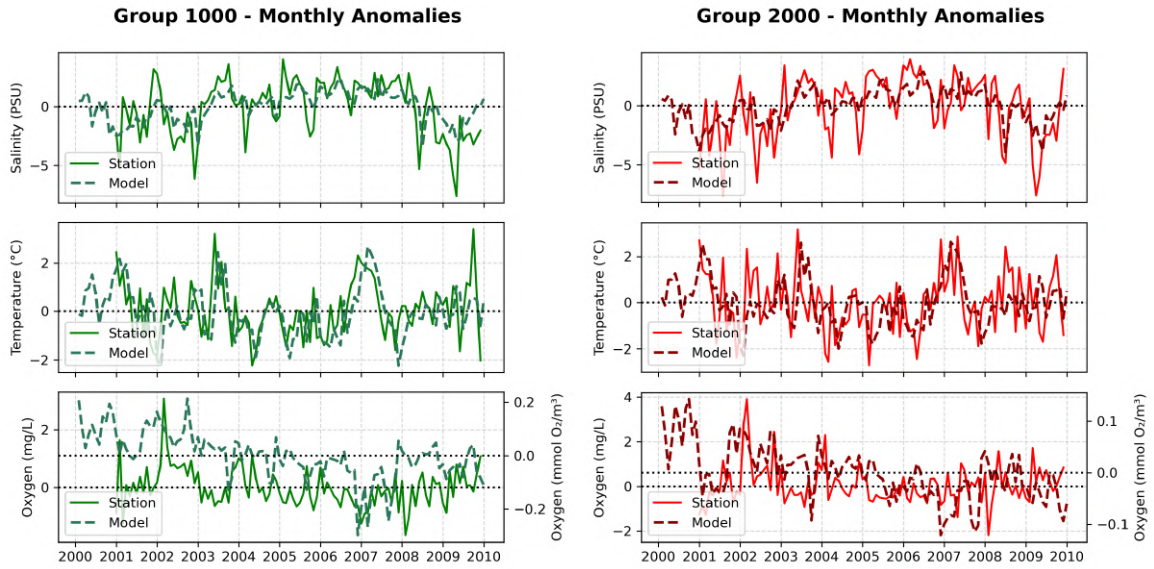

Figure 7.70: Series of comparison plots between anomalies derived from the *monthly mean timeseries* of model data and *in-situ* observations. Each panel, from top to bottom, shows: salinity anomalies (psu), temperature anomalies ($°C$), and dissolved oxygen anomalies. Dissolved oxygen anomalies are represented using two different scales: the native observational scale (mg/L) and the model scale ($mmol/m^3$). For each plot, observations are shown as solid lines with shaded areas indicating the standard deviation, while model data are shown as dashed lines. Panels correspond to station groups as follows: a) 300 m; b) 600 m; c) 1000 m; d) 2000 m.

A more detailed examination of the interannual variability of this field reveals clear temporal patterns. During the period 2001–2003, the observed anomalies are predominantly negative, indicating below-average conditions. From 2003 to 2008, a progressive increase in anomalies is evident, with values gradually stabilizing at positive levels, suggesting a period of relatively elevated conditions. Following 2008, the series once again exhibits distinctly negative anomalies. The simulation is able to closely track these dynamics, coherently reproducing the general evolution of the anomalies

over the entire time span under consideration, and capturing both the timing and magnitude of the main transitions.

Temperature anomalies are similarly well represented by the model, with both amplitude and temporal patterns showing a high degree of consistency with the station observations. Nonetheless, some discrepancies are apparent. A particularly notable case occurs in winter 2007, when a pronounced positive anomaly is recorded. While the simulation accurately reproduces the intensity of this peak, it introduces a temporal lag: for stations belonging to group 1000, the model's anomaly occurs approximately +2 months later than the observed peak. This lag diminishes progressively toward the coast, where the model exhibits improved temporal alignment with the in-situ measurements, suggesting a spatial dependence of the model's phase accuracy.

Oxygen anomaly data exhibit the largest discrepancies when compared to observations. In addition to notable differences in anomaly amplitude, the simulated data display a clear negative trend over time, whereas the slope of the observed anomalies is essentially negligible. This indicates that the model tends to overestimate the long-term decrease in oxygen concentration relative to in-situ measurements. Quantitative details of these discrepancies, including slope values for each layer and station group, are reported in *Table 7.11*.

Group	**Anomaly trend (situ, mmol/m^3/yr)**	**Anomaly trend (model, mmol/m^3/yr)**
300	−1.6043	−0.0250301
600	−2.01379	−0.0212209
1000	−1.9743	−0.0161473
2000	−0.74133	−0.0083897

Table 7.11: Trends of oxygen anomalies for each station group, comparing observed data (*situ*) and modelled data (*model*). Values for the in-situ observations are converted into $mmol/m^3/yr$ to allow for a direct comparison between the datasets.

Examining the oxygen-related graphs, particularly those showing anomalies, reveals a distinct change in trend around early 2007. This behaviour aligns with the shift previously observed in the chlorophyll field, suggesting a comparable change in system dynamics across both datasets during this period.

Time series decomposition, applied to both mean data and anomalies using the same breakpoint as in the chlorophyll analysis (01-01-2007), clearly highlights a regime shift associated with this date. The shift appears as a marked change in time series behaviour, particularly evident in the anomaly field, which shows a clear trend reversal. This effect is strongest along the coastal band, where the change is most pronounced. A detailed representation of this phenomenon is shown in *Figure 7.71*.

Within the model, this phenomenon is most evident near the coastline, where it appears clearly marked. Its intensity progressively decreases offshore, indicating a distinct spatial gradient. Data from monitoring stations show a comparable pattern, confirming the coastal-to-offshore gradient; however, the magnitude observed in the measurements is considerably stronger than that reproduced by the model.

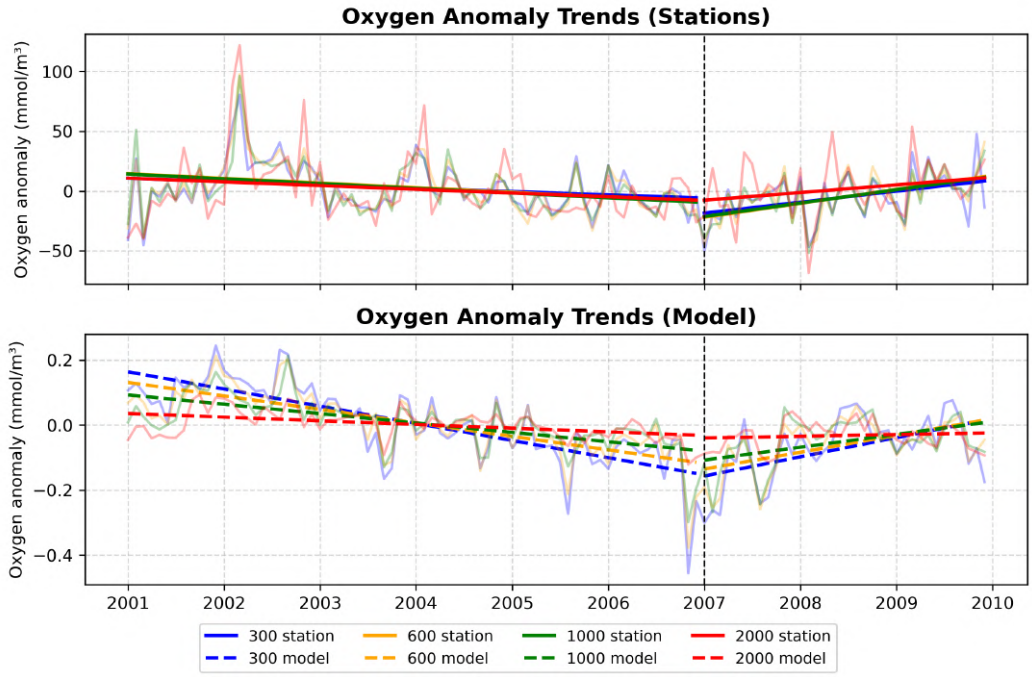

Figure 7.71: Graph of the trends of oxygen anomalies. The color of each trend corresponds to the group of origin stations, while the vertical line indicates the *breakpoint*. From top to bottom: results from *in-situ* stations; results from the model sampled at the corresponding geographic locations.

Detailed values and comparisons are reported in *Table 7.12*.

Group	Pre-2007		Post-2007	
	Station	Model	Station	Model
	(mmol/m^3/yr)		(mmol/m^3/yr)	
300	−2.77	−0.05	9.20	0.06
600	−3.89	−0.04	11.72	0.05
1000	−3.97	−0.03	11.23	0.04
2000	−3.11	−0.01	6.42	0.01

Table 7.12: Trend of the anomalies before and after the *breakpoint* (Jan 1st 2007) computed from model and in-situ data. The results are grouped according to the station's group ID (300, 600, 1000 and 2000).

The time series analysis done using the full data confirms that the effect is more moderate than that observed in the anomalies. Rather than a true inversion of the trend, the data reveal a clear attenuation, reflected in a gradual flattening of the trend line. This behavior indicates a slowdown in the rate of change, suggesting that the system is approaching a quasi-stationary state. Nonetheless, the overall trend remains negative throughout the observation period, meaning the variable continues to decrease, albeit more slowly. A detailed representation of the trends derived from the time series is shown in *Figure 7.72*.

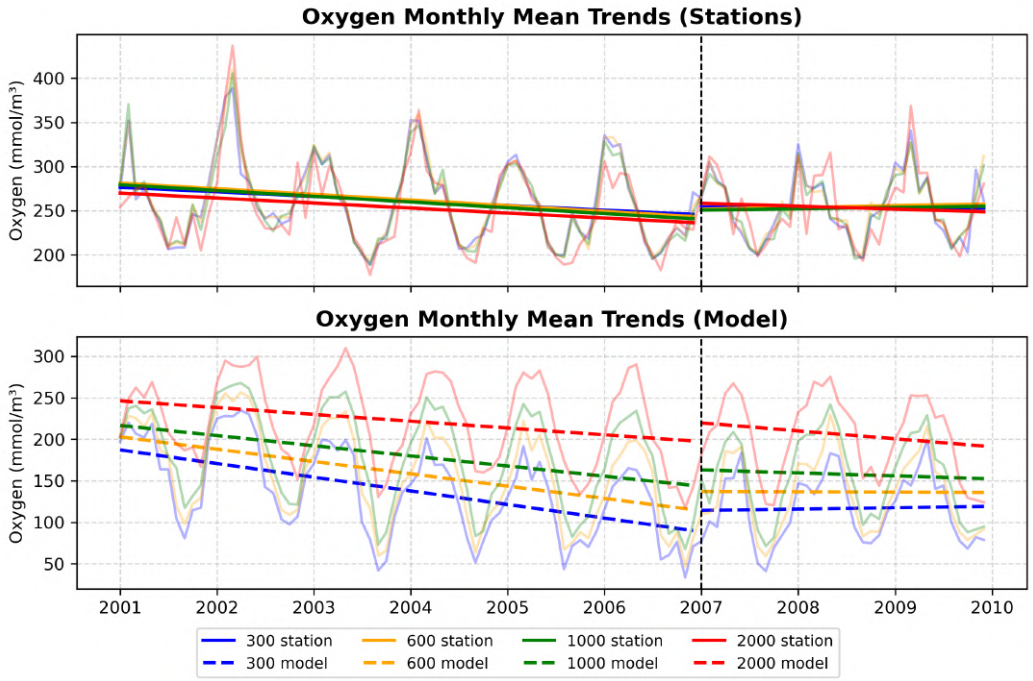

Figure 7.72: Graph of the trends of oxygen time series. The color of each trend corresponds to the group of origin stations, while the vertical line indicates the *breakpoint* used to define the time windows for calculation. From top to bottom: results from *in-situ* stations; results from the model sampled at the corresponding geographic locations.

The value of each trend is reported within *Table 7.13*.

Group	**Pre-2007**		**Post-2007**	
	Station	**Model**	**Station**	**Model**
	($mmol/m^3/yr$)		($mmol/m^3/yr$)	
300	−5.18	−16.45	−0.46	+1.66
600	−6.40	−14.83	+2.02	−0.46
1000	−6.51	−12.24	+1.47	−3.53
2000	−5.66	−8.20	−3.27	−9.55

Table 7.13: Trend of the group means before and after the *breakpoint* (Jan 1st 2007) computed from model and in-situ data. The results are grouped according to the station's group ID.

As a final note regarding the subject of the time series analysis, it should be highlighted that *Table 7.14* reports the correlation values obtained through the application of the Pearson correlation index.

Variable	**Group 300**		**Group 600**		**Group 1000**		**Group 2000**	
	Mean	Anom	Mean	Anom	Mean	Anom	Mean	Anom
Oxygen	0.5615	0.4236	0.5407	0.4052	0.5926	0.3592	0.5084	0.1753
Salinity	0.8440	0.8388	0.8508	0.8454	0.8467	0.8473	0.7610	0.7338
Temperature	0.9952	0.8515	0.9938	0.8195	0.9121	0.8236	0.9881	0.6343

Table 7.14: Pearson correlation coefficients for each variable and station group.

7.3.2 Vertical Profiles

The final validation step of the simulation within the Po River ROFI involved creating a series of vertical profiles in order to compare modelled data with observations provided by ARPAE. The profiles were depth-limited to the end of the first available profile, meaning that each series was truncated at the maximum depth common to both the model and the observations.

The first vertical profiles under analysis are the salinity profiles, shown in *Figure 7.73*.

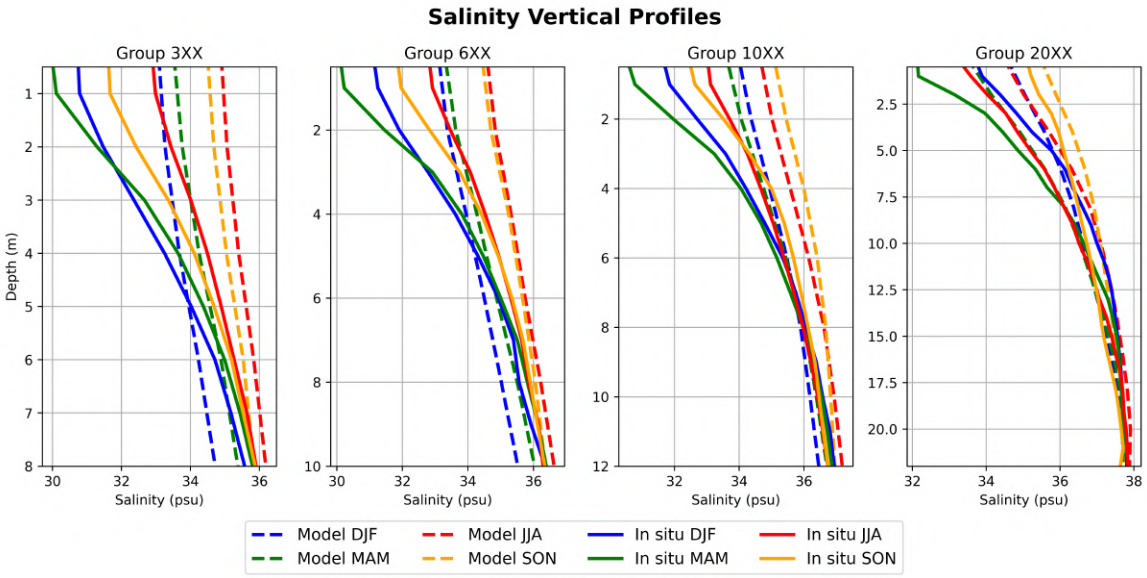

Figure 7.73: Vertical salinity profiles for the comparison between observed data (solid line) and simulated data (dashed line). From left to right: first panel, profiles for group 300 with simulated data at the same coordinates; second panel, group 600; third panel, group 1000; fourth panel, group 2000.

Analysis of the vertical profiles shows that, for all station groups, there are significant discrepancies near the free surface, with a maximum difference of approximately $\sim$ 4 psu. This difference tends to decrease moving away from the coast, dropping to about $\sim$ 2 psu. Furthermore, the discrepancies display a clear seasonal dependence, with the spring period (**MAM**) recording the highest differences between observed and simulated data, likely reflecting the increased influence of freshwater inputs and mixing processes during this period.

Within groups 300 and 600, a notable difference in the shape of the vertical profiles is also observed: the simulated profiles tend to decrease almost linearly with depth, whereas the observed profiles exhibit greater variability, with occasional local maxima and inflection points. The agreement is slightly better in group 600, though only marginally, suggesting a moderate improvement in model performance as distance from the coast increases. This discrepancy is likely due to the limited vertical resolution of the model ($dz = 2$ m), which prevents an accurate reproduction of the finer details of the vertical profile, particularly those influenced by sharp thermohaline gradients or mesoscale processes within the area.

Moving further away from the coast, the simulated profiles show greater agreement with the observations. In particular, beyond approximately $\sim$ 8 m depth, the two

profiles almost overlap, indicating a good match between the datasets and suggesting that the model better captures deeper stratification patterns. The best results are therefore observed in group 2000, which shows the highest coherence, although some superficial differences remain; these differences, while smaller than in groups closer to the coast, are still present and may be attributed to local variability not captured by the model.

The next vertical profiles under analysis are the temperature profiles, presented in the graphs shown in *Figure 7.74*.

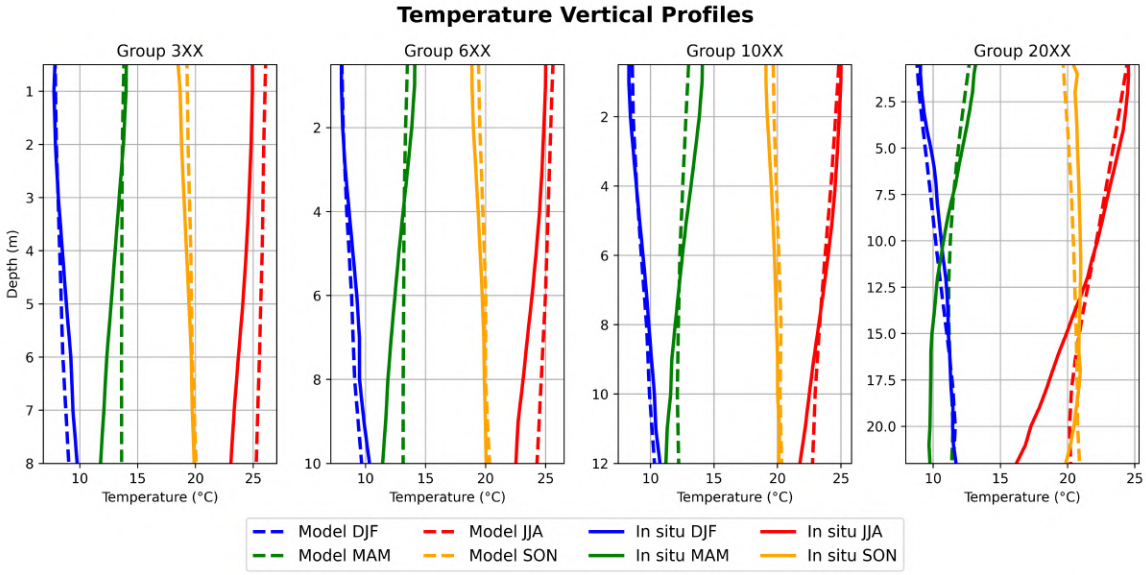

Figure 7.74: Vertical temperature profiles for the comparison between observed data (solid line) and simulated data (dashed line). From left to right: first panel, profiles for group 300 with simulated data in the same coordinates; second panel, group 600; third panel, group 1000; fourth panel, group 2000.

The analysis of the vertical temperature profiles also reveals some discrepancies. Although surface values generally show good agreement between the two datasets, the vertical profiles highlight substantial differences in the distribution of temperature with depth, reflecting limitations in reproducing the full vertical thermohaline structure.

In all station groups, it is possible to observe that during the winter (**DJF**) and autumn (**SON**) seasons there is good agreement both in surface temperature values and in the shape and trend of the corresponding vertical profiles, likely due to more homogeneous water column conditions and reduced stratification during these periods. Conversely, the spring (**MAM**) and summer (**JJA**) seasons show substantial differences. Although surface temperatures generally agree between model and observations, with the only exceptions being a slight underestimation by the model during **MAM** in group 1000 and a slight overestimation during **JJA** in group 300, the vertical profiles diverge significantly with increasing depth. In particular, the model systematically tends to overestimate the observed temperature, with discrepancies becoming more pronounced in deeper layers.

This phenomenon is particularly evident during **JJA** within group 2000, where the differences between the two vertical profiles at the maximum considered depth ($\sim$

22.0 m) reach approximately $\sim 4°$ C. Such differences suggest that the model may inadequately capture seasonal stratification strength or mixing processes, especially in summer months, possibly due to limitations in vertical resolution or parameterizations at the benthic layer.

The last vertical profiles analyzed are the mean dissolved oxygen concentration profiles, shown in *Figure 7.75*.

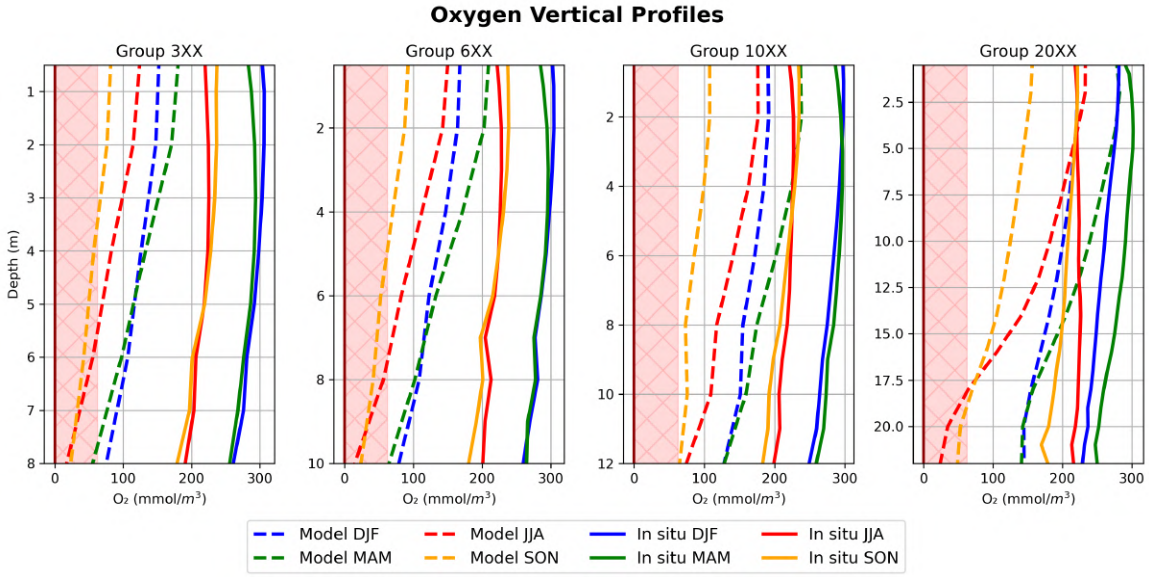

Figure 7.75: Vertical profiles of mean oxygen concentration for the comparison between observed data (solid line) and simulated data (dashed line). From left to right: first panel, profiles for group 300 with simulated data in the same coordinates; second panel, group 600; third panel, group 1000; fourth panel, group 2000. Hypoxy range is shown as a red area with the dark-red line marking anoxy.

These vertical profiles show the poorest performance, revealing a general disagreement both in surface and bottom values. The shapes of the vertical profiles differ substantially: the observed profiles are almost vertical, while the simulated profiles show a progressive decrease towards values close to zero.

As an additional validation dataset, the values obtained from CTD probe sampling conducted by ENEA in 2006 were used, with details provided in Section 4.2.1. The measurement stations were considered as a whole, without further spatial subdivision, and the resulting vertical profiles are presented in *Figure 7.76*.

Examining the temperature profiles reveals a good agreement between simulated and observed data. The main discrepancies occur during the **DJF** and **MAM** seasons, starting from depths greater than 9 m and becoming more pronounced below 12 m. These differences are likely due to the limited number of observations available at such depths and near the seabed. Conversely, during the **JJA** and **SON** seasons, a high level of coherence between the model and the observations is observed throughout most of the water column, except for some localized discrepancies in the deeper layers, which are also plausibly related to the sparse observational coverage.

The salinity profiles show a behavior similar to that already observed in comparison with the ARPAE data, characterized by marked discrepancies in the surface layers, where the model tends to overestimate the observed values with maximum differences

on the order of $\sim$ 3–4 *psu*. These differences progressively decrease with depth, eventually showing a good agreement between simulation and observations in the deeper layers of the water column.

Oxygen profiles also show the discrepancies already observed in previous analyses, which in this case appear even more pronounced. The model once again tends to fall into *hypoxic* regimes, particularly during the **SON** and **JJA** seasons, while the observed data indicates high oxygen concentrations, sometimes under *hyperoxic* conditions, especially in the **MAM** season and near the seabed. This latter behavior raises doubts about the validity of the observed measurements as official reports from ISPRA do not report any evidence of *hyperoxic* phenomena throughout the year 2006 in the area of the CTD sampling, reinforcing the hypothesis that the observed high concentrations may be the result of instrumental anomalies or transient local conditions that are not representative of the general behavior of the system.

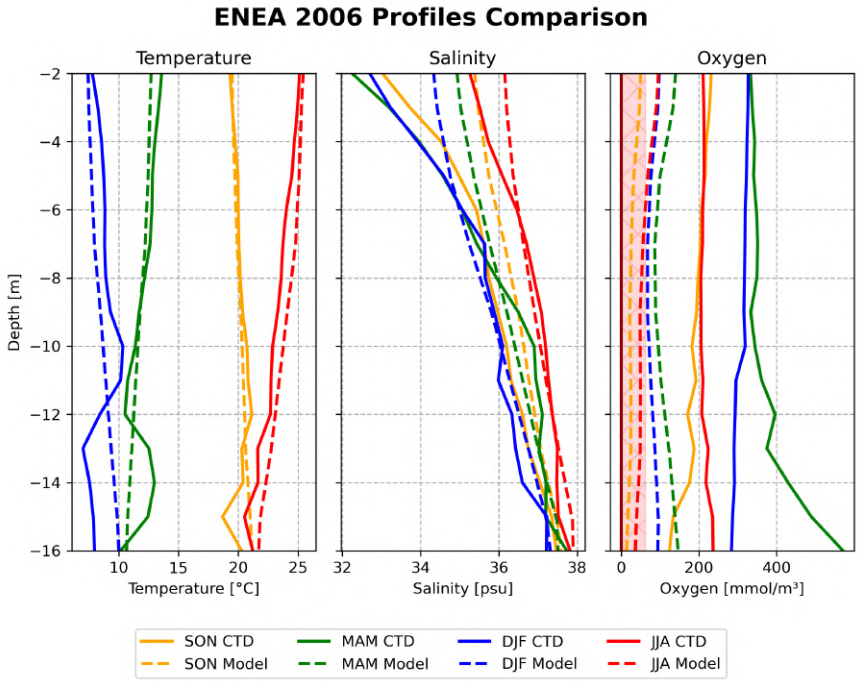

Figure 7.76: Vertical profiles of mean temperature, salinity and oxygen concentration for the comparison between observed data (solid line) and simulated data (dashed line). Hypoxy range is shown as a red area with the dark-red line marking anoxy.

7.3.3 Po's River Effect Using Chlorophyll as a Chemical Tracer

Having verified the behavior of the main bio-geophysical components within the ROFI influence area, a physical validation of the general surface circulation in the same region is performed, in order to identify possible discrepancies between the observed and simulated behavior. To this end, the current generated by the effect of the Po River plume is reconstructed, using the $Chlorophyll - a$ field as a chemical tracer.

Once the ROFI influence area has been defined according to the *clustering* method described in Section 6.9.1, the *bloom* phenomena are extracted following the procedure detailed in Section 6.9.2. After identifying the *bloom* area, the resulting centroids are shown in *Figure 7.77 a) and b).*

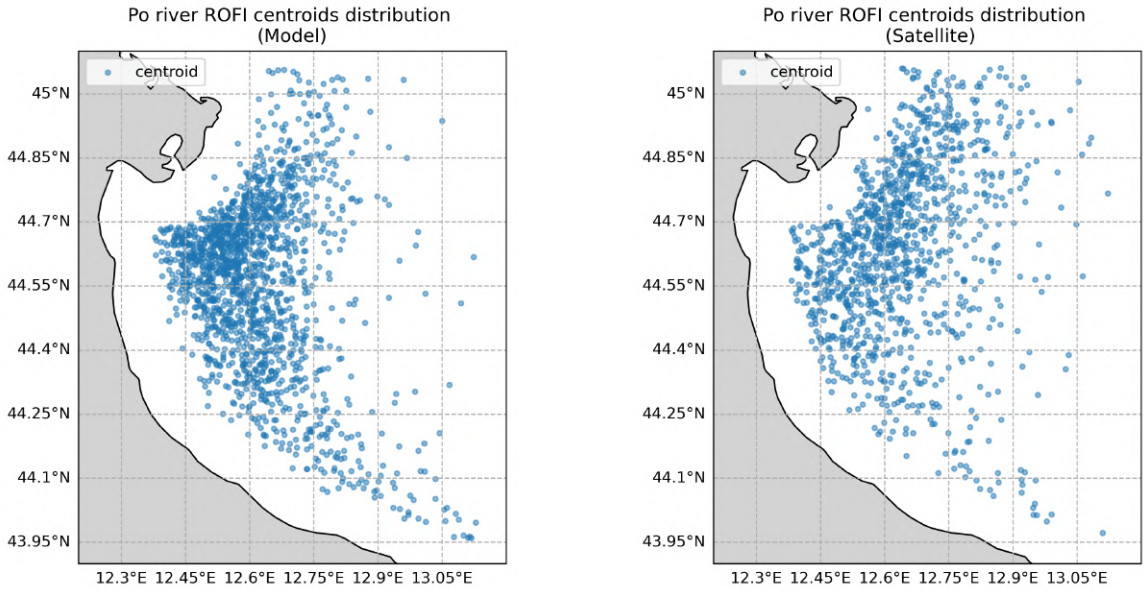

(a) (b)

Figure 7.77: Comparison of the spatial distribution of daily chlorophyll centroids obtained from model data (left) and satellite (right).

The centroids derived from model data appear more concentrated, with a higher density of points southeast of the Po River mouth. Conversely, those from satellite data are more scattered, as also evident in the corresponding *Hexbin* representation shown in *Figure 7.78*.

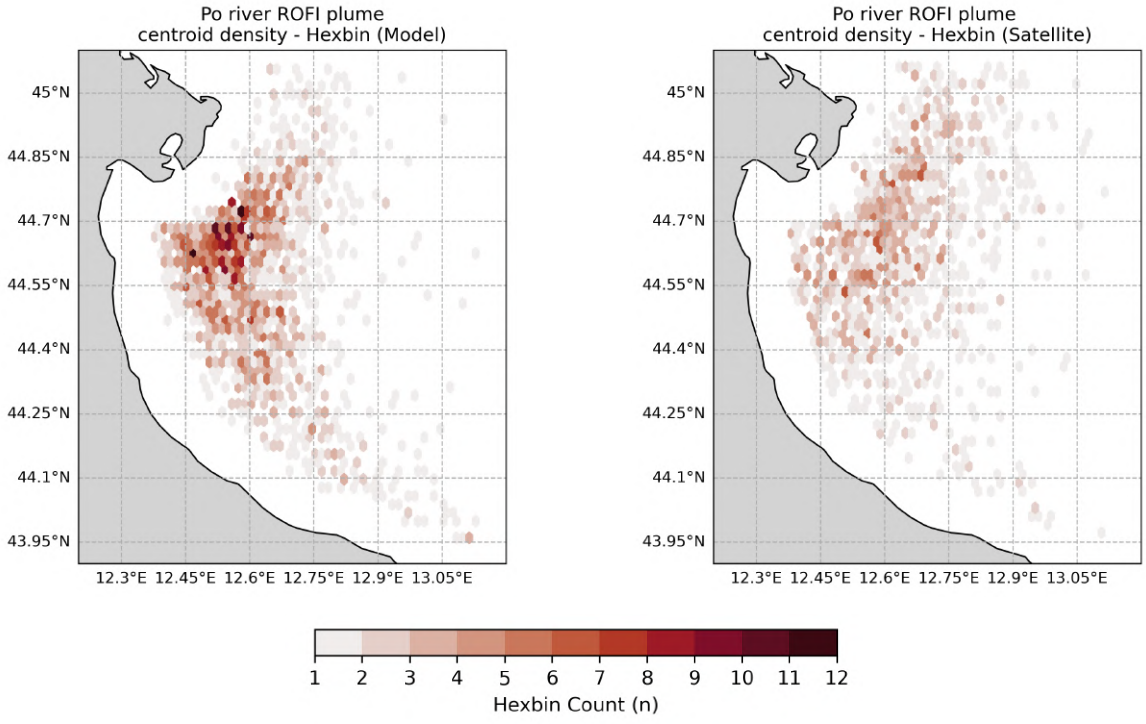

Figure 7.78: Comparison of the *hexbin* density results obtained using the model data (left) and satellite data (right).

The same discrepancies in centroid density that are evident in the *hexbin* representation also emerge when examining the corresponding Kernel Density Estimates (KDEs), as reported in *Figure 7.79*.

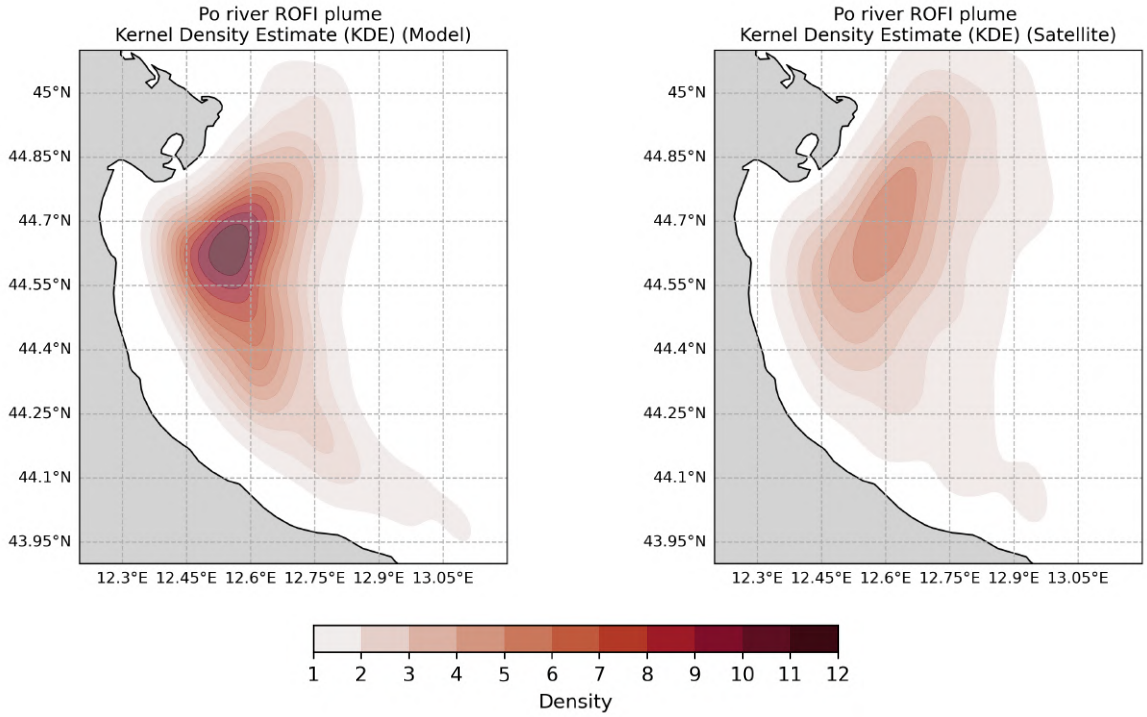

Figure 7.79: Comparison of the *KDE* density results obtained using the model data (left) and satellite data (right).

It was thus observed that the model's behavior appears more idealized, exhibiting a notably less dispersed distribution of centroids in comparison to the observed dataset. This reduced dispersion indicates a higher degree of coherence in the modeled surface current patterns, reflecting the smoothing effect introduced by the numerical representation of the dynamics. Once the centroid distribution is defined, it becomes possible to reconstruct and estimate the trajectories of the surface currents that influence the study area. This reconstruction was carried out by interpolating from the monthly current fields, which were generated through a temporal classification of the centroids. Subsequently, a LOWESS regression was applied to these interpolated data in order to determine the most representative and smoothed trajectory over time, allowing for a coherent and continuous depiction of the surface current evolution across the domain.

The results of this procedure are illustrated in *Figure 7.80*, which provides a detailed comparison of the trajectories derived from both datasets. Observing these results, it is evident that while variations in the monthly trajectories exist, primarily due to fluctuations in centroid density associated with differences already observed in the *bloom* phenomena, there is a clear and substantial agreement between the two datasets at a broader scale. This consistency supports the conclusion that the model is capable of realistically capturing the general dynamics of surface currents in the study area, even if certain finer-scale variations remain influenced by localized processes.

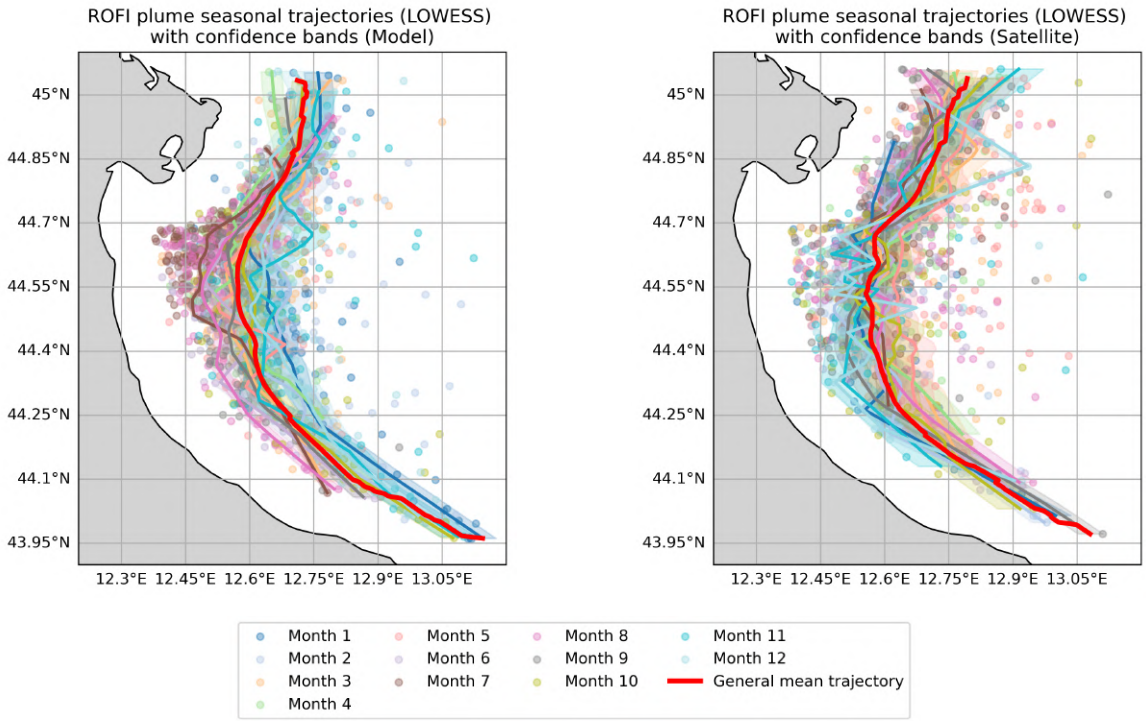

Figure 7.80: Comparison of the trajectories results obtained interpolating the monthly LOWESS trajectories. They are estimated using model data (left) and satellite data (right).

Having established the correct reproduction of the surface current affecting the area, it is possible to estimate the effects associated with chlorophyll. Observing the time series of chlorophyll concentration and *bloom* extent, shown in *Figure 7.81 a) and b)*, it can be noted that, despite the smaller area of analysis, evident discrepancies persist in both the concentrations and the timing of the phenomena.

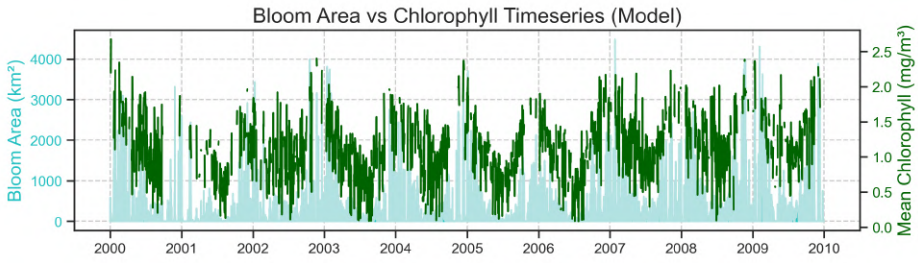

(a)

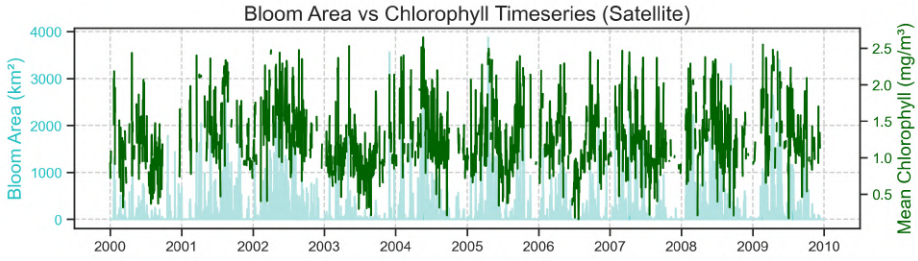

(b)

Figure 7.81: Plots of chlorophyll concentrations and the corresponding *bloom* area. From top to bottom: model results; satellite results.

Nevertheless, the most significant results emerge from the analysis of the corresponding climatologies, shown in *Figure 7.82 a) e b)*.

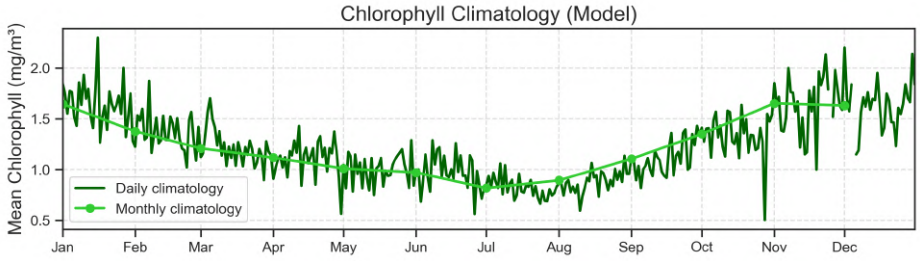

(a)

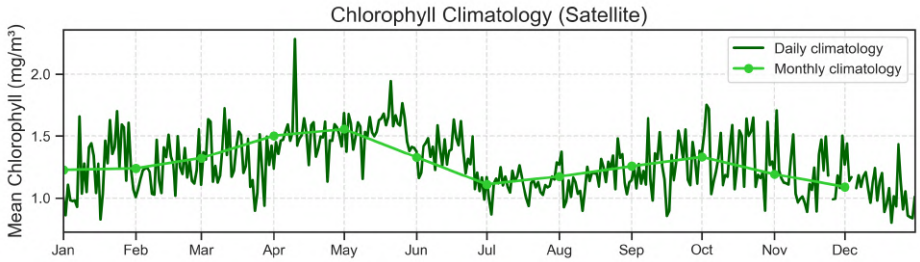

(b)

Figure 7.82: Plots of chlorophyll climatology within the *bloom* area. From top to bottom: model results; satellite results.

It is possible to observe not only a distinct behavior between the two datasets, with the characteristics and timing of the *blooms* already identified in the analyses conducted in Section 7.2, but also that the satellite data display a clear dependence on river discharge. This correlation becomes evident when comparing the climatology with the corresponding Po River discharge, illustrated in *Figure 4.3*. In contrast, the fluvial influence does not appear in the simulated data, which instead exhibit a more monotonic trend dominated by a primary winter *bloom*.

7.4 Dense Water Masses

Following the validation of the main bio-geophysical variables characterizing the model, the focus now shifts to one of the most significant phenomena within the study basin: the formation of *dense water masses*. This process, closely linked to the interaction between atmospheric conditions, riverine inputs, and local hydrodynamic characteristics, represents a crucial factor for the ventilation and circulation of deep basin waters. Its accurate reproduction within the model therefore constitutes a key indicator of the simulation's capability, not only in faithfully describing the physical mechanisms but also in capturing the ecological and environmental implications generated by such water masses.

7.4.1 Dense Water Volumes

The initial analysis was carried out by identifying all model grid cells where the density exceeded the threshold value of $\rho \geq 1029.2$ kg/m^3, a criterion chosen to accurately delineate regions belonging to the *dense water mass*. By counting these identified cells, as detailed in Section 6.10.1, it was possible to estimate the total volume of dense water present within the basin on a monthly basis.

Subsequent temporal processing of the resulting *monthly average* values enabled a detailed reconstruction of the evolution of the *dense water mass* throughout the simulation period. The complete time series of these estimated volumes is presented in *Figure 7.83*, providing a clear visual representation of the seasonal and interannual dynamics of dense water formation within the basin.

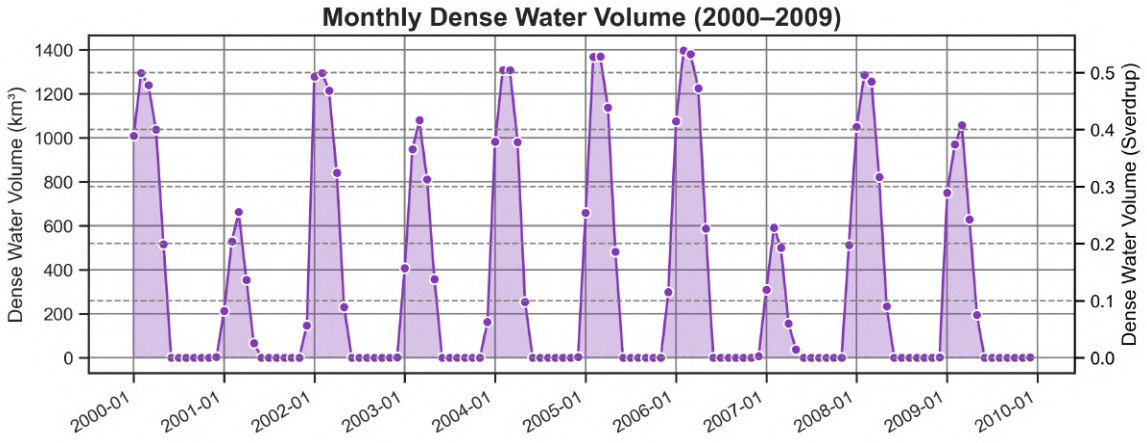

Figure 7.83: Graph showing the time series of volumes of *Dense Water Mass* formed within the study area. Volumes are reported both in km^3 and in *Sverdrup*.

The time series enables a detailed examination of the temporal evolution of *dense water mass* formation within the basin. The volume analysis clearly indicates that the primary formation period is concentrated in the months of January, February, and March (**JFM**), as illustrated in *Figure 7.84*. In contrast, the subsequent months are characterized by a progressive depletion of the basin, with recorded volumes becoming negligible from June onward, thus highlighting a strong seasonal cycle in dense water mass dynamics.

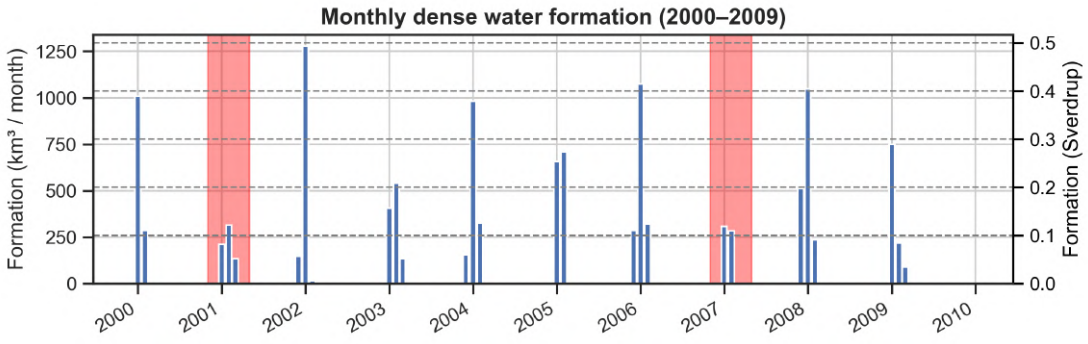

Figure 7.84: Histogram of dense water mass formation regimes within the basin, expressed as monthly-formed volumes. Years characterized by low formation are highlighted in red.

A pronounced interannual variability in the volumes of dense water masses produced is also evident. Specifically, the years 2001 and 2007 are characterized by notably low formation volumes, whereas other years, such as 2005 and 2006, exhibit significantly more intense formation regimes. These interannual differences align with findings reported in other simulations conducted using similar modelling approaches (Dunić et al., 2018), suggesting a degree of robustness in this behaviour across independent studies.

The climatological analysis of dense water mass volumes, illustrated in *Figure 7.85*, further confirms that the highest volumes within the basin consistently occur during the **JFM** period. This is followed by a progressive depletion beginning in April, with volumes diminishing to minimal values by May, thus revealing a clear and recurrent seasonal cycle in the basin's dense water mass dynamics.

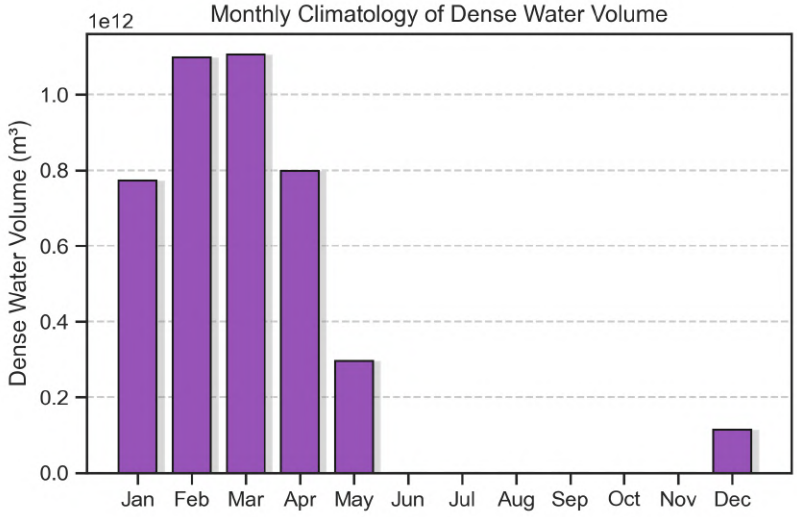

Figure 7.85: Histogram showing the climatology of volumes of *Dense Water Mass* formed within the study basin.

7.4.2 Characteristics of the Dense Water Mass

To investigate the relationships between the *dense water mass* and the regimes of the physical variables used for its identification, the temporal evolution of the main

properties characterizing the dense water in contact with the benthic layer was analyzed. Specifically, the analysis focused on three key aspects: the density regime, expressed as the *potential density anomaly* (PDA); the thermal regime, including relevant anomalies; and the salinity field. The results of this investigation are summarized in *Figure 7.86*.

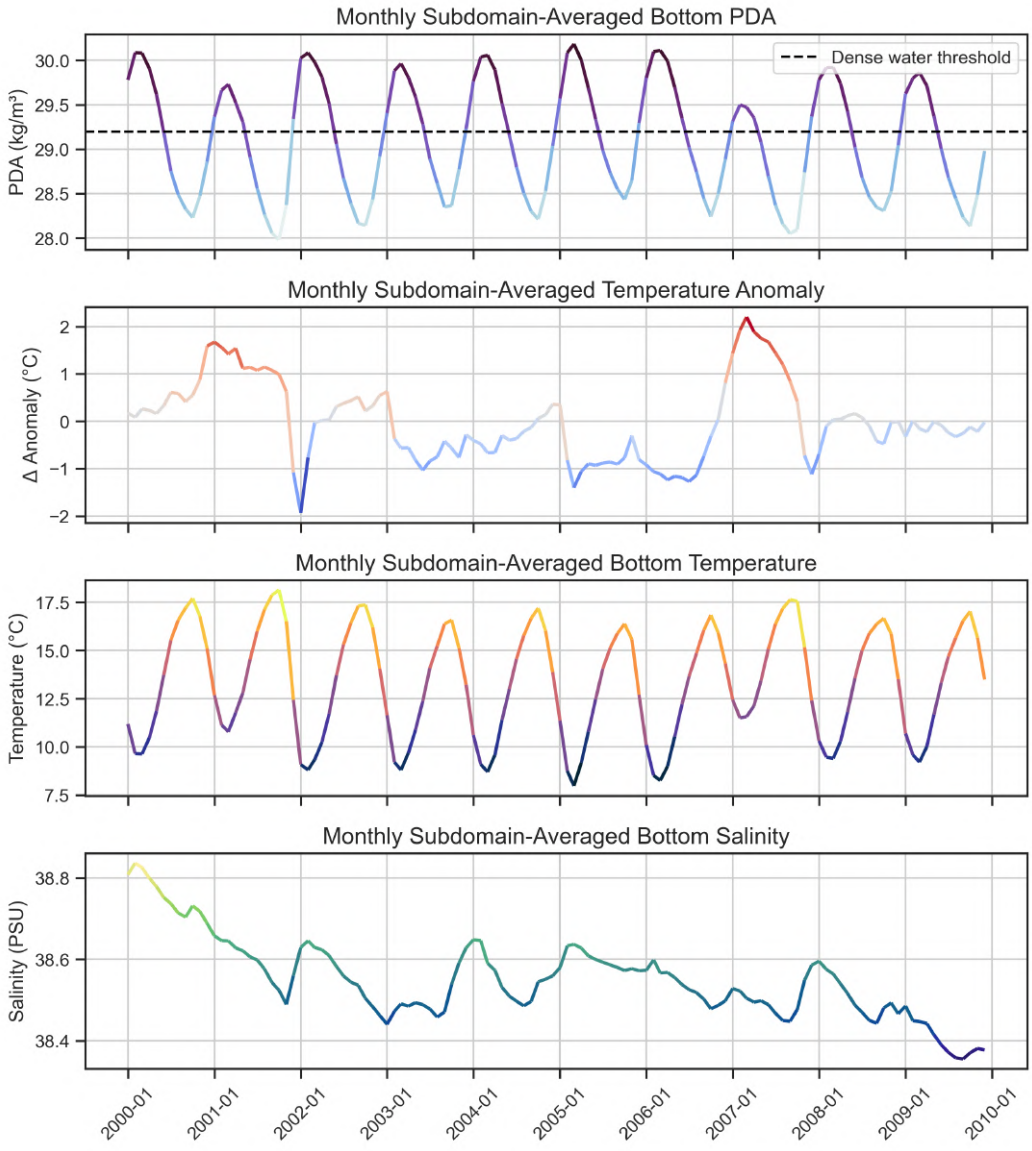

Figure 7.86: Series of graphs illustrating the temporal evolution of the mean physical properties of the *Dense Water Mass*. From the top to bottom panels: potential density anomaly anomalies, temperature anomalies, absolute temperature, and salinity.

The analysis reveals that, for the years 2001 and 2007, the basin-average values of the *potential density anomaly* remained below the established threshold of PDA = 29.2 kg/m^3. This observation offers a plausible explanation for the markedly reduced formation rates of the *dense water mass* recorded in those years. The underlying cause of these low PDA values appears to be significant bottom thermal anomalies, which exceed +2°C. Such temperature anomalies emerge as the primary driver behind the reduced PDA, while the salinity field does not exhibit comparable anomalous variations, suggesting a minor role in these deviations.

To validate the obtained values and, more generally, to assess the accuracy of the vertical profiles as a function of their density field, salinity and temperature data collected during the ADRIA campaigns, described in Section 4.3, were used. The resulting vertical profiles were compared with the corresponding model simulations, whose methodology is reported in Section 6.9.3, and the results are presented in *Figure 7.87*.

Observing the profiles, a good agreement between the simulated and observed data is evident, particularly concerning the vertical salinity profiles. However, some discrepancies persist in the surface layer, similar to those already noted in the chapters validating the biogeochemical parameters within the ROFI area, as shown in the ARPAE vertical profiles in *Figure 7.73* and in the ENEA ones in *Figure 7.76*. Exacly like those cases, the model tends to overestimate the observed values.

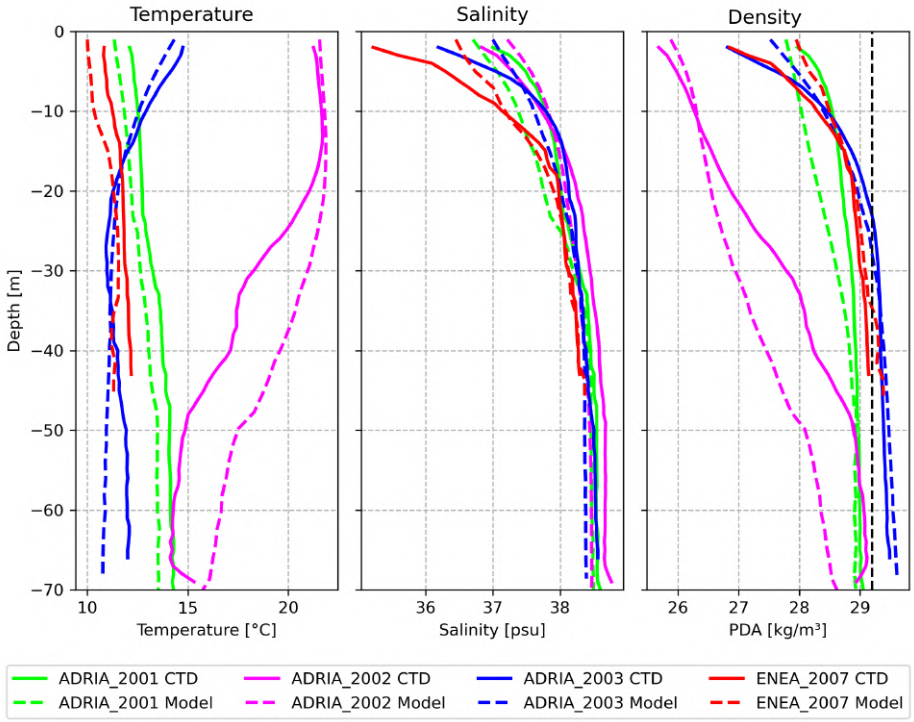

Figure 7.87: Vertical profiles comparing model data (dashed lines) and observations (solid line), relative to the ADRIA 2001 (lime), 2002 (magenta), 2003 (blue), and ENEA 2007 (red) samplings. The black dashed vertical line indicates the density threshold of 1029.2 kg/m^3 for dense water masses.

The temperature profiles reveal a more complex pattern, with the model generally underestimating observations in ADRIA 2001, 2003, and ENEA 2007. However, these differences remain limited, indicating that the model reasonably reproduces the overall thermal structure of the water column. In contrast, ADRIA 2002 shows excellent agreement in the surface layer, suggesting a good representation of near-surface thermal conditions, though significant discrepancies appear below $\sim$ 20 m, implying that deeper structures may require refinement under certain conditions.

The density profiles display behavior similar to temperature, with a systematic overestimation of observed values, particularly evident in 2001, a year of reduced dense water formation. To assess possible bottom densities, data corresponding to the CTD

probe positions within the model-identified dense water area were extracted (*Figure 7.88*).

Extracting values at the same points shows that in low-formation years this overestimation becomes critical. In 2001, the maximum observed density was 1029.15 kg/m^3, just below the dense water threshold (1029.2 kg/m^3), while the model exceeded it as early as February. Probe sampling occurred in late January–early February. For quantitative comparison, the model value at the same grid point, averaged over January and February (monthly means), yielded 1029.1612 kg/m^3, extremely close to the observed one.

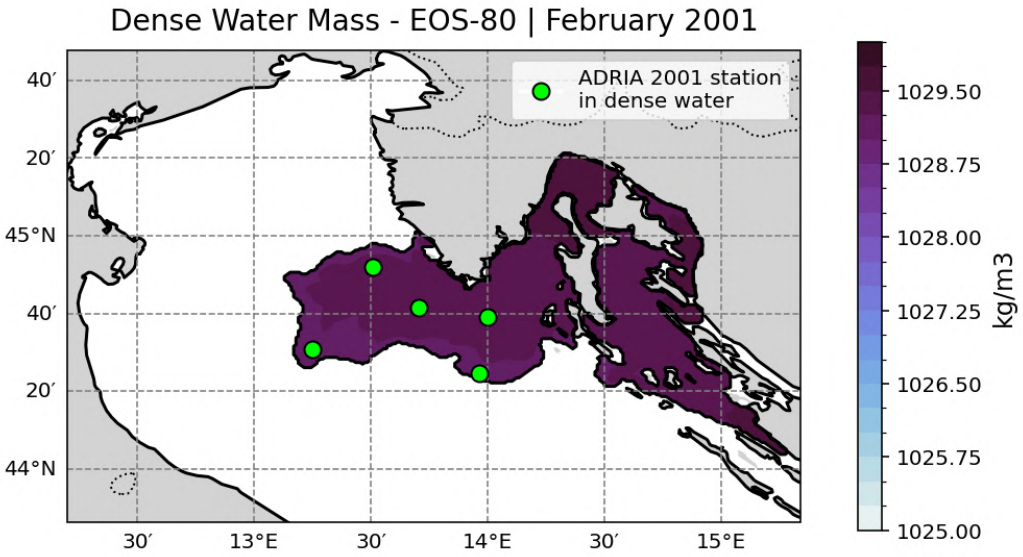

Figure 7.88: Simulated *dense water mass* in February 2001. Lime markers indicate the positions of the ADRIA 2001 CTD samples. The color scale represents density, with values below the threshold of 1029.2 kg/m^3 shown in white.

A qualitative assessment was also performed for the ADRIA 2003 campaign, where the recorded values exceeded the dense water threshold in both observed and simulated data. This consistency supports the model's reliability in capturing key physical processes. Analysis of the volumes in *Figure 7.83* shows that at the end of April and early May, the model recorded the highest values of the entire period, with a distinct peak in May. This temporal agreement further confirms the model's skill in reproducing the seasonal evolution of dense water formation and reinforces its validity for process understanding and predictive applications.

7.4.3 Dense Water Mass in the Subdomains

To further deepen the understanding of the phenomenon and capture possible local differences in the formation and persistence of the *dense water mass*, the analyses were repeated considering two specific subdomains of the basin, according to the subdivision proposed by Pranić et al. (2024) and described in detail in section 6.10.1 defining two distinct areas of the analysis: the northernmost Northern Adriatic area and the Kvarner Bay.

The evolution of the volumes computed for these two subdomains is shown in *Figure 7.89*.

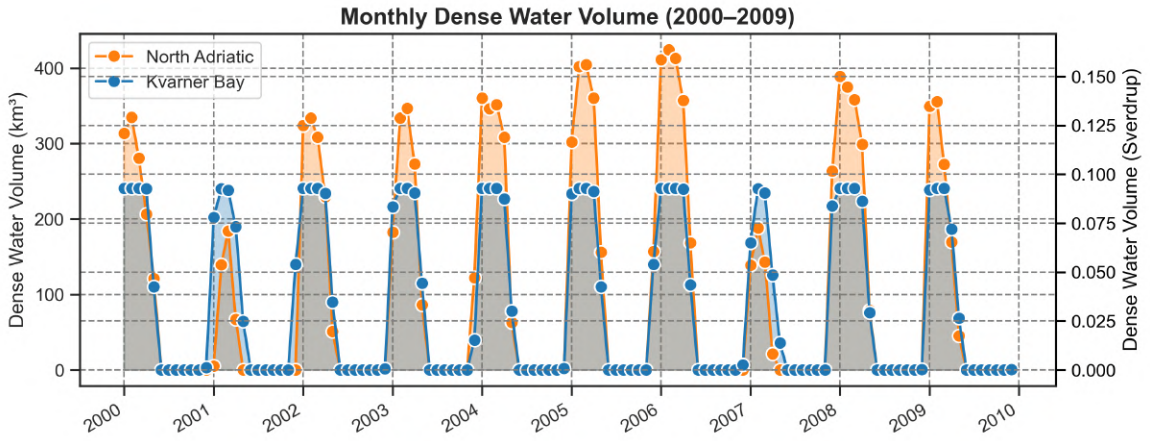

Figure 7.89: Time series of the volumes of *Dense Water Mass* formed in the Kvarner Bay (blue) and the Northern Adriatic subdomain (orange). Volumes are expressed in both km^3 and *Sverdrup*.

Analyzing the evolution of volumes within these subdomains, it emerges that the northern area of the Adriatic basin (orange) is the most affected by a decrease in formation rates during the years 2001 and 2007, resulting in significant reductions in the volumes present, from values above 300 km^3 to less than 200 km^3 in those years.

It is also evident that the behavior of the Kvarner Bay (blue) is more "idealized", with the almost complete absence of the reduction of the volumes during these years. Furthermore it is notable ho the maximum volume formed within this area never exceeds 250 km^3, probably due to the enclosed shape of the basin, leading to the peculiar shape of the timeseries. The climatology of the subdomains, shown in *Figure 7.90* confirms this behaviour.

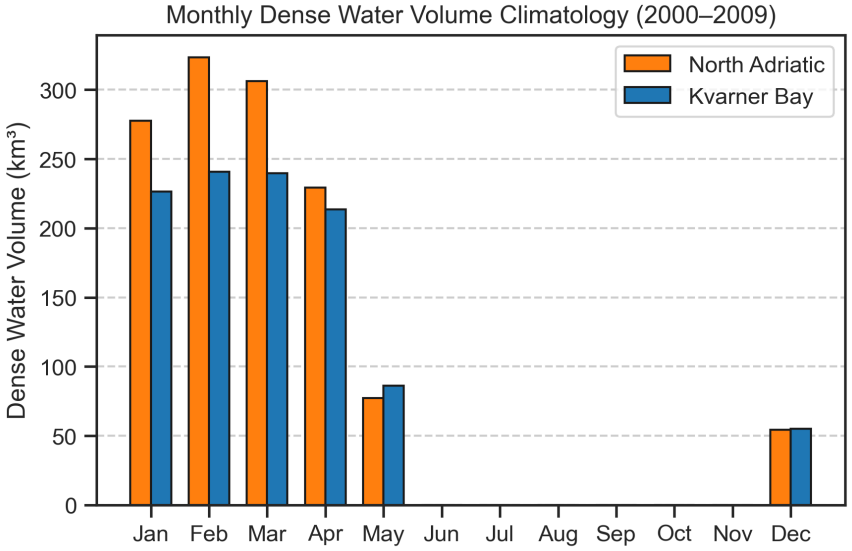

Figure 7.90: Histogram showing the climatology of *Dense Water Mass* volumes formed within the the Kvarner Bay (blue) and the Northern Adriatic subdomain (orange).

To further explore the differences in the characteristics of the *dense water masses* within the subdomains, new time series of the main physical parameters were generated: *Potential Density Anomaly*, temperature and related anomalies, and salinity. These time series allow a detailed comparison of the evolution and properties of the dense masses in the different areas of the basin.

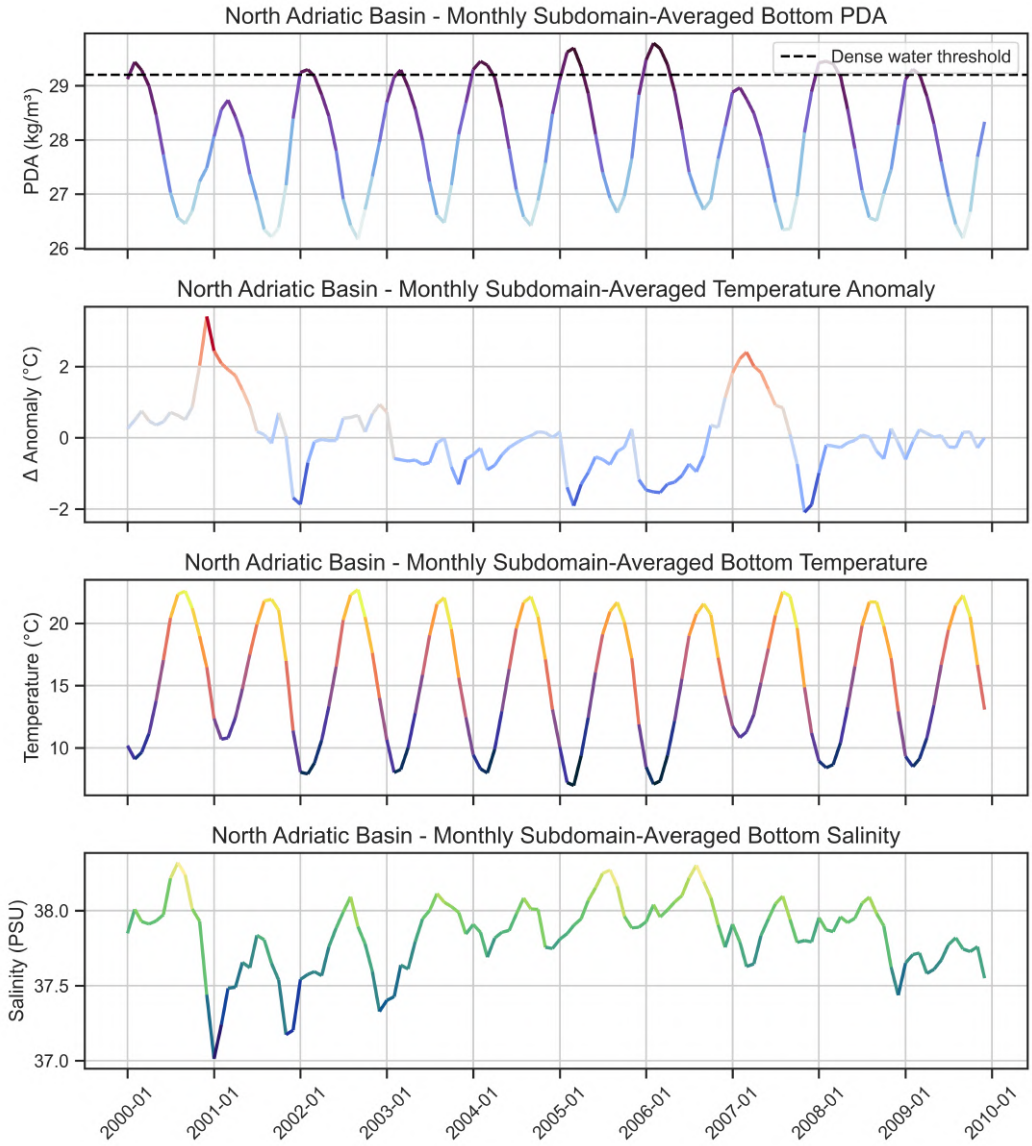

Figure 7.91: Series of graphs showing the temporal evolution of the average physical properties of the *Dense Water Mass* formed within the Northern Adriatic subdomain. From top to bottom, the following are shown: potential density anomalies, temperature anomalies, absolute temperature, and finally salinity.

The results obtained for the two subdomains are reported respectively in *Figure 7.91* for the northern subdomain of the Northern Adriatic and in *Figure 7.92* for the Kvarner Bay.

Almost all the analyzed fields show differences between the two areas. Focusing on the years characterized by low formation regimes, it is observed that in the Kvarner Bay the PDA value still exceeds the threshold of 29.2, whereas in the Northern Adriatic this threshold is not reached. However, in the latter the temperature anomalies are higher compared to those recorded in the Kvarner Bay: for example, in 2001, in the northern Adriatic subdomain, thermal anomalies exceed +3°C, while in the Kvarner Bay they do not reach +2°C. It is noteworthy that this anomaly in the Northern Adriatic is concentrated in December, then decreases in the following months to values comparable to those of the Kvarner Bay.

Finally, the analysis of the salinity field highlights a notable phenomenon: a slight

decreasing trend in salinity within the Kvarner Bay, while no significant variations are observed in the Northern Adriatic.

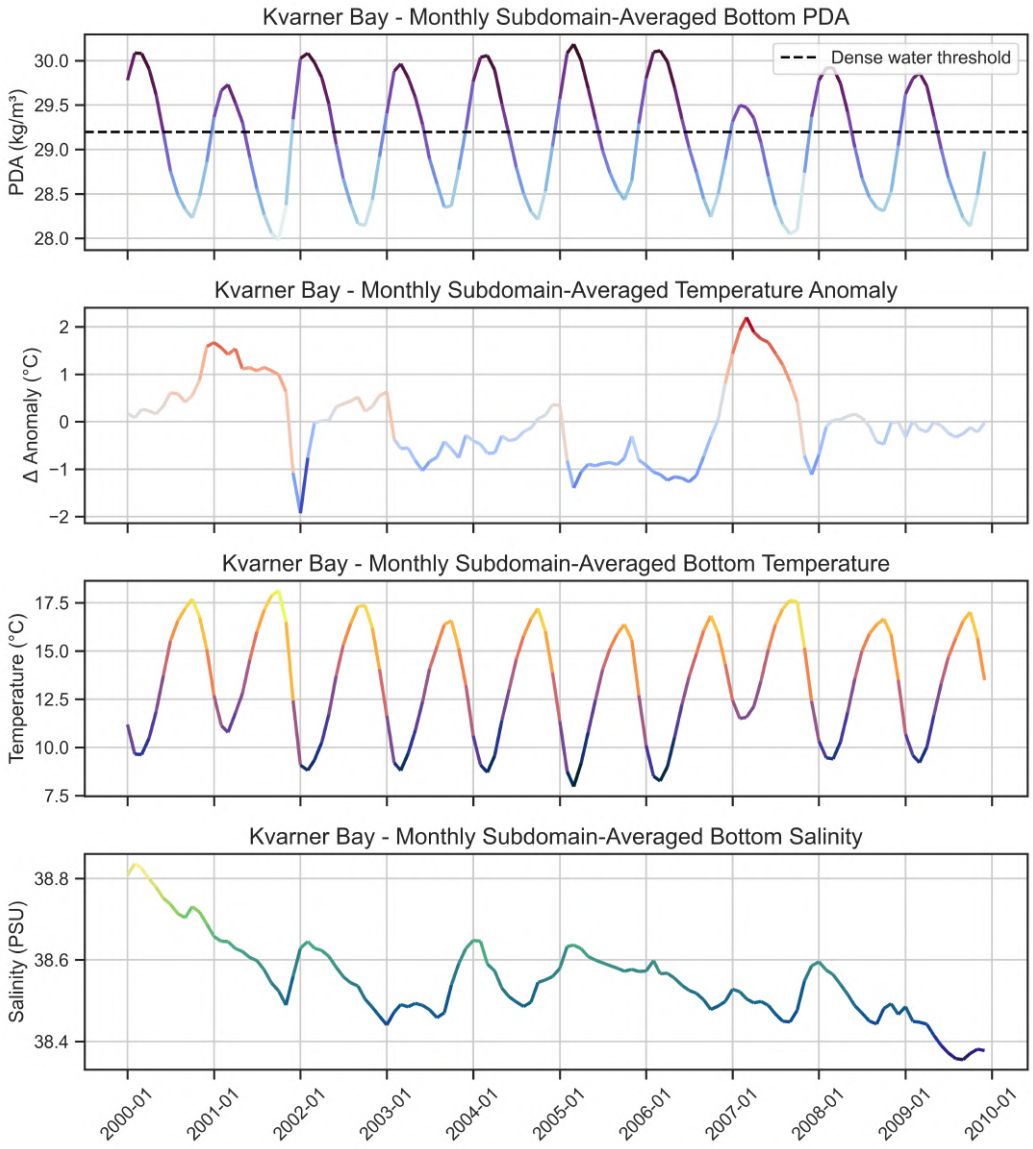

Figure 7.92: Series of graphs showing the temporal evolution of the average physical properties of the *Dense Water Mass* formed within the Kvarner Bay subdomain. From top to bottom, the following are shown: potential density anomalies, temperature anomalies, absolute temperature, and finally salinity.

7.4.4 Dense Water Mass Circulation and Movement

Having examined the formation of the *dense water mass*, including its timing, volumes produced, and main physical characteristics, the final step in validating the model's ability to reproduce the phenomenon involved the construction of a Hovmöller diagram, presented in *Figure 7.93*.

The Hovmöller diagram was constructed along the southern boundary of the domain, corresponding to latitude 43.5° N, with the specific purpose of visualising the progression of the dense water mass as it exits the analysed basin along the *North Adriatic Current*, a current that flows from north to south along the western margin of the

basin. To enhance clarity and focus on the most relevant signal, the diagram was filtered to include only those masses with a *dense water mass* fraction greater than 70%.

The results reveal that the signal of the dense water mass is concentrated between approximately 12.7°E and 13.5°E, corresponding to the western portion of the basin, thereby confirming that its movement is largely guided by the *North Adriatic Current*. Furthermore, the fraction of dense water mass crossing the southern boundary aligns closely with the volume estimates obtained from the simulation. In particular, the years 2001 and 2007 stand out, with observed fractions dropping below 0.6, corroborating earlier findings that these years were characterised by markedly reduced dense water formation regimes.

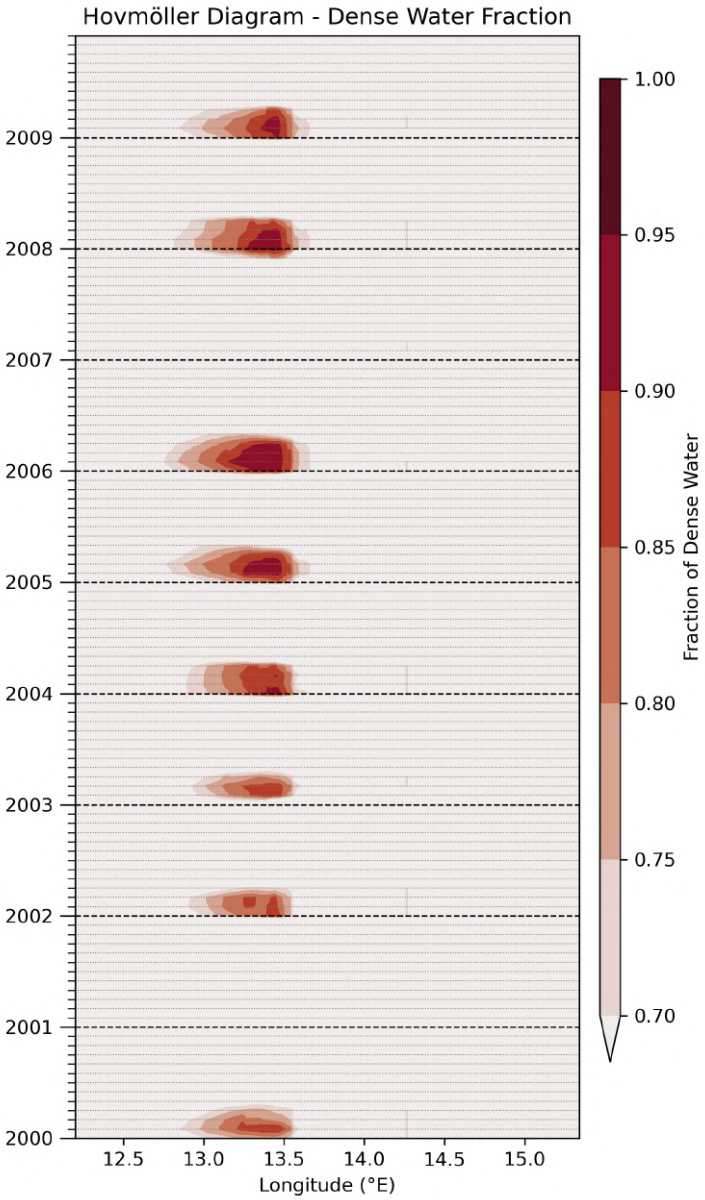

Figure 7.93: Hovmöller diagram showing the fraction of *Dense Water Mass* crossing the southern boundary of the basin (latitude 43.5° N). The color scale indicates the proportion of *Dense Water Mass* present at the basin boundary at each time step.

7.5 Oxygen near the Benthic Layer

After analysing the *dense water masses*, attention shifts to biogeochemical parameters to examine their behaviour within the simulation. The first parameter considered is oxygen, to identify messes whose concentration falls below the *hypoxic* threshold ($O_2 < 62.5\,\text{mmol/m}^3$) or, if present, masses below that of *anoxia* ($O_2 = 0.0\,\text{mmol/m}^3$).

The first step involved constructing a time series to estimate the seabed area within the hypoxic range. Affected areas were quantified as the total monthly bottom area in km^2. The results are shown in *Figure 7.94*.

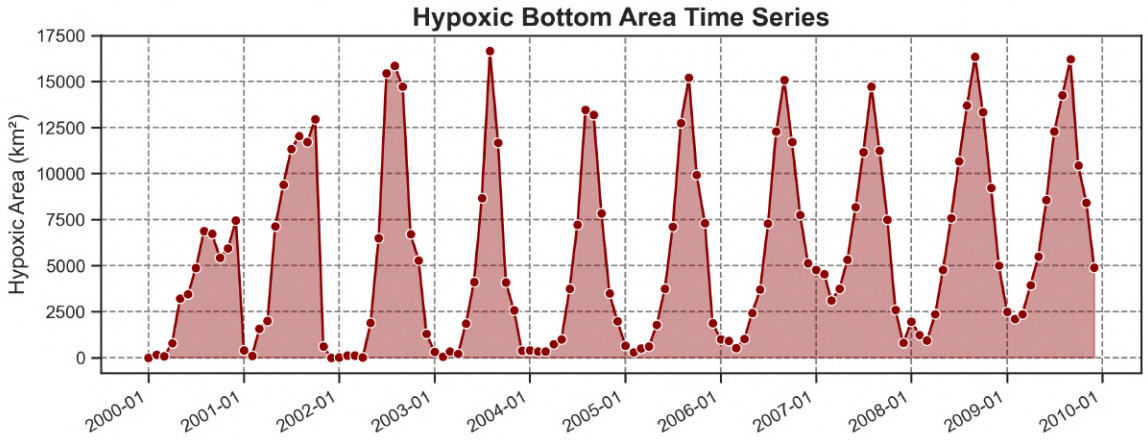

Figure 7.94: Graph showing the time series of the *hypoxic* area formed at the bottom of the basin.

Observing the time series evolution of the area reveals no markers of potential anoxic zones. This results from the absence of cells with null oxygen values in the simulation, with values instead entirely within the hypoxic range.

Marked irregularity is evident, especially in the first simulation years (2000 and 2001), during which no clear cyclicity emerges. Hypoxic masses also occur in atypical periods, such as **DJF**, starting in 2007. Despite these irregularities, from 2002 onwards a clear cyclicity appears, with peaks in **JAS** (July–September), as shown in the climatology in *Figure 7.95*.

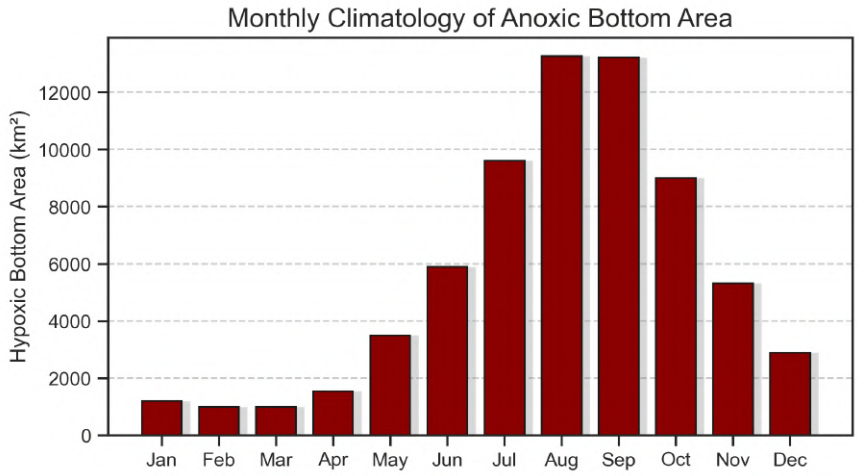

Figure 7.95: Histogram of the climatology of the *hypoxic* area formed within the basin.

Since the overall spatial extent of the *hypoxic* area remains relatively consistent across years, the position and variability of the *hypoxic* front were further analysed to assess possible interannual differences in its extent. This evolution was investigated using the transects described in Section 6.10.2 and shown in *Figure 6.14*, examined both as yearly means and as seasonal means for the **JAS** (July–August–September) period. The results for the yearly averages are presented in *Figure 7.96*.

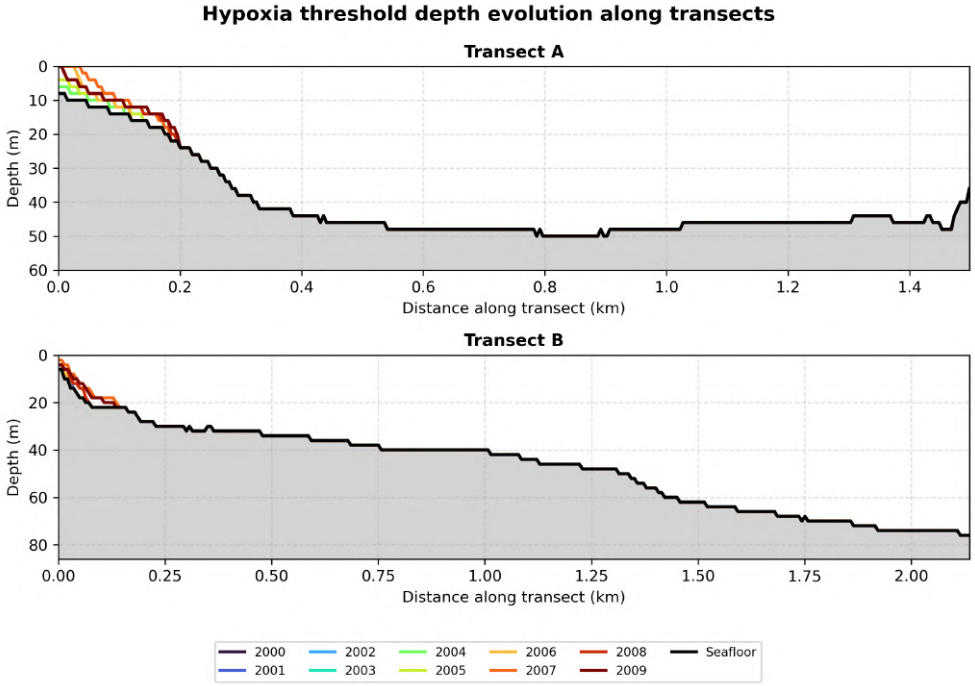

Figure 7.96: Location of the *hypoxic* front along the transects based on yearly mean oxygen values.

While the **JAS** average fronts are shown in *Figure 7.97*.

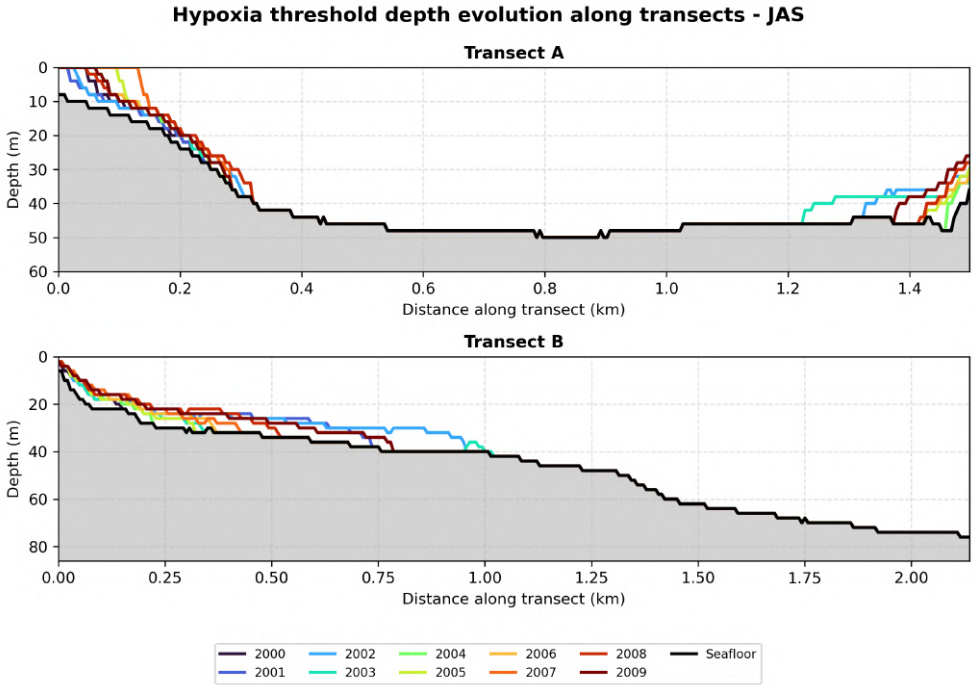

Figure 7.97: Location of the *hypoxic* front along the transects based on **JAS** specific mean oxygen values.

The position of the front, particularly when examining the yearly averaged transect, highlights the presence of a distinct *hypoxic* water mass located along the northern and, more prominently, the western coastline, in correspondence with the Po River's ROFI area. This feature emerges only after 2004, marking an intensification of *hypoxic* conditions within the simulation from that year onward.

In the **JAS**-specific analysis, the same pattern of front extension is observed, showing a progressive increase in the hypoxic area from 2004 through 2009. Two years, however, stand out for their anomalously large extent: 2002 and 2003, the same years that exhibit the largest hypoxic coverage within the timeseries presented in *Figure 7.94*.

Since the nearshore region adjacent to the ROFI area exhibits well-defined *hypoxic* water masses, even in the yearly averaged fields, an additional analysis was conducted to assess the concentration of dissolved oxygen at the bottom of the water column. This comparison was carried out against ARPAE in-situ data, following a procedure analogous to the one employed to generate the timeseries shown in *Figure 7.69*. The resulting bottom-layer oxygen concentrations are presented in *Figure 7.98*.

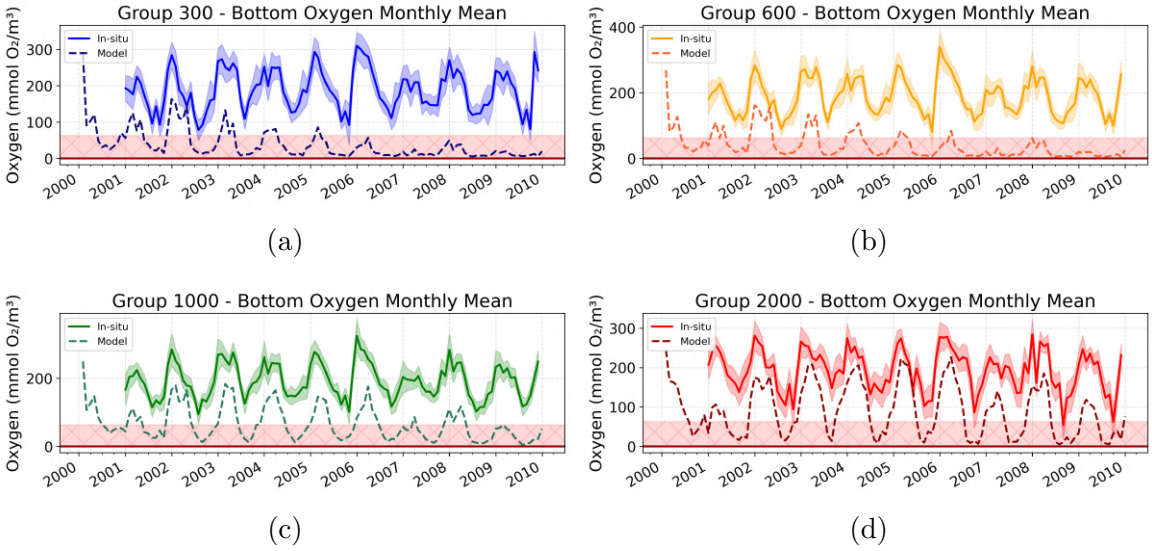

Figure 7.98: Series of comparison plots of the dissolved oxygen concentration between the *monthly mean timeseries* of model data and *in-situ* observations. For each plot, observations are shown as solid lines with shaded areas indicating the standard deviation, while model data are shown as dashed lines. Panels correspond to station groups as follows: a) 300 m; b) 600 m; c) 1000 m; d) 2000 m. Hypoxia range is shown as a red area while the anoxia threshold is shown as a dark-red line.

As shown by the timeseries, the overall seasonality of bottom-layer oxygen concentrations is consistent with that of the observed dataset. The main differences, however, lie in the absolute values. The coastal locations (group 300, located $\sim$ 300 m from the shoreline) exhibit markedly lower simulated oxygen levels compared to ARPAE observations, with persistent *hypoxic* conditions beginning in 2007 and evolving toward a state of nearly continuous anoxia. This effect progressively weakens with increasing distance from the coast: the offshore locations (group 2000, $\sim$ 2 km from the coast) still drops below the hypoxia threshold during the summer months, yet maintains generally higher oxygen values than the nearshore stations and does not reach

a permanent hypoxic regime. The mean value however is still lower than that of the observations.

Interestingly, unlike the surface timeseries shown in *Figure 7.69*, these bottom-layer records do not display a progressive temporal lag accumulation between the simulation and the observational data.

All of these results highlight two main critical issues within the biogeochemical component of the model. The first, already discussed in Section 7.3.2 and particularly in *Figures 7.76* and 7.75, concerns the model's tendency to overestimate oxygen consumption near the seabed, leading to the formation of *hypoxic* conditions. This behaviour can be attributed to an inaccurate parameterization of the *coupling* with the benthic layer, which results in an incorrect exchange of nutrients between the water column and the sediment.

Observational syntheses and historical field studies document a highly variable hypoxic/anoxic footprint in the northern Adriatic. Typical observational maxima reported in the literature are on the order of $\mathcal{O}(10^2 - 10^3)$ km^2 during strong events (Justić, 1991; Stachowitsch, 1991; Degobbis et al., 2000), while multi-decadal analyses indicate a reduction in basin-wide anoxia since the early 1990s but persistent, locally intense hypoxic patches, principally in areas influenced by the Po plume and gyre trapping (Djakovac et al., 2015; Giani et al., 2012).

By contrast, the present simulation displays a pronounced seasonal cycle (i.e. no year-round, basin-wide hypoxia), with remnants of bottom hypoxia persisting in some cells after 2007, but with monthly peak hypoxic extents reaching $\approx 1.5 \times 10^4$ km^2. The model therefore reproduces the observationally reported seasonality and the post-2007 persistence of localized hypoxia, yet it yields peak areas that are an order of magnitude larger than the typical observational reference scale cited above, being further proof that the model exagerates these events.

The second issue concerns the years 2000 and 2001, during which the model exhibits a behaviour not consistent with the typical cyclicity of *hypoxic* events observed in the basin. This anomaly is presumably related to the model spin-up phase, which requires several cycles before the biogeochemical components reach a dynamic equilibrium and a behaviour consistent with the observations.

After the spin-up, from 2002 onward the simulation develops a clear and recurrent seasonal signal: bottom hypoxia appears regularly during the warm season with peak occurrence located in **JAS** (July–September). This timing captures the essential stratification–driven mechanisms, namely, summer stratification and enhanced organic export to the seabed, and thus agrees qualitatively with the literature that places the hypoxic season in mid-summer through mid-autumn (Djakovac et al., 2015; Degobbis et al., 2000; Giani et al., 2012). At the same time, the model's maxima are phased systematically earlier than many observational climatologies, which commonly extend the principal peak into October–November; in other words, the simulation concentrates the strongest hypoxic signal in **JAS** whereas several observational analyses emphasise an August–November window of maximum occurrence and intensity (Djakovac et al., 2015; Giani et al., 2012; Degobbis et al., 2000).

The occasional winter anomaly (notably the 2007 **DJF** signal) also departs from the observational record, where winter is generally a re-oxygenated period except

under exceptional forcing (Djakovac et al., 2015; Cossarini et al., 2012). The 2007 phenomena in particular may find an explanation using the results of the *dense water masses* analysis in which this year was identified as a low-formation year, suggesting a link in these 2 events probably due to an onset of lack of mixing within this year, leading to a longer than usual stratification and lack or re-oxygenation at the bottom.

To verify this hypothesis, a comparison of bottom oxygen values was carried out for February 2007, a period for which *in situ* data are available from the ARPAE and ENEA2007 datasets. For this purpose, all sampling points located within the *hypoxic* area were identified, as shown in *Figure 7.99*. For each point, the bottom oxygen concentration was extracted, and the overall mean value was subsequently calculated and compared with the mean of the corresponding model points, extracted at the same spatial locations.

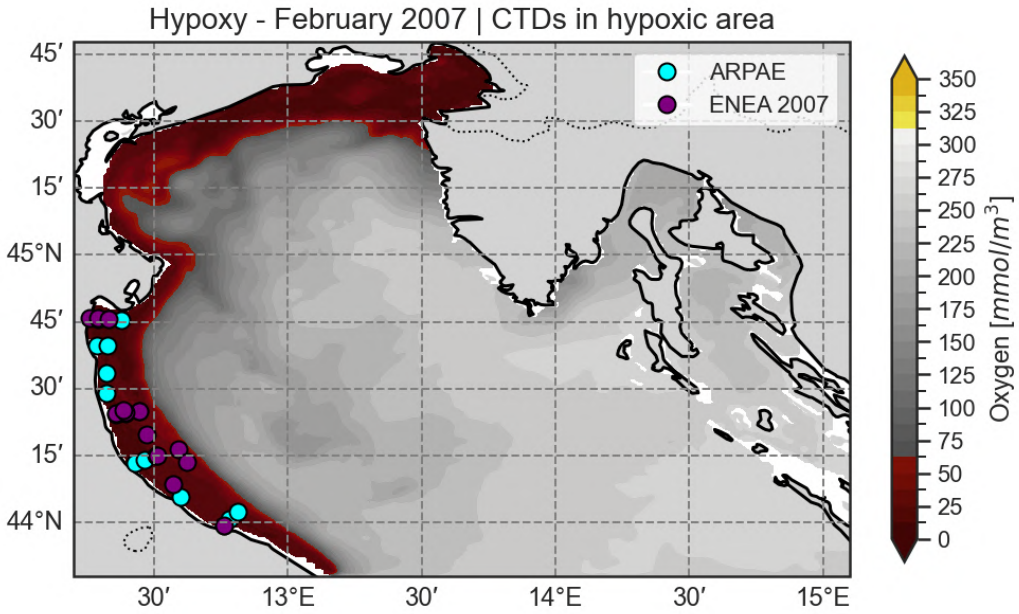

Figure 7.99: Spatial distribution of ARPAE observations (cyan) and ENEA 2007 observations (purple) within the water mass identified by the model as hypoxic in February 2007.

To ensure consistency with the simulation values, the observed bottom oxygen concentration data were converted from their original units of mg/L or ppm to $mmol/m^3$. The comparison results are reported in *Table 7.15*.

Parameter	**Model**	**ARPAE**	**ENEA 2007**
Oxygen at bottom	17.12	248.00	191.49

Table 7.15: Bottom basin oxygen concentration from the model and observed datasets (ARPAE and ENEA 2007). Values are expressed in $mmol/m^3$.

As can be observed, in this case as well the simulation tends to significantly overestimate the intensity of the *hypoxic* phenomenon, which is not detected either in the available observations or in other independent sources.

The final analysis concerning anoxic phenomena focuses on verifying the occurrence of stratification within the domain, which represents the main cause of reduced oxygenation of the water column during the summer period. To this end, a stratification index was computed to assess the actual degree of vertical separation within the water column. The results of this analysis are shown in *Figure 7.100*.

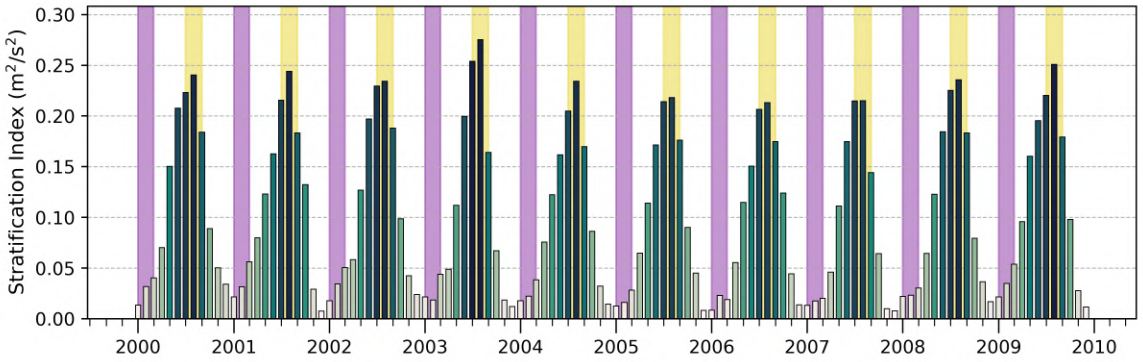

Figure 7.100: Time series of the stratification index. The theoretical time window for the formation of *Dense Water Masses* is highlighted in purple (typically **JFM**), while the window corresponding to *hypoxia* events is shown in yellow (typically **JAS**). The color scale of the histogram bars reflects the values of the stratification index, allowing temporal variations to be easily tracked.

Examining the evolution of the stratification index, it is evident that the highest values generally occur during the **JAS** period, confirming that maximum stratification coincides with the onset of *hypoxic* phenomena. This relationship highlights a direct correlation between the stability of the water column and the reduced oxygenation of bottom waters, thus validating the accurate representation of the stratification process within the simulation. Conversely, during the winter period, particularly within the **JFM** window, very low stratification index values are observed, consistent with the intense mixing activity associated with the formation of *dense water masses*. This behaviour aligns with the reoxygenation processes of the deeper portions of the basin typically observed during this season.

Re-examining the hypoxic event that occurred in the simulation during the winter of 2007, previously discussed, the results show that the stratification index does not exhibit particularly high values during the **JFM** period. This evidence disproves the initial hypothesis that attributed the persistence of the hypoxic event to an anomalous and prolonged stratification resulting from the reduced mixing and formation of the *dense water mass* in that year. Conversely, the relatively low values of the stratification index indicate the presence of active mixing processes, suggesting that the water column was well mixed during the winter season. Therefore, no clear or unique cause could be identified to explain the persistence of the *hypoxic* phenomenon within the simulation.

7.6 Remaining Bio-Geochemical Variables

As the final aspect of the analysis, the *time series* of the mean concentration of the main simulated variables are briefly examined. These variables are grouped according to their respective families, which are defined as follows:

- **Nutrients**, including *phosphates*, *ammonium*, and *nitrates*;
- **Primary producers**, including *diatoms*, *flagellates*, *pico-* and *large phytoplankton*;
- **Secondary producers**, including *Carnivorous* and *Omnivorous mesozooplankton*, *Microzooplankton*, and *Heterotrophic Nanoflagellates*;
- **Particulate Organic Matter (POM)**.

The first family of variables analyzed concerns the *Nutrients*, whose trends are shown in *Figure 7.101*.

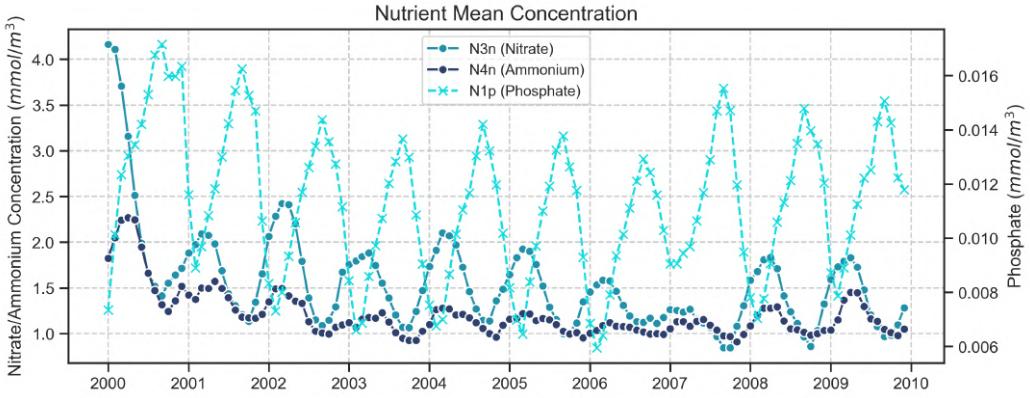

Figure 7.101: Time series of the mean *nutrient* concentrations, expressed in $mmol/m^3$. Due to the low values, a secondary axis has been used for phosphates, with the monthly values indicated by X markers.

Observing the nutrient trends, it can be noted that nitrates and ammonium in the year 2000 exhibit extreme values, particularly in January, coinciding with the start of the simulation. Subsequently, the values tend to stabilize, suggesting that the initial parametrization does not determine the long-term model climatology. Phosphates also show a more irregular behavior during the same year, with variable maximum concentrations, confirming the issues already highlighted during the model spin-up years in the previous sections.

Particularly interesting is the effect observed during the transitional winter between 2006 and 2007, a period already identified in many sections as a turning point for trend changes in the case of chlorophyll at the basin level and oxygen in the ROFI area of the Po. During this phase, no true minimum is observed in the time series: concentrations remain relatively high and subsequently show a trend change, confirming the persistence of significant dynamics also for the nutrient components. The values of the trends are reported in *Table 7.16*.

Variable	Window		
	2001–2009	2001–2007	2007–2009
N_1p	0.000037	-0.000092	0.000695
N_3n	-0.062	-0.104	0.048
N_4n	-0.023	-0.049	0.026

Table 7.16: Annual slope values for the simulated nutrients. The year 2000 is not used as it is the *spin-up* year of the model.

The next family of variables analyzed concerns the *Primary Producers*, whose trends are shown in *Figure 7.102*.

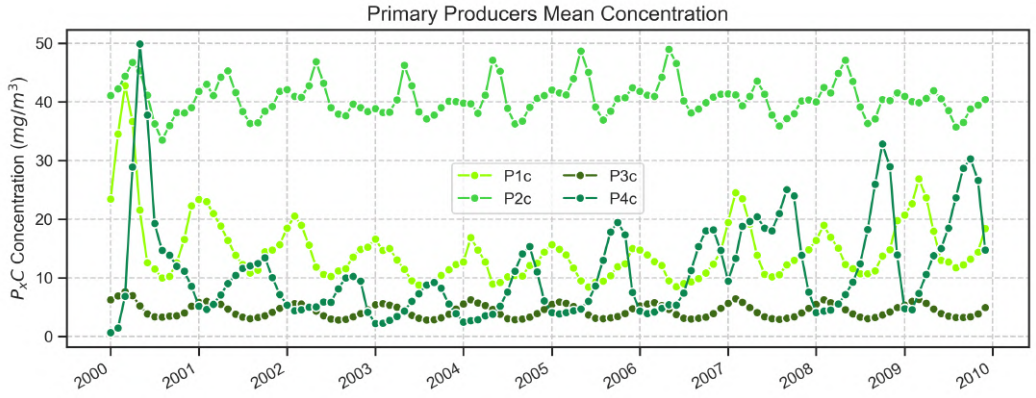

Figure 7.102: Time series of the mean *primary producers* concentrations, expressed in mg/m^3. The variable shows are: *diatoms* ($P1c$); *flagellates* ($P2c$); *pico-* ($P3c$) and *large phytoplankton* ($P4c$).

Analyzing the primary producers, it can be observed that both *diatoms* ($P1c$) and *large phytoplankton* ($P4c$) are influenced by the model initialization, with extremely high concentrations during the first year. Similar to what was observed for nutrients, anomalous effects are detected during the transitional winter between 2006 and 2007, causing variations in the trends; however, in this case, the behaviors are more complex and no general trend reversal is observed.

Diatoms exhibit a peculiar pattern: the overall trend appears positive, while the trends calculated over the two sub-windows are both negative, although in the second window a reduction in the negative slope is observed. This phenomenon is likely attributable to the "jump" in concentrations between the two periods, with mean values increasing from 13.327 mg/m^3 to 15.691 mg/m^3. The general increase in concentrations over these intervals leads to a higher overall mean, making the overall trend appear positive despite the two sub-trends being negative.

The remaining species within the primary producers group exhibit a more linear behavior, showing a simple amplification of the trend between the first and second time windows, without reversals or complex phenomena as observed for the diatoms. The values are reported in *Table 7.17*

Variable	Window		
	2001–2009	2001–2007	2007–2009
P1c	0.101	-0.404	-0.095
P2c	-0.065	-0.001	-0.484
P3c	-0.009	-0.057	-0.179
P4c	1.454	1.404	1.613

Table 7.17: Annual slope values per year for each phytoplankton functional group (*P1c–P4c*), grouped by time window. The year 2000 is not used as it is the *spin-up* year of the model.

The next family of variables analyzed concerns the *Secondary Producers*, whose trends are shown in *Figure 7.102*.

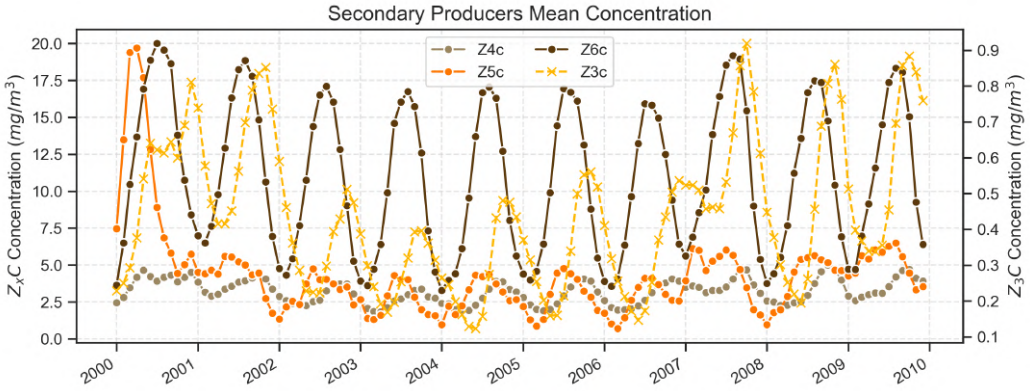

Figure 7.103: Time series of the mean *secondary producers* concentrations, expressed in mg/m^3. The variable shows are: *Carnivorous Mesozooplankton* (*Z3c*); *Omnivorous Mesozooplankton* (*Z4c*); *Microzooplankton* (*Z5c*) and *Heterotrophic Nanoflagellates* (*Z6c*).

The analysis of secondary producers indicates that *Microzooplankton* (*Z5c*) and *Carnivorous Mesozooplankton* (*Z3c*) are the species most strongly influenced by the model spin-up. In particular, *Z3c* displays elevated concentrations that persist until 2001, a behavior that is unique among the examined variables. This phenomenon appears to be linked to the effects previously observed on oxygen, as illustrated in *Figure 7.94*. The interannual variability of *Z3c* is especially pronounced: following the spin-up period, the average concentrations decrease sharply, before rising again at the beginning of 2007, eventually returning to levels comparable to those observed during the initial spin-up phase. This pattern suggests a strong sensitivity of *Z3c* to early model initialization and to subsequent changes in the ecosystem dynamics.

In contrast, the species *Z4c* and *Z5c* generally exhibit a trend amplification over time, but without any particularly distinctive anomalies or abrupt variations. The species *Z6c*, meanwhile, demonstrates behavior similar to that observed for diatoms, with a pronounced increase in its trend during the second time window. In this case, the observed variation can be attributed primarily to an increase in the overall mean concentration, which rises from 10.590773 mg/m^3 to 11.492386 mg/m^3, indicating a steady strengthening of *Z6c* abundance across the period under analysis.

Variable	Window		
	2001–2009	2001–2007	2007–2009
Z3c	0.016	0.0007	0.039
Z4c	0.072	0.041	0.157
Z5c	0.161	0.0007	0.237
Z6c	0.136	0.113	0.381

Table 7.18: Annual slope values per year for each zooplankton functional group (*Z3c–Z6c*), grouped by time window. The year 2000 is not used as it is the *spin-up* year of the model.

The final variable analyzed is the *Particulate Organic Matter*, whose trends are shown in *Figure 7.104*.

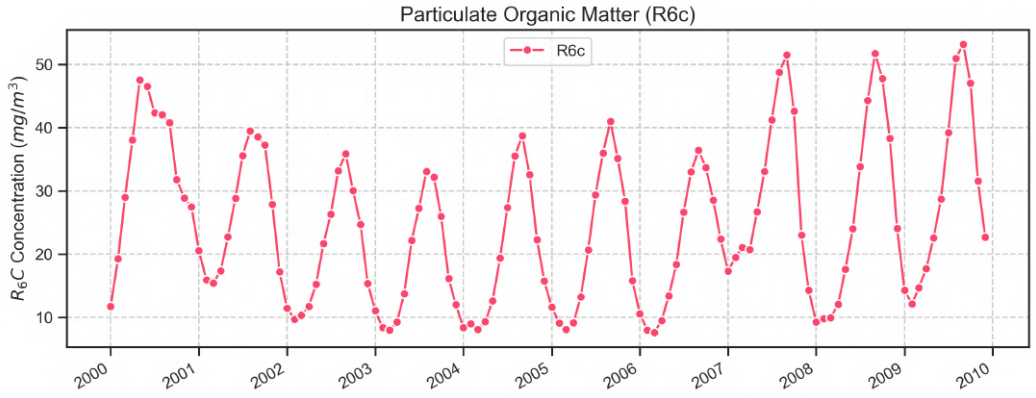

Figure 7.104: Time series of the mean *particulate organic matter* concentrations, expressed in mg/m^3

Here as well, all the phenomena previously observed in the other species families emerge. The effect of the model spin-up during the year 2000 is clearly noticeable, as is the change in trend and mean value starting from early 2007. The trend and mean values for this species are reported in *Table 7.19*.

Variable	Window		
	2001–2009	2001–2007	2007–2009
Slope per Year ($year^{-1}$)	1.227	0.938	3.074
Mean Concentration ($mmol/m^3$)	23.725	22.444	28.799

Table 7.19: Annual slope and mean concentration for the primary variable R6c, grouped by time window. The year 2000 is not used as it is the *spin-up* year of the model.

7.7 Investigating the Breakpoints

As highlighted by the previous analyses, a common *breakpoint* within the simulation can be identified during the winter of 2007. This is partially confirmed by the *Chlorophyll-a* trend analysis discussed in Section 7.2.4, as well as by the *surface dissolved oxygen* trend analysis presented in Section 7.3.1.

Both of these analyses reveal a marked shift in the overall trends of their respective variables, corroborated by either satellite or in-situ observations. Although these are the only two variables with observational support confirming this behavioural change, a similar phenomenon is observable across all variables examined in this study, from the temporal evolution of the biogeochemical parameters (Section 7.6) to the drops in correlation within the Sea Surface Temperature (Section 7.1.10), where the *shift* occurs slightly earlier. Cyclical processes such as the formation of *dense water masses* (Section 7.4) and the occurrence of *hypoxic* events within the basin (Section 7.5) also display a pronounced alteration during the winter of 2007. Collectively, these analyses indicate that a significant event took place during this period, marking a notable change in the system's behaviour. The following and final validation section aims to investigate and identify the potential causes of this event through a series of dedicated analyses.

The first step in investigating the cause of this *breakpoint* involves identifying the potential driver responsible for the observed shift. To this end, two core components of the simulation are analysed: the NEMO physical module and the BFM biogeochemical module. The working hypothesis is that the temperature shift acts as the primary trigger for the subsequent changes observed across the system, given that it represents the earliest deviation, with an onset in early 2006. To test this hypothesis, the Root Mean Square Error (RMSE) is computed for both components between simulated and satellite data, and their long-term trends are examined. The datasets are further divided into the two subsets according to the identified *breakpoint* of **January 1st, 2007**, consistent with the results from the previous analyses. The outcomes of this comparison are presented in *Figure 7.105*.

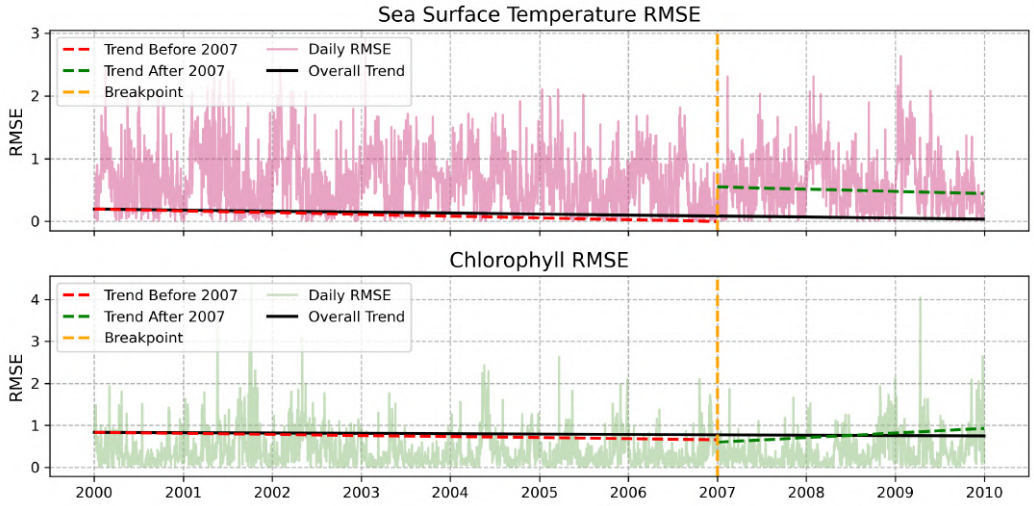

Figure 7.105: RMSE for the Sea Surface Temperature (top) and *Chlorophyll* − *a* (bottom). In each plot, the overall trend is shown by the black line, with the two subsets indicated in red (before the breakpoint) and green (after). The breakpoint is marked by an orange vertical dashed line.

Observing these results, the inversion in the chlorophyll trend clearly reappears, further supporting the presence of a behavioural shift within the simulation at the identified breakpoint. Conversely, the Sea Surface Temperature does not exhibit a comparable inversion, suggesting that the two phenomena are not directly linked. This indicates that while the biogeochemical system undergoes a structural change around 2007, it is not primarily driven by variations in surface temperature.

Given the absence of a clear cause–effect relationship between the two modules, the focus now shifts to examining potential variations in the water masses entering the basin within the model. Such changes could have introduced water with differing nutrient concentrations, either enriched or depleted, thereby triggering the observed shift in the biogeochemical dynamics of the simulation.

Two possible mechanisms are therefore considered:

- the intrusion of different salinity (more or less saline) waters from the southern boundary, potentially linked to an inversion of the BiOS (Adriatic-Ionian Bimodal Oscillating System) circulation;
- the increased input of fresher, nutrient-rich waters from the Po River, which could enhance productivity and alter the basin's nutrient balance.

The first hypothesis considers a shift in the Adriatic–Ionian Bimodal Oscillating System (BiOS), a quasi-decadal feedback between the Adriatic and Ionian Seas that forces the North Ionian Gyre (NIG) to alternate between cyclonic and anticyclonic upper-layer circulation. This alternation strongly influences which intermediate and surface waters are advected into the southern and northern Adriatic (Civitarese et al., 2010; Civitarese et al., 2023). Mechanistically, a cyclonic NIG promotes rapid advection of saltier Levantine/Cretan intermediate waters into the Adriatic, raising intermediate salinity and density, whereas an anticyclonic NIG deflects Modified Atlantic Water (MAW) northward, causing relative freshening and elevated nutrient content in the inflowing waters (Civitarese et al., 2010; Gačić et al., 2010). These alternations modify the preconditioning for dense-water formation by altering salinity, vertical nutricline position, and nutrient fluxes, and can therefore affect both physical ventilation and biogeochemical states on decadal timescales (Civitarese et al., 2010; Gačić et al., 2010; Civitarese et al., 2023).

In the context of the model, a cyclonic NIG phase delivering more saline, eastern-Mediterranean-type waters to the northern Adriatic would raise intermediate salinity and density, modify nutricline depth, and change the nutrient inventory, potentially triggering abrupt shifts in modeled biogeochemical variables through altered winter mixing and nutrient-driven primary production and oxygen dynamics (Civitarese et al., 2010; Gačić et al., 2010). Conversely, an anticyclonic inflow of fresher MAW would decrease intermediate salinity and adjust nutrient composition oppositely; thus, the sign of the biogeochemical response depends on which water mass, saline Levantine/Aegean or fresher MAW, is advected (Civitarese et al., 2010; Civitarese et al., 2023).

Regarding timing, observations and modeling studies report NIG/BiOS state changes in the mid-2000s. Gačić et al. (2010) and Civitarese et al. (2010) document an Ionian circulation transition beginning around 2006, with basin-scale signatures through 2006–2007, linked to changes in salinity and nutrient advection into the Adriatic. More

recent reconstructions using altimetry and tide-gauge data corroborate quasi-decadal reversals in 2006–2007 (Meli, 2024). Experimental and numerical studies further indicate that internal thermohaline feedbacks can produce such reversals without dominant wind forcing, supporting a BiOS-driven change in advected water masses during 2006–2007 (Rubino et al., 2020; Gačić et al., 2010; Civitarese et al., 2023). That said, the literature does not define a single precise calendar date for a BiOS inversion; NIG phase changes are gradual, with ±1 year uncertainty depending on the indicator, and different diagnostics (altimetry, sea-level, hydrography, nutrients) may identify the inflection at slightly different times (Meli, 2024; Civitarese et al., 2010).

To investigate this, Hovmöller diagrams for both the southern boundary and the Po Delta were computed at the bottom of the water column, to minimize the influence of the ROFI. The resulting diagrams are presented in *Figure 7.106*.

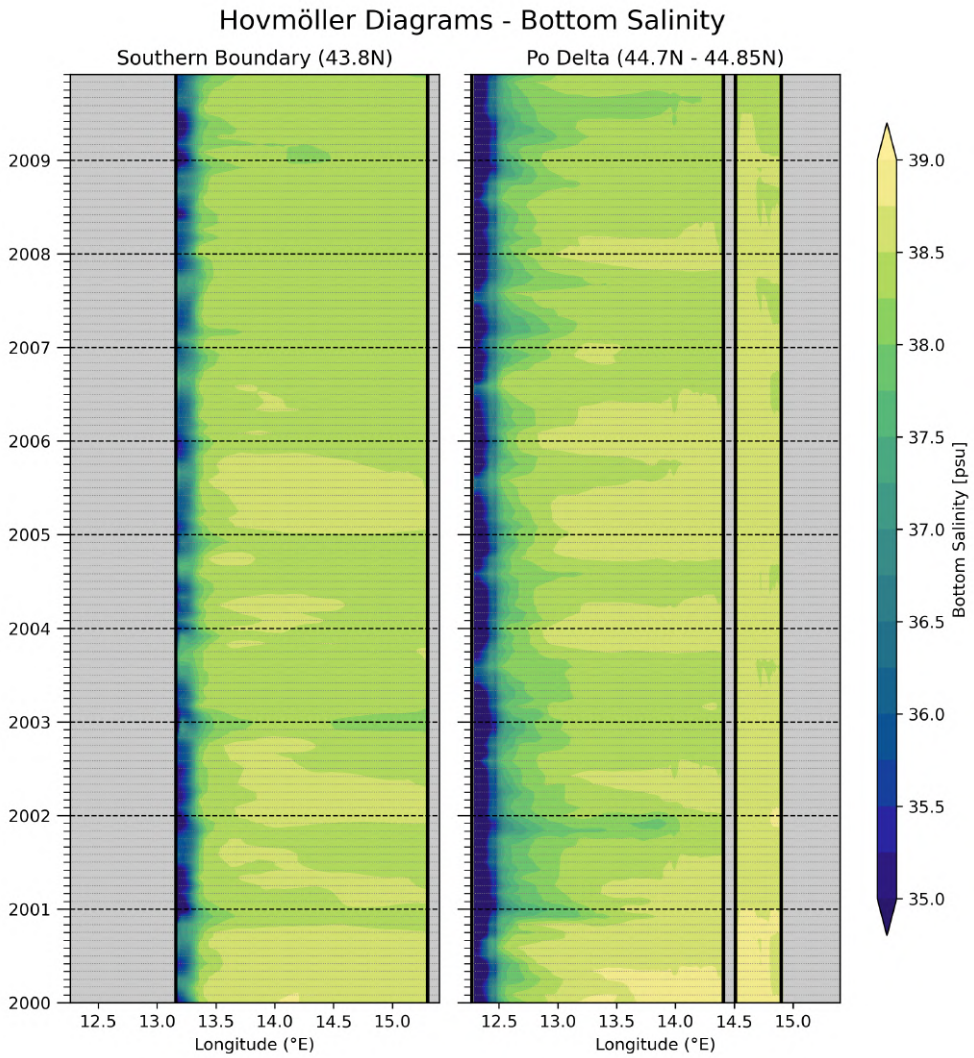

Figure 7.106: Hovmöller diagram of salinity computed at the bottom of the water column for two section: the open southern boundary (left), located at 43.8N, and the Po Delta (right) chosen between 44.7N and 44.85N. Shaded areas identify land.

Observing the southern boundary graph (left), if the anticyclonic phase of the NIG is present as hypothesized, the intrusion of a less saline water mass should be visible. Indeed, after a maximum in 2005, starting from 2006 a slight reduction in the salinity

of the water mass is recorded, stabilizing around $\sim 38 \div 38.5$ *psu* from values higher than 38.5 *psu*. This represents a significant decrease for the Northern Adriatic region and supports the presence of an anticyclonic NIG phase. The Po Delta graph (right) also shows a decreasing salinity trend, consistent with a slight expansion of the ROFI area, as evidenced by the gradual increase in low-salinity values.

To further investigate potential effects associated with the ROFI and the Po River discharge the analysis shifts to the evolution of the associated flow and freshwater input into the basin. Such analysis is done following the same procedure used for the chlorophyll trend analysis in section 7.2.4, thanks to which the breakpoint for the river flow is computed and identified as exactly January 1st, 2007, perfectly aligning with all previous analyses. This breakpoint corresponds to a distinct reversal of the flow trend, signalling the beginning of a sustained increase in river discharge. The evolution of such trends is plotted in *Figure 7.107*.

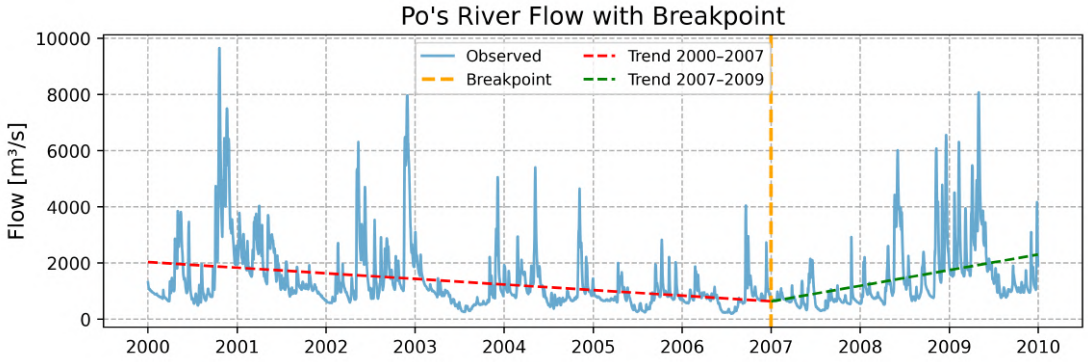

Figure 7.107: Evolution of the Po's observed river flow during the timeframe of the simulation. The trends before the breakpoint is shown in red while the one after is shown in green. The breakpoint is highlighted using a vertical orange dashed line.

As shown, the identified *breakpoint* marks a clear inversion in the river flow regime, with a substantial increase in the amount of freshwater entering the basin. This shift not only introduces large freshwater masses, contributing to a basin-wide reduction in salinity, but also enhances the input of nutrients into the water column, thereby influencing phytoplankton populations and altering their overall dynamics.

The specific trends for the river floe regimes before and after this *breakpoint* are reported in *Table 7.20*.

Window	**Slope** (m^3/s *per year*)
2000–2007	-199.17
2007–2009	556.81

Table 7.20: Linear flow trend slopes for the two time windows. Values are in m^3/s *per year*.

Furthermore, a second Hovmöller diagram was generated at the surface layer to see the effects of such variations in the river discharge. The results are presented in *Figure 7.108*. By focusing the analysis on this area two distinct trends emerge, both visible from the evolution of the low-salinity mass (blue colors). The first, spanning from the beginning of the simulation to roughly 2007, shows a decrease of the area associated

with such mass and, by consequence, the freshwater input into the basin. The second, from approximately 2007 to the end of the simulation, exhibits a progressive increase in the low-salinity mass, matching the evolution and the shift in the river flow regime.

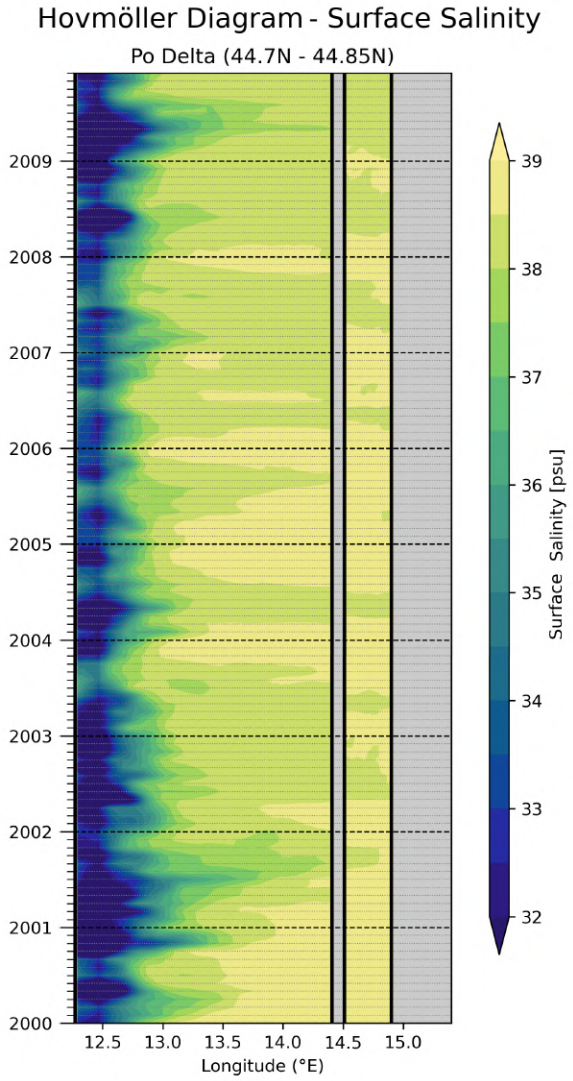

Figure 7.108: Hovmöller diagram of salinity computed at the surface for the Po Delta whose chosen latitude is between 44.7N and 44.85N. Shaded areas identify land.

Having identified both phenomena, an hypothesis can be done. Overall, although the influence of a low-salinity water mass linked to the anticyclonic phase of the Northern Ionian Gyre (NIG) cannot be entirely excluded, it appears secondary compared to the pronounced alteration in the Po River discharge regime. This shift in freshwater input emerges as the primary driver behind the changes observed in the biogeochemical fields. The event exerts a dual effect on the basin: it simultaneously lowers the overall salinity and enhances the nutrient supply, thus offering a consistent and coherent explanation for the transitions documented throughout the simulation period.

The temporal evolution of salinity within the basin further supports this interpretation. The patterns observed in the basin-averaged salinity suggest that the variability results from the combined action of both processes, the influence of the NIG and the Po River outflow, each acting with different intensities and at distinct depths within

the water column. To better disentangle their respective contributions, the evolution of salinity and its associated long-term trends were analyzed for three representative layers: the surface, the bottom, and the vertically averaged water column. The corresponding basin-wide time series and fitted trends are reported in *Figure 7.109*.

Although all three time series display a clear inversion in trend around the 2007 *breakpoint*, subtle differences emerge in the exact timing of the flex points, suggesting that distinct physical mechanisms govern the salinity dynamics at different depths. In particular, the delay observed in the bottom layer response may reflect the slower propagation of the signal from surface-driven processes, whereas the surface layer reacts more promptly to the hydrological regime shifts induced by variations in river discharge and regional circulation.

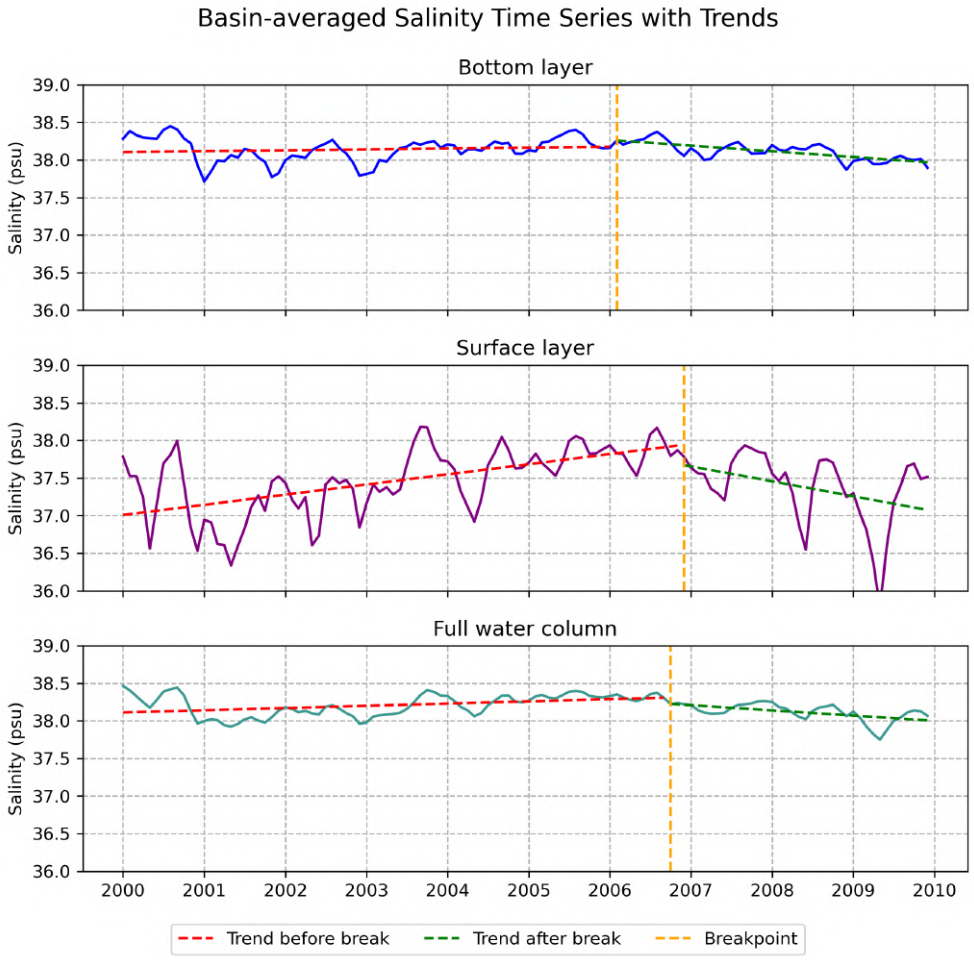

Figure 7.109: Salinity timeseries for all 3 layering methods. From top to bottom: bottom layer (blue); surface layer (purple) and full water column (indigo). The breakpoint is identified as an orange dashed line while trend before and after such breakpoint are shown in red (before) and green (after).

A closer examination of the three layers reveals distinct timing and dynamics in their respective trend inversions. The flex point identified in the bottom-layer time series occurs almost simultaneously with the reversal observed in the Hovmöller diagrams, a correspondence that supports the hypothesis of a link to the onset of the anticyclonic phase of the Northern Ionian Gyre (NIG). This synchronization suggests that the

deep-water signal primarily reflects the large-scale circulation changes associated with the gyre's regime shift rather than local forcing.

In contrast, the breakpoint detected in the surface layer occurs roughly one month before the inversion of the Po river flow regime. This temporal lead can likely be attributed to the combined effects of increased freshwater input and the concurrent arrival of low-salinity water masses advected into the basin during the NIG anticyclonic phase. The strong correspondence between the reversal in river-flow trends and the surface salinity breakpoint thus provides compelling evidence that the observed salinity transition in the upper layer is predominantly controlled by hydrological forcing from the river system.

The exact dates of the computed *breakpoints* for each of the analyzed layers are reported in *Table 7.21*, providing a quantitative summary of these depth-dependent dynamics.

Layer	**Breakpoint Date**	**Trend** (psu/yr)	
		Before	**After**
Bottom	2006-02-01	0.012	-0.076
Surface	2006-12-01	0.135	-0.199
Full column	2006-10-01	0.029	-0.069

Table 7.21: Breakpoint dates and salinity trends (before and after breakpoint) for the surface, bottom, and full water column layers.

Taken together, these two phenomena provide a consistent basis for a broad hypothesis explaining the shift in basin dynamics observed on the biogeochemical side of the simulation. Specifically, the overall decrease in salinity, driven by both the anticyclonic NIG phase and the enhanced Po River discharge, combined with the increased nutrient input resulting from the intensified river flow, could plausibly account for the inversion of nutrient trends and the observed rise in chlorophyll concentrations within the basin.

However, these mechanisms alone are insufficient to explain the pronounced drops in *coherence* and *correlation* identified for the Sea Surface Temperature in section 7.1.10. To explore a potential driver for these temperature-related events, the focus now shifts to the *Net Downward Heat Flux* at the air–sea interface.

A note regarding the CMEMS dataset used for this analysis: due to data availability constraints, the **reanalysis L4** product is employed in place of the previously used **L3s** data. While this substitution introduces certain limitations, particularly regarding the absence of in-situ collinear observations, as discussed in section 3, the unavailability of L3s data makes this choice necessary for a consistent temporal coverage. Consequently, the results presented in this section should be interpreted with these caveats in mind.

Furthermore, since the reanalysis dataset lacks cloud-cover information, the model data are analyzed in their unmasked form, without the application of any cloud-filtering procedure, to maintain methodological consistency between the two datasets.

The analysis addressing this specific question is structured around the following hypothesis: both the model and the satellite record a distinct event during the winter

marking the transition between 2005 and 2006. However, the two datasets exhibit different responses to this event, which ultimately leads to the progressive degradation of the $105 \div 125$ *days* component, as discussed in section 7.1.10.

To investigate this, the **DJF** (December–January–February) seasons are compared across two timeframes: **2000–2005** and **2006–2009**. Since the full-field plots do not display particularly pronounced events, they are omitted here; instead, only the corresponding anomaly maps are presented in *Figure 7.110*, as they provide clearer insights into the differences between the two periods.

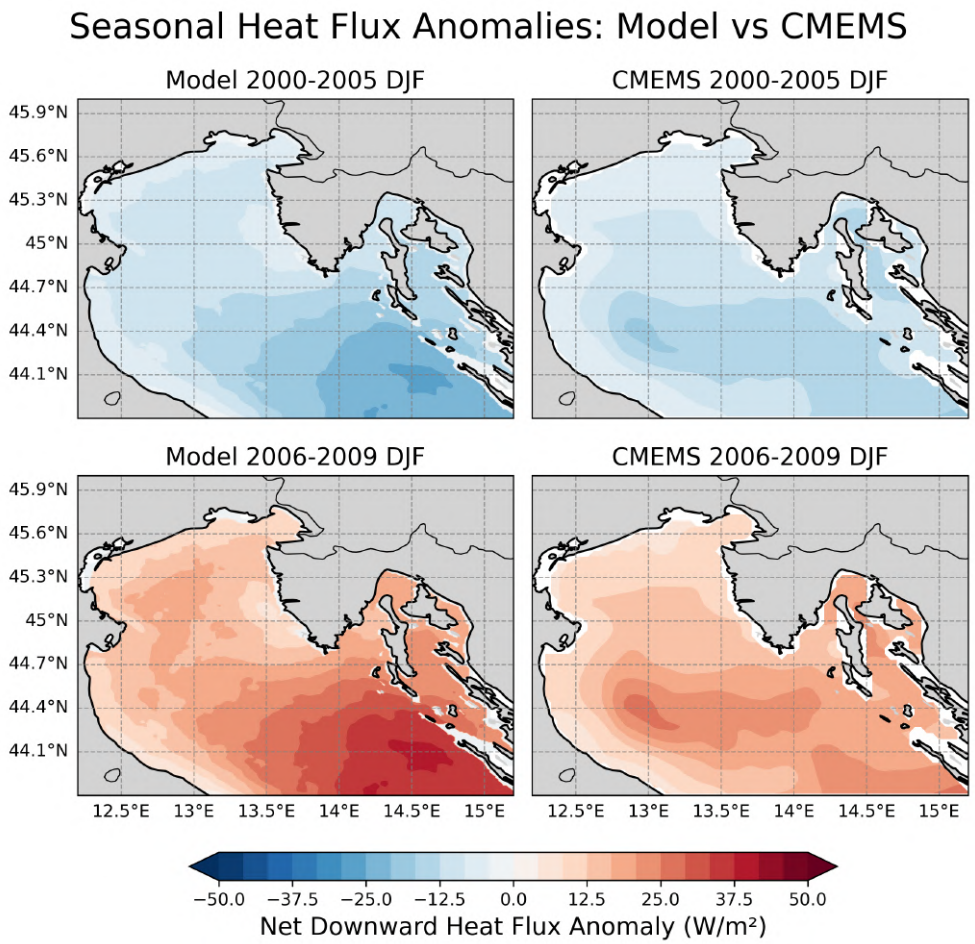

Figure 7.110: Net Downward Heat Flux Anomalies for the DJF seasons for the model data (left) and CMEMS data (right). Top row shows the 2000-2005 timeframe while the bottom shows the 2006-2009 one.

It is important to note that the degradation in correlation between the two datasets becomes evident when the band-pass filter is applied. However, the fields analyzed here correspond to the *full, unfiltered* data. While this mismatch may somewhat limit the direct comparability of results, since these data do not undergo the same temporal filtering, the approach remains justified by the constraints of data availability. Specifically, the model outputs are only available as monthly means, preventing the application of the desired filtering procedure.

The difference between the two analyzed timeframes is evident: both datasets display a net negative anomaly component for the heat flux during the first period and a net

positive one in the second. Although this transition is visible in both products, the model's response is considerably stronger, as indicated by the larger and more pronounced positive anomaly observed in the southern portion of the basin. Conversely, the satellite dataset shows a much weaker anomaly. This distinction is fundamental for understanding the behaviour of the Sea Surface Temperature. Since we this event revolves around the anomaly component of the net downward heat flux, the shift from negative to positive anomalies marks a transition from winters in which the ocean experiences anomalously enhanced heat loss to winters in which the surface layer receives anomalously increased heat input. Physically, such anomaly reversals modify the perturbation applied to the surface heat budget: positive flux anomalies tend to warm the upper ocean, weaken winter cooling, reduce mixed-layer deepening, and limit the entrainment of colder subsurface waters. Both datasets detect this anomaly transition during the 2005–2006 winter, and both show corresponding adjustments in the SST fields, confirming that an externally forced event is consistently captured.

What differentiates the two products is therefore not the presence of the anomaly-driven shift, but the amplitude with which it is represented. The model exhibits a considerably stronger positive heat-flux anomaly, and consequently produces a stronger SST warming response. The satellite, on the other hand, registers the same anomaly sign change but with much lower magnitude, leading to a more subdued SST perturbation. This mismatch in anomaly intensity is precisely what propagates into the discrepancies documented in Section 7.1.10. While the timing of the event remains coherent between model and satellite, marking a success in the long-term variability reproduced by the simulation, their progressively divergent SST responses, rooted in the differing strengths of the underlying heat-flux anomalies, ultimately lead to the degradation in coherence and correlation of the 105-125 day component. Thus, the divergence arises not from whether the anomaly shift occurred, but from how strongly each dataset translates that shift into surface temperature variability.

Nonetheless, these results must be interpreted with caution due to the caveats previously discussed, particularly the limitations associated with the temporal resolution and filtering constraints of the available datasets.

Chapter 8
Conclusions and Future Works

This thesis has delivered a comprehensive, multi–scale validation of the coupled NEMO–BFM modelling system applied to the Northern Adriatic Sea for the decade 2000–2009. By combining satellite Sea Surface Temperature (SST) and chlorophyll data, in–situ measurements from ARPAE/DAPHNE stations and ADRIA cruises, river discharge records, and an extensive set of statistical, spectral and spatial diagnostics, the work provides a robust assessment of how well the model captures the physical and biogeochemical processes shaping this shallow, river–dominated basin.

The physical validation of the Sea Surface Temperature demonstrates that the coupled system successfully reproduces the main seasonal cycle and the bulk statistical characteristics of the observed field, as confirmed by the seasonal decomposition, scatterplots, and regression analyses. In addition to capturing the mean seasonal structure, the model also reproduces the interannual variability of the observed SST, correctly reflecting year-to-year fluctuations in both basin-wide temperatures and seasonal extrema. The inversion of the surface heat-flux regime identified in early 2006 is likewise represented, indicating that the coupled system responds coherently to large-scale atmospheric forcing anomalies.

However, the model exhibits persistent amplitude biases: during both winter and summer, it tends to underestimate cold extremes and overestimate warm extremes, with SST errors on the order of $\pm 2^{\circ}$C. Despite this, the simulation accurately follows the interannual evolution of these extremes. In years when observed winter minima are particularly low or summer maxima particularly high, the model reproduces the corresponding anomalies with the correct sign and timing, albeit affected by such bias. This behaviour indicates that the system captures the variability of the thermal range even if its absolute amplitude is biased.

Despite the overall agreement with satellite observations, degradations in spectral coherence emerge in the 105–125 day frequency band. The spectral and wavelet diagnostics reveal a loss of coherence in these mid-period components, indicating that while the model captures the broad climatological structure, it struggles to reproduce intermediate-timescale variability. As detailed in Section 7.7, DJF anomaly diagnostics link these discrepancies to a differing response of the model and satellite datasets to a shift in the Net Downward Heat Flux regime in early 2006.

Further systematic discrepancies arise when comparing the simulation to in-situ CTD measurements, most notably a temporal offset of approximately one month in the seasonal phasing of temperature minima and maxima, with the model consistently lagging the observations.

The biogeochemical validation of Chlorophyll reveals a difference in both the timing and spatial distribution of phytoplankton blooms with the observed data, which

arises not from an arbitrary model failure but from a systematic structural bias in how the simulation represents coastal versus offshore productivity. As discussed in Section 7.2.2, the model over-emphasises the coastal component of primary production, generating intense nearshore blooms that dominate the basin signal. This coastal overweighting shifts the basin-scale chlorophyll maximum toward mid–late winter, not because the model miscalculates the timing of the bloom per se, but because it amplifies the wintertime nutrient-rich, nearshore-driven response at the expense of the offshore contribution. Conversely, the model under-represents the microbial-driven, open-sea chlorophyll blooms that characterise the offshore domain in satellite observations. As a result, open-water peaks are substantially damped, and the spatial pattern of offshore chlorophyll is overly smoothed, failing to reproduce the finer-scale microbial processes driving offshore spring productivity.

A second, equally relevant bias concerns the long-term chlorophyll trends. Satellite and in-situ observations show a basin-averaged negative trend, consistent with the gradual oligotrophication documented in the literature, whereas the model exhibits an increasing trend over the same period. Although this initially appears to reflect a major discrepancy, the trend analysis indicates that the mismatch is largely confined to the distribution of coastal versus offshore variability. Once a breakpoint around 2007 is identified and the time series is separated accordingly, the post- and pre-2007 model trends align spatially with those of the satellite product, reproducing both the inversion in the trend sign and the spatial structure of the dominant empirical pattern. The largest discrepancies remain concentrated along the Po ROFI and the surrounding coastal margins. In these regions, the model displays trend behaviour that is opposite to both satellite and in-situ datasets, a divergence that can be attributed to the simplified representation of riverine forcing. In particular, the parameterisation of the river forcings introduce approximations in both the temporal variability and the spatial distribution of freshwater and nutrient loads, which in turn amplify the coastal nutrient-driven component and distort the long-term evolution of nearshore chlorophyll.

Trend-break analyses further reveal a coherent behavioural shift emerging in the winter of 2007, a transition that is detectable, and in some cases corroborated by observations, notably for chlorophyll and surface dissolved oxygen (see Sections 7.2.4 and 7.3.1). The post-2007 rise in modeled chlorophyll is consistent across functional groups and appears linked to an inversion in the Po's river flow regime (Section 7.7) which, through increased freshwater discharge into the basin, enhances nutrient availability and modifies benthic–pelagic exchanges.

A deeper temporal analysis using spectral techniques further supports these interpretations. As shown in Figure 7.63, the model exhibits reduced spectral power at sub-seasonal periods between approximately 18–22 days and, more substantially, between 32–90 days. Conversely, both model and satellite datasets record a matching peak around $\sim$ 146 days. The model also displays enhanced energy at longer periods, characterised by an intensified annual peak around 300 days. The satellite record, on the other hand, shows additional variability associated with multi-year ($\sim$ 720 day) fluctuations, which the hindcast cannot reproduce due to its limited temporal coverage. Collectively, these findings indicate that the model under-represents mesoscale and sub-seasonal dynamics, particularly those governing offshore microbial productivity, while disproportionately emphasising slower, basin-scale modes of variability.

The model also reproduces the formation and cascading of North Adriatic Dense Water. The dense–water volume diagnostics and transect analyses show patterns consistent with the known sequence of summer–autumn preconditioning followed by Bora–driven winter cooling. The downslope propagation along bathymetric corridors is also consistent with the expected pathways described in the literature. These results demonstrate that the physical core of the model is capable of representing winter convection, dense–water generation and cross–shelf exchange processes with reasonable accuracy.

The benthic oxygen diagnostics in reveal the model's largest biogeochemical shortcoming, in that the simulated hypoxic footprints are seasonally persistent and spatially extensive compared to observational syntheses. Time series of bottom hypoxic area in Figure 7.95 and the climatology in Figure 7.96 show a JAS peak, and transect analyses in Figures 7.97 and 7.98 place the hypoxic front predominantly along the western shelf and in the Po-influenced regions. Quantitatively, peak monthly hypoxic extents in the model approach approximately 1.5×10^4 km^2, an order of magnitude larger than many historical observational maxima cited in the literature. A direct comparison with February 2007 observations, highlights a notable mismatch, with the model reporting a mean bottom oxygen of 17.12 mmol/m^3 while ARPAE and ENEA observations report means of 248.00 and 191.49 mmol/m^3 respectively, after unit conversion, a discrepancy that indicates the model substantially overestimates bottom oxygen at the bottom of the water column and underestimates observed oxygen concentrations. This points to an excessive benthic oxygen demand or an unbalanced benthic–pelagic exchange in the model parameterization, and it is consistent with the elevated particulate organic matter export and with the increased biological production documented by the chlorophyll and particulate organic matter diagnostics.

The remaining biogeochemical fields support a coherent narrative, whereby many planktonic and particulate state variables show trend shifts or amplitude changes around the 2006–2007 window. Zooplankton groups Z3c–Z6c exhibit varying slope behaviour across the two time windows, while particulate organic matter displays a pronounced mean increase and steeper post-2007 slope. These internal consistencies within the model results, while valuable, do not substitute for improving the match with observations in magnitude, seasonality and trend, particularly in the coastal plume and bottom oxygen sectors.

Taken together, the coupled model succeeds at reproducing many first-order spatial and seasonal patterns of the Northern Adriatic Sea, it reproduces episodic dense water production and basic plume footprints, and it captures the broad timing of hypoxic seasonal cycles, thereby demonstrating utility for mechanistic studies and hypothesis testing. The principal model deficiencies are concentrated in three inter-related domains: firstly, a tendency to overestimate phytoplankton biomass and particulate export, producing chlorophyll magnitudes and trends that diverge from satellite and in situ observations; secondly, an excessive benthic oxygen demand and a very approximated benthic parametrization yield expansive hypoxic areas and low bottom oxygen values relative to observations; and thirdly, a sensitivity to river forcing and regional circulation changes that imposes abrupt regime shifts when the prescribed river flow and circulation signals change, with the Po flow breakpoint serving as a striking example. These deficiencies are not independent, rather they form a feedback loop in which

river-driven nutrient inputs and plume dynamics set phytoplankton production patterns, particulate export feeds benthic demand, and benthic remineralization controls bottom oxygen, therefore small errors in any element propagate systemically. The thesis therefore identifies both where the model performs well, and where targeted improvements will yield the largest reduction in model–observation bias.

8.1 Future Works

The results of this thesis point to several concrete directions for future development. Refinement of river forcing is essential. This includes the acquisition and implementation of improved time–varying nutrient loads, temperature records and sediment fluxes from the Po and other rivers. Enhancing the representation of river mouth dynamics, possibly through explicit estuarine sub–models or embedded higher–resolution grids, would likely reduce coastal biases and improve plume structure.

Increased horizontal resolution should be considered, particularly along the western Adriatic coast where lagoonal systems and narrow bathymetric features strongly shape circulation. Unstructured–grid or nested-grid approaches could provide the necessary flexibility to resolve these coastal complexities.

On the biogeochemical side, the BFM module would benefit from improved representation of phytoplankton photoacclimation, flexible chlorophyll–to–carbon ratios, and more detailed grazing dynamics. Implementing a more sophisticated sediment diagenesis model would also improve the simulation of benthic oxygen demand and hypoxia development. In addition, expanding the trophic web to include a broader set of functional groups and species would enhance ecosystem realism, albeit at a higher computational cost, and would increase system resilience, since a more diversified food web mitigates the risk of trophic collapse when specific primary-producer groups decline. Finally, introducing stochastic formulations for key physiological and Geider parameters by sampling from parameter ensembles rather than prescribing single deterministic values would provide a more realistic representation of biological variability and improve the robustness of modeled ecosystem responses.

To address timing and spectral discrepancies, future hindcasts should incorporate higher–frequency atmospheric forcing, more accurate river discharge and temperature records, and possibly data assimilation of satellite chlorophyll during key periods. Assimilation could significantly reduce timing errors and correct amplitude underestimation in bloom phases.

A major step forward would be the development of ensemble modelling approaches to quantify uncertainty in river forcing, biological parameters, atmospheric fields and boundary conditions. Ensemble simulations would allow probabilistic estimation of hypoxia risk and dense–water formation under varying climate and land-use scenarios.

Finally, the validation methodology developed in this thesis, which includes spatial error analysis, harmonic decomposition, spectral diagnostics, wavelet coherence, ROFI clustering and trajectory tracking, should be adopted as a systematic toolkit for future model development. The ability to diagnose errors at specific temporal and spatial scales is invaluable for targeted improvement efforts, and the framework is fully transferable to other coastal modelling applications.

Bibliography

Amorosi, A., Sammartino, I., Dinelli, E., Campo, B., Guercia, T., Trincardi, F., and Pellegrini, C. (2022). Provenance and sediment dispersal in the po-adriatic source-to-sink system unraveled by bulk-sediment geochemistry and its linkage to catchment geology. *Earth-Science Reviews*, 234:104202.

Aragão, L., Mentaschi, L., Pinardi, N., Verri, G., Senatore, A., and Di Sabatino, S. (2024). The freshwater discharge into the adriatic sea revisited. *Frontiers in Climate*, 6.

Arakawa, A. and Lamb, V. R. (1977). Computational design of the basic dynamical processes of the ucla general circulation model. In *Methods in Computational Physics*, volume 17, pages 174–267. Academic Press.

ARPAE Emilia-Romagna (2009). Qualità ambientale delle acque marino-costiere 2009. Technical report, Agenzia Regionale per la Protezione Ambientale dell'Emilia-Romagna.

ARPAE Emilia-Romagna (2024). Fiume po, sezione idrometrica di pontelagoscuro – portate e indicatori (webbook). `https://webbook.arpae.it/indicatore/Portata-dei-fiumi-00001/`.

Artegiani, A., Bregant, D., Paschini, E., Pinardi, N., Raicich, F., and Russo, A. (1997a). The adriatic sea general circulation. part i: Air–sea interactions and water mass structure. *Journal of Physical Oceanography*, 27(8):1492–1514.

Artegiani, A., Bregant, D., Paschini, E., Pinardi, N., Raicich, F., and Russo, A. (1997b). The adriatic sea general circulation. part ii: Baroclinic circulation structure. *Journal of Physical Oceanography*, 27(8):1515–1532.

Arthur, D. and Vassilvitskii, S. (2007). k-means++: The advantages of careful seeding. In *Proceedings of the Eighteenth Annual ACM–SIAM Symposium on Discrete Algorithms (SODA)*, pages 1027–1035.

Azam, F., Fenchel, T., Field, J. G., Gray, J. S., Meyer-Reil, L. A., and Thingstad, F. (1983). The ecological role of water-column microbes in the sea. *Marine Ecology Progress Series*, 10:257–263.

Babagolimatikolaei, J., Schultz, D. M., Parkes, B., and Draycott, S. (2025). Impacts of the po river on adriatic sea hydrodynamics and interbasin exchanges. *Journal of Geophysical Research: Oceans*, 130(7):e2024JC022196.

Bailey, S. W. and Werdell, P. J. (2006). A multi-sensor approach for the on-orbit validation of ocean color satellite data products. *Remote Sensing of Environment*, 102:12–23.

Bendat, J. S. and Piersol, A. G. (2010). *Random Data: Analysis and Measurement Procedures*. Wiley, 4th edition.

Bergamasco, A., Oguz, T., and Malanotte-Rizzoli, P. (1999). Modeling dense water mass formation and winter circulation in the northern and central adriatic sea. *Journal of Marine Systems*, 20(1-4):279–300.

Berthon, J.-F. and Zibordi, G. (2004). Bio-optical relationships for the northern adriatic sea. *International Journal of Remote Sensing*, 25(7–8):1527–1532.

Beven, K. J. (2001). *Rainfall-Runoff Modelling: The Primer*. John Wiley & Sons Ltd., Chichester.

Bloomfield, P. (2000). *Fourier Analysis of Time Series: An Introduction*. Wiley.

Boldrin, A., Carniel, S., Giani, M., Marini, M., Aubry, F. B., Campanelli, A., Grilli, F., and Russo, A. (2009). The northern adriatic sea ecosystem: Present situation and trends between 1970 and 2004. *Marine Ecology Progress Series*, 375:77–94.

Bowman, A. W. and Azzalini, A. (1997). *Applied Smoothing Techniques for Data Analysis*. Oxford University Press.

Braun, S. (2001). Windows. In Braun, S., editor, *Encyclopedia of Vibration*, pages 1587–1595. Elsevier, Oxford.

Bretherton, F. P., Davis, R. E., and Fandry, C. B. (1976). A technique for objective analysis and design of oceanographic experiments applied to mode-73. *Deep Sea Research and Oceanographic Abstracts*, 23(7):559–582.

Butterworth, S. (1930). On the theory of filter amplifiers.

Campbell, J. W. (1995). The lognormal distribution as a model for bio-optical variability in the sea. *Journal of Geophysical Research: Oceans*, 100(C7):13237–13254.

Canuto, V. M., Howard, A. M., Cheng, Y., and Dubovikov, M. S. (2010). Ocean turbulence. iii: New giss vertical mixing scheme: Part i. theory and validation. *Journal of Physical Oceanography*, 40:235–258.

Castellari, S., Pinardi, N., and Leaman, K. (1998). A model study of air–sea interactions in the mediterranean sea. *Journal of Marine Systems*, 18:89–114.

Chiapolino, A., Saurel, R., and Nkonga, B. (2017). Sharpening diffuse interfaces with compressible fluids on unstructured meshes. *Journal of Computational Physics*, 340:389–417.

Civitarese, G., Gačić, M., Batistić, M., Bensi, M., Cardin, V., Dulčić, J., Garić, R., and Menna, M. (2023). The bios mechanism: History, theory, implications. *Progress in Oceanography*, 216:103056.

Civitarese, G., Gačić, M., Lipizer, M., and Eusebi Borzelli, G. L. (2010). On the impact of the bimodal oscillating system (bios) on the biogeochemistry and biology of the adriatic and ionian seas (eastern mediterranean). *Biogeosciences*, 7:3987–3997.

Clementi, E., Aydogdu, A., Goglio, A. C., Pistoia, J., Escudier, R., Drudi, M., Grandi, A., Mariani, A., Lyubartsev, V., Lecci, R., Cretí, S., Coppini, G., Masina, S., and Pinardi, N. (2021). Mediterranean sea physical analysis and forecast (cmems med-currents, eas6 system) (version 1) [data set]. Version 1.

Cleveland, R. B., Cleveland, W. S., McRae, J. E., and Terpenning, I. (1990). Stl: A seasonal-trend decomposition procedure based on loess. *Journal of Official Statistics*, 6(1):3–73.

Cleveland, W. S. (1979). Robust locally weighted regression and smoothing scatterplots. *Journal of the American Statistical Association*, 74(368):829–836.

CMEMS - SST Production Centre (2024). Product user manual (pum) for cmems mediterranean and black sea sea surface temperature products. `https://documentation.marine.copernicus.eu/PUM/CMEMS-SST-PUM-010-010.pdf`. Accessed August 2025.

Cossarini, G., Solidoro, C., Conversi, A., et al. (2012). Dynamics of biogeochemical properties in temperate coastal areas of freshwater influence: lessons from the northern adriatic sea. *Estuarine, Coastal and Shelf Science*, 115:63–73.

Cozzi, S. and Giani, M. (2011). River water and nutrient discharges in the northern adriatic sea: Current importance and long term changes. *Continental Shelf Research*, 31(18):1881–1893.

Cushman-Roisin, B., Gačić, M., Poulain, P.-M., and Artegiani, A., editors (2001). *Physical Oceanography of the Adriatic Sea: Past, Present and Future*. Kluwer Academic Publishers, Dordrecht.

de Wit, M. and Bendoricchio, G. (2001). Nutrient fluxes in the po basin. *Science of the Total Environment*, 273:147–161.

Degobbis, D., Precali, R., Ivancić, I., Smodlaka, N., Fuks, D., and Kveder, S. (2000). Long-term changes in the northern adriatic ecosystem related to anthropogenic eutrophication. *International Journal of Environment and Pollution*, 13(1-2):495–533.

Deserti, M. et al. (2005). Relationships between northern adriatic sea mucilage events and environmental factors. *Science of the Total Environment*, 353:1–12.

Diaz, R. J. and Rosenberg, R. (2008). Spreading dead zones and consequences for marine ecosystems. *Science*, 321:926–929.

Djakovac, T., Supić, N., Bernardi Aubry, F., Degobbis, D., and Giani, M. (2015). Mechanisms of hypoxia frequency changes in the northern adriatic sea during the period 1972–2012. *Journal of Marine Systems*, 141:179–189.

Dunić, N., Vilibić, I., Šepić, J., et al. (2018). Dense water formation and bios-induced variability in the adriatic sea simulated using an ocean regional circulation model. *Climate Dynamics*, 51:1211–1236.

E.U. Copernicus Marine Service Information (CMEMS) (2023). Mediterranean sea, bio-geo-chemical, l3, daily satellite observations (1997-ongoing). Marine Data Store (MDS). Accessed on 04-Aug-2025.

E.U. Copernicus Marine Service Information (CMEMS) (2024). Mediterranean sea - high resolution l3s sea surface temperature reprocessed. Marine Data Store (MDS). Accessed on 04-Aug-2025.

Faganeli, J., Ogrinc, N., Kovač, N., Kukovec, K., Falnoga, I., Mozetič, P., and Bajt, O. (2009). Carbon and nitrogen isotope composition of particulate organic matter in relation to mucilage formation in the northern adriatic sea. *Marine Chemistry*, 114:102–109.

Farrell, J. A. (2008). *Aided Navigation: GPS with High Rate Sensors*. McGraw-Hill.

Filippucci, P. (2022). *High-Resolution Remote Sensing For Rainfall And River Discharge Estimation: applications to the Po River (PhD thesis)*. PhD thesis, TU Wien (University of Natural Resources and Life Sciences, Vienna) / partner institutions.

Fiori, E., Zavatarelli, M., Pinardi, N., Mazziotti, C., and Ferrari, C. R. (2016). Observed and simulated trophic index (trix) values for the adriatic sea basin. *Nat. Hazards Earth Syst. Sci. Discuss.* Received: 2 March 2016; Revised: 9 August 2016; Accepted: 11 August 2016.

Flather, R. A. (1976). A tidal model of the northwest european continental shelf. *Mémoires de la Société Royale des Sciences de Liège*, 6:141–164.

Gačić, M., Eusebi Borzelli, G. L., Civitarese, G., Cardin, V., and Yari, S. (2010). Can internal processes sustain reversals of the ocean upper circulation? the ionian sea example. *Geophysical Research Letters*, 37(L09608).

GEBCO Bathymetric Compilation Group (2021). The gebco_2021 grid – a continuous terrain model of the global oceans and land. Technical report, Seabed2030 Global Center, National Oceanography Centre, UK.

Geider, R. J., MacIntyre, H. L., and Kana, T. M. (1996). A dynamic model of photoadaptation in phytoplankton. *Limnology and Oceanography*, 41(1):1–15.

Geider, R. J., MacIntyre, H. L., and Kana, T. M. (1997). A dynamic model of phytoplankton growth and acclimation: responses of the balanced growth rate and chlorophyll *a*:carbon ratio to light, nutrient limitation and temperature. *Marine Ecology Progress Series*, 148:187–200.

Giani, M., Djakovac, T., Degobbis, D., Cozzi, S., Solidoro, C., and Fonda Umani, S. (2012). Recent changes in the marine ecosystems of the northern adriatic sea. *Estuarine, Coastal and Shelf Science*, 115:1–13.

Giorgetti, A. (1999). Climatological analysis of the adriatic sea thermohaline characteristics. *Bollettino di Geofisica Teorica ed Applicata*, 40(1):53–73.

Gonzalez, R. C. and Woods, R. E. (2008). *Digital Image Processing*. Pearson Prentice Hall, 3rd edition.

Govorov, M. (2025). Exploration-based statistical learning for selecting kernel density estimates of spatial point patterns. *Transactions in GIS*, 29(3):1025–1042.

Graham, J. A. and et al. (2018). Amm15: a new high-resolution nemo configuration for operational modelling of the north-west european continental shelf. *Geoscientific Model Development*, 11:681–696.

Griffies, S. M. and Hallberg, R. W. (2000). Biharmonic friction with a smagorinsky-like viscosity for use in large-scale eddy-permitting ocean models. *Monthly Weather Review*, 128:2935–2946.

Griffiths, J., Kadin, M., Nascimento, F., Tamelander, T., Tornroos, A., Bonaglia, S., Bonsdorff, E., Bruckert, S., Gardmark, A., Järnström, H., and et al. (2017). The importance of benthic–pelagic coupling for marine ecosystem functioning in a changing world. *Global Change Biology*, 23(6):2179–2196.

Grilli, F., Accoroni, S., Acri, F., Bernardi Aubry, F., Bergami, C., Cabrini, M., Campanelli, A., Giani, M., Guicciardi, S., Marini, M., et al. (2020). Seasonal and interannual trends of oceanographic parameters over 40 years in the northern adriatic sea in relation to nutrient loadings using the emodnet chemistry data portal. *Water*, 12(8):2280.

Grinsted, A., Moore, J. C., and Jevrejeva, S. (2004). Application of the cross wavelet transform and wavelet coherence to geophysical time series. *Nonlinear Processes in Geophysics*, 11:561–566.

Hecht, M. W. and Smith, R. D. (2008). Lateral mixing in the eddying regime and a new broad-ranging formulation. *Journal of Geophysical Research*, 113:C05003.

Huber, P. J. (1981). *Robust Statistics*. Wiley, New York.

Hyndman, R. J. and Athanasopoulos, G. (2018). *Forecasting: principles and practice*. OTexts.

ISPRA - Istituto Superiore per la Protezione e la Ricerca Ambientale (2012). Manuali e linee guida per il monitoraggio marino-costiero. Technical report, ISPRA.

Jeffries, M. A. and Lee, C. M. (2007). A climatology of the northern adriatic sea's response to bora and river forcing. *Journal of Geophysical Research: Oceans*, 112:C03S02.

Jolliff, J. K., Kindle, J. C., Shulman, I., Penta, B., Friedrichs, M. A. M., Helber, R., and Arnone, R. A. (2008). Summary diagrams for coupled hydrodynamic-ecosystem model skill assessment. *Journal of Marine Systems*, 76(1-2):64–82.

Justić, D. (1991). Hypoxic conditions in the northern adriatic sea: historical development and ecological significance. *Geological Society, London, Special Publications*, 58:89–102.

Krause, P., Boyle, D. P., and Bäse, F. (2005). Comparison of different efficiency criteria for hydrological model assessment. *Advances in Geosciences*, 5:89–97.

Kuzmić, M., Janeković, I., Book, J. W., Martin, P. J., and Doyle, J. D. (2006). Modeling the northern adriatic double-gyre response to intense bora wind: A revisit. *Journal of Geophysical Research: Oceans*, 111(C3):C03S13.

Lee, J. and Park, J. (2021). Visualization techniques for spatial dispersion analysis using hexbin density mapping. *Scientific Research and Essays*, 16(4):143–150.

Legates, D. R. and McCabe, G. J. (1999). Evaluating the use of "goodness-of-fit" measures in hydrologic and hydroclimatic model validation. *Water Resources Research*, 35(1):233–241.

Legendre, L. and Rassoulzadegan, F. (1995). Plankton and nutrient dynamics in marine waters. *Ophelia*, 41(1):153–172.

Lloyd, S. P. (1982). Least squares quantization in pcm. *IEEE Transactions on Information Theory*, 28(2):129–137.

Lovato, T. and Butenschön, M. (2023). *Coupling BFM with Ocean Models: the NEMO model V4.2 (Nucleus for the European Modelling of the Ocean).* Bologna, Italy, release 2.0 edition. pp. 30.

Ludwig, W., Dumont, E., Meybeck, M., and Heussner, S. (2009). River discharges of nutrients to the mediterranean and black sea: Major drivers and processes. *Global Biogeochemical Cycles*, 23(4).

Luo, J. et al. (2024). Saltwater intrusion in the po river delta (italy) during drought conditions: analyzing its spatio-temporal evolution and potential impact on agriculture. *International Soil and Water Conservation Research*, 12:714–.

Lévy, B., Madec, G., Penduff, T., Durand, E., Birol, F., Lengaigne, M., and Loutre, M.-F. (2001). Choice of an advection scheme for biogeochemical models. *Geophysical Research Letters*, 28:3725–3728.

MacQueen, J. (1967). Some methods for classification and analysis of multivariate observations. *Proceedings of the Fifth Berkeley Symposium on Mathematical Statistics and Probability*, 1:281–297.

Madec, G. and Delecluse, P. (1998). Ocean modelling on parallel machines: From the primitive equations to the opa code. *International Journal of High Performance Computing Applications*, 12:151–187.

Madec, G. and Team, T. N. (2016). Nemo ocean engine v3.6: Primitive equations, tracers and eos-80 implementation. Technical Report Note du Pôle de modélisation No. 27, Institut Pierre-Simon Laplace (IPSL) / Pôle de Modélisation.

Malanotte-Rizzoli, P. (2014). Physical forcing and physical/biochemical variability of the adriatic sea. Technical report, Massachusetts Institute of Technology.

Mallat, S. (1999). *A Wavelet Tour of Signal Processing.* Academic Press.

Manca, B. B., Kovačević, V., Gačić, M., and Viezzoli, D. (2002). Dense water formation in the southern adriatic sea and spreading into the ionian sea in the period 1997–1999. *Journal of Marine Systems*, 33-34:133–154.

Marini, M. and Grilli, F. (2023). The role of nitrogen and phosphorus in eutrophication of the northern adriatic sea: History and future scenarios. *Applied Sciences*, 13(16):9267.

McClain, C. R., Feldman, G. C., and Hooker, S. B. (2006). An overview of the seawifs project and strategies for producing global, long-term ocean color data sets. *Proceedings of SPIE*, 5880:1–12.

Meli, M. (2024). The potential recording of north ionian gyre's reversals as a decadal signal in sea level during the instrumental period. *Scientific Reports*, 14:4907.

Mihanović, H., Vilibić, I., Carniel, S., Tudor, M., Russo, A., Bergamasco, A., et al. (2013). Exceptional dense water formation on the adriatic shelf in the winter of 2012. *Ocean Science*, 9:561–572.

Miller, C. B. (2004). *Biological Oceanography*. Blackwell Science, Malden, MA, 2nd edition.

Montanari, A., Nguyen, H., Rubinetti, S., Ceola, S., Galelli, S., Rubino, A., and Zanchettin, D. (2023). Why the 2022 po river drought is the worst in the past two centuries. *Science Advances*, 9:eadg8304.

Moriasi, D. N., Arnold, J. G., Van Liew, M. W., Bingner, R. L., Harmel, R. D., and Veith, T. L. (2007). Model evaluation guidelines for systematic quantification of accuracy in watershed simulations. *Transactions of the ASABE*, 50(3):885–900.

Mozetič, P., Solidoro, C., Cossarini, G., Socal, G., Precali, R., Francé, J., Bianchi, F., De Vittor, C., Smodlaka, N., and Fonda Umani, S. (2010). Recent trends towards oligotrophication of the northern adriatic: Evidence from chlorophyll-a time series. *Estuaries and Coasts*, 33(2):362–375.

Mueller, D. S., Wagner, C. R., Rehmel, M. S., Oberg, K. A., and Rainville, F. (2013). Measuring discharge with acoustic doppler current profilers from a moving boat. Technical report, U.S. Geological Survey, Techniques and Methods 3–A22.

Murphy, A. H. (1992). Skill scores based on the mean square error and their relationships to the correlation coefficient. *Monthly Weather Review*, 120(3):518–525.

Mussap, G. and Zavatarelli, M. (2017). A numerical study of the benthic–pelagic coupling in a shallow shelf sea (gulf of trieste). *Regional Studies in Marine Science*, 9:24–34.

Nash, J. and Sutcliffe, J. (1970). River flow forecasting through conceptual models part i — a discussion of principles. *Journal of Hydrology*, 10(3):282–290.

NEMO Consortium (2016). *Module eosbn2: EOS-80 Equation of State Implementation*. Documentazione ufficiale del modulo eosbn2.

Ø'Callaghan, J. M. and Stevens, C. L. (2017). Evaluating the surface response of discharge events in a new zealand gulf-rofi. *Frontiers in Marine Science*, 4:232.

Oddo, P., Falchetti, S., Viola, S., Pennucci, G., Storto, A., Borrione, I., Giorli, G., Cozzani, E., Russo, A., and Tollefsen, C. (2022). Evaluation of different maritime rapid environmental assessment procedures with a focus on acoustic performance. *The Journal of the Acoustical Society of America*, 152(5):2962–2981.

Oddo, P. and Guarnieri, A. (2011). A study of the hydrographic conditions in the adriatic sea from numerical modelling and direct observations (2000–2008). *Ocean Science*, 7:549–567.

Oddo, P. and Pinardi, N. (2008). Lateral open boundary conditions for nested limited area models: A scale selective approach. *Ocean Modelling*, 20(2):134–156.

Oddo, P., Pinardi, N., and Zavatarelli, M. (2005). A numerical study of the interannual variability of the adriatic sea (2000–2002). *Science of The Total Environment*, 353(1):39–56. Mucilages in the Adriatic and Tyrrhenian Seas.

Oke, P. R., Sakov, P., Cahill, M., Dunn, J., Feng, M., Griffin, D. A., Holbrook, N. J., Ridge, C., Schiller, A., and Webster, I. (2002). A comparison of three two-way nested regional ocean models. *Continental Shelf Research*, 25(7-8):883–902.

Oppenheim, A. V. and Schafer, R. W. (2014). *Discrete-Time Signal Processing*. Prentice Hall.

Orlanski, I. (1976). A simple boundary condition for unbounded hyperbolic flows. *Journal of Computational Physics*, 21(3):251–269.

Pedregosa, F., Varoquaux, G., Gramfort, A., Michel, V., Thirion, B., Grisel, O., Blondel, M., Prettenhofer, P., Weiss, R., Dubourg, V., Vanderplas, J., Passos, A., Cournapeau, D., Brucher, M., Perrot, M., and Duchesnay, E. (2011). Scikit-learn: Machine learning in python. *Journal of Machine Learning Research*, 12:2825–2830.

Penna, A., Capellacci, S., and Ricci, F. (2004). The influence of the po river discharge on phytoplankton bloom dynamics along the coastline of pesaro (italy) in the adriatic sea. *Marine Pollution Bulletin*, 48:321–326.

Percival, D. B. and Walden, A. T. (1993). *Spectral Analysis for Physical Applications*. Cambridge University Press.

Percival, D. B. and Walden, A. T. (2000). *Wavelet Methods for Time Series Analysis*. Cambridge University Press.

Pisano, A., Fanelli, C., Massi, A., Tronconi, C., Cesarini, C., La Padula, F., Buongiorno Nardelli, B., and Ciani, D. (2024). *Sea Surface Temperature Production Centre: Mediterranean Sea and Black Sea SST Reprocessing (QUID) – Products: SST_MED_SST_L4_REP_OBSERVATIONS_010_021, SST_BS_SST_L4_REP_OBSERVATIONS_010_022, SST_BS_PHY_L3S_MY_010_041, SST_MED_PHY_L3S_MY_010_042*. Copernicus Marine Environment Monitoring Service (CMEMS), issue 4.0 edition. Approval date: 15/11/2024.

Polimene, L. et al. (2006). The adriatic sea ecosystem seasonal cycle: validation of a coupled physical–biogeochemical model. *Journal of Geophysical Research: Oceans*, 111:C03S14.

Pranić, P., Denamiel, C., Janeković, I., and Vilibić, I. (2023). Multi-model analysis of the adriatic dense-water dynamics. *Ocean Science*, 19:649–670.

Pranić, P., Denamiel, C., and Vilibić, I. (2024). Kilometre-scale assessment of the adriatic dense water multi-decadal dynamics. Preprint.

Press, W. H., Teukolsky, S. A., Vetterling, W. T., and Flannery, B. P. (2007). *Numerical Recipes 3rd Edition: The Art of Scientific Computing*. Cambridge University Press.

Rantz, S. E. et al. (1982). *Measurement and Computation of Streamflow: Volume 1. Measurement of Stage and Discharge*. U.S. Geological Survey Water-Supply Paper 2175.

Reffray, G., Bourdallé-Badie, R., and Calone, C. (2015). Modelling turbulent vertical mixing sensitivity using a 1-d version of nemo. *Geoscientific Model Development*, 8(1):69–86.

Reynolds, R. W., Smith, T. M., Liu, C., Chelton, D. B., Casey, K. S., and Schlax, M. G. (2007). Daily high-resolution-blended analyses for sea surface temperature. *Journal of Climate*, 20(22):5473–5496.

Ricci, F., Capellacci, S., Campanelli, A., Grilli, F., Marini, M., Penna, A., et al. (2022). Long-term dynamics of annual and seasonal physical and biogeochemical properties: Role of minor river discharges in the north-western adriatic coast. *Estuarine, Coastal and Shelf Science*, 272:107902.

Rousseeuw, P. J. (1987). Silhouettes: a graphical aid to the interpretation and validation of cluster analysis. *Journal of Computational and Applied Mathematics*, 20:53–65.

Rubino, A., Gačić, M., Bensi, M., Kovacević, V., et al. (2020). Experimental evidence of long-term oceanic circulation reversals without wind influence in the north ionian sea. *Scientific Reports*, 10:1905.

Scroccaro, I., Zavatarelli, M., Lovato, T., Lanucara, P., and Valentini, A. (2022). The northern adriatic forecasting system for circulation and biogeochemistry: Implementation and preliminary results. *Water*, 14(17):2729.

Smith, J. O. (1997). *Introduction to Digital Filters: With Audio Applications*. W3K Publishing.

Solidoro, C., Bastianini, M., Bandelj, V., Codermatz, R., Cossarini, G., Melaku Canu, D., Ravagnan, E., Salon, S., and Trevisani, S. (2009). Current state, scales of variability, and trends of biogeochemical properties in the northern adriatic sea. *Journal of Geophysical Research: Oceans*, 114:C07S91.

Song, Y. T. and Haidvogel, D. B. (1994). A semi-implicit ocean circulation model using a generalized topography-following coordinate system. *Journal of Computational Physics*, 115(1):228–244.

Spalding, M., Fox, H., Allen, G., Davidson, N., Ferdaña, Z., Finlayson, M., Halpern, B., Jorge, M., Lombana, A., Lourie, S., Recchia, C., and Robertson, J. (2007). Marine ecoregions of the world: A bioregionalization of coastal and shelf areas. *BioScience*, 57(7):573–583.

Stachowitsch, M. (1991). Anoxia in the northern adriatic sea: rapid death, slow recovery. *Geological Society, London, Special Publications*, 58:119–129.

Stow, C. A., Bricker, S. B., Millard, E., et al. (2009). Application of a novel efficiency metric to model assessment: The modeling efficiency factor. *Environmental Modelling & Software*, 24:1020–1030.

Strang, G. (1968). On the construction and comparison of difference schemes. *SIAM Journal on Numerical Analysis*, 5(3):506–517.

Supić, N. and Vilibić, I. (2006). Dense water characteristics in the northern adriatic in the 1967–2000 interval with respect to surface fluxes and po river discharge rates. *Estuarine, Coastal and Shelf Science*, 66:580–593.

Taylor, K. E. (2001). Summarizing multiple aspects of model performance in a single diagram. *Journal of Geophysical Research: Atmospheres*, 106(D7):7183–7192.

Torrence, C. and Compo, G. P. (1998). A practical guide to wavelet analysis. *Bulletin of the American Meteorological Society*, 79(1):61–78.

Umlauf, L. and Burchard, H. (2003). A generic length-scale model for geophysical turbulence closure. *Journal of Marine Research*, 61:235–265.

UNESCO - International Council for the Exploration of the Sea (1980). International Equation of State of Seawater – 1980 (EOS-80). Technical Report 56, Intergovernmental Oceanographic Commission, UNESCO, Paris. Report of the Joint Panel on Oceanographic Tables and Standards.

van Leer, B. (1979). Towards the ultimate conservative difference scheme. II. MUSCL scheme. *Journal of Computational Physics*, 32:101–136.

Verri, G. et al. (2022). Climate projections of salt-wedge intrusions in a po river delta. *Preprint*.

Vichi, M., Lovato, T., Butenschön, M., Tedesco, L., Lazzari, P., Cossarini, G., Masina, S., Pinardi, N., Solidoro, C., and Zavatarelli, M. (2023). *The Biogeochemical Flux Model (BFM): Equation Description and User Manual*. Bologna, Italy, release 1.3 edition. BFM version 5.3, pp. 104.

Vichi, M., Zavatarelli, V., and Pinardi, N. (1998). Seasonal modulation of microbially mediated carbon fluxes in the northern adriatic sea: a model study. *Marine Ecology Progress Series*, 173:57–71.

Vilibić, I., Pranić, P., and Denamiel, C. (2023). North adriatic dense water: lessons learned since the pioneering work of mira zore-armanda 60 years ago. *Acta Adriatica*, 64(1):53–78.

Vodopivec, M., Zaimi, K., and Peliz, Á. (2022). The freshwater balance of the adriatic sea: A sensitivity study. *Journal of Geophysical Research: Oceans*, 127(11):e2022JC018870.

Volpe, G., Colella, S., Brando, V. E., Forneris, V., Padula, F. L., Di Cicco, A., Sammartino, M., Pisano, A., Sprovieri, M., Burca, M., and Santoleri, R. (2019). Mediterranean ocean colour level 3 operational multi-sensor processing. *Ocean Science*, 15(1):127–146.

Vörösmarty, C. J., Fekete, B. M., and Tucker, B. A. (2003). Po river, pontelagoscuro (gauging station) — discharge datasets (pangaea). `https://doi.pangaea.de/10.1594/PANGAEA.96881`.

Wang, X., Pinardi, N., Zavatarelli, M., Bortoluzzi, G., Russo, A., Vichi, M., Fonda Umani, S., Solidoro, C., Falcieri, F., and Tesi, T. (2005). A study of the hydrographic conditions in the adriatic sea from numerical modelling and direct observations (2000–2008). *Ocean Science*, 1(1):1–21.

Welch, P. D. (1967). The use of fast fourier transform for the estimation of power spectra: A method based on time averaging over short, modified periodograms. *IEEE Transactions on Audio and Electroacoustics*, 15(2):70–73.

Willmott, C. J. (1981). On the validation of models. *Physical Geography*, 2(2):184–194.

Witkin, A. P. (1983). Scale-space filtering. In *Proceedings of the 8th International Joint Conference on Artificial Intelligence (IJCAI)*, pages 945–951, Karlsruhe, Germany.

Zanchettin, D., Traverso, P., and Tomasino, M. (2008). Po river discharges: A preliminary analysis of a 200-year time series. *Climatic Change*, 89(3–4):411–433.

Zavatarelli, M., Baretta, J. W., Baretta-Bekker, J. G., and Pinardi, N. (2000). The dynamics of the adriatic sea ecosystem: An idealized model study. *Deep-Sea Research Part I: Oceanographic Research Papers*, 47(5):937–970.

Zavatarelli, M. and Pinardi, N. (2003). The adriatic sea modelling system: a nested approach. *Annales Geophysicae*, 21:345–364.

Zhou, K., He, Z., Xiao, M., and Zhang, Z. (2014). Parallel monte carlo simulation of aerosol dynamics. *Advances in Mechanical Engineering*, 2014:1–12.